Research Report

DETERMINING BEARING STRESS FOR MSE RETAINING STRUCTURES

Submitted to the

Alabama Department of Transportation

Prepared by

J. Brian Anderson
Chukwuma C. Okafor

July 2024

Highway Research Center
Harbert Engineering Center
Auburn University, Alabama 36849

1. Report No.	2. Government Accession No.	3. Recipient Catalog No.

4. Title and Subtitle **DETERMINING BEARING STRESS FOR MSE RETAINING STRUCTURES**	5. Report Date 6. Performing Organization Code
7. Author(s) J. Brian Anderson and Chukwuma C. Okafor	8. Performing Organization Report No.
9. Performing Organization Name and Address Highway Research Center Department of Civil and Environmental Engineering 238 Harbert Engineering Center Auburn, AL 36849	10. Work Unit No. (TRAIS) 11. Contract or Grant No.
12. Sponsoring Agency Name and Address Highway Research Center Department of Civil and Environmental Engineering 238 Harbert Engineering Center Auburn, AL 36849	13. Type of Report and Period Covered 14. Sponsoring Agency Code

15. Supplementary Notes

16. Abstract

This study investigated the bearing stress imparted by a Mechanically Stabilized Earth (MSE) retaining system. Use of the MSE system is notable for the associated cost efficiency, flexibility, and high deformation tolerance compared to traditional concrete retaining systems. There have been recent cases highlighting the need for substantial foundation strengthening in MSE walls to satisfy bearing capacity requirements. Meanwhile, current methods used for design stress estimation in such flexible structures might be inadequate, as it does not account for many of the features that make an MSE system an attractive option, hence, it is important to study the performance of a full scale MSE system. This research utilized full-scale testing and numerical simulations to examine the mechanical behavior of MSE systems and developed numerical models to simulate the experimental setup. Two alternative bearing stress functions are presented over the conventional rigid block assumption, which tends to overestimate stresses:

$\sigma_v = \frac{W_{fill} + qL}{L}$ or $\sigma_v = \frac{W_{fill} + qL - P_v}{L}$ when $H \le 6m$ where: W_{fill} is weight of the MSE reinforced fill, q is the traffic surcharge stress, L is the width of the MSE reinforced fill, H is the height of the MSE reinforced fill, P_v is the vertical loading on the facing panels due to friction. The results from these alternatives showed stress magnitudes that were closer to the measured stresses as well as the stresses from numerical simulations indicating better suitability in estimating the bearing stress for reinforced soil walls.

17. Key Words: mechanically stabilized earth, retaining wall, bearing capacity, full scale test	18. Distribution Statement No restrictions. This document is available to the public through the National Technical Information Service, Springfield, Virginia 22161

19. Security Classification (of this report) Unclassified	20. Security Classification (of this page) Unclassified	21. No. of pages	22. Price

FORM DOT F 1700.7

Research Report No.

DETERMINING BEARING STRESS FOR MSE RETAINING STRUCTURES

Submitted to the

Alabama Department of Transportation

Prepared by

J. Brian Anderson
Chukwuma C. Okafor

July 2024

DISCLAIMERS

The contents of this report reflect the views of the authors, who are responsible for the facts and the accuracy of the data presented herein. The contents do not necessarily reflect the official views or policies of Auburn University or the Federal Highway Administration. This report does not constitute a standard, specification, or regulation.

NOT INTENDED FOR CONSTRUCTION, BIDDING, OR PERMIT PURPOSES

J. Brian Anderson, Ph.D., P.E.

Research Supervisor

ABSTRACT

This study investigated the bearing stress imparted by a Mechanically Stabilized Earth (MSE) retaining system. Use of the MSE system is notable for the associated cost efficiency, flexibility, and high deformation tolerance compared to traditional concrete retaining systems. There have been recent cases highlighting the need for substantial foundation strengthening in MSE walls to satisfy bearing capacity requirements. Meanwhile, current methods used for design stress estimation in such flexible structures might be inadequate, as it does not account for many of the features that make an MSE system an attractive option, hence, it is important to study the performance of a full scale MSE system. This research utilized full-scale testing and numerical simulations to examine the mechanical behavior of MSE systems and developed numerical models to simulate the experimental setup. Two alternative bearing stress functions are presented over the conventional rigid block assumption, which tends to overestimate stresses:

$$\sigma_v = \frac{W_{fill} + qL}{L} \text{ or } \sigma_v = \frac{W_{fill} + qL - P_v}{L} \text{ when } H \le 6m$$

where:
- W_{fill} is weight of the MSE reinforced fill
- q is the traffic surcharge stress
- L is the width of the MSE reinforced fill
- H is the height of the MSE reinforced fill
- P_v is the vertical loading on the facing panels due to friction

The results from these alternatives showed stress magnitudes that were closer to the measured stresses as well as the stresses from numerical simulations indicating better suitability in estimating the bearing stress for reinforced soil walls.

ACKNOWLEDGEMENTS

This project was sponsored by the Alabama Department of Transportation (ALDOT) - Project 930-961. The funding, cooperation, and assistance of many individuals from each of these organizations are gratefully acknowledged. The researchers acknowledge the assistance and patience of Bureau of Materials and Tests current and past personnel, namely Scott George and Kaye Davis.

This project would not have been possible to complete without the Advanced Structural Engineering Laboratory at Auburn University. ASEL would not have been possible without the efforts of Alabama Governor Kay Ivey, Auburn University President Christopher Roberts, and Auburn Senior Vice President for Research Steven Taylor.

ASEL professional personnel and researchers were essential to the experiment. The researchers acknowledge Ashton Babb, Rob Crosby, Caleb Fleming, Josh McLeod, Sam Dunlop, Guy Biessan, Tyler Belk, Anthony Mathews, Augie Loehr, George Cowles, Haden Jackson, and Eddierobert Polanco-Nova.

Materials for construction of the laboratory MSE experiment were generously provided by our partners at Keely Tayloe and Tim Garrett at Vulcan Materials, Keith Brabant, David Hutchinson, Peter Anderson, Mark Goode, Anthony Fisher with the Reinforced Earth Company, and Robert King at Tencate Geosynthetics.

TABLE OF CONTENTS

LIST OF TABLES

LIST OF FIGURES

CHAPTER 1: INTRODUCTION

1.1 Background

The construction of new or expansion of existing roadways often requires establishing grade separation. While sloping is an option, very often, difficult access, limited real estate and limited right-of-way inhibits the use of stable slopes. Earth retention systems (retaining walls) provide the required grade changes within the limited amount of right-of-way. There are several types of retaining walls used in highway infrastructure: concrete cantilever, sheet piling, soil nails, mechanically stabilized earth (MSE) walls, geosynthetic reinforced soil (GRS) walls, etc.

The MSE system is a special type of retaining wall that uses tensile inclusions to reinforce soil and improve shear strength. Soil is sufficiently strong in compression but easily fails when a tensile force is applied. Most failures manifest as shear failure, occurring when the applied shear stress is greater than the shear strength of the soil. Randomly placed reinforcement elements (analogous to fiber reinforced soil or fiber reinforced concrete) increase the shear strength of the soil, thereby increasing the amount of stress that can be applied before failure (Clayton et al. 2014). These tensile elements, when placed in a definite manner result in a composite of soil and reinforcement, exhibiting a strength increase based on soil-reinforcement frictional interaction, hence, the term “reinforced soil”. This concept is largely attributed to French architect, Henri Vidal who experimented using sand and pine needles and patented the reinforced earth technology in 1963. (Schlosser and Bastick 1991).

Compared to other conventional retention system (e.g., reinforced concrete walls), MSE walls offer a host of advantages including but not limited to less site preparation, less space requirement for construction, less time and construction equipment requirement, less foundation

support requirement, higher settlement tolerance, and cost effectiveness. MSE walls offer significant cost advantages compared to reinforced concrete wall systems at sites with poor foundation soils. The elimination of costs for foundation improvements such as stone columns, piles, and pile caps in cases where the foundation soils are weak have resulted in cost savings of greater than 50 percent on completed projects (Berg et al. 2009). MSE technology has a broad range of applications including but not limited to highways grade separation, access ramps, true bridge abutments, railway track beds, protective structures, waterways, waterfront structures and dams.

A typical MSE wall system (Figure 1) consists of the original ground, a concrete leveling pad, wall facing panels and coping, soil reinforcements, select backfill material, and any loads and surcharges. Facings used for MSE walls, which are typically proprietary, include segmental precast panels, dry-cast modular blocks, metallic series of interconnected half cylinders, welded wire grids, gabions, and geosynthetics. The reinforcement for an MSE wall can be either metallic or various types of geosynthetic reinforcements. Metallic reinforcements include welded wire mesh and steel strip and bar mats. Geosynthetic reinforcements include high-density polyethylene geogrids, PVC coated polyester geogrids, geosynthetic strips, and geotextiles.

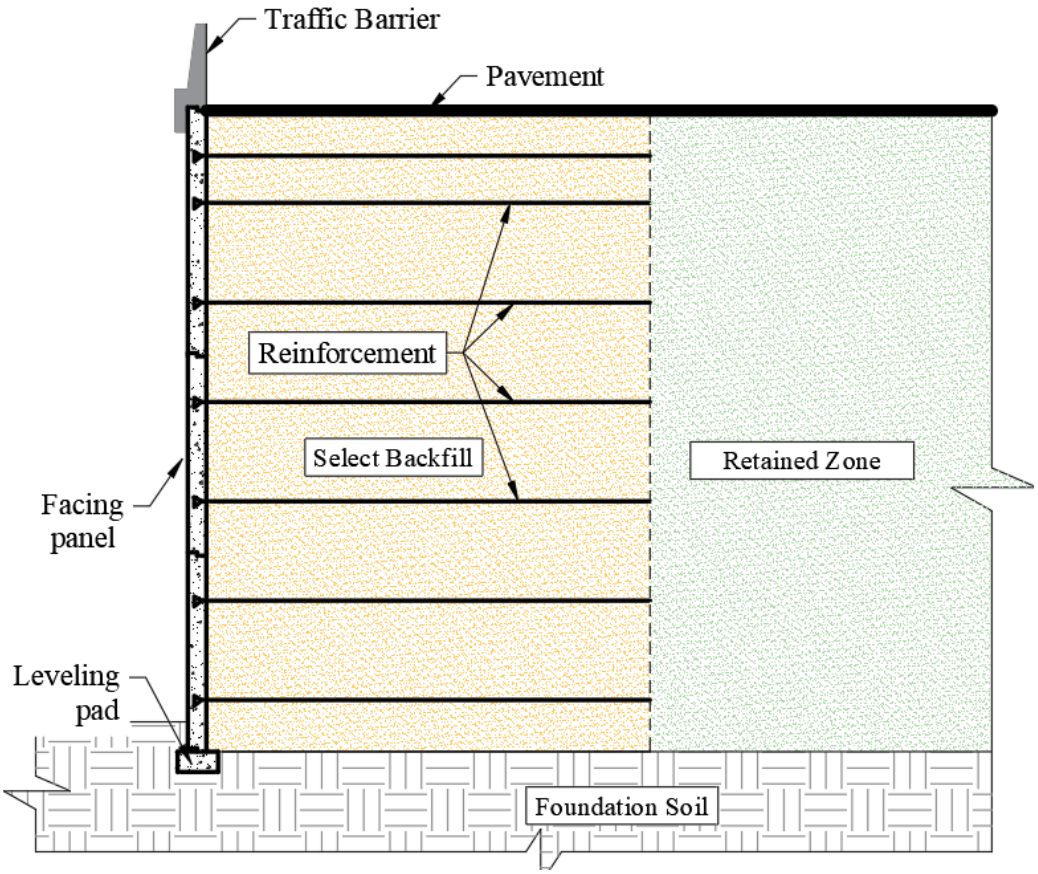

Figure 1. Typical section of an MSE wall.

1.2 Problem Statement

The largest loads from an MSE structure are often due to the mass of reinforced backfill. The foundations soils beneath the backfill must have sufficient bearing capacity so that the MSE wall and backfill meets both strength and serviceability limit states. According to Alabama Department of Transportation's Bureau of Materials and Tests, there have been many recent cases where MSE walls required significant, costly foundation strengthening to meet bearing capacity requirements. As stated in the guidelines for the design and construction of MSE walls (FHWA GEC 11 Berg et al. 2009), one of the major benefits of the MSE system over conventional reinforced concrete type walls is the ability to tolerate more deformations which can result in stress release and redistribution. However, the design approach for the bearing capacity requirements

uses the Meyerhof method which assumes that the MSE system is rigid. Hence, the guidance for estimation of bearing stresses from FHWA GEC 11 (Berg et al. 2009) may be too conservative and the foundation stresses due to the MSE retaining structures are significantly lower than those used in design. It would be useful to measure the stresses at the base of an MSE retaining structure to verify these contact stresses, and possibly develop a modified approach to determining the design stress distribution peculiar to the MSE system.

It is understood that the impact of bearing capacity on MSE type structures is a combination of the available foundation strength as well as the load imposed by the horizonal, or sloping backfill. It is hypothesized that the uncertainty in either or both quantities contribute to the perceived discrepancy in the true bearing capacity.

The assumption of a rigid mass and the use of the Meyerhof approach in the bearing capacity check penalizes the design two folds. By reducing the width from the reinforced length to an effective length ($L' = L - 2e$, considering eccentricity), the bearing stress is increased, and the bearing capacity is reduced.

Also, the lateral stress from the retained soil is considered in calculating eccentricity but ignored in the forces contributing to the bearing stress (i.e., assuming that the interface friction between the reinforced zone and the retained zone is zero). It is unclear how this affects bearing stress and bearing capacity; however, this study will focus on the vertical stress exerted by the MSE system on the foundation. This is clearly not to question Meyerhof's solution for eccentrically loaded rigid footings but rather its suitability for the flexible MSE system.

While the design guidelines clearly state that MSE structures are suited to areas where foundation soils are poor, the design consideration in evaluating external stability assumes a rigid

structure constructed on a competent foundation to satisfy the bearing capacity requirement. It is important to understand how the presence of soft spots and differential settlement in the foundation affects the bearing stresses.

One may ask if this work is necessary since the design guidelines have successfully provided safe MSE structures, but masking analytical flaws with safety factors does not provide optimal design outcomes. This has resulted in money spent for costly foundation remediation programs for existing MSE walls, however, while such elaborate programs can be justified for cases where excessive settlement is expected, they should not be justified based on bearing requirements (bearing stress and bearing capacity) which have inherent inconsistencies. Moreso, there are other ways of dealing with issues of settlement (like surcharging) which may require less money and construction time.

1.3 Research Objective

The objective of this study was to determine the stress distribution at the base of the reinforced mass, and to present a simple alternative function(s) to estimate the foundation bearing stresses in order to minimize the over-conservatism associated with current design methods.

1.4 Scope of Work

The scope of work to complete the research objective includes:

- Instrumentation of a typical MSE wall with pressure cells to measure the vertical stresses beneath the wall.
- Observing the performance of an MSE wall when subjected to differential settlement.
- Observation of the stress redistribution behavior of the MSE technology by including a poor bearing zone.

- Conducting three-dimensional finite element modeling to simulate the instrumented walls and additional MSE walls configurations.
- Presenting alternatives for predicting bearing stress at the base of MSE retaining structures based on the results of the field testing, soil properties, and finite element models.
- Provide recommendations regarding the current design guidelines.

1.5 Research Methodology

A full scale, steel-reinforced, mechanically stabilized earth wall was constructed, instrumented, and monitored in the laboratory. Vibrating wire earth pressure cells were used to monitor the bearing stresses at the foundation level. Foil strain gages were used to monitor strain development in the steel straps. Draw wire potentiometers were used to measure facing lateral displacement. Two inclinometer casings were used to monitor lateral movement within the reinforced backfill, one for the slope inclinometer and the other for the in-place shape array (SAAV). Settlement plates were used to monitor settlement at the foundation. Air bladders were used to introduce soft spots in the foundation to simulate poor bearing capacity and differential settlement in those spots. Finally, sandbags were used to simulate a normal traffic surcharge, and concrete beams were used to increase the surcharge load. The effects of localized soft spots within the foundation and induced differential settlement on the bearing stress distribution at the foundation level were studied.

Finite element modeling using Plaxis-3D was used to further the study of the factors affecting the bearing stress. Factors such as wall height, facing-reinforced zone friction, magnitude of compaction, soil-reinforcement interface, reinforced fill properties, retained fill properties, foundation stiffness, reinforcement stiffness and reinforcement length were considered in a

parametric study which were then compared to the presented functions used in the estimation of the bearing stresses at the base of an MSE wall.

CHAPTER 2: REVIEW OF RELEVANT LITERATURE

2.1 Shear Strength Theory

Soils have sufficient strength in resisting compressive stresses but mostly fail in shear as a result of the application of excessive shear stress (Holtz and Kovacs 1981). The soil grains tend to slide over one another on a plane called the failure plane. Geotechnical designs are mostly based on knowing the line in space on the shear-normal stress plot which approximates the behavior of soils at failure. Mohr (1900) proposed a failure criterion (equation 1) stating that materials (soils) fail when the shear stress on the failure plane at failure reaches some unique function of the normal stress on that plane.

$$\tau_{ff} = f(\sigma_{ff}) \tag{1}$$

where τ_{ff} and σ_{ff} are the shear stress on and normal stress on the failure plane at failure respectively.

If the principal stress at failure of an element is known, the Mohr circle can be sketched to represent the state of stress for the element, conversely, the limiting envelope of the shear stress then gives the Mohr failure envelop below which any Mohr circle would represent a stable stress condition.

Coulomb (1776) also developed two components of the shear strength from studies on lateral pressure exerted on retaining walls. The stress-dependent component was called the angle of internal friction (ϕ) and the stress-independent component was the intrinsic cohesion (c). Coulomb's components are presented in equation 2.

$$\tau_f = \sigma \tan\phi + c \tag{2}$$

where τ_f and σ are the shear strength and applied normal stress respectively.

A combination of Mohr and Coulomb components became the Mohr-Coulomb failure criterion expressed in equation 3. This expression gives a linear approximation of the true behavior of soil.

$$\tau_{ff} = \sigma_{ff} \tan\phi + c \tag{3}$$

where τ_{ff} is the shear strength at failure on the failure plane and σ_{ff} is the applied normal stress at failure on the failure plane.

Various laboratory and field tests are used to determine the shear strength of soil which involves determining the Mohr-Coulomb failure envelope which defines the state of stress at failure. Laboratory tests commonly used are the direct shear test and the triaxial test. Vane shear test directly measures shear strength in the field, while other field tests like the standard penetration test (SPT) and the cone penetration test (CPT) rely on correlations.

2.2 Earth Retaining Structures

But for exceptional cases, excavations of significant height in soil without support cannot stay intact over time. Retaining walls are usually needed to give support to soil with a purely vertical or almost vertical side. This is often needed for several reasons including but not limited to providing grade separation requirements for construction of new or expansion of existing highway infrastructure, providing platforms by excavating into existing grade, bridge deck abutments, quay structures, etc.

There are many types of retaining structures, most of which can be classified into gravity walls, embedded walls, and composite walls (Clayton et al. 2014, Potts and Zdravkovic 2001).

Gravity walls primarily rely on the self-weight of the wall material to resist driving forces, therefore, they are typically large masses of rocks, or mass concrete. Embedded walls rely on the moment capacity of structural members sufficiently embedded into the ground. Examples include sheet-pile walls (steel) and bored-pile walls (reinforced concrete). Additional support can be provided to the upper part of the wall by propping, or by anchoring into the natural ground on the retained side of the wall (Clayton et al. 2014). Composite walls are based on combining the working principles of gravity and embedded walls. Ground anchors with facing units and sheet piles with select backfill are also classified as composite walls (Clayton et al. 2014) but the most common forms are reinforced earth systems using granular backfill and tensile inclusions.

Retaining walls are also classified based on the construction method typically bottom-up construction and top-bottom construction. The suitability of either choice depends on the nature of the project as most excavation projects require a top-down construction while most embankment projects require a bottom-top construction. Furthermore, gravity walls are mostly bottom-top constructed, embedded walls are mostly top-bottom constructed and composite walls can be either top-bottom or bottom-top constructed.

2.3 Earth Pressure Theory

Most forces acting on retaining walls are from lateral earth pressure. Most retaining walls are equipped with drainage systems to avoid water build up, but hydrostatic pressure can also be considered, and in some cases, can be the largest load on the wall. The lateral earth pressure is commonly determined by multiplying the effective vertical earth pressure by a constant K_H. The constant K_H is the coefficient of lateral earth pressure and is the ratio of the horizontal effective stress to the vertical effective stress. At any point along the wall profile, the vertical effective stress

is calculated using equations 4 and 5 based on the effective stress principle. Then the lateral earth pressure can then be calculated using equations 6 and 7.

$$\sigma'_v = \sigma_v - u \tag{4}$$

$$\sigma'_v = \gamma_{soil} H \tag{5}$$

$$\sigma'_h = K_H \sigma'_v \tag{6}$$

$$\sigma_h = K_H \sigma'_h + u \tag{7}$$

where: σ' is the effective stress

σ is the total stress

σ'_v is the effective vertical stress

γ_{soil} is the soil unit weight

H is the depth through soil to the point of interest

u is the pore water pressure ($u = \gamma_w H_w$)

γ_w is the unit weight of water

H_w is the water pressure head measured to the point of interest

σ'_h is the effective horizontal stress

σ_h is the total horizontal stress

There are typically three coefficients of lateral earth pressure all describing three different states of lateral earth pressure depending on the type of wall movement, namely, earth pressure

coefficient at rest (K_o), active earth pressure coefficient (K_a), and passive earth pressure coefficient (K_p).

2.3.1 Coefficient of Lateral Earth Pressure at Rest

The lateral earth pressure at rest is the horizontal component of the earth pressure when there is no lateral soil deformation (i.e., rigid systems). The lateral earth pressure is calculated by multiplying the vertical stress by the earth pressure coefficient at rest (K_o). At this state, the Mohr circle does not touch the failure Mohr-Coulomb failure envelope (Figure 3) indicating that failure has not occurred. K_o is estimated using equations 8 through 11.

- For cohesionless soils (Jaky 1948):

$$K_o = 1 - \sin\phi' \tag{8}$$

- For cohesionless soils with sloping backfill (Kezdi 1972 after Jaky):

$$K_{o\beta} = (1 - \sin\phi')(1 + \sin\beta) \tag{9}$$

- For cohesive soils (Tschebotarioff 1973):

$$K_o = \frac{v}{1 - v} \tag{10}$$

- For over-consolidated soils (Mayne and Kulhawy 1982):

$$K_{o(OC)} = K_{o(NC)} OCR^{\sin\phi'} \tag{11}$$

where: ϕ' is effective friction angle.

β is backfill slope angle from horizontal.

v is void ratio.

OCR is over-consolidation ratio.

2.3.2 Rankine and Coulomb Theories on Active and Passive Stress States

Rankine (1857) and Coulomb (1776) methods are the most frequently used in determining active and passive earth pressure coefficients. As the wall moves relative to the supported soil, the shear stress in the soil mass increases and eventually, the shear strength is fully mobilized, and shear failure occurs.

The stress state is considered active if the wall tends to move away from the soil mass. For the active case, K_o decreases till it reaches the value of the active lateral earth pressure coefficient (K_a). This reduction results in a lower minor principal stress compared to the "at-rest" state, the Mohr's circle, while increasing due to an increased differential between vertical and horizontal stresses, shifts to the left (Figure 3) till it touches the failure envelope indicating failure.

The stress state is passive if the wall tends to push into the soil mass. For the passive case, K_o increases until it reaches the value of the passive lateral earth pressure coefficient (K_p). This increase results in a much larger major principal stress compared to the "at-rest" state, the Mohr's circle, while increasing due to the difference between vertical and horizontal stresses, shifts to the right (Figure 3) till it touches the failure envelope indicating failure.

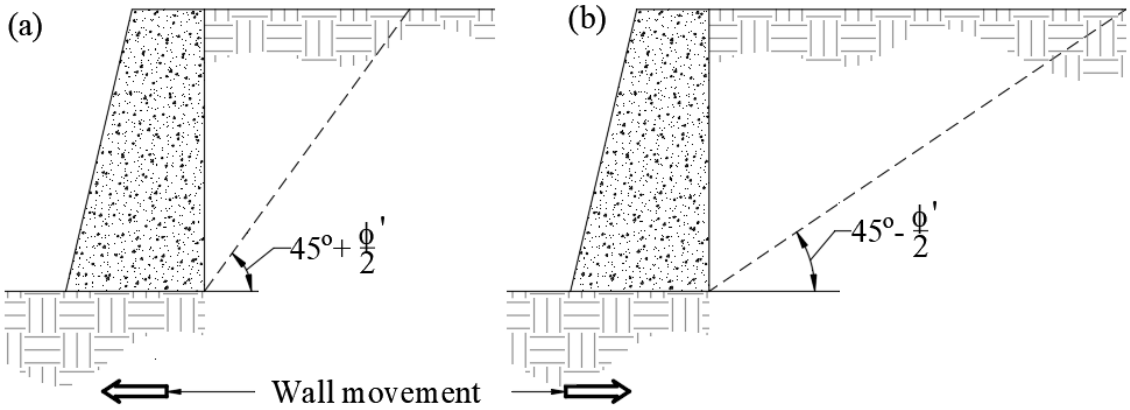

Figure 2. Failure plane and wall movement direction for (a) active state and (b) passive state.

It is important to note that the linear failure wedge is from an idealized case of a rigid wall rotating about the toe (Clayton et al. 2014), the movement of most retaining walls are more complex and the failure wedge resulting from such movements is not linear. For most general cases of a soil whose failure is governed by a Mohr-Coulomb criterion, and which has a friction component, the correct failure surface under active conditions consists of a log spiral, however, in the active state, the log-spiral shape is reasonably approximated by a straight line, and the resultant load predicted using the simple straight-line failure mechanism is within 10 percent of that obtained with the more exact log-spiral mechanism (Clough and Duncan 1991).

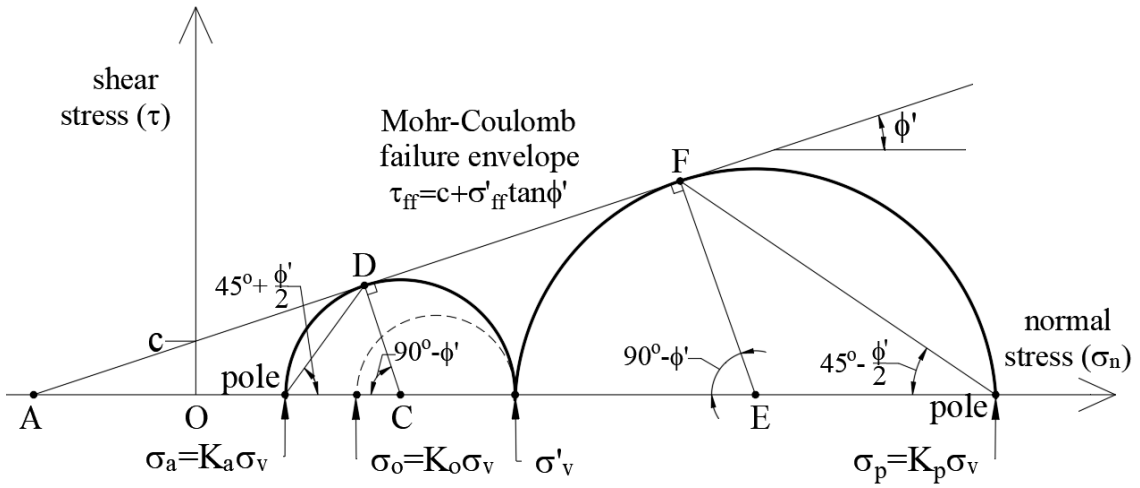

Figure 3. Soil stress states for at rest, active and passive conditions.

The most common expressions used to estimate the coefficient based on both active and passive states (K_a and K_p) are outlined in equations 12 through 17 assuming plane strain conditions.

- For the simple case of a smooth, rigid, vertical wall supporting a horizontal granular backfill, based on Rankine's theory:

$$K_a = \frac{1-\sin\phi'}{1+\sin\phi'} = \tan^2\left[45-\frac{\phi'}{2}\right] \tag{12}$$

$$K_p = \frac{1+\sin\phi'}{1-\sin\phi'} = \tan^2\left[45+\frac{\phi'}{2}\right] = \frac{1}{K_a} \tag{13}$$

- For the case of a vertical wall supporting an inclined granular backfill, based on Rankine's theory:

$$K_a = \cos\beta\left[\frac{\cos\beta-\sqrt{(\cos^2\beta-\cos^2\phi'}}{\cos\beta+\sqrt{(\cos^2\beta-\cos^2\phi'}}\right] \tag{14}$$

$$K_p = \cos\beta\left[\frac{\cos\beta + \sqrt{(\cos^2\beta - \cos^2\phi')}}{\cos\beta - \sqrt{(\cos^2\beta - \cos^2\phi')}}\right] \quad (15)$$

- Coulomb's theory considering wall-fill friction, fill inclination, and wall back face angle with vertical:

$$K_a = \frac{\sin^2(\theta+\phi')}{\sin^2\theta\sin(\theta-\delta)\left[1+\sqrt{\frac{\sin(\phi'+\delta)\sin(\phi'-\beta)}{\sin(\theta-\delta)\sin(\theta+\beta)}}\right]^2} \quad (16)$$

$$K_p = \frac{\sin^2(\theta+\phi')}{\sin^2\theta\sin(\theta+\delta)\left[1-\sqrt{\frac{\sin(\phi'+\delta)\sin(\phi'-\beta)}{\sin(\theta-\delta)\sin(\theta+\beta)}}\right]^2} \quad (17)$$

where: δ is friction angle between wall and soil.

β is backfill slope angle from horizontal.

θ is the wall back face angle with vertical.

2.3.3 Wall Movement and Lateral Earth Pressure Coefficients

In general, wall movement directed away from the retained earth results in an active earth pressure state while movement that pushes against the retained earth results in a passive state. For normally consolidated granular fill, the movement required to reach passive state is much larger than that required to reach active state. This is because the volume of soil in passive failure wedge is larger than in the active state, hence a larger compressible volume. Also, the change in applied stress is larger in the passive state than in the active state. Therefore, in the passive case, more wall displacement is required before the shear stress is applied to the farthest part of the shear surface from the wall (Clayton et al. 2014). The movement required to reach minimum active or passive pressure is a function of the wall height and soil type (AASHTO 2014). Table 1 shows the ratio of

the required movement (δ_H) to the wall height (H) for different soil types (Clough and Duncan 1991)

Table 1. Required wall-soil relative movement to reach earth pressure states.

	δ_H/H	
Type of Backfill	**Active**	**Passive**
Dense sand	0.001	0.01
Medium dense sand	0.002	0.02
Loose sand	0.004	0.04
Compacted silt	0.002	0.02
Compacted lean clay	0.010	0.05
Compacted fat clay	0.010	0.05

2.4 Reinforced Earth Concept

The MSE technology was introduced by Henri Vidal in the 1960s (Clayton et al. 2014), but the concept of soil reinforcement has been around much longer dating back to the straw-reinforced bricks of the great wall of China (Jones 1996). The soil reinforcement technique is based on altering the stress patterns in a volume of soil using tensile elements, which enable the accommodation of higher applied loading (Clayton et al. 2014). Depending on the orientation of the tensile elements, the shear capacity of the soil could be increased (Woods and Jewell 1990), however, a direct idealization of an element of reinforcement, oriented at an angle using a direct shear box test, showed that the effect reduces the shear stress that the soil must resist and at the same time, increases the normal effective stress in the soil thus allowing for additional frictional resistance to be mobilized on the shear failure plane (Clayton et al. 2014, Woods and Jewell 1990, Jewell and Wroth 1987) (equations 18 and 19, Figure 4).

$$\sigma_n = \frac{(N + P_R \cos\theta)}{A} \tag{18}$$

$$\tau = \frac{(S - P_R \sin\theta)}{A} \tag{19}$$

where σ_n is the normal stress, τ is the shear stress, N is the normal force, S is the shear force, P_R is the tensile force in the reinforcement and A is the cross-sectional area of the test sample. The tensile reinforcements act advantageously when oriented in the same directions that the tensile strain from the shear loading occurs (Clayton et al. 2014). Ultimately, there is a stress transfer between the soil and reinforcement that takes place continuously along the reinforcement, improving the tensile properties of the composite because of the interaction between the reinforcement and the soil (Berg et al. 2009).

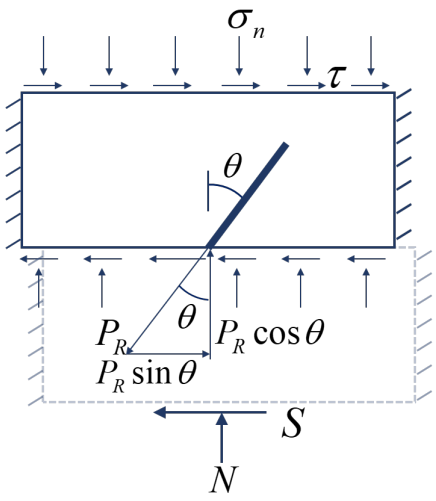

Figure 4. Direct idealization of the effect of a single reinforcement in a direct shear box test (after Woods and Jewell 1990).

Two popular concepts were used to evaluate the effect of reinforcement in increasing the shear strength of soils. Schlosser and Long (1974) proposed the concept of apparent anisotropic cohesion (Figure 5a). Anisotropic in the sense that the increase in strength only occurs in the horizontal (x-y) plane covered by the reinforcement and not in the vertical plane. This concept proposes a shear strength increase through a rise in the magnitude of the major principal stress, leading to a Mohr circle that exceeds the unreinforced soil failure envelop. A new envelope, drawn

for the reinforced Mohr circle leads to the idea of an apparent cohesion. The presence of geosynthetic reinforcement is said to give the soil an added anisotropic, apparent cohesion. This apparent cohesion, however, does not apply to cases at very low confining pressure (Ingold 1982). Yang (1972) proposed that the reinforcement causes an apparent increase in the confining pressure (Figure 5b). As the reinforced soil is loaded, tensile forces are generated in the reinforcement which then generates a reactive compressive force leading to the increase in the minor principal stress.

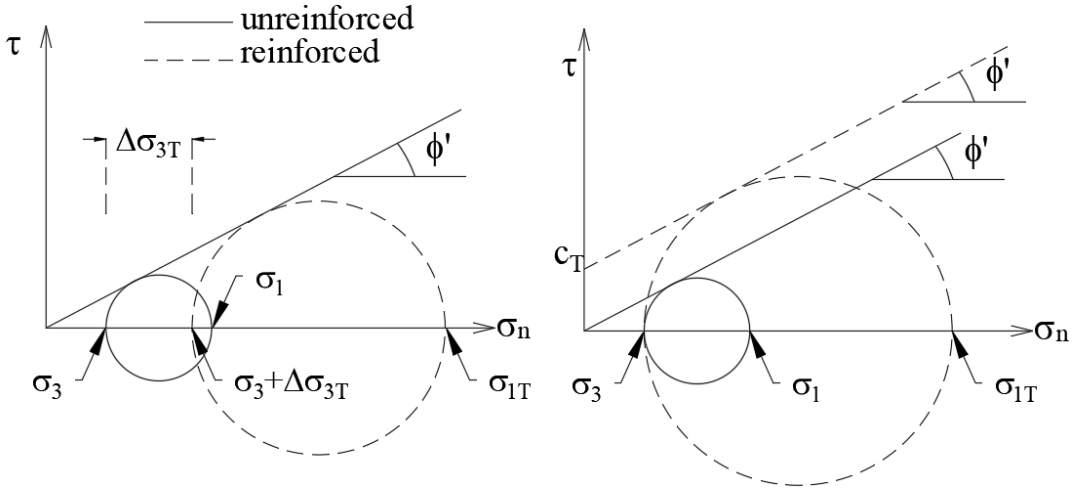

Figure 5. Concepts of soil reinforcement: (a) apparent confining pressure and (b) apparent anisotropic cohesion.

2.4.1 Stress Transfer Mechanism

The improvement of the soil-reinforcement composite is as a result of stress transfer between the soil and reinforcement. Depending on the geometric characteristics of the reinforcement, the stress transfer is either by pure friction, or passive resistance, or a combination of both.

Friction develops at locations where there is a relative shear displacement and corresponding shear stress between soil and the reinforcement surface (Figure 6). Reinforcing

elements dependent on friction should be aligned with the direction of soil reinforcement relative movement (Berg et al. 2009). This is the case for reinforcing elements with smooth uniform surfaces such as steel strips, longitudinal bars, geotextile, and geosynthetic straps. The primary mode of action of such elements is tension.

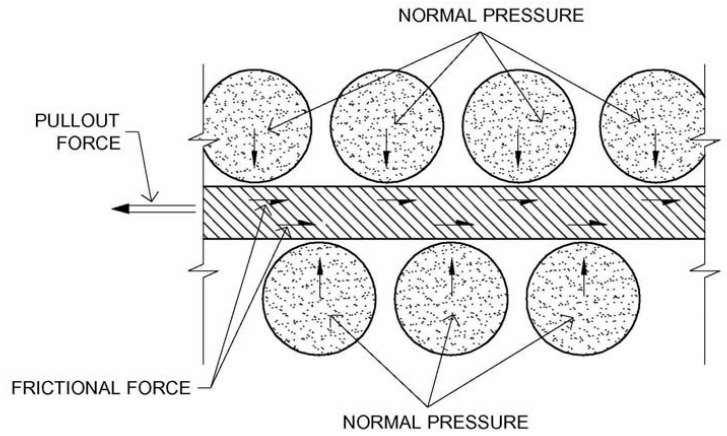

Figure 6. Frictional soil-reinforcement stress transfer mechanism (Berg et al. 2009).

For reinforcing elements with transverse sections, passive resistance (bearing) occurs through the development of bearing type stresses on transverse reinforcement surfaces normal to the direction of soil reinforcement relative movement (Figure 7). Passive resistance is generally considered to be the primary interaction for bar mat, wire mesh reinforcements, and geogrids with relatively stiff cross machine direction ribs (Berg et al. 2009). Element types with enough section in both longitudinal and transverse directions (e.g., ribbed steel straps) use a combination of friction and passive resistance.

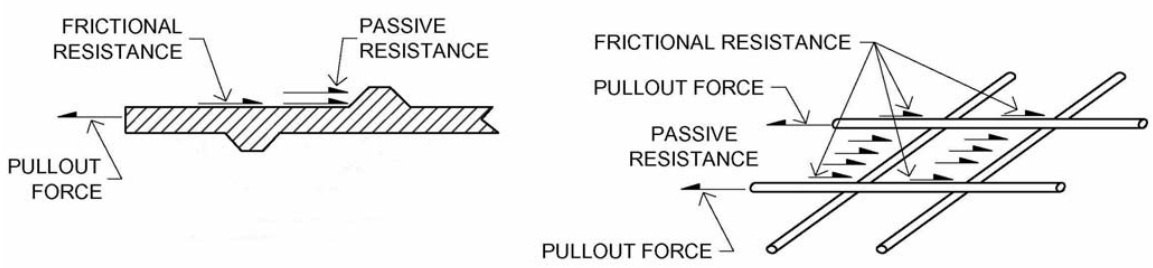

Figure 7. Soil passive resistance on reinforcement surfaces (Berg et al. 2009).

The contribution of each transfer mechanism for a particular reinforcement will depend on the roughness of the surface, normal effective stress, grid opening dimensions, thickness of the transverse members, and elongation characteristics of the reinforcement. Soil properties such as grain size, grain size distribution, particle shape, density, water content, cohesion, and stiffness also affect the development of the soil-reinforcement interaction (Berg et al. 2009).

2.4.2 Application

Jones (1996) presents a more comprehensive list of application areas for reinforced earth as outlined below. This section only introduces a few of the application areas and not an exhaustive list.

2.4.2.1 Bridgeworks

Mechanically stabilized earth systems are commonly used as bridge abutments. This can be as a true abutment (Figure 8) where the bridge beam is supported by a footing resting directly on the reinforced soil, or a system where piles are used to support the beams and the MSE wall built around the piles.

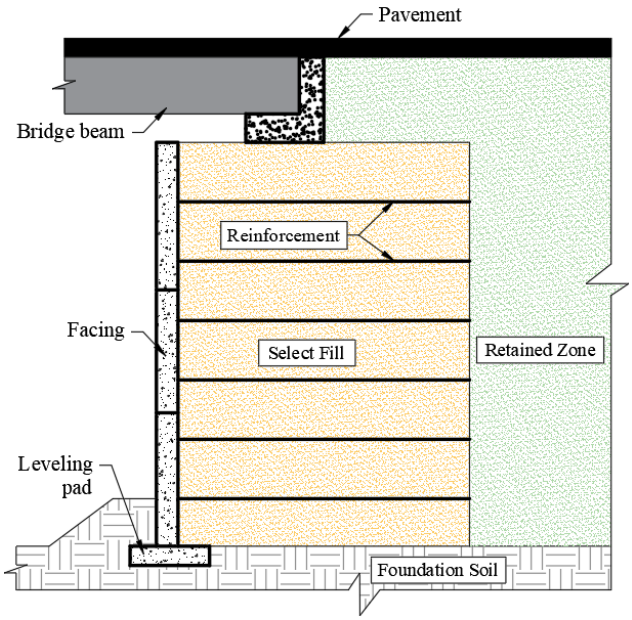

Figure 8. MSE wall as a bridge abutment.

2.4.2.2 Dams

Because of the mass of the reinforced fill, MSE walls can be used in the construction of a new dam (Figure 9) or in raising the height of an existing dam to increase capacity. The downstream side of the dam can be purely vertical which reduces real estate requirements compared to unreinforced earth fill dams.

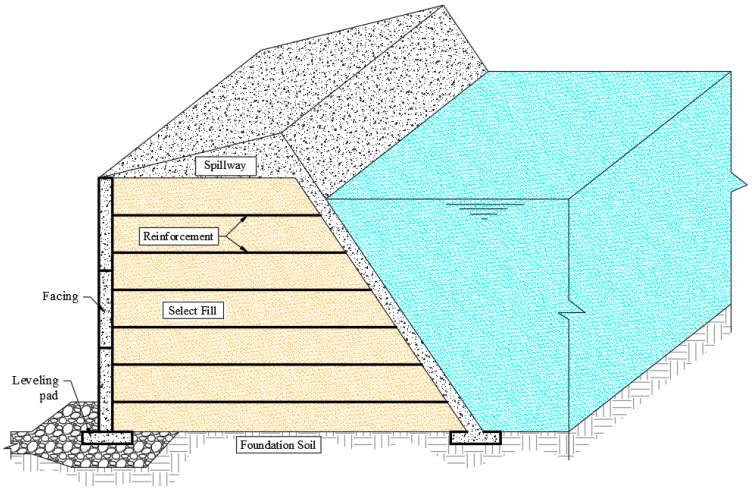

Figure 9. MSE reinforced earth fill dam.

2. 4.2.3 Highways

Grade separation requirements are often encountered in the construction of new or expansion of existing roadways. MSE walls are commonly used in highway infrastructure to accommodate changes in grade within the limited amount of right-of-way. Figure 10 illustrates a multi-tier MSE wall system supporting a multi-grade highway infrastructure.

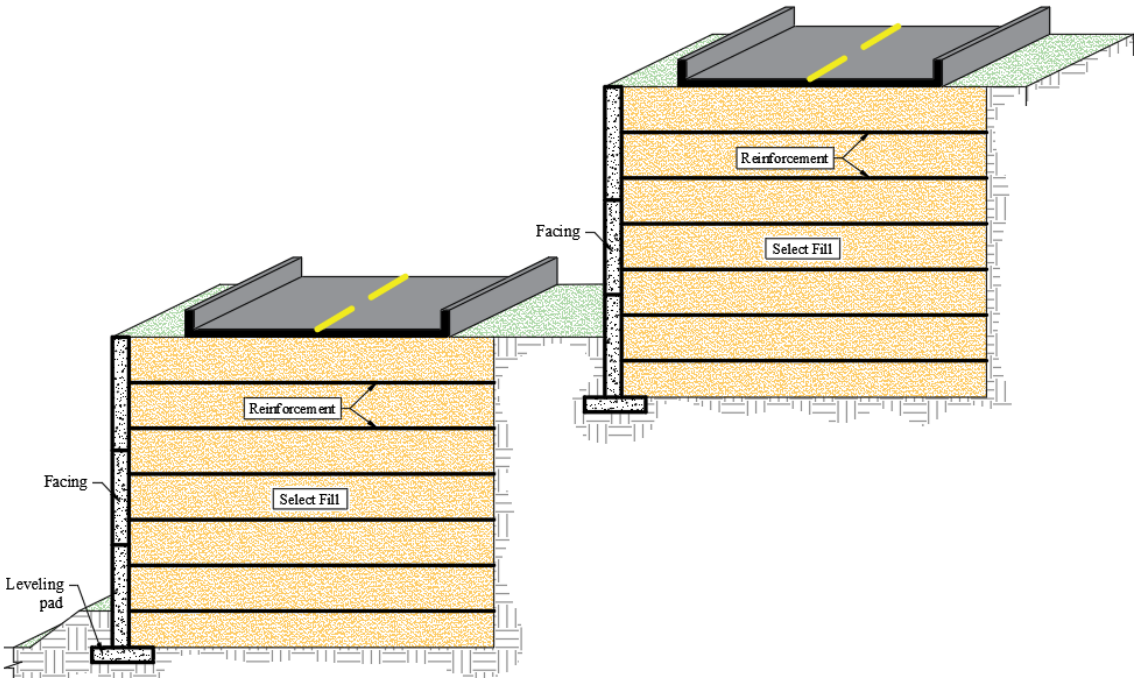

Figure 10. Stepped MSE highway structure.

2. 4.2.4 Military

Reinforced earth technology can also be used as protective structures. Figure 11 shows 2002's ammunition storage igloo built for the Battle Creek Air National Guard in Michigan designed by the Reinforced Earth Company (RECo). The earth-covered structure was designed for the US Army Corps of Engineers using concrete arches and reinforced earth. The system protects the surrounding area from accidental detonation. Since full scale testing was conducted, hundreds

of storage igloos and other Reinforced Earth protective structures have been installed by militaries around the world (RECo 2023).

Figure 11. MSE system used in an ammunition storage igloo (RECo 2023).

2. 4.2.5 Railways

Reinforced earth solutions are used for railway embankments using reinforced soil slopes on the sides of the embankment to provide stability over poor subsoil (Jones 1996). Like highway embankments, reinforced soil wall systems can also be used to directly support a railway. This reduces the space required to safely construct a sloping embankment and reduces construction time.

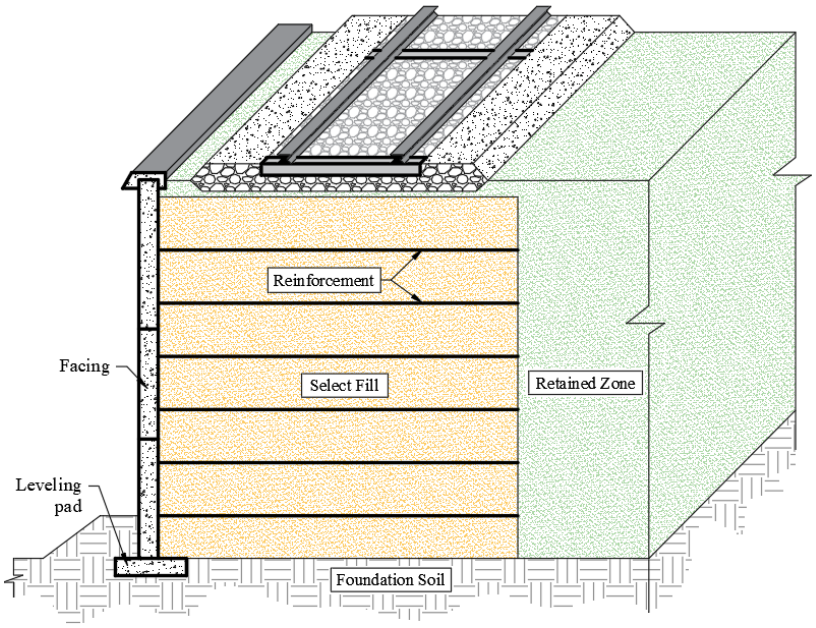

Figure 12. MSE Wall supporting a railway.

2.5 The MSE Technology

2.5.1 Components of the MSE

Key aspects of the MSE wall system include the select backfill material, the soil reinforcement, and the facing elements. Other components include the foundation, leveling pad, drainage, retained soil, etc.

2.5.1.1 Foundation

This is the natural material upon which the MSE wall system is built. Material testing and exploration for material properties of the foundation is usually focused on determining bearing capacity, settlement potential and the level of ground water table. MSE wall systems have enough flexibility to tolerate differential settlement, but in cases where the foundation is very weak, foundation remediation programs may be implemented to increase the bearing capacity or

minimize settlements. Such techniques may include surcharging, dynamic compaction, stone columns, and use of light weight fills (Berg et al. 2009).

2.5.1.2 Leveling Pad

This is typically made of unreinforced concrete, however, unreinforced or geosynthetic-reinforced gravel, or sand can be used. The dimensions depend on the facing types, usually, the width is 3 times the facing thickness. A typical dimension of the leveling pad for a precast facing panel would be 150 x 300 mm. The leveling pad is non load bearing and only serves to keep the facing elements on the same level. For sloping terrains, the leveling pads can be stepped to accommodate undulations in elevation (Figure 13).

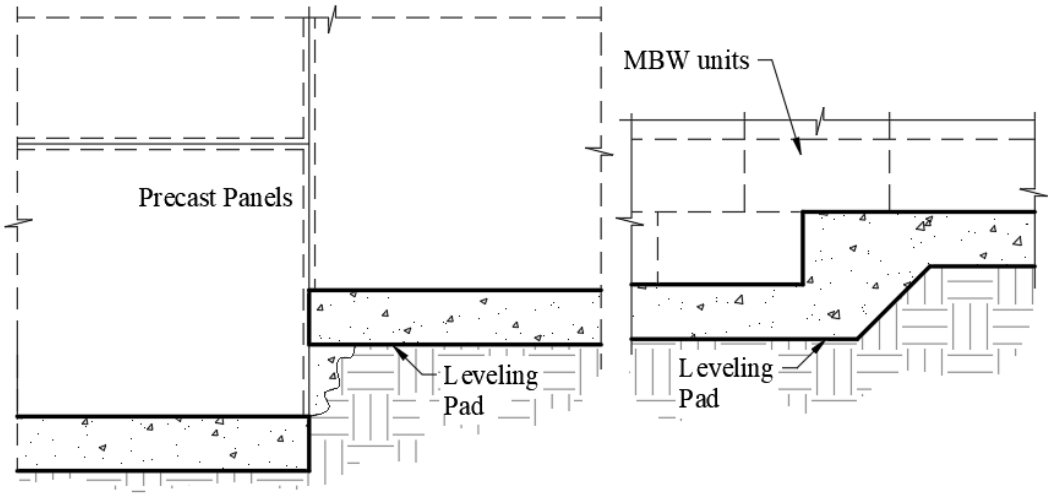

Figure 13. Leveling pad step details for precast panels and MBW facing units.

2.5.1.3 Facing

In an MSE type structure, the reinforcement layers are mechanically connected to the facing units. The type of facing elements used is based on a few criteria including backfill protection, settlement tolerances, aesthetic requirements, and drainage paths provision. (Berg et al. 2009). Facings used for MSE walls, which are typically proprietary, include segmental precast

panels, dry-cast modular blocks (MBW), metallic series of interconnected half cylinders, welded wire grids, gabions, and geosynthetics.

Segmental precast panels (Figure 14) can have most of the reinforcement types with various facing-reinforcement connection mechanisms. The shapes are typically square panels, rectangular panels, and cruciform panels. Square and cruciform panels are typically 1.5 m x 1.5 m, rectangular panels are typically 1.5 m x 3 m, custom sizes are made to fit geometric irregularities. The precast panels surface finishes can be plain concrete, custom bricks, ashlar stone and artistic murals.

MBW (Figure 14) are small concrete, solid, or hollow units specifically made for use as retaining wall facings and typically use geosynthetic reinforcement. Steel grids with two longitudinal wires can be but are rarely used with MBWs. Nominal size ranges are 100 – 300 mm for the height, 200 – 450 mm for the exposed length, and 200 – 600 mm for the width. Most units are dry-stacked and don't require mortar and are specifically made to mechanically connect to the reinforcement. Other facing types include bent welded wire mesh, gabions, and folded geosynthetic sheets etc.

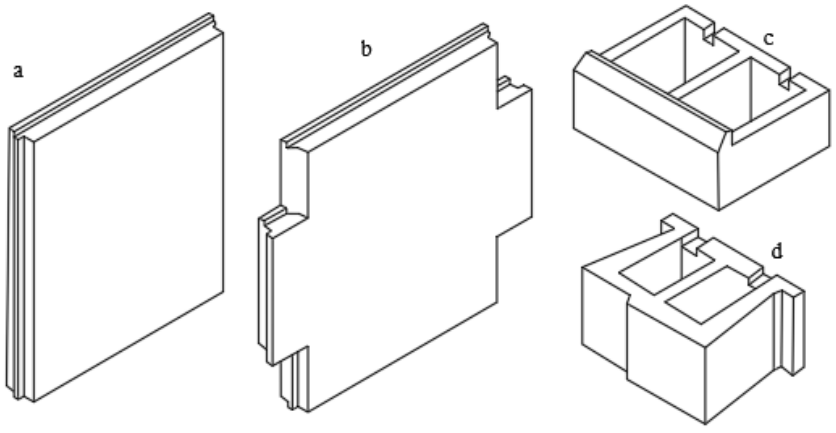

Figure 14. Facing types (a) rectangular precast panel (b) cruciform precast panel, (c) & (d) typical modular block units.

2.5.1.4 Select Backfill

The bulk of the material in the MSE is the select backfill (usually sand and/or crushed gravel) which renders it economically conservative compared to reinforced concrete walls. Select materials, usually free draining granular soils are typically used for the backfill. The backfill material should be well graded, free from organic elements with a plasticity index not more than 6 and with fines content no more than 15% (Berg et al. 2009). Unstable, poor draining soils susceptible to piping and internal erosion are not suitable and often leads to material loss and clogging of drainage systems, and buildup of pore pressure and seepage forces (Terzaghi et al. 1996, and Cedergren 1989), all having a destabilizing effect on the MSE structure (Berg et al. 2009).

2.5.1.5 Reinforcement

The type of reinforcing element is broadly categorized into inextensible and extensible reinforcement. An inextensible reinforcement (usually metallic) is a stiff element with stiffness much higher than the soil. An extensible (non-metallic) reinforcement is usually more ductile, with stiffness less than that of the soil. In general, an inextensible reinforcement requires much less deformation to fully mobilize the ultimate tensile force while extensible reinforcement require much higher deformations to occur before the ultimate force is fully mobilized (Woods and Jewell 1990).

Stiff, inextensible reinforcement is typically made of steel including steel straps, steel ladder and welded bar mats.

- Steel strips are commercially available, 50 mm wide and 4 mm thick, usually ribbed top and bottom resulting in high adherence. These reinforcing strips are hot-dip ribbed

galvanized steel strips with a single bolt hole at one end. The strips are structurally connected to the galvanized tie strips in the facing panels using a high strength nut/bolt/washer assembly. Advantages of high adherence reinforcing strips include their high tensile strength, high pullout resistance, and their ability to rotate in the horizontal plane to clear obstructions such as bridge abutment piles and drainage structures (Berg et al. 2009, RECo 2018).

- High adherence reinforcing ladders have two parallel round steel bars welded to a series of cross bars along the full length of the bars, offering extremely high pullout capacity. One end of the ladder is equipped with a flat connection plate welded between the longitudinal bars. Similar to the steel strips, the single hole in the plate allows the same bolted connection to facing panels, so the steel ladders offer the same advantages of rotational capability and metal loss protection, as the steel strips do (RECo 2018).

- Steel grids are welded wire grid using two to six W7.5 to W24 longitudinal bars and W11 to W20 transverse bars. Based on design requirements, longitudinal bars are spaced at either 150 or 200 mm while transverse bars are spaced 230 to 600 mm (Berg et al. 2009). Bar mats are connected to the facing using a pre-attached clevis loop and a steel connector rod that simultaneously engages loops at the ends of each longitudinal rod. Bar mat reinforcements develop a high pull-out resistance and are especially advantageous in low height walls and where select fill has a high fine content (RECo 2018).

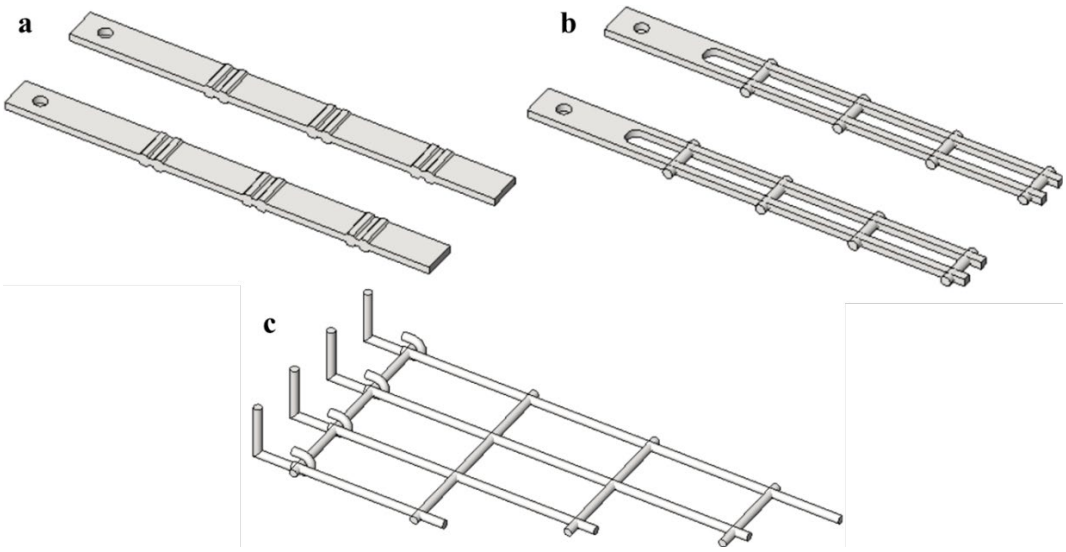

Figure 15. Steel reinforcement types: (a) steel strips, (b) steel ladders, and (c) welded bar mats.

Geogrids are predominantly used for the extensible type of reinforcement, mainly High-Density Polyethylene (HDPE) geogrid and PVC coated polyester (PET) geogrid. Geogrids are generally classified as uniaxial (strength considered only in one direction), biaxial (same strength in two directions), and triaxial (same strength in three directions) (Figure 16). Other types of extensible soil reinforcement include geotextiles and geosynthetic straps (Berg et al. 2009).

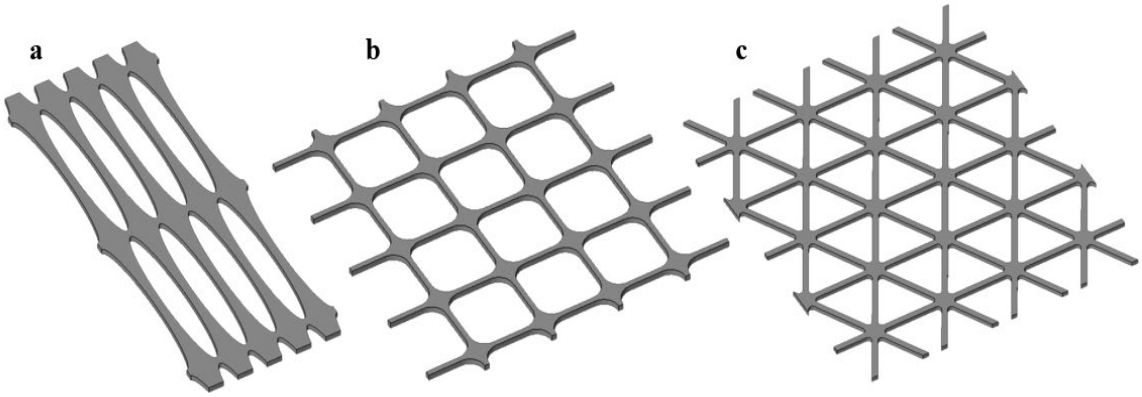

Figure 16. Geogrid reinforcement types: (a) uniaxial, (b) biaxial and (c) triaxial geogrid.

2.5.1.6 Drainage

In most cases, a means of drainage is incorporated within the MSE system, most importantly when the reinforced fill is not free draining. Terzaghi et al. (1996) and Cedergren (1989) suggested that an increase in seepage forces can occur during severe rainstorms if the permeability of the fill is less than or equal to 0.002 cm/sec. Using poor draining material for the reinforced fill also heightens the risk of internal erosion, as water will tend to flow out through the facing units. Potential sources for saturation of the reinforced backfill include surface water runoff and rising ground water table. Several features (Figure 17) are used to facilitate internal drainage within the MSE.

- To prevent erosion through the facing units, a filter is provided at all joints, the material type for the filter is dependent upon the facing type. A geotextile fabric is used for precast facing panels, while a drainage aggregate fill is used for MBW units. A geotextile fabric can also be used behind the drainage fill as a filter.
- A blanket drain, usually below the reinforced fill, is used for walls built on sites with the possibility of ground water rising to the fill level. A chimney drain provides drainage behind the reinforced fill as well to improve drainage. A chimney drain can as well be extended beyond the reinforced fill into the retained fill to ensure that flowing water is intercepted before it reaches the reinforced mass. A perforated pipe with a minimum diameter of 150 mm is used to collect the water to an external drainage channel.

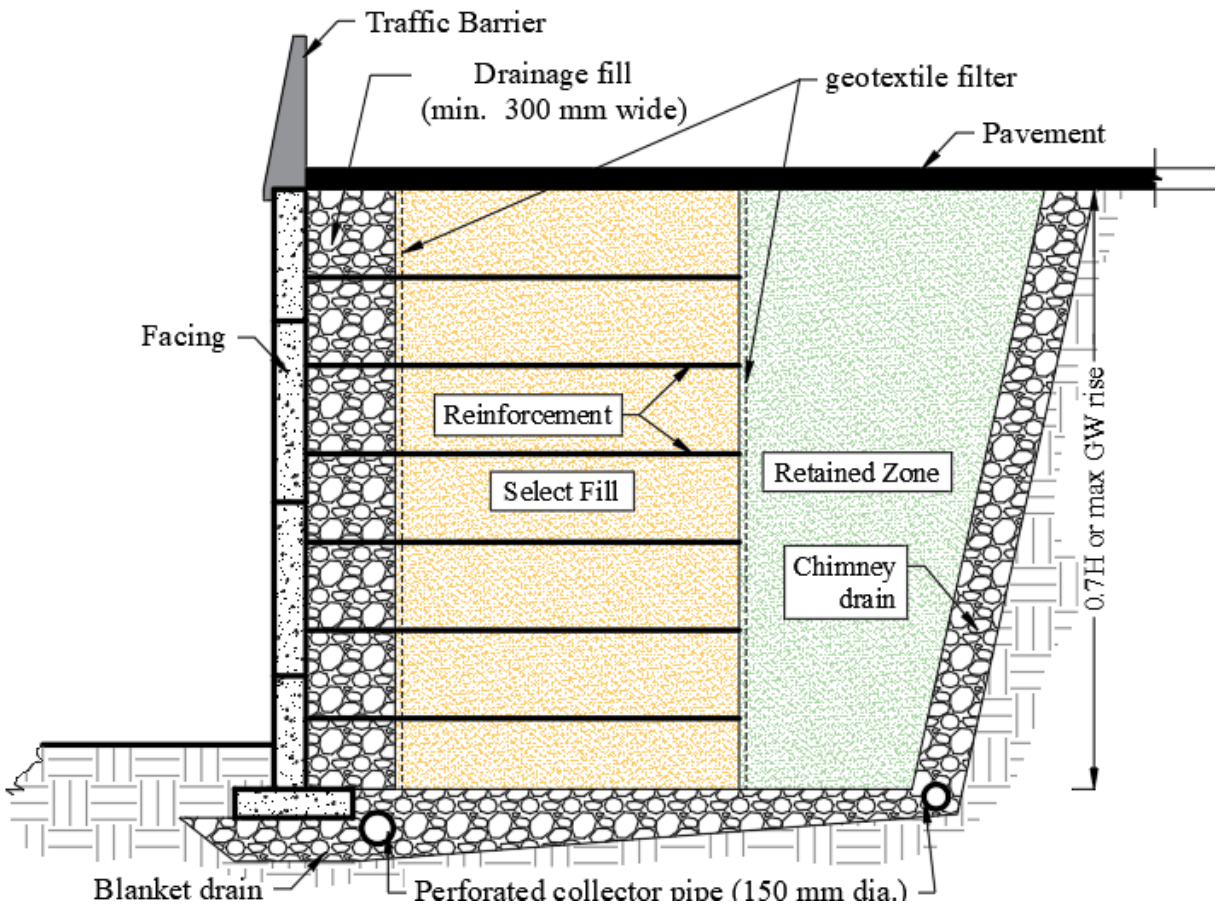

Figure 17. Internal drainage features in an MSE wall system.

2.5.2 Construction Guidelines from Berg et al. (2009) and RECo (2020)

- *Foundation Preparation:* The MSE system is a bottom-up construction. The foundation is prepared first, this could involve removal organic matter and unstable topsoil. The foundation is then compacted, further improvement may be required.
- *Leveling Pad:* The leveling pad is put in place, this is usually unreinforced concrete or compacted gravel, or sand reinforced with geosynthetics. The leveling pad is not a structural support and solely used as a guide to keep the facing panels level.
- *First Tier of Facing Units:* The first row of facing units is placed next and should be simultaneous with placement of soil backfill. For segmental facing panels, braces are used

to keep the first-row panels in position to maintain stability while the backfill is compacted. One brace is required for each panel with height greater than 0.9 m, and two braces are required for each panel with height greater than 1.95 m (Berg et al. 2009, RECo 2020). Geotextile fabric is placed at each panel-panel joint to prevent loss of fill material.

- *Reinforced fill and compaction:* The reinforced wall fill is placed and compacted. About 300 mm from the back of the panels is left unfilled until the first reinforcement is securely in place and filled over, this is to prevent compaction effort from displacing the facing panels out of alignment. The fill is usually compacted to 95 to 100% of the maximum density and water content 1 to 2% dry of optimum. For coarse fill materials (30% of the fill material greater than 19 mm in size), compaction should be a minimum of 70% of the material's relative density. The fill should be placed in small lifts with no more than 300 mm of uniform loose fill height. Compaction is done with a vibratory compactor (except for uniform sands); however, lighter compaction equipment or mechanical tamper should be used within 0.9 m of the facing panel to avoid unwanted panel movement. Compaction should be done at least once after each lift.
- *First Reinforcement Layer:* The reinforcing strips are mechanically connected to the embedded tie strip in the facing panel. The reinforcing strips are placed perpendicular to the facing panels unless expressly stated. The fill should be at least 50 mm above the reinforcement tie level. Metal track equipment must never come in contact with reinforcing strips.
- *Subsequent Tiers:* Erection of the next row of panels should commence only when the backfill and compaction have reached the top of the half panels (Figure 18). Subsequent rows of panels do not need braces and should be kept aligned with placed panels using

wedges and clamps. During construction, the wooden wedges are left in place for at least two, but no more than three rows. (RECo 2020). Bearing pads are placed at the top of each panel before placing the next row to prevent concrete-to-concrete contact. The outlined sequence should be repeated till the wall is complete. After completion, all wedges and clamps must be removed.

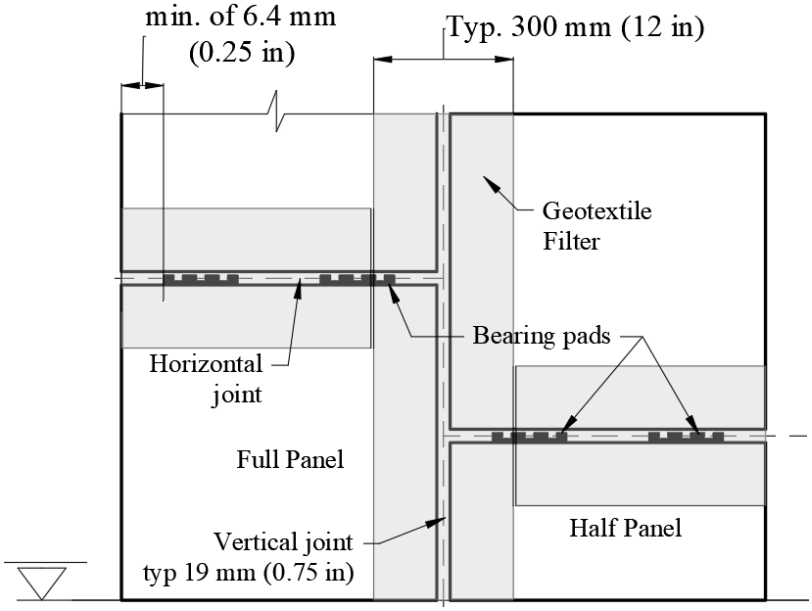

Figure 18. Typical joint materials and details for precast facing panels.

2.5.3 MSE Wall Design

Chapter 4 of the FHWA GEC 11 (Berg et al. 2009) design guideline focuses on the design of MSE walls using the Load and Resistance Factor Design (LRFD) platform. The LRFD approach is not very different from the Allowable Stress Design (ASD) method put forward earlier by Elias et al. (2001) in the FHWA-NHI-00-043 manual. The primary change is in the way the loads and resistances are compared and even so, the load and resistance factors are currently calibrated by fitting to ASD results. Therefore, designs using LRFD procedure should not significantly vary from past, expected ASD designs (Berg et al. 2009). Most of the steps are similar to traditional

retaining wall designs but the evaluations for both internal and external stability significantly differ for MSE walls compared to other externally stabilized walls.

2.5.3.1 Evaluation of External Stability

External stability controls external details like length and height of reinforced zones while internal stability governs reinforcement strength and spacing (Clayton et al. 2014). The evaluation of the external stability for MSE structures includes checks for sliding, eccentricity, bearing capacity, settlement/lateral deformation analysis, and overall slope stability at service limit state (Figure 19). Compound and global stability checks are also required as well as appropriate surface and sub-surface drainage systems (Berg et al. 2009).

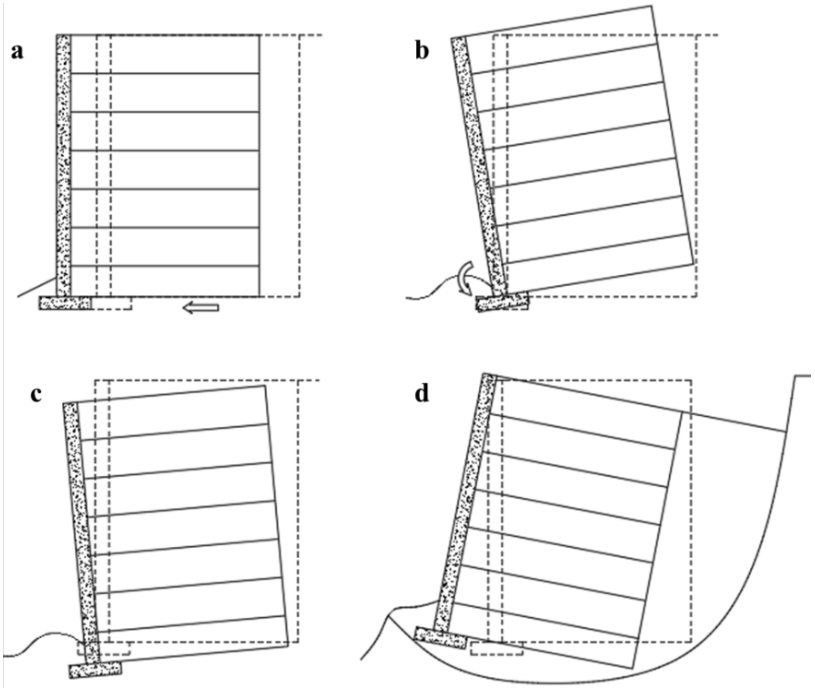

Figure 19. Failure modes: (a) sliding, (b) limiting eccentricity, (c) bearing capacity and (d) deep seated failure.

Regardless of the approach (LRFD or ASD), the basic steps taken for the evaluation of external stability are summarized herein for the simple case of a wall with horizontal backslope

and traffic surcharge (Figure 20). The factor of safety (FS) is applied in the case of ASD while the load and resistance factors are applied appropriately in the case of LRFD.

2.5.3.1.1 Sliding Stability

To satisfy the stability requirement against sliding at the base of the reinforced mass, the horizontal resisting forces (P_r) must be greater than the corresponding driving forces (P_d).

(1) Thrust from retained fill.

$$F_1 = \frac{1}{2}\gamma_b H^2 K_{ab} \tag{20}$$

where K_{ab} is the coefficient of active earth pressure calculated using properties of the retained soil and γ_b is the unit weight of the retained soil.

(2) Thrust from uniform surcharge.

$$F_2 = K_{ab} q H \tag{21}$$

(3) Calculate driving force.

$$P_d = F_1 + F_2 \tag{22}$$

(4) Calculate resisting force.

$$P_r = V_1 \mu = \gamma_r H L \mu \tag{23}$$

where μ is the minimum between $tan(\phi_{foundation})$, $tan(\phi_{reinforced\ zone})$ and $tan(\rho)$, ρ is the soil-reinforcement friction angle determined using interface direct shear tests.

(5) Starting value of L is usually $0.7H$ and L is increased if the sliding check fails.

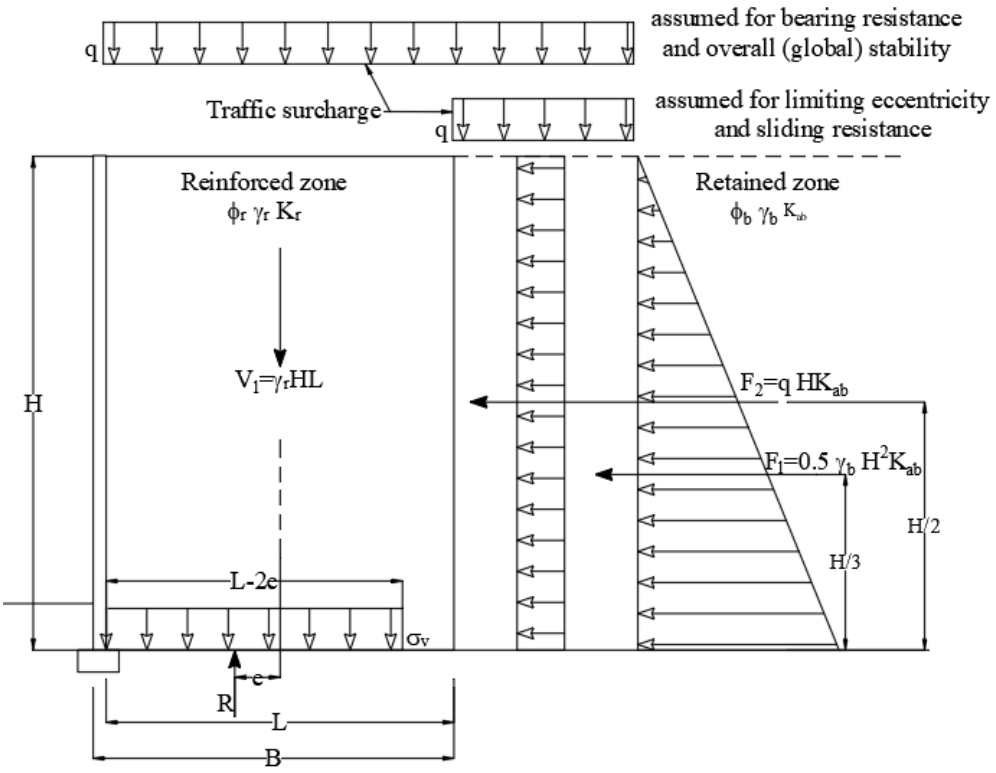

Figure 20. External analysis: nominal earth pressures; horizontal backslope with traffic surcharge (after AASHTO, 2007).

2.5.3.1.2 Limiting Eccentricity.

To satisfy the eccentricity limit check, the eccentricity, e (distance between the resultant force and the centerline) must be less than $L/6$ in soil and $L/4$ in rock when using the ASD approach, and $L/4$ in soil and $3L/8$ in rock when using the LRFD approach. The weight and width of the wall facing, and the live load above the reinforced fill are typically ignored and L is increased if this check fails.

$$e = \frac{L}{2} - \frac{\sum M_D - \sum M_R}{\sum V} \tag{24}$$

where M_D is overturning moment and M_R is resisting moment.

Equation 21 can be simplified further to $e = \frac{\sum M_D}{\sum V}$ (25)

Hence $$e = \frac{F_1(H/3) + F_2(H/2)}{V_1} \tag{26}$$

2.5.3.1.3 Bearing Capacity

To satisfy the capacity requirement, the estimated applied vertical pressure (σ_{V-F}) must be sufficiently less than the allowable bearing resistance (q_R). The ASD approach divides the ultimate bearing capacity (q_n) by the factor of safety and compares that σ_{V-F}. The LRFD approach applies load factors to determine σ_{V-F} and then a strength reduction factor, ϕ (usually equal to 0.65) to determine the factored bearing resistance (q_R).

$$e_B = \frac{F_1(H/3) + F_2(H/2)}{V_1 + qL} \tag{27}$$

$$\sigma_{V-F} = \frac{\gamma_r HL + qL}{L - 2e_B} \tag{28}$$

Estimation of the bearing capacity of the foundation (q_n) is similar to that of shallow foundations, for a level grade and no ground water influence (equation 26).

$$q_n = c_f N_c + 0.5 L' \gamma_f N_\gamma \tag{29}$$

where c_f is the cohesion of the foundation, N_c and N_γ are dimensionless factors, γ_f is the unit weight of the foundation, q_R is the factored bearing resistance and L' is the effective length from the bearing stress calculation ($L' = L - 2e_B$). For equations 25 and 26, $L - 2e_B$ is taken as L if e_B is negative.

2.5.3.2 Evaluation of Internal Stability

Internal instability in MSE walls occurs in when:

- the tensile force (and or shear force) in the reinforcement is large enough to cause elongation or rupture in the reinforcement leading to excessive deformation or collapse.
- the tensile force in the reinforcement is larger than the frictional pullout capacity of the reinforcement-soil composite leading to excessive deformation or collapse.

To evaluate the internal stability of MSE walls, depending on the type of reinforcement used (extensible or inextensible), a potential critical failure surface is assumed based upon empirical observations and theoretical studies. This critical failure surface has been assumed to be approximately bilinear in the case of inextensible reinforcements, approximately linear in the case of extensible reinforcements (Figure 21) and passes through the toe of the wall in both cases (Berg et al. 2009).

2.5.3.2.1 Reinforcement Rupture/Breakage

To ensure stability against breakage of reinforcement, the applied maximum tensile force in each reinforcement ($T_{\max}$) must be sufficiently less than the allowable tensile strength (T_a).

$$T_{\max} = \sigma_H S_v \tag{30}$$

where σ_H is the factored horizontal stress at the reinforcement level and S_v is the vertical spacing between reinforcement layers. S_v is limited to 600 mm when geosynthetic reinforcement is used.

$$\sigma_H = \gamma_p (K_r \sigma_v + \Delta\sigma_H) \tag{31}$$

$$\sigma_v = \gamma_{soil} Z + q + \Delta\sigma_v \tag{32}$$

where γ_p is a load factor, $\Delta\sigma_H$ is the horizontal stress at reinforcement level from any concentrated horizontal load, γ_{soil} is the unit weight of the reinforced soil, Z is the depth to the reinforcement

level, q is the traffic surcharge and $\Delta\sigma_v$ is the additional vertical stress from concentrated vertical loads.

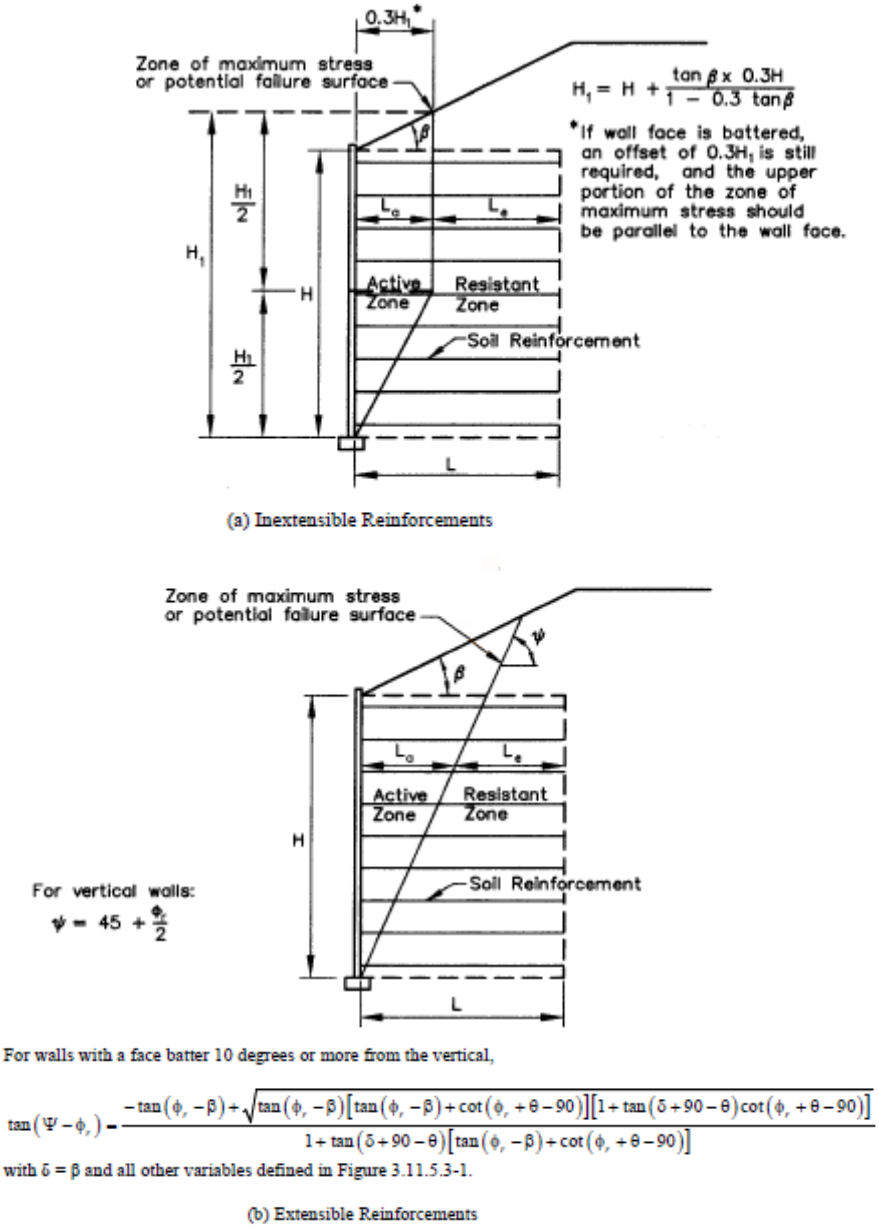

Figure 21. Location of potential critical surface for internal stability design of MSE Walls (a) inextensible reinforcements and (b) extensible reinforcements (AASHTO 2014).

K_r is estimated by interpolating the depth values for each reinforcement tie level using Figure 22. The plot gives multiples of the ratio of K_r to K_a. K_a is calculated using equation 12.

For wall face batters equal to or greater than 10°, a simplified version of the Coulomb equation shown in equation 33 (after Berg et al. 2009) can be used.

$$K_a = \frac{\sin^2(\theta + \phi'_r)}{\sin^3\theta\left[1 + \frac{\sin\phi'_r}{\sin\theta}\right]} \tag{33}$$

where θ is the inclination of the back of the facing as measured from the horizontal starting in front of the wall.

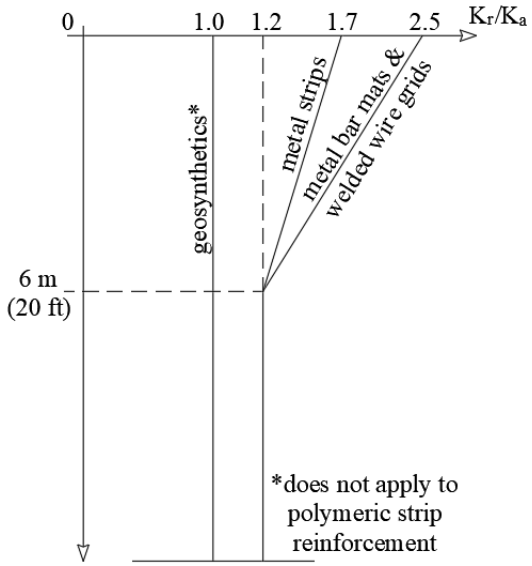

Figure 22. Variation of the coefficient of lateral stress ratio (K_r/K_a) with depth in a MSE wall (after Berg et al. 2009, AASHTO 2014).

The maximum load (per unit width of reinforcement) is calculated using equation 34 where R_c is the ratio of the reinforcement width to the center-center horizontal spacing between discrete reinforcement (i.e., R_c = 1 for full reinforcement coverage). The maximum applied load can also be evaluated in terms of facing panel width.

$$P_{TMAX-UWR} = \frac{T_{max}}{R_c} \tag{34}$$

The number of reinforcement and type of reinforcement is then selected such that the maximum applied tensile load is less than the allowable tensile load (T_{al}) in the reinforcement while accounting for limiting factors like corrosion, creep, installation, etc. A resistance factor or a general factor of safety is applied to T_{al} depending on the design approach.

$$T_{\max} \le T_{al} R_c \tag{35}$$

(a) for steel reinforcement,

$$T_{al} = \frac{A_c F_y}{b} \tag{36}$$

where A_c is the steel section area (can account for steel corrosion), F_y is minimum yield strength, and b is gross reinforcement width.

(b) for geosynthetic reinforcement,

$$T_{al} = \frac{T_{ult}}{RF} \tag{37}$$

where T_{ult} is the minimum ultimate tensile strength and RF is the combined reduction factor that accounts for creep, long term degradation, installation damage, and chemical aging.

2.5.3.2.2 Reinforcement Pullout.

The pullout resistance of the reinforcement is checked at each level against pullout failure. The length of the reinforcement resisting pullout (L_e) is the portion within the resistance zone just behind the active zone in Figure 21. L_e must not be less than 0.9 m. L_a is the reinforcement length within the active failing wedge, hence total reinforcement length L, is the sum of the effective length, and the length within the active failing wedge as illustrated in Figure 21.

$$L = L_a + L_e \tag{38}$$

$$L_e \geq \frac{T_{\max}}{F^* \alpha \sigma_v C R_c} \tag{39}$$

where L_e = effective reinforcement length in the resisting zone.

$T_{\max}$ = maximum reinforcement tensile load.

α = scale effect correction factor determined from product testing, default values are 1.0, 0.8, and 0.6 for all steel, geogrids, and geotextiles respectively.

σ_v = unfactored vertical stress at the reinforcement level in the resistant zone (does not include live load).

C = overall reinforcement surface area geometry factor based on the gross perimeter of the reinforcement and is equal to 2 for strip, grid and sheet-type reinforcements, i.e., two sides.

R_c = reinforcement coverage ratio.

F^* = pullout friction factor determined from product specific tests and can be estimated using Figure 23.

a resistance factor (φ) can be applied to the pullout resistance, or a factor of safety (FS) can be applied to the tensile load depending on the design approach used.

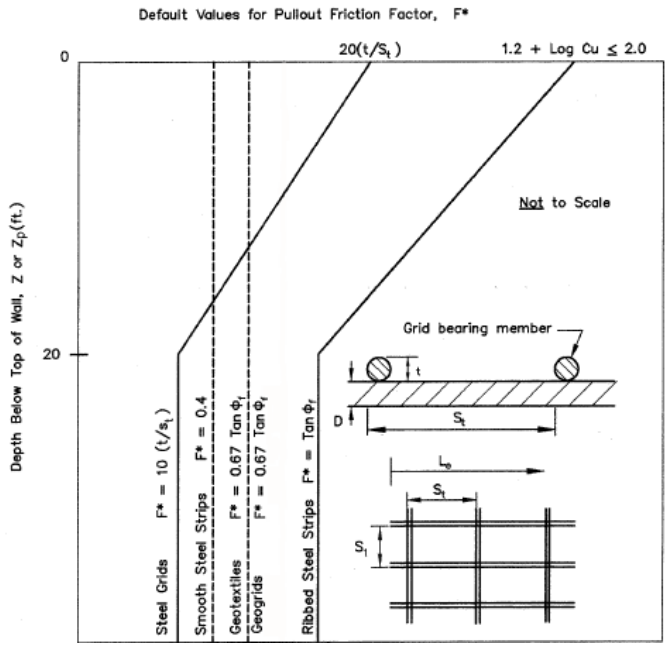

Figure 23. Default Values for the Pullout Friction Factor, F* (AASHTO 2014).

2.5.4 Previous Studies

As MSE retaining structures have been in use for many years, there are several cases where instrumentation has been used to better understand the behavior of these structures. Farrag and Morvant (2004) instrumented a segmental MSE structure mainly to evaluate the stresses in the reinforcement and ability to use lower quality backfill. Leshchinksy (2007) instrumented a geogrid-reinforced MSE wall on a compressible foundation. The focus was on measuring strain in the MSE reinforcements and distress of the entire structure with inclinometers and settlement cells. Stuedlein (2010) and Studelin et al. (2011) used an extensive instrumentation program to monitor one of the tallest MSE retaining structures ever constructed at SeaTac airport. The results of the strain gage and settlement sensor data showed the wall performed satisfactorily and cleared the way for the use of even larger MSE walls. Most of these cases used instrumentation to evaluate the performance of the reinforced fill.

Some studies have reported measured stresses for an MSE structure. Bastick et al. (1993) instrumented two sections of a wall. One section had a trapezoidal reinforcement arrangement and the other had a uniform reinforcement arrangement. The results of the measured stresses at the foundation showed identical stress distribution for both wall sections. The stress distributions were compared to a uniform overburden stress distribution. The measured stresses at a distance behind the reinforced zone were equivalent to the overburden stress, there was a decrease in stress magnitude just behind the reinforced zone that was attributed to overturning, there was an increase to the maximum values at about one meter behind the facing, and a rapid decrease just behind the facing panels. Directly under the facing panels, load transducers indicated loads about 2.5 times the weight of the panels further indicating the presence of an overturning moment.

Runser et al. (2001) instrumented a 17-m high wall reinforced with steel strips. Similar to the findings by Bastick et al. (1993), measured values of foundation bearing stress were generally in good agreement with values calculated using soil unit weight and depth, except that the average force from the facing panels on the leveling pad was twice that of the weight of the panels themselves.

Budge (2004) instrumented a steel mat-reinforced, 11-m high wall with surcharge. The vertical stress distribution showed low vertical stresses near the face of the wall, stresses increased to a maximum value at about 1.8 m from the wall face, then decreased to the overburden stress at about 9 m from the facing. Budge compared the measured bearing stress to the Meyerhof distribution and stated that the measured vertical stress distribution is not reflective of the design stresses required by AASHTO because the Meyerhof equation assumes higher toe stresses due to eccentric loading, and that due to the significant wall height (11 m with maximum surcharge), the

eccentricity becomes large, producing large calculated vertical stresses near the toe of the wall that was not seen in the field measurements.

Liang and Almoh (2004) stated that there is a need for a reconsideration of the vertical earth pressure distribution function after comparing the measured vertical stresses from a 15.8 m wall to the Meyerhof, and Trapezoidal distributions. The wall was reinforced with steel straps. A comparison between the measured pressure distribution and the commonly used distributions (Meyerhof, Trapezoidal, and uniform overburden distribution) showed that the three vertical pressure distribution functions have the common shortcomings, such as, not accommodating for the influence of the wall facing connections and wall facing materials, the interface friction between the retained and the reinforced soil masses, and the assumption of a rigid reinforced soil mass.

2.6 Summary Regarding Review of Relevant Literature

Retaining walls have a rich variety of applications including highway infrastructure, dams, railways, and protective structures. Mechanically stabilized earth structures offer a host of advantages over conventional concrete walls including ease of construction, lower cost, and less construction time.

There have been cases where robust foundation remediation programs were used to improve the bearing capacity of foundation soil to meet the bearing requirement as directed in the design guidelines. Meanwhile, there are inherent inconsistencies associated with the evaluation of the bearing stress from the reinforced mass. One of such is the assumption of a rigid block in evaluating design stresses for the MSE structure. This method was not developed for a flexible structure like the MSE but was originally used for eccentrically loaded rigid footings. This

assumption also implies zero stress redistribution and a complete transfer of all applied load to the foundation.

A review of previous studies with reported foundation stress measurement revealed that the foundation stress function used in design over-estimate the actual stress magnitude and distribution and that there is a need to reconsider the function used in evaluating the design bearing stress. To this effect, this study focuses on determining the bearing stress distribution beneath an MSE wall. Additionally, to further understand the behavior of the MSE structure with emphasis on the foundation stress distribution, loss of foundation support was investigated by introducing a yielding zone within the foundation, and the effect of foundation differential settlement on the overall performance of the MSE structure was also evaluated.

CHAPTER 3: MSE EXPERIMENTAL SETUP AND CONSTRUCTION

As indicated in the problem statement, adopting an approach used in evaluating the stability of a rigid structure for a flexible structure like the MSE leads to over-estimation of driving factors. The assumption that the reinforced wall is rigid allows for complete transfer of lateral stresses from the retained zone, leading to eccentricity, thus increasing the vertical stress (usually greater than $\gamma_f H$) and resulting in an overturning moment. This assumption also allows for a transfer of all applied surcharge from the top of the wall to the foundation. This study will focus on evaluating the ability of equation 25 to accurately represent the true stress distribution at the base of the MSE reinforced zone using full scale testing and numerical modeling.

3.1 MSE Wall Setup

The initial plan was to instrument and monitor an MSE structure constructed in the field but there was no ongoing projects with wall sections tall enough to give significant results. Hence, to examine the bearing stresses in a typical MSE structure, a full scale MSE wall was constructed and monitored in the Advanced Structural Engineering Laboratory (ASEL).

3.1.1 The Geochamber

The MSE system was constructed in the Geochamber, which is 7.2 m long, 3 m wide, and 6 m deep (Figure 24). The optimal configuration was to construct a foundation of sand by filling the Geochamber to half capacity (approximately 3 m below floor level). The chamber had a drainage outlet 0.6 m above the chamber floor that drained into a pit outside the chamber, equipped with a pump. Therefore, a 0.6m thick drainage layer was constructed with crushed stone. Also, to minimize frictional interaction between the MSE wall and the walls of the Geochamber, the sides were all covered with polythene sheets.

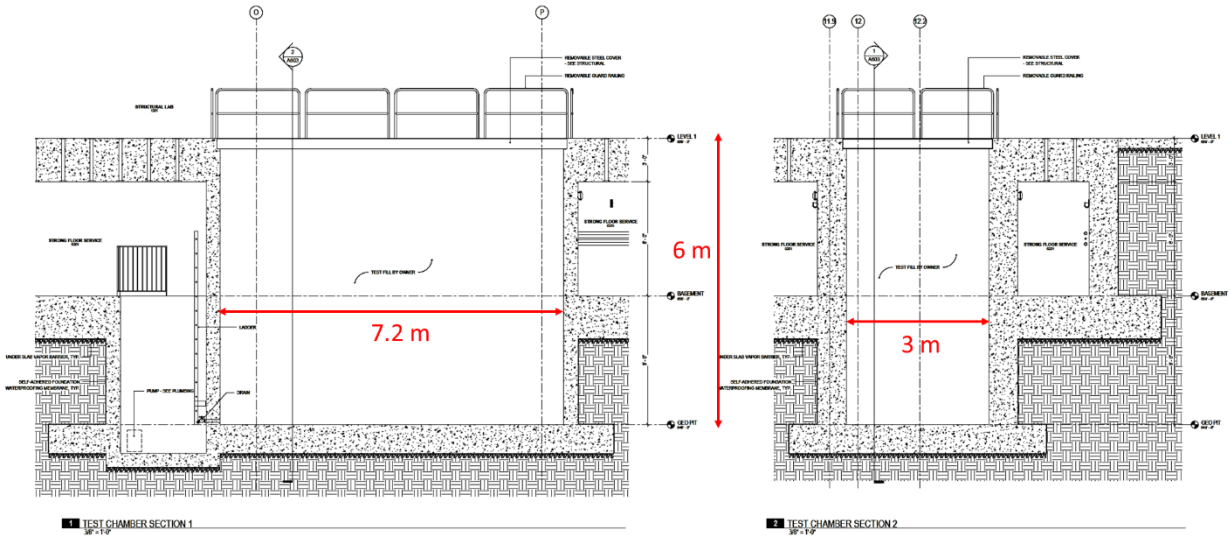

Figure 24. Sections showing the Geochamber configuration.

3.1.2 Woodwall

The proposed MSE wall was 4.8 m tall. The foundation for the MSE structure was 3 m thick, and the Geochamber is 6 m deep; hence, to build the wall, an extra 1.8 m was needed above the strong floor. This was achieved by building a confining wall above the strong floor. The confining wall was made with 150 mm x 150 mm timbers with bracing attached to the strong floor. The timber wall was designed to resist a combination of lateral pressure from the fill, traffic surcharge and a 712 kN rail axle weight (Cooper E80 rail loading), and consisted of a modular system of walls, braces and tiedowns (Figure 25). Two 4.8 m long sections were constructed to support the long sides of the proposed MSE structure, backed up into a 3.6 m section for the south end of the wall.

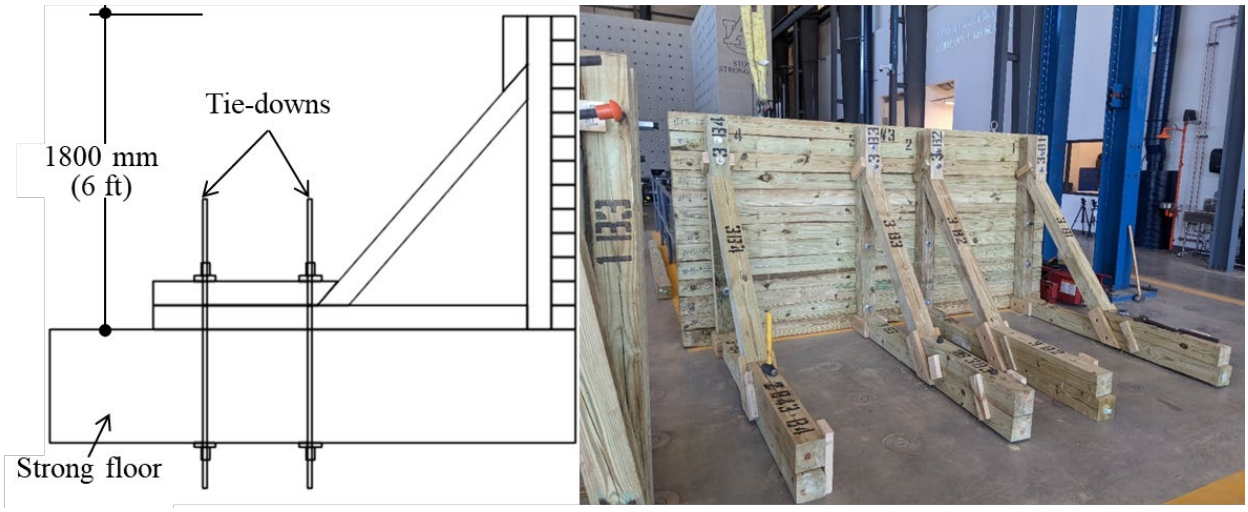

Figure 25. Confining wall constructed and assembled for the MSE height above strong floor.

3.1.3 The MSE Structure

The reinforced wall was designed by the Reinforced Earth Company (RECo). The reinforced zone was 3.3 m long with seven (7) rows of ribbed steel strips. The facing panels were 84 mm thick precast panels with ashlar stone finish. The panels were each 1.5 m wide, two panels were placed in each row to fit the width of the chamber, leaving 19 mm for the vertical joint between two panels, and 15 mm between the side of each panel and the walls of the Geochamber. The panel heights were selected such that the finished face has a staggered arrangement of the panels. The setup for the full-scale MSE wall is shown in Figure 26.

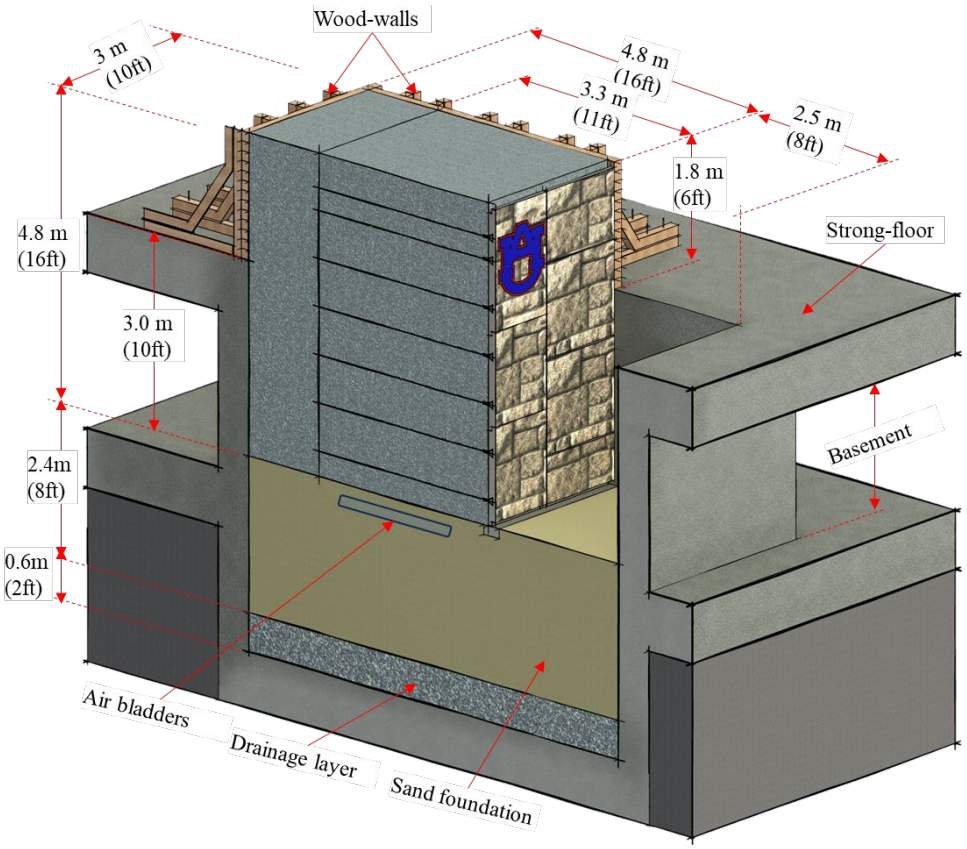

Figure 26. 3D section of the MSE wall in the Geochamber.

3.2 Instrumentation Plan and Monitoring

3.2. 1 Earth Pressure

Geokon vibrating wire earth pressure cells 4800 series (Figure 27) were used to measure the vertical earth pressure at the base of the reinforced mass. The cells measure total stresses, simultaneous measurement of the pore pressures would be needed to estimate the effective stresses, however, the reinforced fill was dry throughout the project duration, hence measured total stresses were analogous to the effective stresses.

The cell consists of two flat plates welded together at their periphery. The plates were separated by a small gap filled with de-aired hydraulic fluid and hydraulically connected to a

pressure transducer. The earth pressure acts to press the two plates against each other thus building up a pressure inside the fluid. The pressure transducer converts the fluid pressure into an electric signal. A thermistor, also located inside the pressure transducer housing, measures the temperature at the installation site (Geokon 2021). A test was conducted to determine the stability of each cell and sensitivity to temperature by connecting the cells to a data logger without any imposed load. Data collected over 24 hours showed that all cells were stable and produced repeatable readings after resets.

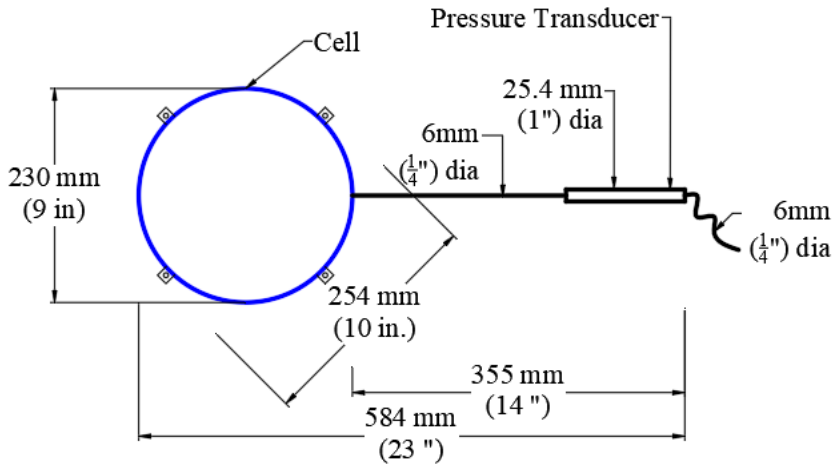

Figure 27. Schematic diagram of the earth pressure cells.

3.2.2 Settlement.

The instrumentation plan included four (4) settlement plates used to monitor settlements at various points on the foundation level (SP-01, SP-02, SP-03 and SP-04), and four mini-settlement plates used to monitor settlement at the top of the wall (SP-T-1, SP-T-2, SP-T-3 and SP-T-4). A settlement plate (according to ASTM D6598 – 19) consists of a flat base (plywood or steel), to which a steel riser rod was attached, which is then encased in a PVC pipe to prevent drag forces from the surrounding fill material. A survey target was attached to the tip of the riser rods and

monitored with a surveying instrument relative to an external reference. Figure 28 shows a schematic diagram of the design for construction of the settlement plates.

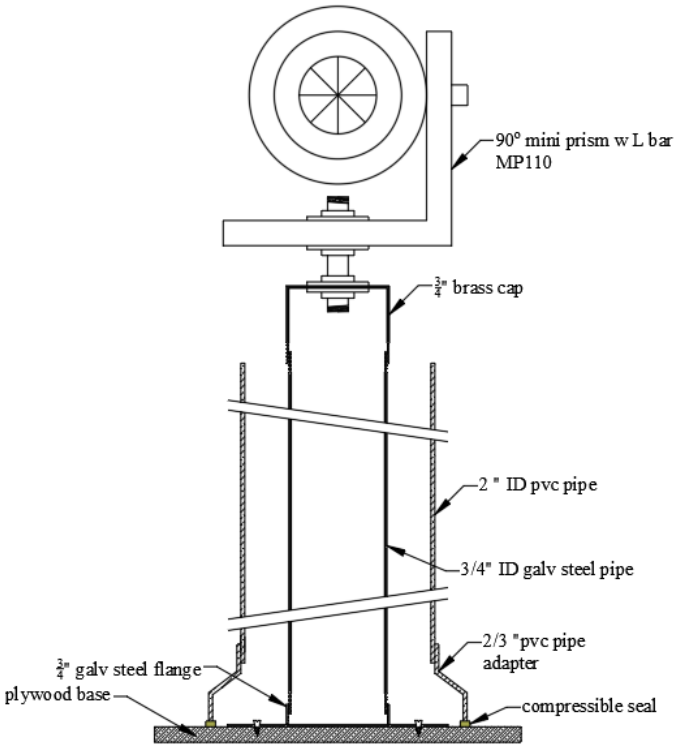

Figure 28. Schematic diagram of the settlement plates.

Settlement plates were fabricated in the lab following the Geokon Model 4625 (Geokon 2023) Settlement Plate System, designed primarily as an inexpensive means for monitoring in areas where significant settlement or substantial material displacement is expected. Two 15 mm plywood boards 0.3 m x 0.3 m were screwed together to form a thick platform, galvanized steel pipes attached to a galvanized steel flange were used as riser rods and a reflective mini prism attached to each end of the riser rods. 50 mm PVC pipes were used as isolation casings, and compressible foam was used as a compressible seal.

3.2.3 Lateral Deformations

3.2.3.1 Vertical Inclinometer

A slope inclinometer was used for monitoring lateral deformation within the reinforced mass. The system included a portable probe, a portable readout, an installed inclinometer casing and casing caps. The casing had four (4) tracking grooves corresponding to two orthogonal lines. The grooves served to control the orientation of the probe by securing the wheels on the probe. The probe contains a gravity-sensing transducer designed to measure inclination with respect to the vertical axis, hence, the inclinometer measures deformation normal to the axis of the pipe (Dunnicliff and Green 1988).

The inclinometer casing is usually installed with grouting at the bottom to provide a fixed reference. Then the inclination at the bottom is measured, followed by inclination measurements at intervals. This first set of measurements are compared to subsequent measurements and the differences are used to calculate the horizontal deformation along the vertical axis.

The deflection of each segment is calculated as the product of the segment length (L) and the sine of the inclination angle (θ) such that the absolute lateral deformation is the sum of the deflection from all the segments as shown in equation (40)

$$total\ deflection = \sum L.\sin(\theta) \tag{40}$$

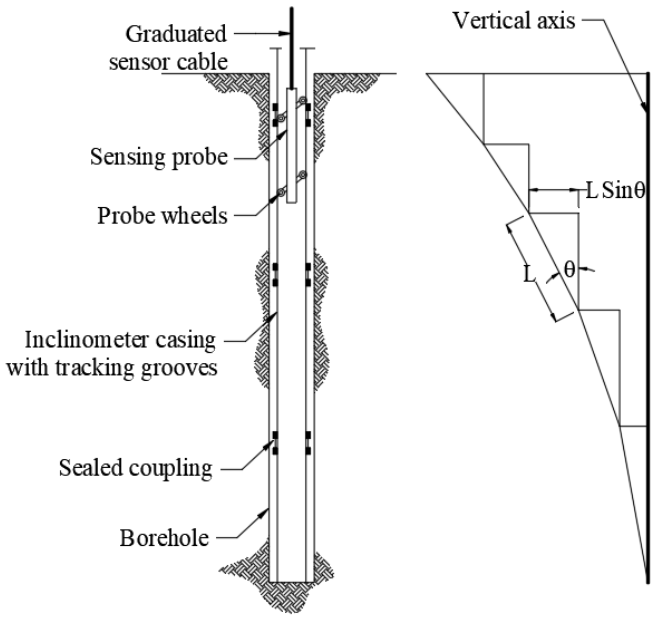

Figure 29. Schematic diagram of the working principle of the inclinometer.

3.2.3.2 Vertical Shape Array (SAAV)

Measurand's shape array was used alongside the slope inclinometer to monitor lateral deformation within the reinforced mass. The shape array consists of several rigid segments separated by flexible joints. Each rigid segment is equipped with sensors which measure tilt relative to gravity. Each segment has an accelerometer made with microelectromechanical system (MEMS) technology, an analog-to-digital converter, a digital temperature sensor and a microprocessor. The MEMS sensors are triaxial accelerometers and measure tilt relative to gravity in X, Y, and Z directions (Figure 30). The SAAV uses the X and Y tilts to find the XYZ path of the sensorized array when vertical but can also be used to measure vertical deformation when installed horizontally and can also be used to measure convergence (e.g., in a tunnel or culvert) (Measurand 2022).

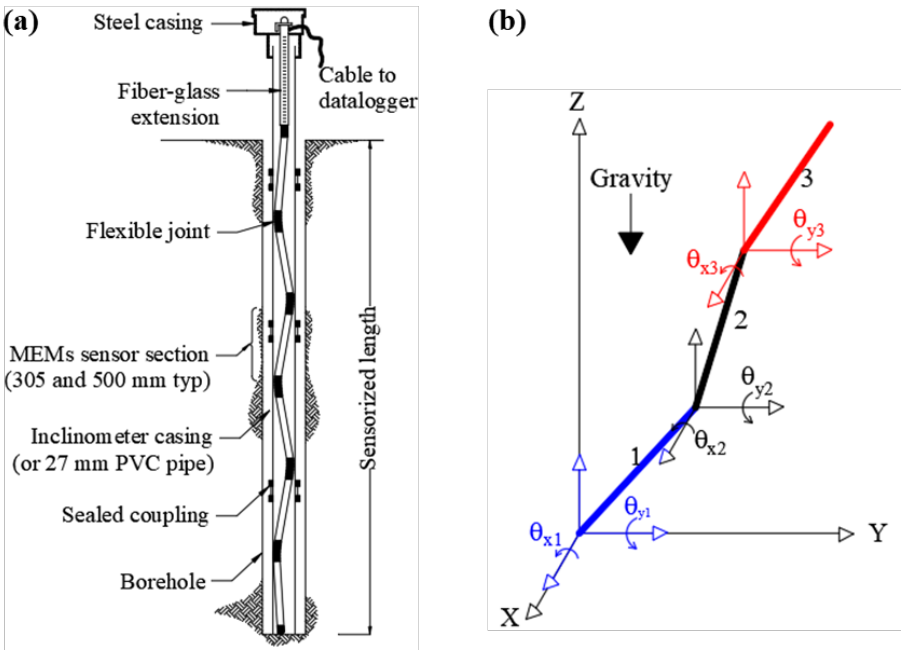

Figure 30. (a) schematic diagram of an installed shape array (b) tilts and positions for a multiple segment array.

The SAAV has a similar working principle to the slope inclinometer and can be installed in an inclinometer casing and pipes of various sizes. The SAAV however has a fixed sensorized length hence a fixed measurement profile. Like the vertical inclinometer, it requires a reference point that is fixed, or if movable, can be observed from external reference to account for end movement. The SAAV has the advantage of continuous automated measurement compared to the inclinometer, and measures X and Y deformations at known depth intervals when installed vertically.

3.2.3.3 Draw Wire Potentiometers

Six (6) string potentiometers were used to measure the lateral deformation at the wall facing. The string potentiometer, also known as the draw-wire potentiometer (Figure 31) transforms a linear movement into variable resistance (Micro-Epsilon 2023). A measuring wire made of highly flexible stainless-steel core is wound onto a drum to which a potentiometer or a

digital encoder is attached (Micro-Epsilon 2023). There is a linear relationship between the string position and resistance, hence, distance can be measured by pulling on the string and reading the change in the digital output. The distance is measured along the same axis as the string and should not be tilted beyond 3 degrees.

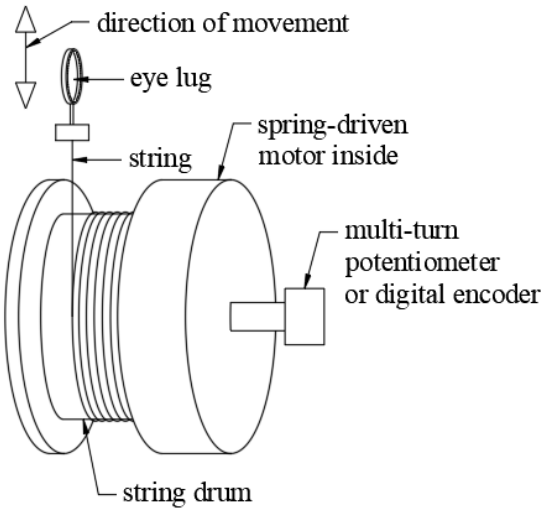

Figure 31. Principle of the string potentiometer.

3.2.4 Reinforcement Strain

The soil reinforcement is typically a structural element primarily capable of sustaining tensile loads. Strain gages were used to monitor the reinforcement strain, the tensile strains are then converted to tensile forces using the material properties (i.e., stress-strain properties) based on Hooke's law. The tensile strain results usually give an indication of the yielding wedge in the backfill behind the facing units, which shows the length of the reinforcement contributing to load resistance.

The foil resistance strain gage has the advantage of low cost over built-up strain sensors, typically small enough that it can be attached to various materials in areas where built-up sensors could not. The circuit is usually in the form of a Wheatstone bridge, the resistance of the gage

changes as the material to which it is attached is subjected to tension or compression (i.e., a change in the material dimensions). A Wheatstone bridge circuit consists of four resistors and a voltage supply. When one active resistor is used, it is a quarter bridge strain circuit (Figure 32), when two resistors are active, it is a half bridge and when all resistors are active, it is a full bridge circuit.

The three-wire foil gage is preferred to the two-wire gage because the third wire is connected to the input channel to nullify temperature induced resistance changes (Campbell Scientific 2011). The quarter bridge circuit compared to the half and full bridge circuits is easier to install and does not require knowledge of the Poisson's ratio of the material. Any error in the Poisson's ratio used in the calculations will carry through to the result for half and full bridge circuits. The quarter bridge, compared to half and full bridge circuits, has the disadvantage of lead wire resistance effects but this can be minimized by adjusting the gage factor and using the adjusted gage factor in calculating the member strains (Campbell Scientific 2011).

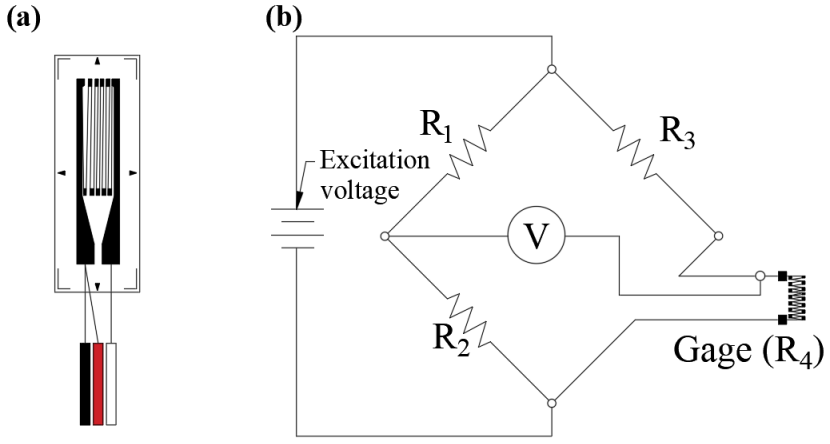

Figure 32. (a) three-wire foil resistor gage (b) quarter bridge strain circuit for a three-wire gage.

To use one active gage, resistance must be supplied for the other three legs of the Wheatstone bridge, hence a bridge completion terminal input module, matching the nominal

resistance of the gage, goes along with using a quarter bridge strain gage when using the Campbell Scientific's system.

Figure 33. Four-wire full-bridge terminal input module (Campbell Scientific 2023).

3.2.5 Data Collection

A program was written and compiled in CRBasic for the instrumentation plan. Campbell Scientific's CR1000 was used as the main data logger for the project. A vibrating wire module with one multiplex was connected to the CR1000 to enable it to read the vibrating wire earth pressure cells. Four (4) multiplexers were connected directly to the CR1000 for the strain gages. A strain completion module (120 ohms) was used for each strain gage in order to complete the Wheatstone bridge circuit. Six (6) draw wire potentiometers were used in measuring the precast panels' lateral displacement. The potentiometers were connected to the remaining channels on the CR1000. Since the channels on the CR1000 were used up, Campbell Scientific's CR6 datalogger was used for the shape array. The connections and data logging scheme are shown in Figure 34.

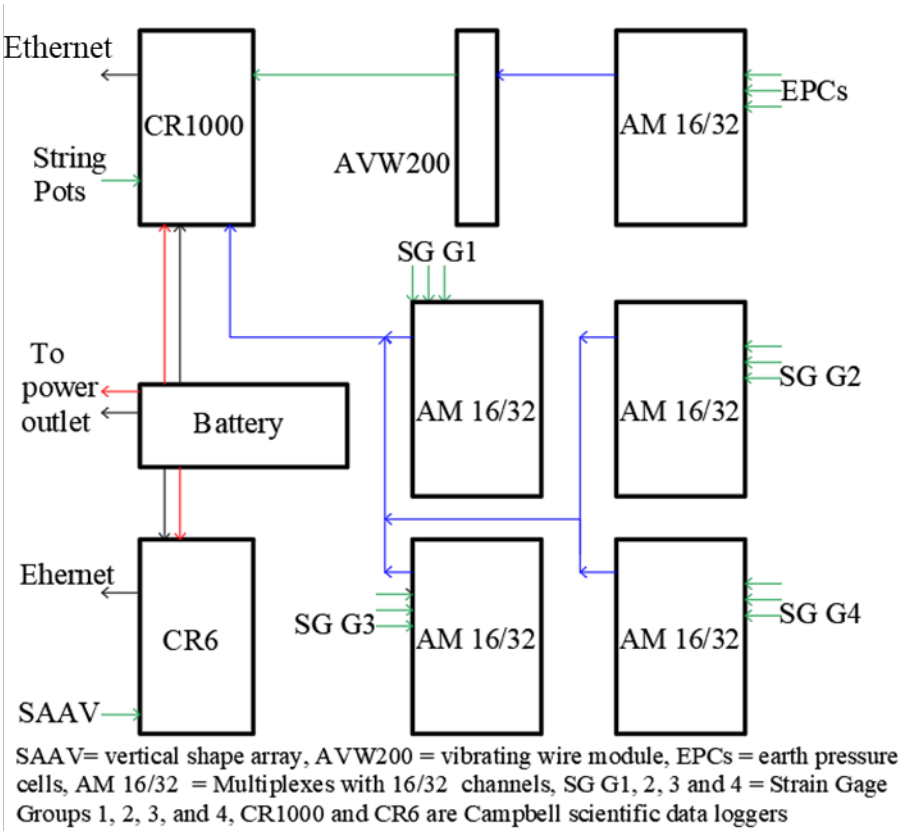

Figure 34. Data logging plan for all the instruments.

3.2.6 Monitoring

3.2.6.1 Total Station

A Topcon GTS-235W measures geospatial data of a point (usually reflective targets). Continuous routine surveys were used to monitor progressive movement of survey targets at various points of interest. This was used to monitor settlement using the reflective mini prisms attached to the settlement plate riser rods. Reflective survey targets were glued near the top and bottom of each facing panels, the total station was then used to monitor the progressive movement of each point to determine the lateral displacement.

Figure 35. Topcon GTS-235W total station (Precision Geosystems)

3.2.6.2 Leica 3D Scanner

The Leica RTC360 is a high-speed 3D laser scanner with integrated HDR spherical imaging system and Visual Inertial System (VIS) for real time registration (Leica Geosystems 2023). The system is capable of conducting multiple setups and automatically linking them to create point clouds that represent physical observation. The scanner has a blind spot directly beneath it, through the tripod which widens with elevation, and was considered when choosing the location and the orientation of the scanner during routine scans. The Cyclone Register-360 software was used to register the scans, conduct further alignment, clean the point cloud, and take preliminary measurements and takeoffs. Further post-processing, meshing, and surface analysis were done using the Cyclone 3DR program.

Figure 36. Leica RTC360 3D laser scanner.

3.2.7 Layout and Plans

The instrumentation and monitoring plan was designed to evaluate internal and external stability when subjected to localized foundation subsidence. Figure 37 shows the planned layout of the instruments at the foundation level as well as the planned location of the soft zone in the foundation. Figure 38 shows a plan view of the steel straps, indicating the groups to be equipped with strain gages. Figure 39 shows a section of the experimental setup with the instruments and setup of the total station and 3D scanner. The red, dotted line shows the geometry of the bi-linear active failing wedge assumed by the coherent gravity design method for steel reinforced MSE walls. The strain gages were distributed on instrumented steel straps such that there are gages following the line of failure. Figure 40 shows the positions of the survey targets on the facing panels. The total station was set up close to the Geochamber in order to see deep enough to the facing panels below the strong floor and at the same time see the survey targets on the settlement plates above the wall. The 3D scanner was mounted at an elevation above the Geochamber to ensure that the wall facing panels and all settlement plates are captured in the scans. The RTC360 scanner was mounted horizontally to eliminate the effect of the blind spot.

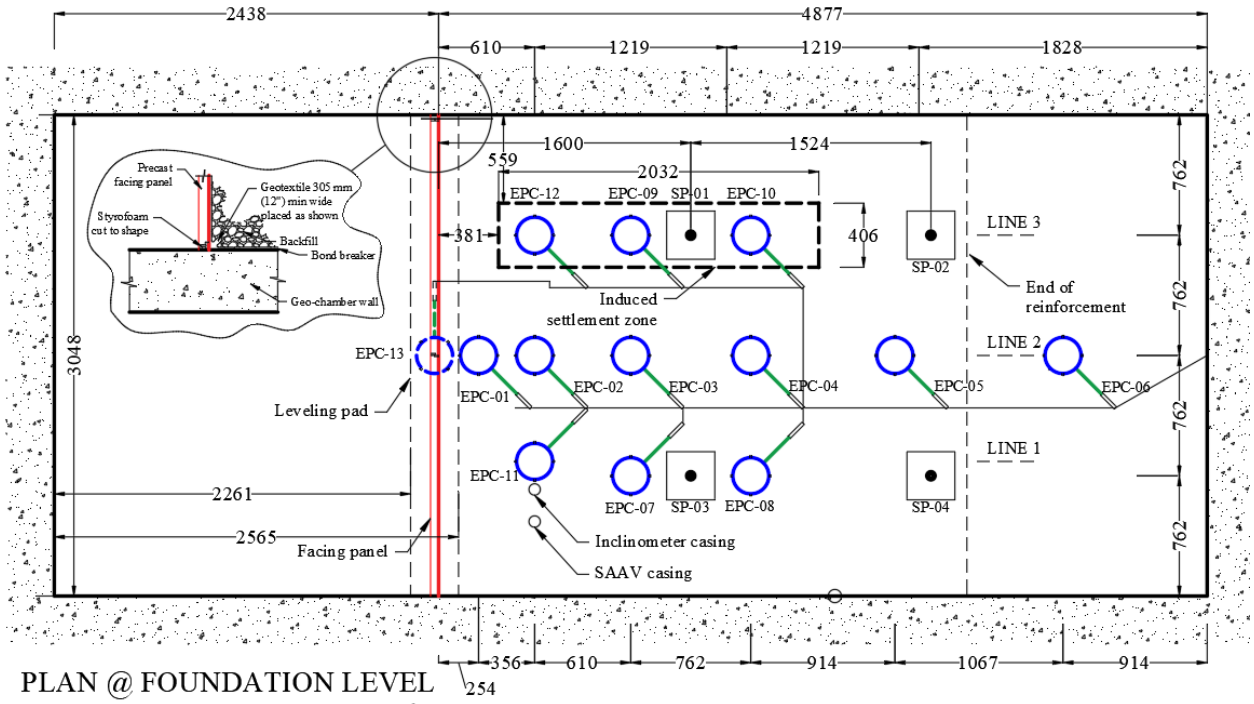

PLAN @ FOUNDATION LEVEL
All dimensions in mm, 1 mm = $\frac{1}{25.4}$ in

Figure 37. Instrumentation layout plan at the foundation level.

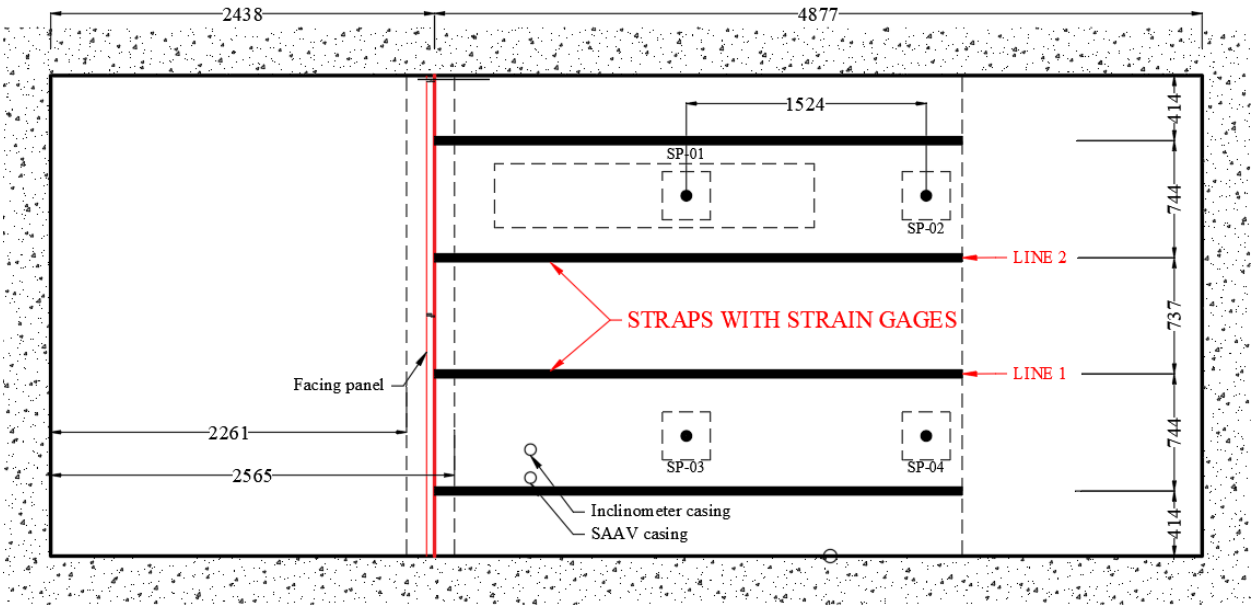

PLAN @ FIRST LEVEL OF REINFORCEMENT
All dimensions in mm, 1 mm = $\frac{1}{25.4}$ in

Figure 38. Layout of reinforcement indicating the straps to attach strain gages on.

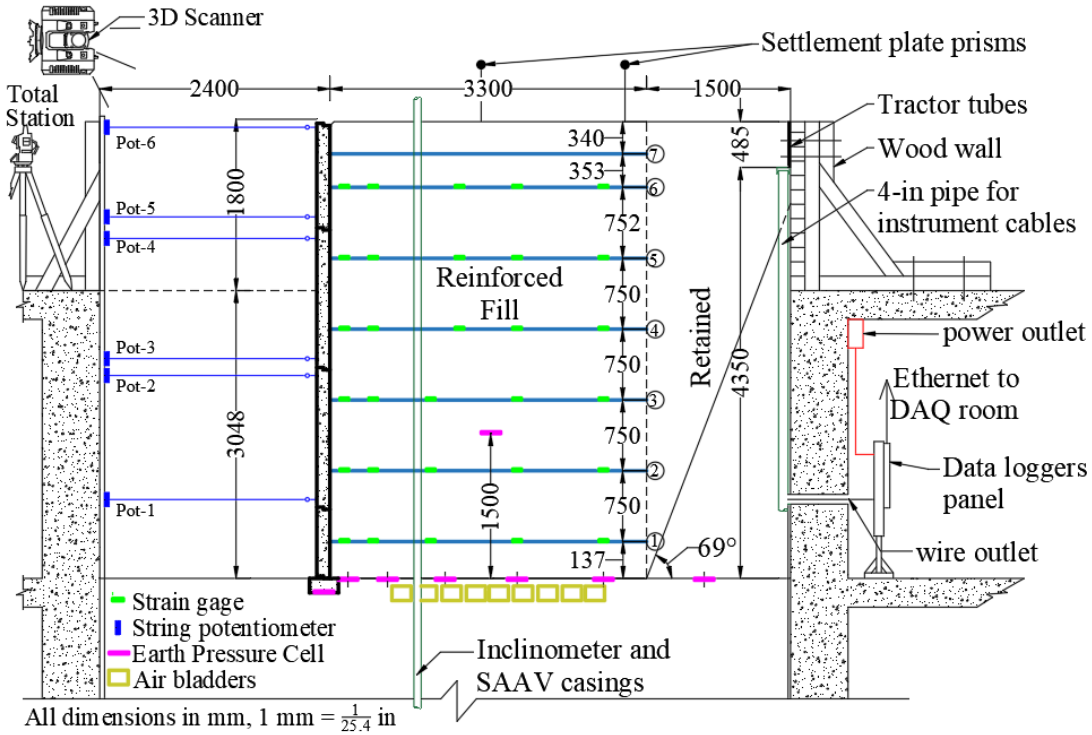

Figure 39. Full instrumentation and monitoring layout section.

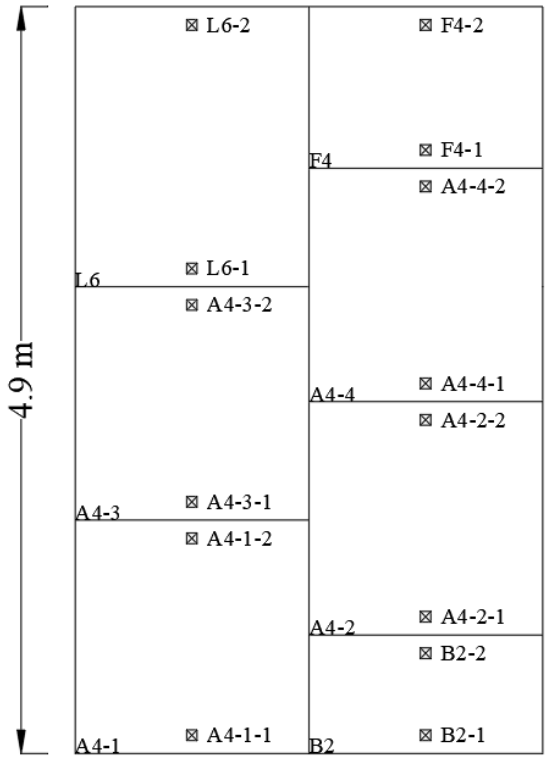

Figure 40 Concrete panels with survey target tags for measurement of facing displacement.

3.3 MSE Wall Construction

3.3.1 Materials and Equipment

3.3.1.1 Drainage Layer

An open graded aggregate (AASHTO's #67 grade) was used to fill the first 0.6 m of the Geochamber to cover the drainage outlet pipe. The material is a crushed granite with aggregate sizes ranging from 2.36 mm to 19 mm (Nicks 2013). No further tests were conducted on the #67 stone as its primary purpose was solely for drainage.

3.3.1.2 Foundation Soil

The M&M river-sand was used for the foundation fill up to the 3 m mark in the Geochamber. The properties of the material for the foundation fill were determined through laboratory testing. Sieve analysis tests conducted on the material (following ASTM C136/C136M-19) showed a poorly graded sand with less than 1% fines content (Figure 41), an effective grain size of 0.23 mm and maximum aggregate size of 4.75 mm. The coefficient of uniformity (C_U) is 4.0 and the coefficient of curvature (C_C) was 1.05. The minimum and maximum dry unit weight were 15 kN/m^3 and 19 kN/m^3, respectively. Direct shear tests conducted on the material (following ASTM D3080-04) showed a cohesionless behavior with a slope of 0.8583 resulting to a friction angle of 41^o (Figure 42). Consolidated drained triaxial tests were conducted (following ASTM D7181-20) for the foundation fill material, the results showed zero cohesion and a friction angle of 41.5^o (Figure 43). Figure 44 shows the deviatoric stress versus axial strain plots for the sand material. The secant moduli were 36700 kPa and 56700 kPa for confining stresses of 103 kPa and 206 kPa respectively.

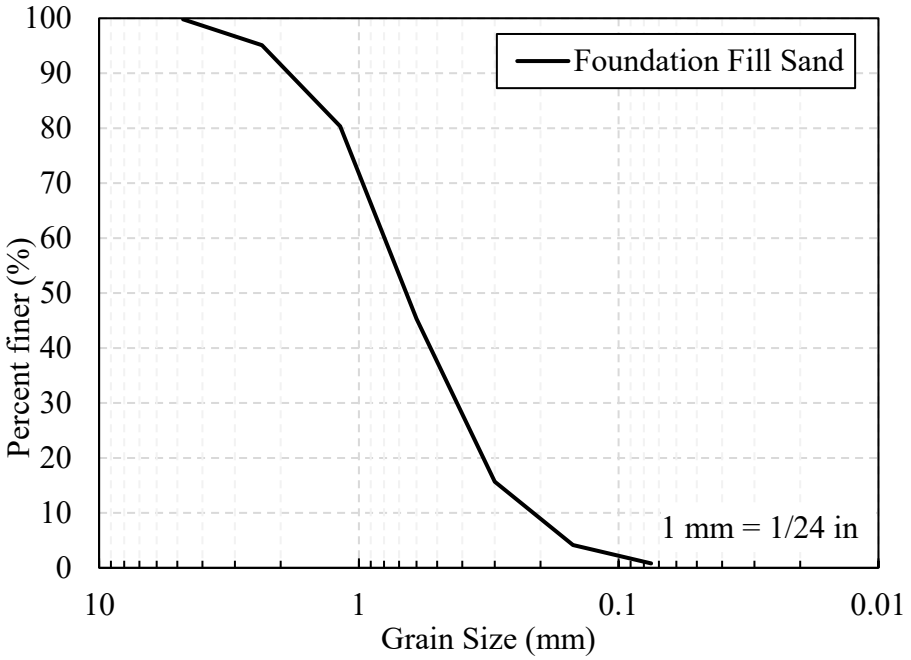

Figure 41. Grain size distribution for the foundation fill material.

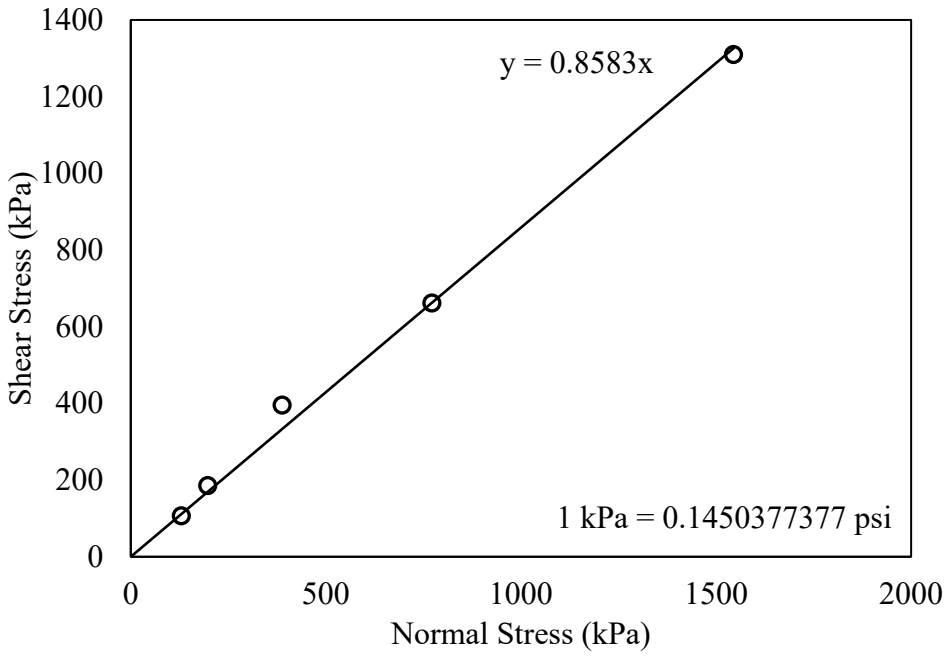

Figure 42. Direct shear test result for foundation fill sand.

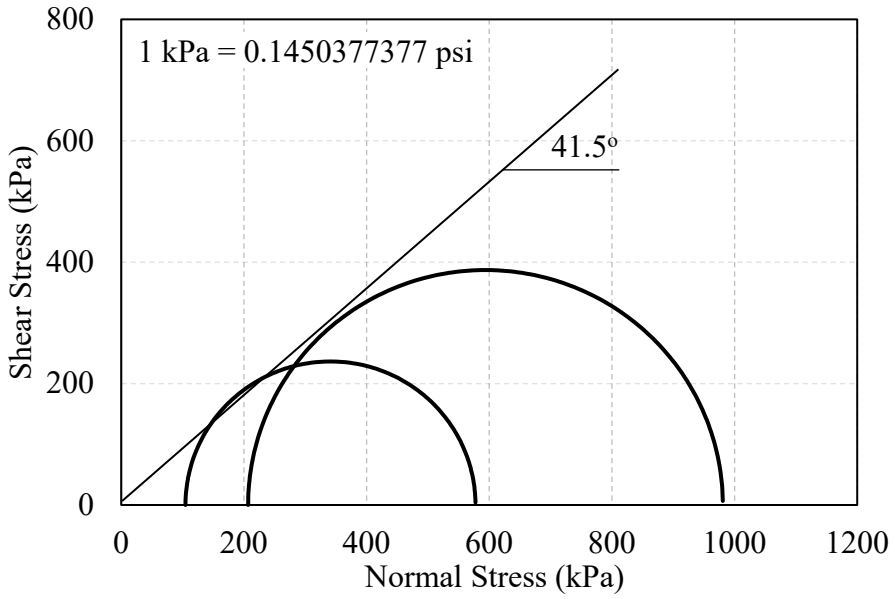

Figure 43. Mohr-Coulomb failure envelop for foundation fill sand.

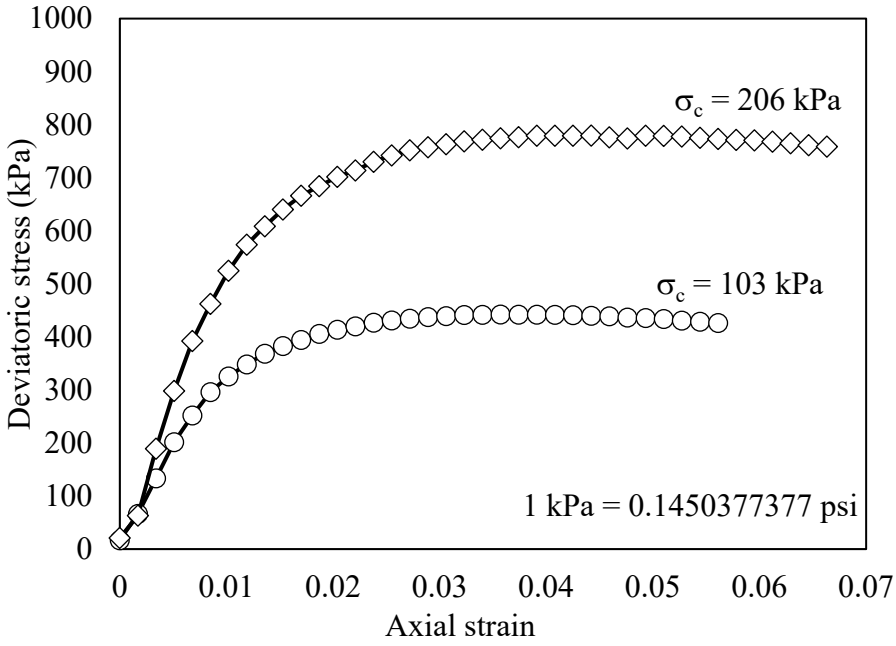

Figure 44. Deviatoric stress vs strain plots for foundation fill sand.

3.3.1.3 Reinforced Fill

AASHTO's grade #57 stone was used for the reinforced fill as well as the retained fill. Vulcan Materials donated 1434 kN of the #57 aggregate used for the wall construction. Laboratory tests were conducted on the material to determine the properties.

A vibratory plate test was conducted on the #57 material to determine the maximum unit weight. Table 2 shows a summary of the results from the tests, the average unit weight of the specimens in loose (uncompacted) state is 14.8 kN/m^3 while the average unit weight of the compacted specimens is 16.7 kN/m^3.

Table 2. Summary of results from unit weight tests

S/N	Loose Unit Weight kN/m^3	Compacted Unit Weight kN/m^3
Specimen 1	14.6	16.8
Specimen 2	14.9	16.7
Specimen 3	14.9	16.5
Average	**14.8**	**16.7**

A grain size distribution test was conducted on the #57 material using a set of sieves for coarse aggregates. The test result (Figure 45) showed zero fines content with an effective grain size of 7 mm and maximum aggregate size of 25 mm. The coefficient of uniformity (C_U) was 2.21 and the coefficient of curvature (C_C) was 1.06.

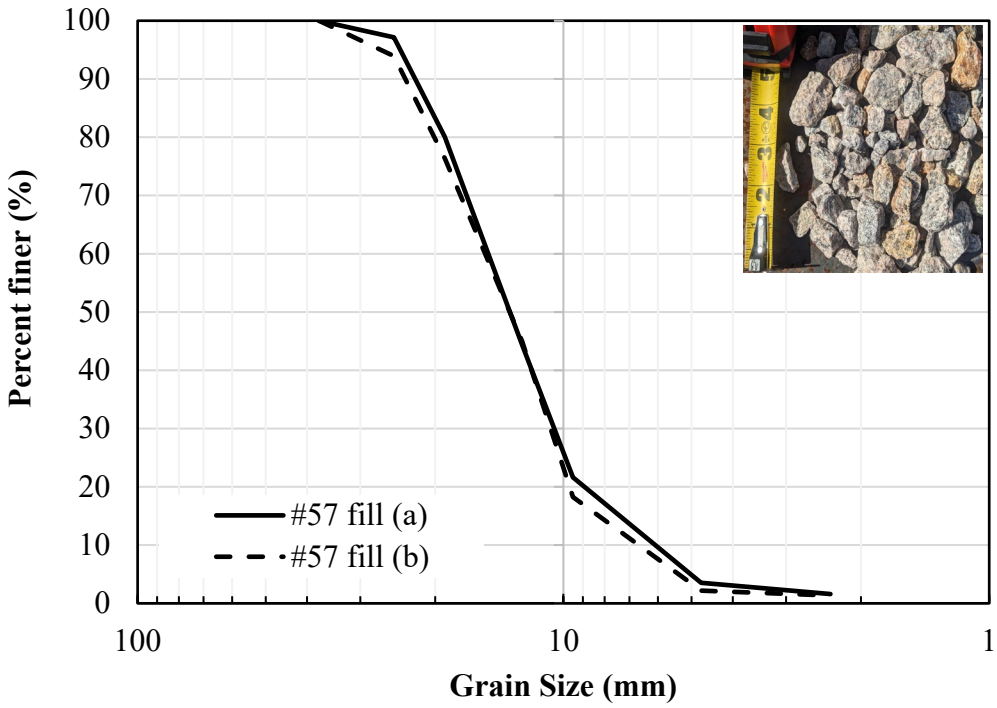

Figure 45. Plot of sieve analyses results for the #57 stone

The maximum particle sizes for direct shear test and triaxial test are 1/10th and 1/6th of the width or diameter of the device, respectively based on ASTM standard (after Nicks 2013). The maximum particle size of the #57 stone is about 1/3rd of the standard testing devices, hence a large-scale testing device is needed to perform shear strength tests on the #57 stone. Large scale direct shear test results published by Nicks (2013) indicated a friction angle of 52^{o} and 56^{o} for dry and saturated conditions respectively.

A large scale triaxial test was set up at ASEL to conduct triaxial tests on the #57 aggregate following ASTM D7181-20. Karol Warner's large scale triaxial cell for 150 mm diameter specimen was used for the tests. The prepared specimens were 150 mm diameter and 300 mm height. Two Durham-Geo pore pressure transducers (Model E124) were used to monitor the cell pressure and specimen pore water pressure. The Material Test Systems' (MTS) Landmark

Servohydraulic load frame model 370.10 equipped with a 98 kN capacity load cell was used to load the specimen (Figure 46). The Campbell Scientific's CR1000 data logger was used to collect the data during testing.

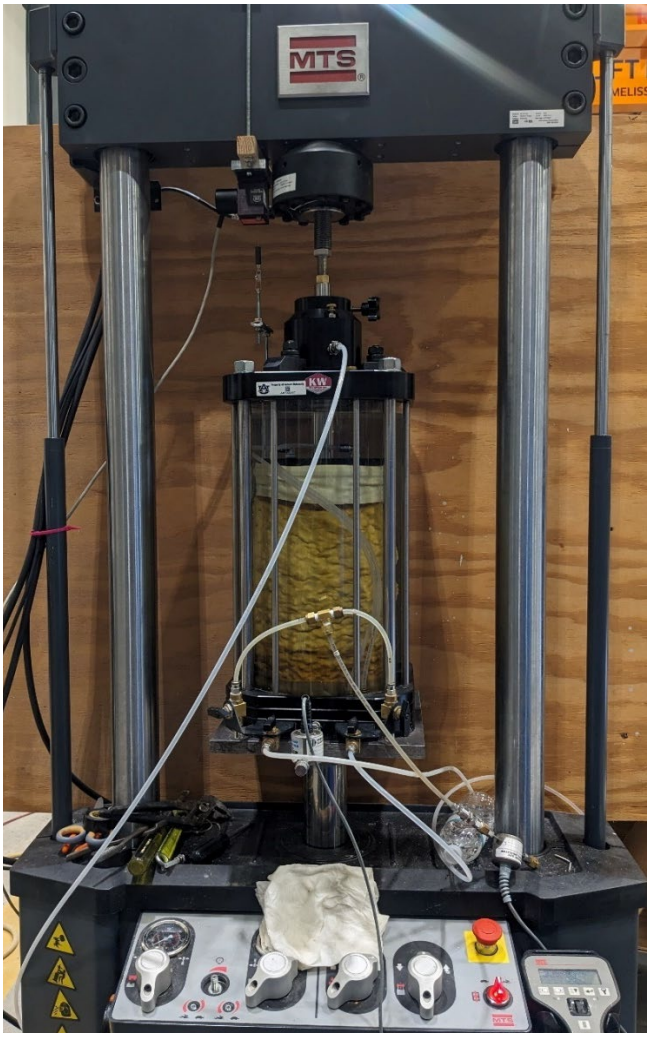

Figure 46. Large-scale triaxial test setup.

Consolidated drained triaxial tests were conducted using the #57 aggregate, the results showed a cohesionless behavior (c'=0) and a friction angle of 48^{o} (Figure 47). Figure 48 shows the deviatoric stress versus axial strain plots. The secant moduli were 23800 kPa, 31000 kPa and 31000 kPa for confining stresses of 48 kPa, 69 kPa and 89 kPa respectively.

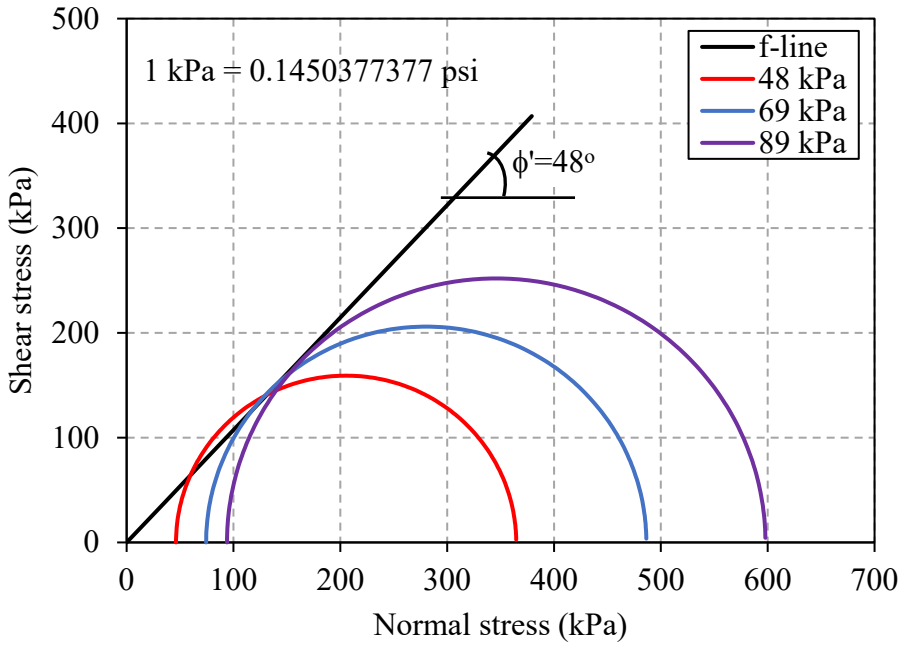

Figure 47. Mohr-Coulomb failure envelop for the #57 crushed stone.

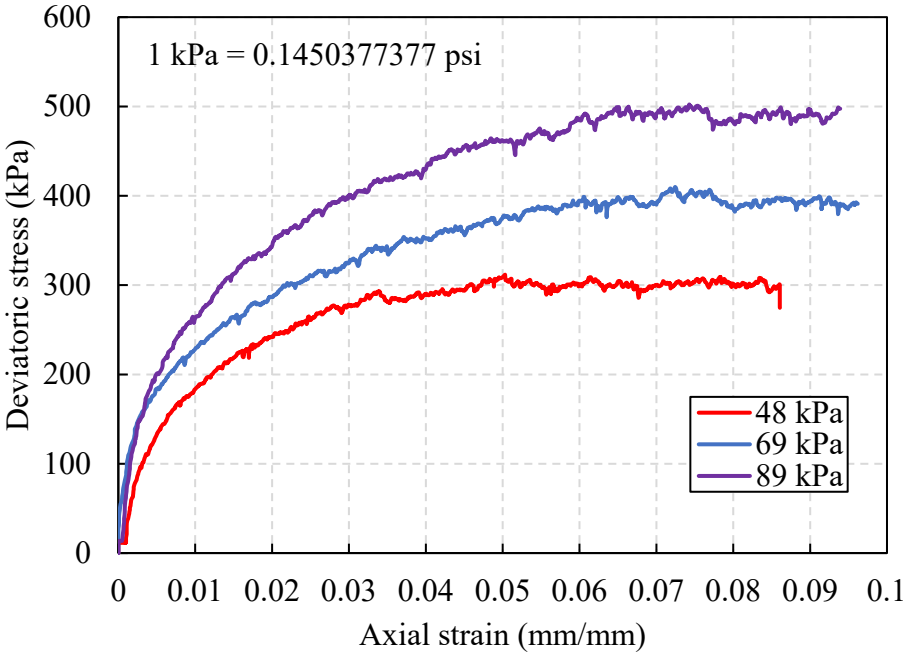

Figure 48. Deviatoric stress vs strain plots for the #57 crushed stone.

3.3.1.4 Air Bladders

Air bladders (10 Nos) were used to simulate pockets of soft soil and induce differential settlement in the foundation for the proposed wall. A flexible hose with a valve was attached to the bladders. Each bladder had an inflated length of 406 mm, width of 203 mm and a height of about 178 mm as shown in Figure 49.

Figure 49. Inflated air bladder used for simulating zone of soft soil in foundation.

A test was conducted to ensure that the bladder would hold the expected stress ranges. The bladder was inflated, then placed in a wooden box. The box was 600 mm x 600 mm and 1200 mm deep. The bladder was buried 600 mm from the box floor and then filled to the top with sand. The setup was then placed under a load frame from which an axial load was applied (Figure 50).

Figure 50. Setup for the sandbox testing for the air bladders.

Figure 51 shows the applied load versus displacement of the load frame. The load was applied using displacement control to avoid sudden failure of the setup. A maximum displacement of 63 mm was reached, at which time the wooden box started to fail, and the test was stopped. The maximum load applied was 15 kN. After the setup was dismantled, the bladder was still intact with the same level of inflated air when the test was setup.

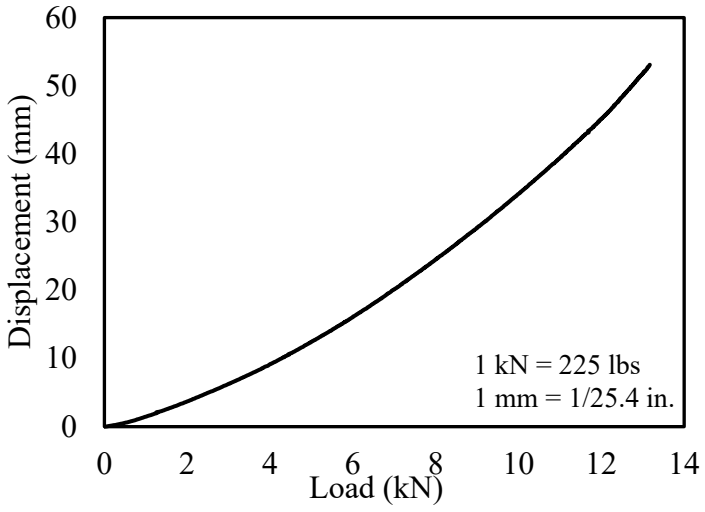

Figure 51. Load vs displacement plot from test on air bladder.

3.3.1.5 Reinforcing Steel and Strain Gages

Twenty-eight (28) steel straps were delivered by RECo to be used as soil reinforcement. The straps were the high adherence type ribbed steel, 50 mm wide and 4 mm thick, and 3.3 m long. The steel surface was prepared according to strain gage manufacturer directions and three-wire foil strain gages with nominal resistance of 120 ohms and nominal gage factor of 2.11 were attached to the straps (Figure 52). The strain gage wires were wrapped in duct tape to protect the wires from the angular aggregates. Strain gage wires were attached to the manufactured lead wires using button splices.

Figure 52. Strain gage installation on reinforcement straps.

A tensile test was conducted on specimens from the steel straps. The MTS dynamic high force test system model 311.31 with hydraulic wedge grips was used to apply a tensile load to the test specimens. The test was conducted according to ASTM A370-21 on standard specimens of 18 in overall length without reduced sections. The first specimen was tested at a rate of 0.25 in/min (half of the maximum free running rate specified in ASTM A370-21 section 8.4.1). The remaining specimens were tested at a rate of 13 mm/min since there was no perceived advantage for running at a slower rate. Two strain gages were glued on the steel specimens to measure axial and

transverse strains, and a Campbell Scientific's CR1000 logger was used to collect load and strain gage data. Load and displacement data was also collected using the MTS station builder system. The glued-on strain gages stopped responding after about 8000 με so there was no data from that after yielding. The image in Figure 53 shows a failed specimen in the test setup.

Figure 53. Failed steel specimen in the MTS tensile test setup.

Figure 54 shows plots of the load vs strain results for the four tests. The orange line shows data from collected with the CR1000 from the loadcell and strain gages while the blue lines show data from the loadcell, and displacement retrieved from the MTS. The average values for the yield strength, ultimate strength, secant modulus and Poisson ratio from the four tests were 553000 kPa, 725000 kPa, 211 GPa and 0.27 respectively (Table 3).

Table 3. Summary of steel strap tensile test results.

Specimen ID	Yield strength kPa	Ultimate strength kPa	Elastic modulus Gpa	Poisson ratio
1	543000	716000	220	0.29
2	582000	764000	220	0.27
3	554000	720000	187	0.29
4	532000	699000	220	0.23
Average	**552000**	**725000**	**211**	**0.27**

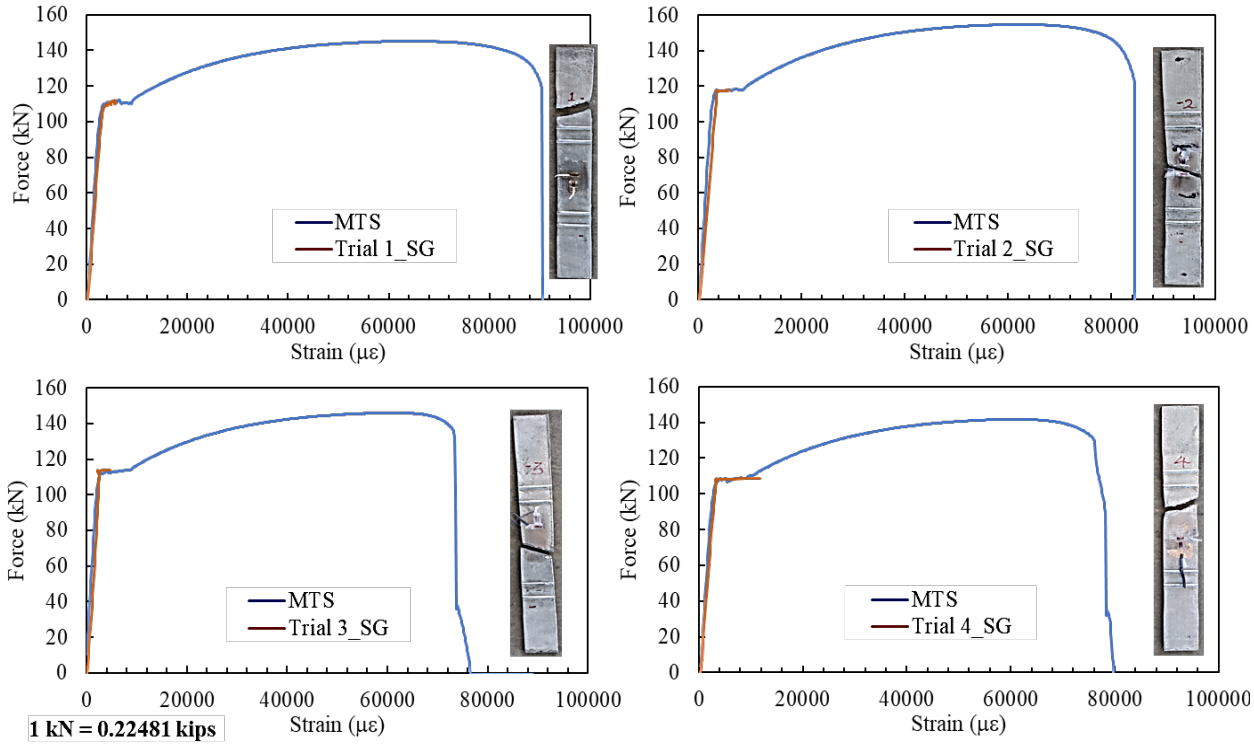

Figure 54. Results from tensile tests on four steel strap specimens

3.3.1.6 #57 stone – plastic sheet interface friction

A series of large-scale direct shear tests were conducted on the #57 stone – plastic sheet interface which showed friction angles >35° without reaching failure and with significant data fluctuations. Ultimately, the standard 64 mm diameter direct shear testing device was used (test setup shown in Figure 55) to perform a direct shear test to determine the interface friction between

the plastic sheet and the MSE mass, using #57 stone fraction passing through the 9.5 mm sieve size to conform to the relative specimen particle size of the testing apparatus. The results showed an interface friction angle of 29° (Figure 56).

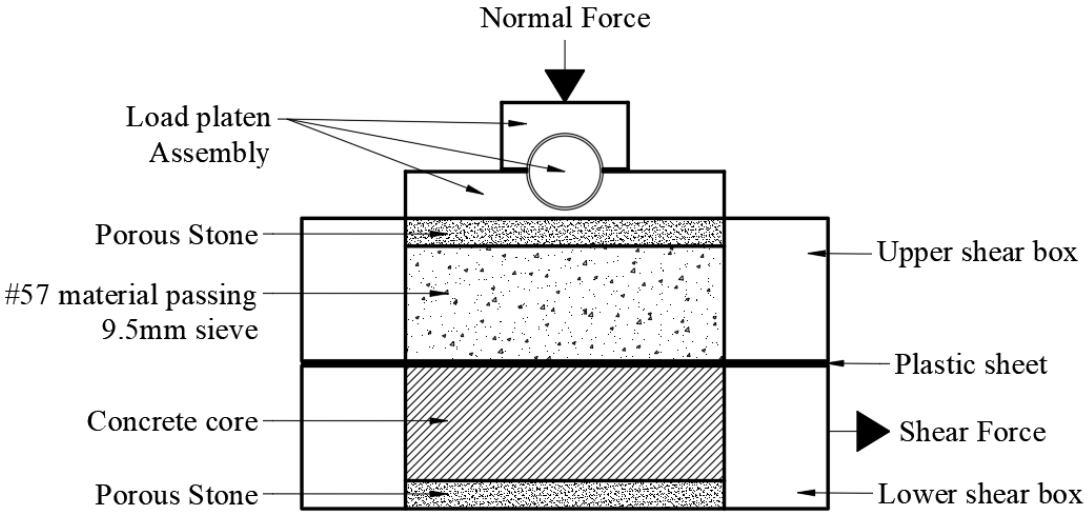

Figure 55. Direct shear test setup for the gravel-to-plastic sheet interface.

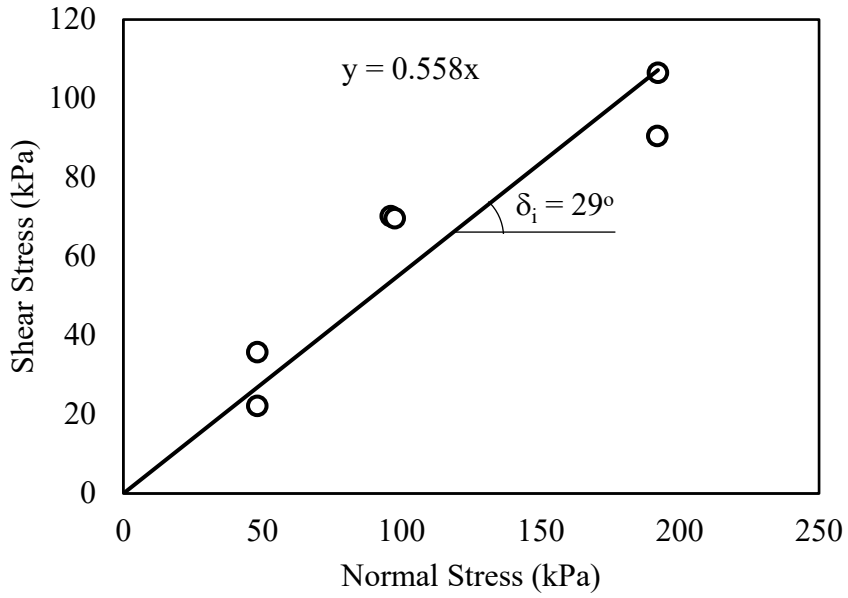

Figure 56. Shear vs Norma Stress for #57 stone – plastic sheet interface friction

3.3.1.6 Leveling Pad

Typical dimensions of the leveling pad for a precast facing panel are 150 x 300 mm. The leveling pad for the MSE wall was made from mass concrete. Previous studies (Bastick et al. 1993 and Runser et al. 2001) have reported load concentration at the base of the facing panels (about two to three times the panel weight), to facilitate stress release and redistribution, the leveling pad was cast in three modules with dimensions shown in Figure 57. A template of a contact type earth pressure cell was placed in the formwork before casting the concrete to provide housing for the cell to measure stresses below the pad.

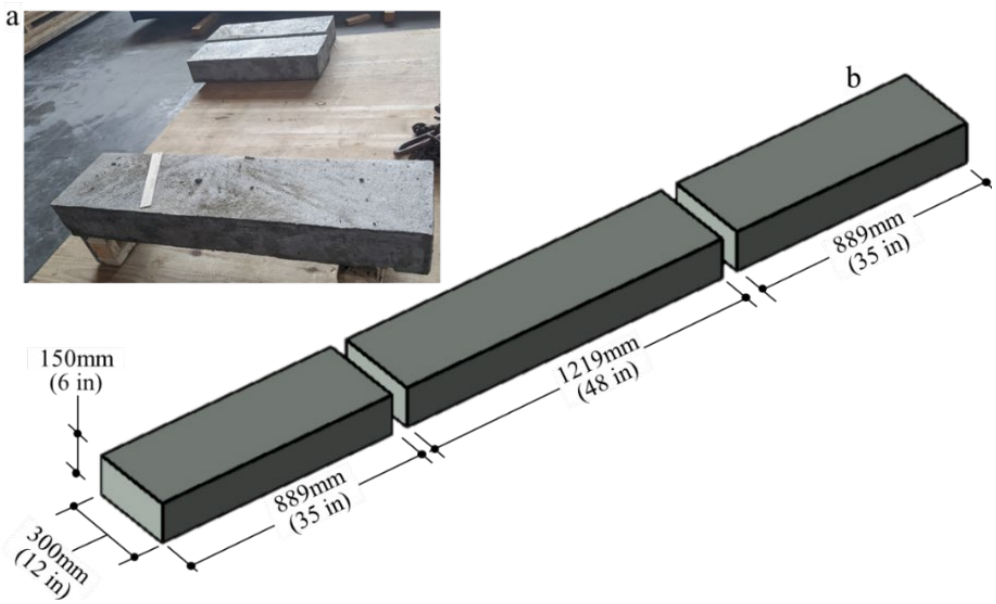

Figure 57. (a) Finished concrete level pad (b) schematic diagram of the leveling pads.

3.3.1.7 Facing Panels, Bolts, Lifting Clutches, Bearing Pads and Geotextile.

The facing panels (Figure 58) and the accessories for placement were delivered by RECo, consisting of precast reinforced concrete panels with ashlar stone finish. The panel type and dimensions are summarized in Table 4.

Figure 58. Precast concrete facing panels for the MSE wall.

Table 4. Precast facing panel designation and dimensions.

Panel ID	Nos # 	Width m 	Length m
A4	4	1.50	1.50
B2	1	1.50	0.73
L6	1	1.50	1.85
F4	1	1.50	1.10

Each panel width had two columns of reinforcement tie strap that connects to the reinforcement straps using ASTM A449 bolts as shown in Figure 59. At the top of each panel, there was a cast-in lifting lug to which concrete lifting clutches (Figure 60a) were connected to facilitate safe installation. Each panel also had two grooves at the top to place bearing pads. 25 mm thick rubber bearing pads (Figure 60b) were used to prevent concrete-to-concrete contact in the horizontal joints. Geotextile sheets, 300 mm wide were placed over the horizontal and vertical joints using spray glue (Figure 60c).

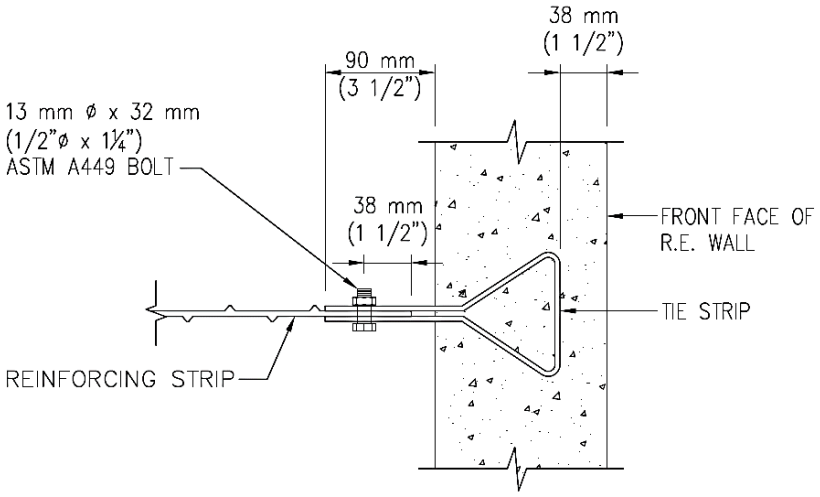

Figure 59. Reinforcing strap connection to tie strap (RECo).

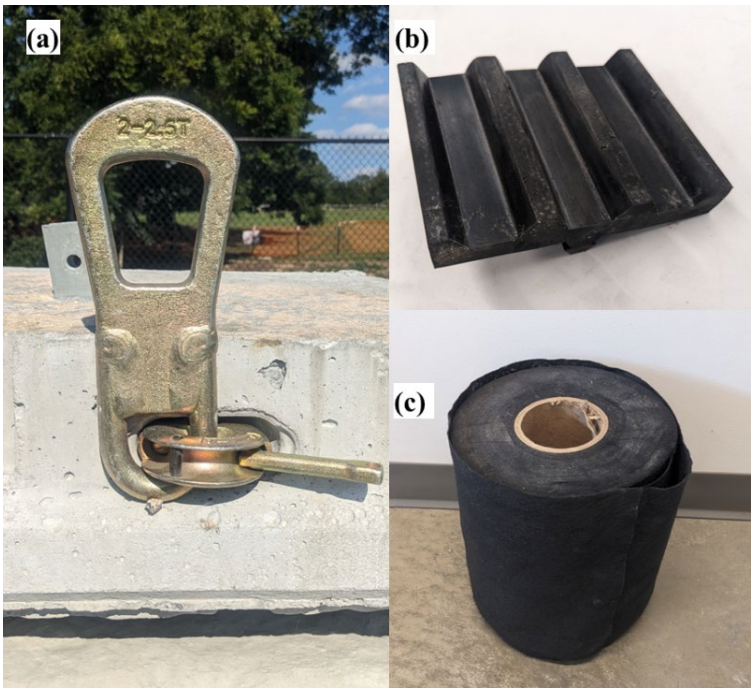

Figure 60. (a) lifting clutch, (b) rubber bearing pad and (c) geotextile.

3.3.1.8 Clamps, External Bracing, Wooden Wedges and Spacers

The clamps, wooden wedges and wooden spacers illustrated in Figure 61 were fabricated in the laboratory. The standard clamps were used to hold aligned adjacent panels in place at each

vertical joint. The clamp shown in Figure 61b was used at the top of the panels and fastened to a wooden brace with a fixed supported end. The wedges were used to control the horizontal spacing and facing panel tilt, and the spacer was used to maintain the vertical joint spacing.

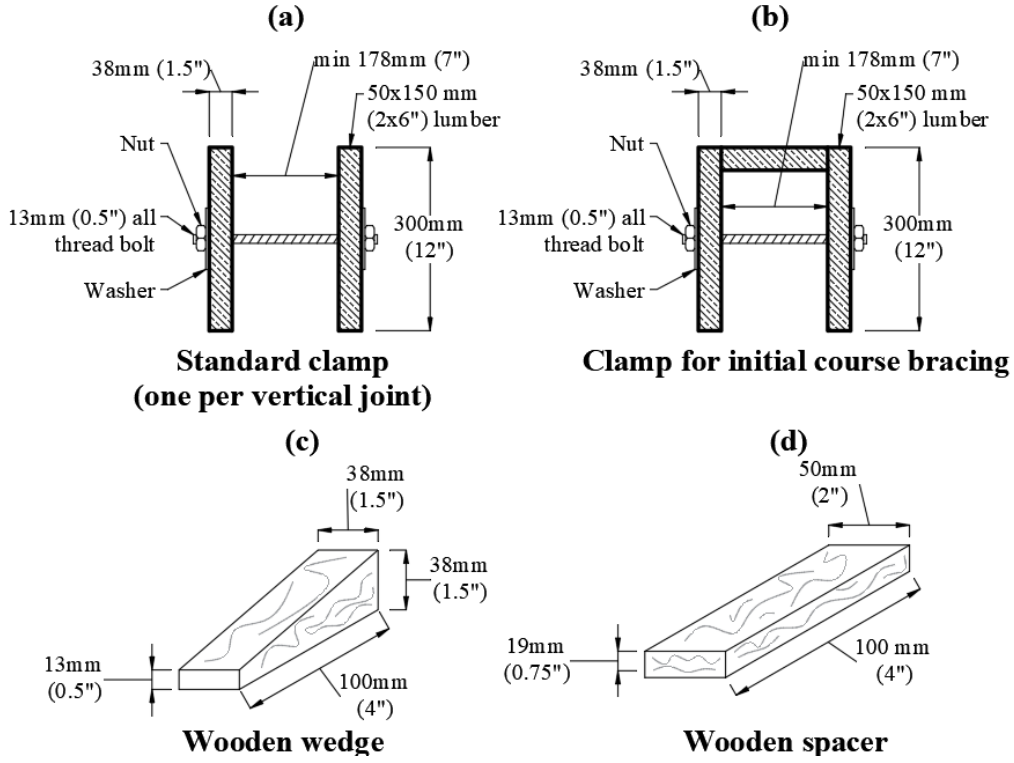

Figure 61. Clamps, wooden wedges, and spacers.

3.3.1.9 Compactor

Bomag's multipurpose compactor BMP 8500 (Figure 62) was used to compact the fill materials. The compactor was remote-controlled with both front and rear vibrating drums. It was positioned in the Geochamber using the single point lifting lug and driven over the fill making several passes. A Bosch's DH1020VC electric jack hammer with a circular rammer plate was used to compact the area within 0.9 m behind the concrete facing panels, and the sides of the Geochamber where the BMP 8500 could not get to.

Figure 62. (a) remote-controlled multipurpose compactor (Bomag 2023) (b). Bosch's electric jack hammer with rammer.

3.3.2 Construction

This section details the construction of the MSE wall in the Geochamber and some of the steps taken are specific to the given constraints encountered. The construction follows the Reinforced Earth's manual for construction of MSE walls with rectangular panels and the steps outlined in section 2.5.2 of this document. For brevity, all images referred to in this section are presented in Appendix A.

A drainage layer was constructed over the first 0.6 m in the Geo-chamber using the #67 crushed stone, followed by the sand foundation, with a geosynthetic layer in-between to separate both layers.

Air bladders were used to simulate soft soil pockets and induce differential settlement in the foundation. The bladders were installed in a trench 2 m long, 406 mm wide, and 25.4 mm deep. The bladders were placed in the trench (Figure 137) and covered with about 76 mm of the

foundation sand. The inlet hoses for the air bladders were passed through one of the holes in the Geochamber.

The earth pressure cells, and settlement plates were placed atop the sand foundation following the instrumentation plan. The cables were passed through a different hole in the wall that was to connect to the data logger (Figure 139). 76 mm of fine sand was placed on the earth pressure cells to minimize arching effects of the larger #57 aggregates around the cells. This also mitigates having points load from the angular aggregates used for the reinforced fill.

The leveling pads described in section 3.3.1.6 were installed with the top surface at the same level as the foundation. Earth pressure cell 13 (EPC_13) was placed beneath the leveling pad in a mold that was set before casting of the leveling pad (Figure 138 and Figure 139).

After the leveling pad was put in place, construction of the MSE wall commenced and the steps are summarized as follows:

Step 1: The first row of panels (one half panel and one square panel) were placed, the two panels were aligned, externally braced and a clamp was used to hold the two adjacent panels. A wooden spacer was placed between the two adjacent panels (Figure 140).

Step 2: A batter of about 13 mm was applied to the panels to account for expected displacement during compaction, the amount of batter was adjusted accordingly in the subsequent panels depending on the observed displacement. Wedges were placed at the base of the precast panels. A layer of geotextile was placed to cover the vertical joint. Styrofoam was cut to shape and was used as filler material between the panel and the chamber sidewalls. Geofabric was also placed to cover

the vertical joints between the panels and the chamber side walls (Figure 140 and Figure 141).

Step 3: The #57 stone backfill was placed up to 300 mm behind the facing panel to avoid pushout of the panels, the fill was compacted. Compaction was done primarily with the remote-controlled vibratory compactor. The sides of the wall and areas close to the facing panel were compacted using a jack hammer (Figure 141).

Step 4: The reinforcing straps were connected and aligned. The strain gage cables exposed to the #57 stone were further placed in a hose for extra protection. The strain gage wires were passed through the hole reserved for instrument cables and were then connected to the data logger (Figure 142).

Step 5: More backfill was placed and compacted above the first set of reinforcement before placing more fill directly behind the facing panels. The backfill was placed in the middle of the reinforcement lengths using a skid steer (Figure 143).

Step 6: The fill was placed to the top of the half-panel and compacted.

Step 7: Bearing pads were placed in the provided space atop the precast panel, the horizontal clamp was removed, and the next full-size panel was placed, braced externally, with a spacer in-between the two adjacent panels, geofabric at both horizontal and all vertical joint and filler Styrofoam placed (Figure 143).

Step 8: More backfill was placed and compacted (in 300 mm lifts) to the next reinforcement tie level. A PVC pipe was placed next to the hole for instrument cables to pass through. When backfill was placed to the next reinforcement tie level, a hole was

cut in the PVC, then the cables were lowered down the PVC pipe and passed through the hole to the data logger (Figure 142 and Figure 143).

Step 9: The straps were connected and aligned. The strain gage cables were passed through the PVC to the data logger. Each strain gage on the straps were tested with a multimeter before passing through the PVC.

Step 10: Steps 6 to 9 were repeated while placing the alternating panels till construction reached the strong floor level (Figure 143).

Step 11: When construction reached the top of the strong floor, the confining wood walls (fabricated to serve as confinement for the remaining 1.8 m of the MSE wall above the strong floor level) were placed and tightened down appropriately (Figure 144).

Step 12: A pair of tractor tubes were placed on the back confining wall and was equipped with a pressure transducer and a pressure regulator. This system will be used to supply the horizontal stress needed to fully mobilize an active wedge behind the reinforced zone (Figure 144).

Step 13: Steps 6 to 9 were repeated while placing the alternating panels till construction was finished 1.8 m above the strong floor level (Figure 145).

An earth pressure cell (EPC_14) was placed after 1.5 m of reinforced backfill and the last one (EPC_15) was placed close to the top of the wall to monitor applied surcharge. Construction of the reinforced fill started with installation of the leveling pad on February 7, 2023, and ended with the compaction of the final layer of gravel on March 29, 2023. A wooden brace was constructed in front of the MSE to which the draw wire potentiometers were affixed. The potentiometers were connected to the data logger on April 6, 2023.

3.4 Experimental Setup and Construction Summary

This assumption of a rigid reinforced mass allows for the transfer of all applied surcharge from the top of the wall to the foundation. This is unlikely to be the case as the MSE's flexibility allows for stress redistribution, and load shedding can occur within the reinforced composite. Because of the non-availability of a suitable proposed wall to be constructed in the field, a full scale MSE wall was constructed in the Geochamber in the lab.

The Geochamber, 6 m deep, was filled with foundation material up to 3 m, and a 4.8-m wall was constructed atop the foundation level. The top 1.8 m of the MSE wall was confined by a wood wall specifically designed and fabricated for this purpose.

The standard wall height to reinforced width ration of 0.7H was used hence the reinforced zone is 3.3 m long. The high adherence ribbed steel strips were used as reinforcement, segmental precast concrete panels with ashlar stone finish were used for the facing and both the reinforced fill and random backfill were placed and compacted using the #57 crushed aggregate.

Air bladders were installed in the foundation to simulate a poor bearing zone and to induce foundation differential settlement. Vibrating wire total earth pressure cells were used to measure earth pressure. Settlement plates with mini-prism survey targets were used to monitor settlement. Slope inclinometer and vertical shape array were used to monitor lateral deformation within the reinforced mass. Draw wire potentiometers and stick-on survey targets were used to measure facing lateral displacement. Three-wire foil resistor strain gages were used to monitor reinforcement strains. A total station was used to monitor the movement of all survey targets. Additionally, a 3D laser scanner was used to monitor deformation of the MSE wall.

Laboratory tests were conducted on the construction materials following ASTM standards. Construction of the MSE wall was completed following the steps outlined in the Reinforced Earth's manual for construction of MSE walls with rectangular panels and the steps outlined in FHWA GEC 11.

CHAPTER 4: MSE WALL TESTING AND RESULTS

This section describes testing of the completed MSE wall (including inducing differential settlement and surcharge loading), and the results from the instrumentation and monitoring programs.

4.1 Testing

The completed MSE wall was monitored for end of construction behavior before testing commenced. The testing stages included:

1. Monitoring of the wall after construction before any testing.
2. Inducing differential settlement: the valves from the air bladders were opened on May 10, 2023, to trigger settlement in the foundation.
3. Simulating traffic load (14 kPa): according to Berg et al. (2009), and AASHTO (2007), for external stability, traffic load for MSE walls parallel to traffic has an equivalent height of soil, h_{eq} equal to 600 mm. Heavy duty super-sacks of 600 mm height were filled with sand (same as the foundation sand) and arranged on the wall surface to simulate a uniform surcharge over the covered area, this was completed on May 12, 2023. The sandbags exerted a uniform pressure of about 14 kPa over an area of 5.4 m^2 resulting in a total load of 74 kN.
4. Increased surcharge (26 kPa): additional loads were added by placing concrete beams on top of the sandbags. An additional 66 kN was added on 17th May 2023 by placing four rectangular concrete beams and one concrete T-beam. Each rectangular beam weighs 5 kN while each T-beam weighed 46 kN.

5. Increased surcharge (43 kPa): Another 92 kN was added by placing two more concrete T-beams on May 18, 2023.
6. Increased surcharge (52 kPa): Finally, on 19th May 2023, the load was increased by 46 kN by adding another T-beam, bringing the external load supported by the MSE structure to a total of 278 kN. Figure 63 shows the completed wall with all imposed loads.

This testing sequence was followed in order to evaluate whether having a soft foundation zone and induced differential settlement severely impacts the performance of the MSE wall.

Figure 63. Completed MSE wall with all imposed surcharge loads.

4.2 Experimental Results

4.2.1 Settlement

4.2.1.1 Total Station

Routine surveys were carried out using the total station to track movement of the settlement plates by measuring the position of the survey targets on top of the riser rods. The settlement plates used to monitor settlement of the foundation are labeled SP-01, SP-02, SP-03 and SP-04, and the ones used to monitor settlement at the top of the wall are labeled SP-T-1, SP-T-2, SP-T-3, and SP-T-4. Figure 64 shows the results for the settlement observed after construction and during testing. After deflating the bladders to induce settlement, SP-01, which is the only settlement plate within the soft zone showed settlement reaching 97 mm. Observations showed no settlement at all other settlement plates.

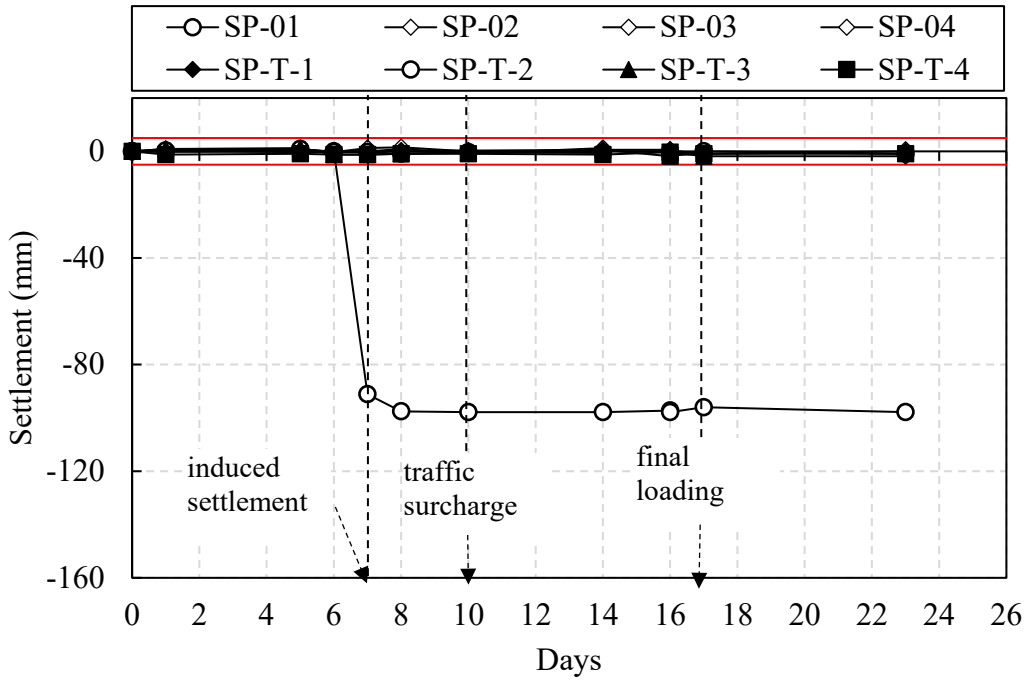

Figure 64. Total station settlement measurements.

The observed settlement at all the settlement plates did not show any increase in magnitude during and after surcharge loading. The red lines indicate the measurement error evaluated by comparing scans between two control points before and after each routine survey.

4.2.1.2 3D Scanner

Scans were routinely performed using the 3D scanner, each successive scan was linked to the previous one and preregistered. The scans were further aligned and optimized to concentrate on just the MSE structure. Figure 65 shows cloud points of a scan setup performed at the end of construction of the MSE wall, the cloud is a group of points from each scan setup with precise location of each point in space (x, y, and z coordinate system). The cloud from each scan setup, after data cleaning to focus on just the MSE structure, contains an average of 6 million points.

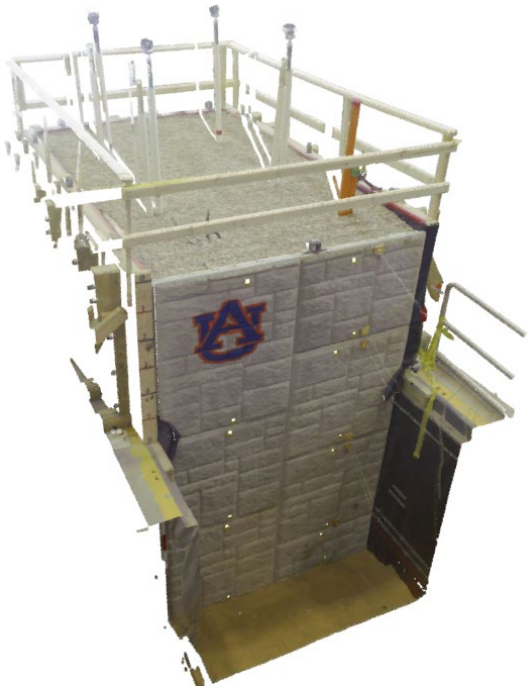

Figure 65. 3D point cloud for scan setup at the end of construction.

The clouds from two scan setups were compared by creating a cloud-to-cloud inspection file. This command sets one cloud as the reference and the other cloud as the measure and computes the deviation of points between the two cloud groups over a specified maximum separation distance. Deviation measurement labels were created at each settlement plate measurement point following the tags for the total station surveys. The labels show computed deviations for x, y, and z coordinates as well as the total displacement in 3D. Figure 66 shows the cloud-to-cloud inspection for scans between the end of construction and after inducing settlement. SP-01 shows a deviation 97 mm in the z-direction, validating the observations made using the total station. The deviations at all other measurement points showed zero settlements, again, confirming total station surveying results. Figure 67 shows the cloud-to-cloud inspection for scans after inducing settlement and at the end of surcharge loading. The result shows that no further settlement occurred during and after loading with 100% of the points within 0.5 mm.

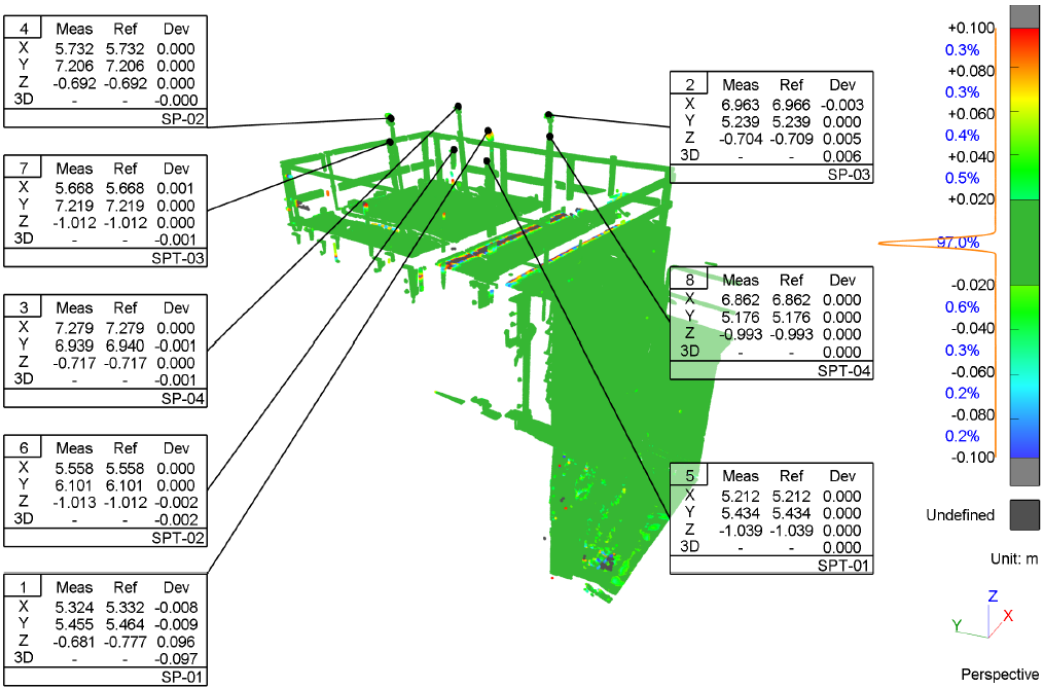

Figure 66. Cloud inspection with deviation measurement labels for settlement plates between scans before and just after inducing the differential settlement.

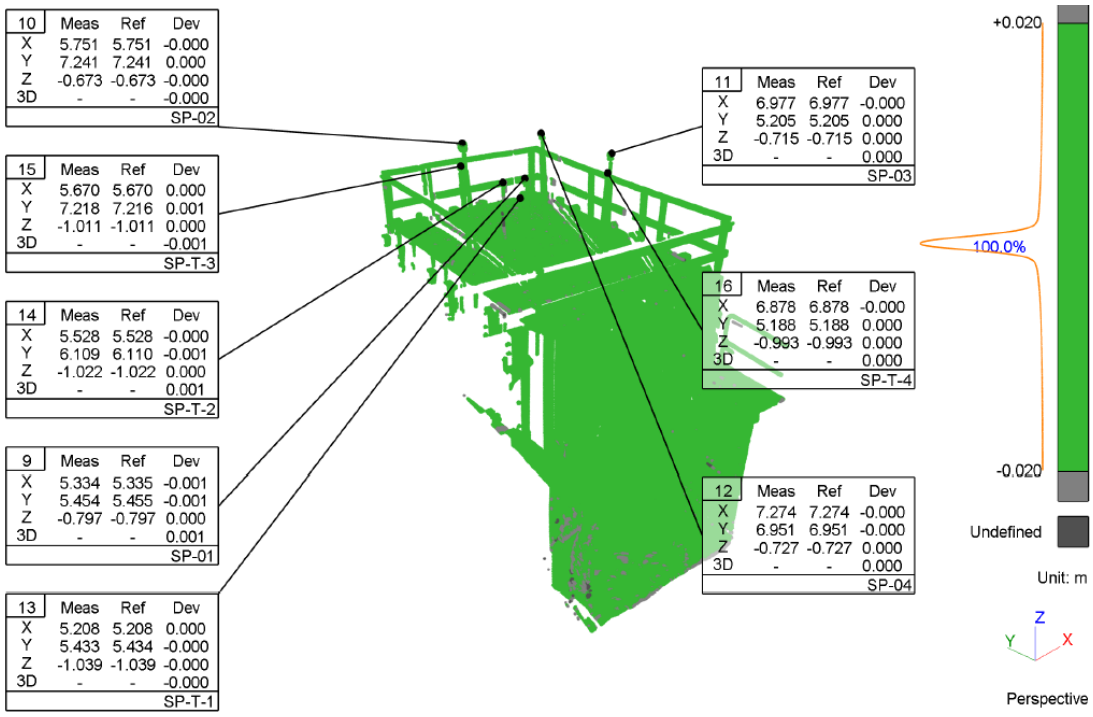

Figure 67. Cloud inspection with deviation measurement labels for settlement plates between scans before and after all surcharge loading.

4.2.2 Lateral Deformation

4.2.2.1 Within the Reinforced Mass

The lateral deformation within the reinforced mass was monitored using a slope inclinometer and a vertical shape array (SAAV). The casings for both instruments were installed next to each other with about 150 mm spacing in-between, both casings were positioned at 0.6 m from the back of the facing panels into the reinforced mass. Installation of the SAAV was completed after construction, so the first measurement could only be taken post construction, this was also the case for the inclinometer. Figure 68 shows the lateral deformation from the SAAV and the inclinometer form the start of measurement to the end of surcharge loading, and as can be seen, the magnitudes of displacement were very small with the maximum value of about 1 mm.

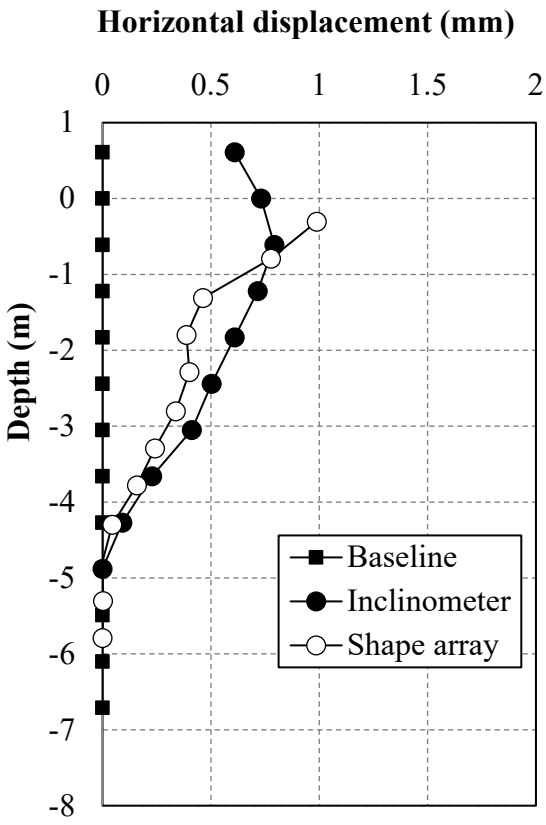

Figure 68. Lateral deformation within reinforced mass from inclinometer and SAAV at the end of testing.

4.2.2.2 Facing Horizontal Displacement.

4.2.2.2.1 Draw Wire Potentiometer

Six (6) draw wire potentiometers were attached to panels A4-2, A4-4, and F4 as already shown in Figure 39. Each panel had two potentiometers attached, one at the top and the other at the bottom. All six potentiometers were affixed to the concrete facing panels after completion of the MSE construction, so the presented results are post construction displacements. Figure 69 shows the lateral facing displacement from the start of measurement to the end of surcharge loading, and much like deformations within the reinforced mass, the magnitudes of displacement were very small with the maximum value of about 1 mm.

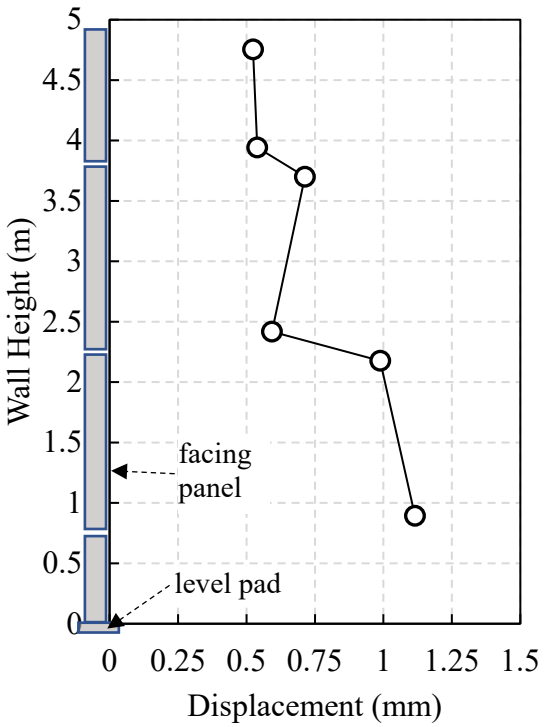

Figure 69. Draw wire potentiometer results for facing panels' lateral displacement at the end of testing.

4.2.2.2.2 Total Station

Reflective, glue-on survey targets were attached to the facing panels as already shown in Figure 40 and routine total station surveys included tracking these facing panels targets. Figure 70 shows the results for the panels' lateral displacement observed using the total station from the end of construction to the end of testing. The red lines indicate the measurement error as stated in section 4.2.2.1. The result showed very small displacements, with a maximum value of about 3 mm, and all deduced displacements within the measurement error.

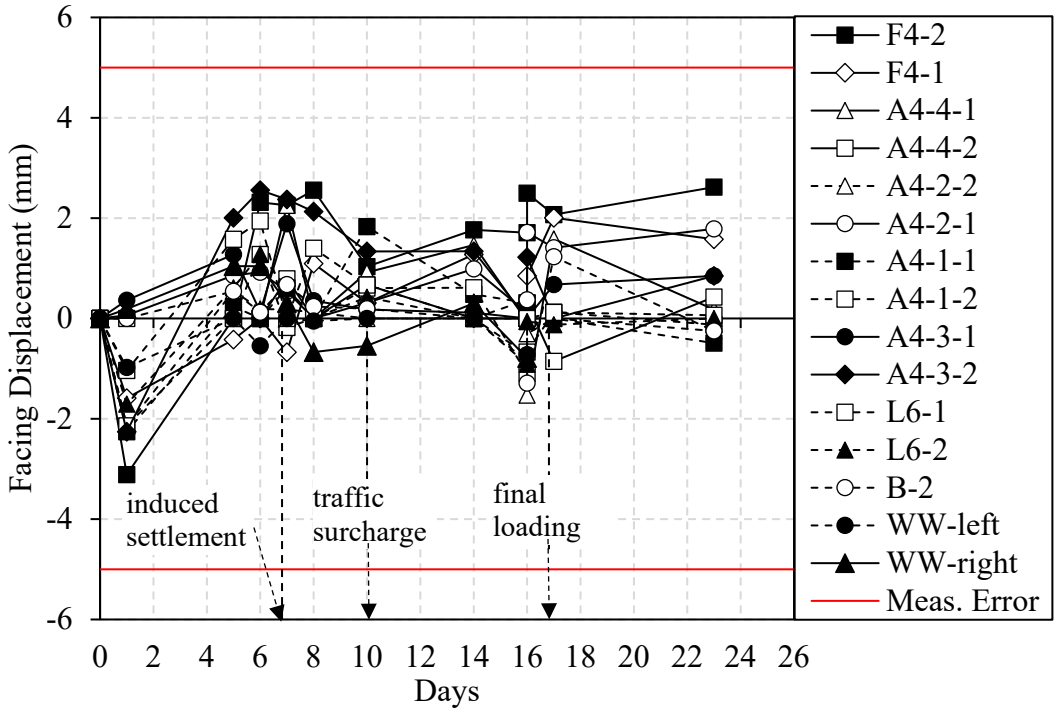

Figure 70. Total station facing displacement measurements.

4.2.2.2.3 3D Scanner

Deviation measurement labels were created on the for the facing panels' survey targets on a cloud-to-cloud inspection file. The reference cloud was from a scan before the bladders were deflated and the measure cloud was from a scan after load testing. The labels show computed deviations in 3D (Figure 71). Table 5 shows a summary of the inspection analysis with lateral displacement shown in the column for y-coordinate deviation. The results show very small displacement values alternating between zero and 1 mm, which agrees better with the draw wire potentiometer results indicating that the slightly higher displacements observed with the total station are associated with an error in measurement.

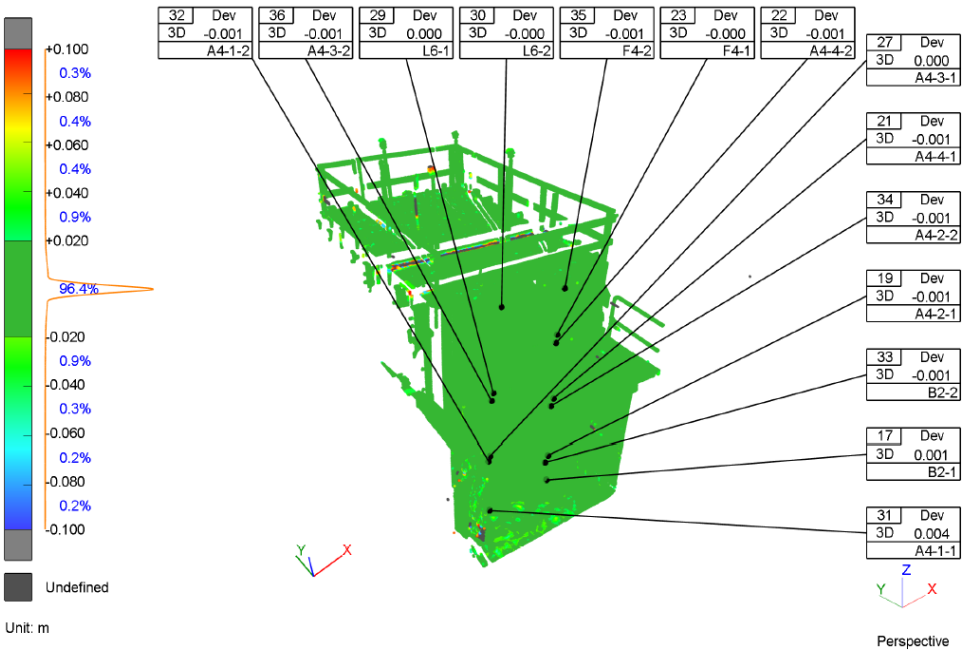

Figure 71. Cloud inspection with deviation measurement labels for facing panels' survey targets between scans before inducing foundation settlement and after loading.

Table 5. Summary of deviation measurements from cloud inspection analysis for scans before foundation settlement and surcharge after loading

Name	MeasX (m)	Meas Y (m)	Meas Z (m)	Ref X (m)	Ref Y (m)	Ref Z (m)	Dev X (m)	Dev Y (m)	Dev Z (m)	Dev 3D (m)
B2-1	6.597	3.592	-7.214	6.597	3.592	-7.214	0.000	0.000	0.001	0.001
B2-2	6.502	3.605	-6.644	6.502	3.605	-6.644	0.000	0.001	0.000	-0.001
A4-1-1	5.169	3.913	-7.235	5.165	3.912	-7.236	0.003	0.001	0.001	0.004
A4-1-2	5.142	3.939	-5.875	5.143	3.939	-5.874	0.000	0.001	0.000	-0.001
A4-2-1	6.574	3.594	-6.491	6.574	3.594	-6.490	0.000	0.000	-0.001	-0.001
A4-2-2	6.506	3.582	-5.155	6.506	3.582	-5.155	0.000	0.001	0.000	-0.001
A4-3-1	5.163	3.913	-5.738	5.163	3.913	-5.738	0.000	0.000	0.000	0.000
A4-3-2	5.144	3.884	-4.405	5.144	3.883	-4.406	0.000	0.001	0.001	-0.001
A4-4-1	6.536	3.561	-4.971	6.536	3.561	-4.972	0.000	0.000	0.001	-0.001
A4-4-2	6.432	3.545	-3.646	6.431	3.544	-3.646	0.001	0.001	0.000	-0.001
F4-1	6.456	3.550	-3.487	6.456	3.550	-3.487	0.000	0.000	0.000	0.000
F4-2	6.521	3.529	-2.589	6.522	3.529	-2.589	0.000	0.001	0.000	-0.001
L6-1	5.171	3.874	-4.243	5.171	3.874	-4.243	0.000	0.000	0.000	0.000
L6-2	5.264	3.821	-2.552	5.263	3.821	-2.551	0.000	0.000	0.000	0.000

4.2.3 Reinforcement Strains

The foil resistance strain gages were attached to two middle columns of the ribbed steel, one was closer to the soft spot zone as shown in instrumentation layout (Figure 38). Voltage readings were continuously collected during construction and during testing. The collected data were then converted to strain using a gage factor modified to account for extra resistance due to the lead cables as well as the spliced-on cables. Figure 72, Figure 73, Figure 74, and Figure 75 show the measured strain in the steel straps at the end of construction, at the time before inducing the settlement, after inducing settlement, and at the end of surcharge loading respectively. The plot series with continuous lines and triangular markers (line 1) are for the steel straps further from the induced settlement zone and the series with broken lines and circular markers (line 2) are for the steel straps right next to the induced settlement zone. Within half of the wall height (reinforcement levels 3 and 4), the measured strains in line 2 are significantly higher than in line 1, this is as expected since line 2 has less foundation support. A maximum strain magnitude of 635 με was observed in the strap next to the induced settlement zone on tie-level 4 at the end of construction which is only about 21% of the strain at yield point from the steel tensile tests.

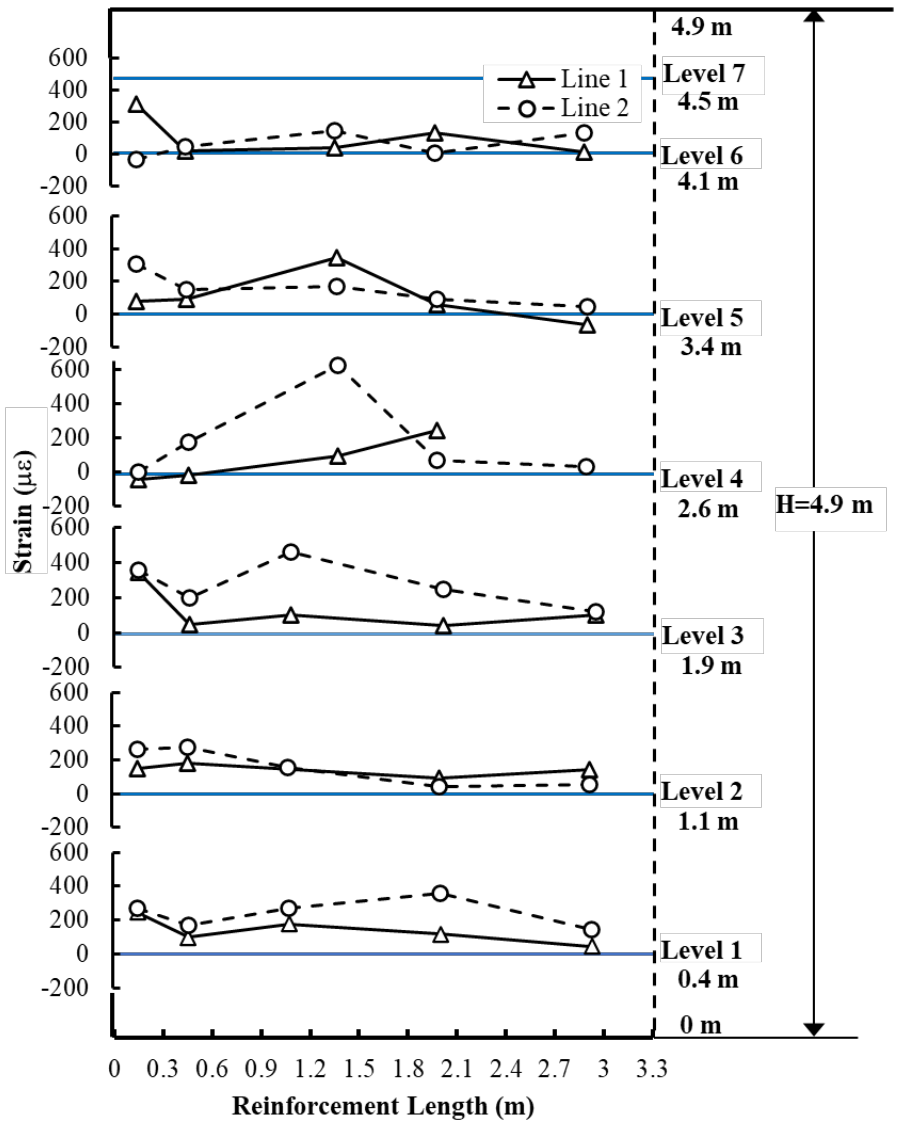

Figure 72. Measured reinforcement strains (levels 1-6) at the end of construction.

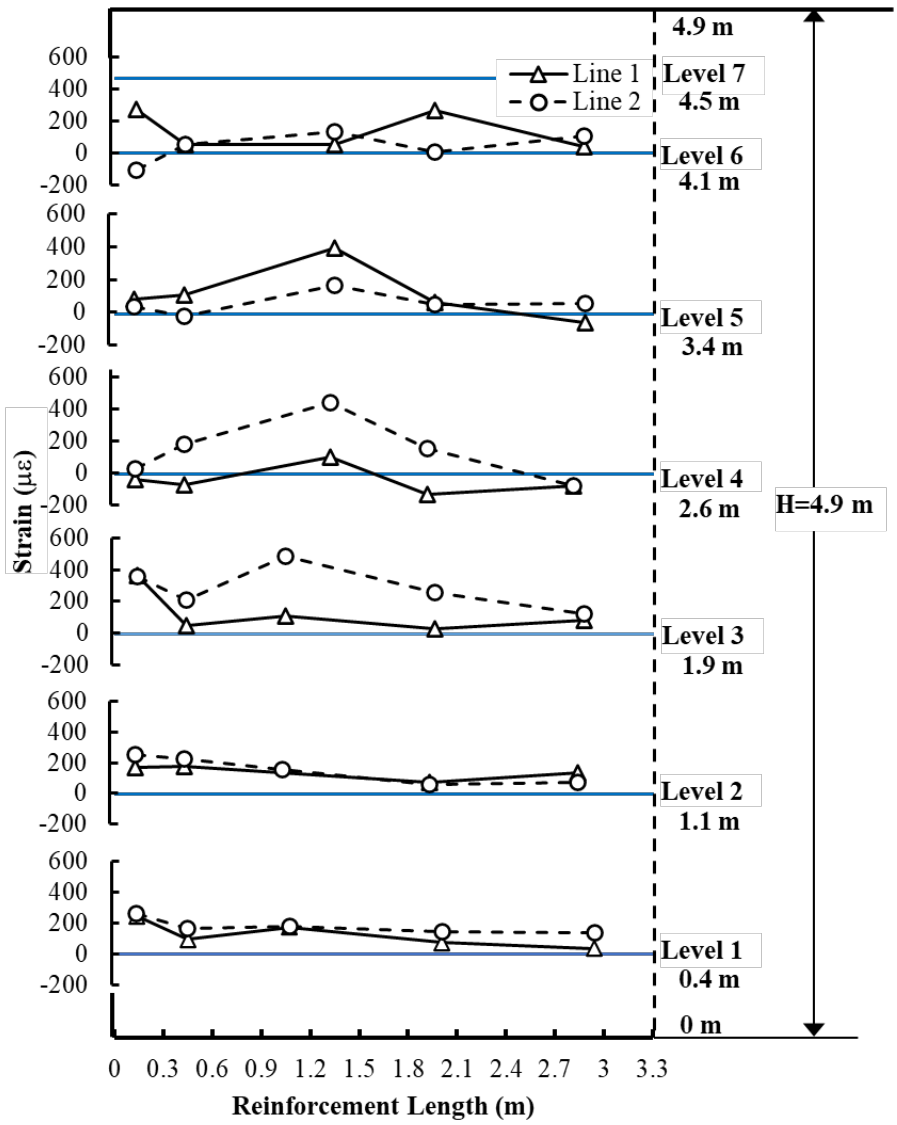

Figure 73. Measured reinforcement strains (levels 1-6) just before inducing settlement.

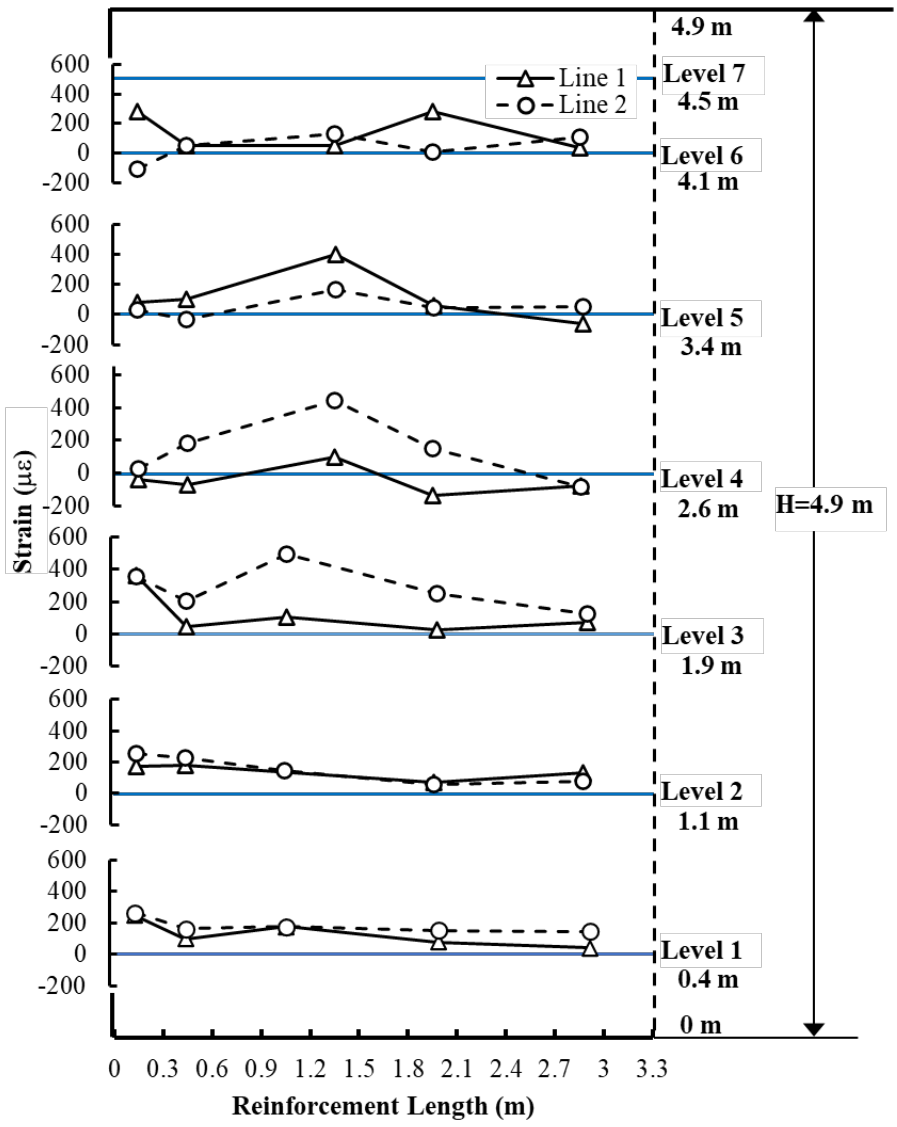

Figure 74. Measured reinforcement strains (levels 1-6) after inducing settlement.

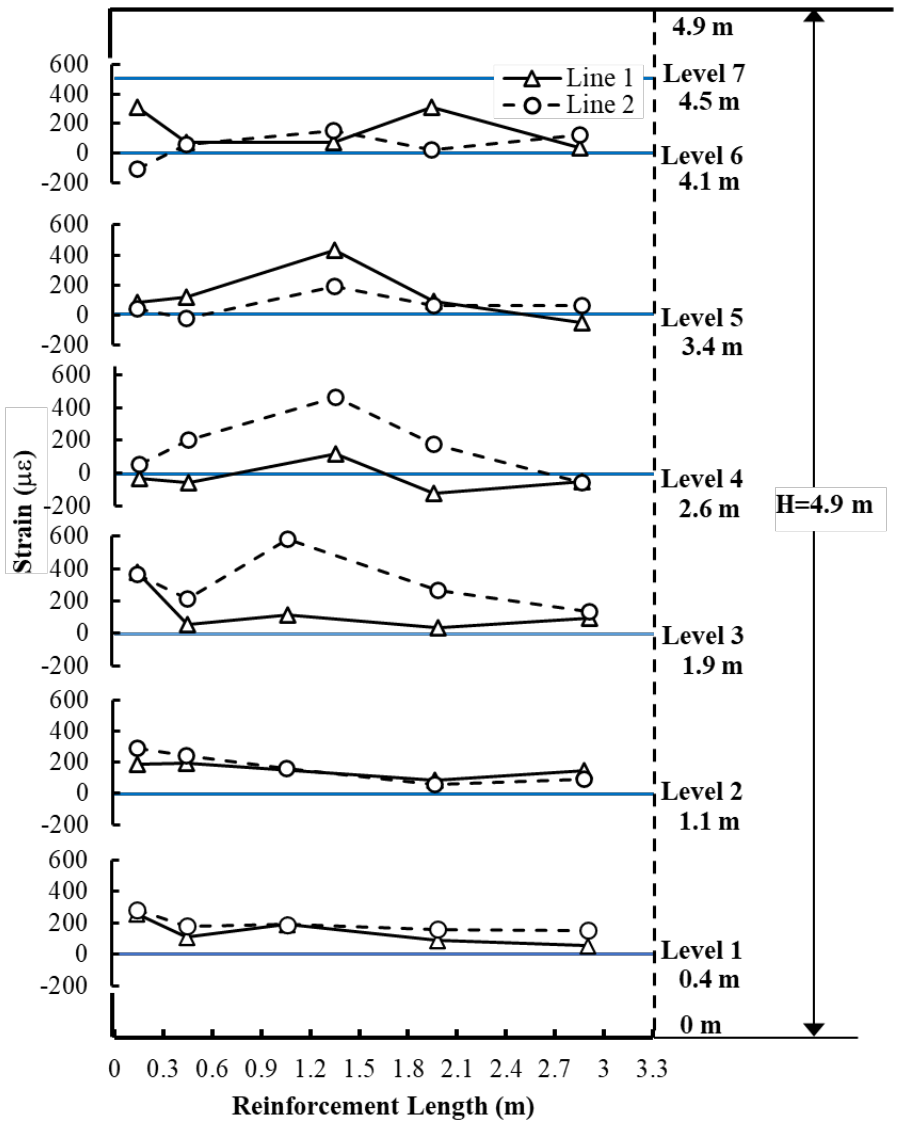

Figure 75. Measured reinforcement strains (levels 1-6) at the end of surcharge loading.

4.2.4 Bearing Pressure

The total earth pressure cells used in measuring vertical foundation pressure were placed in three lines as shown in Figure 37. Line 1 has three cells furthest from the soft zone, line 2 has six cells and runs along the centerline while line three has three cells directly above the soft spot zone. The readings were continuously collected during construction and during testing. Figure 76 shows the measured vertical stresses at the end of construction for the three described lines of cells.

The broken line shows the magnitude of stress from the self-weight of the compacted fill and the corresponding surcharge load (i.e., $\gamma_{fill}H + q_{\text{surcharge}}$ and $q_{\text{surcharge}} = 0$ for end of construction). Figure 77, Figure 78, Figure 79, Figure 80, and Figure 81 show similar plots for test stages after inducing settlement, 14 kPa surcharge loading, 26 kPa surcharge loading, 43 kPa surcharge loading, and 52 kPa surcharge loading respectively.

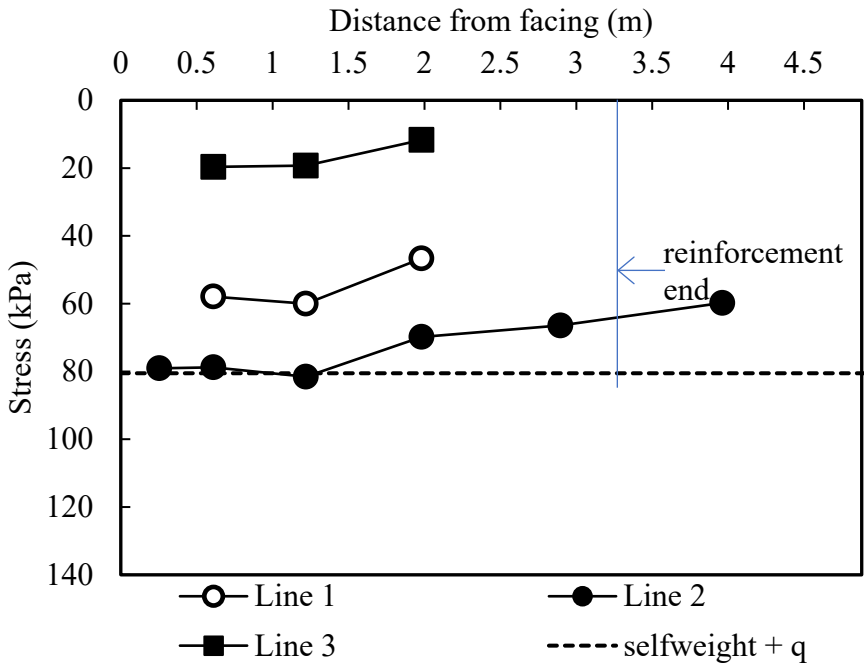

Figure 76. Measured vertical stress at the end of construction before inducing settlement.

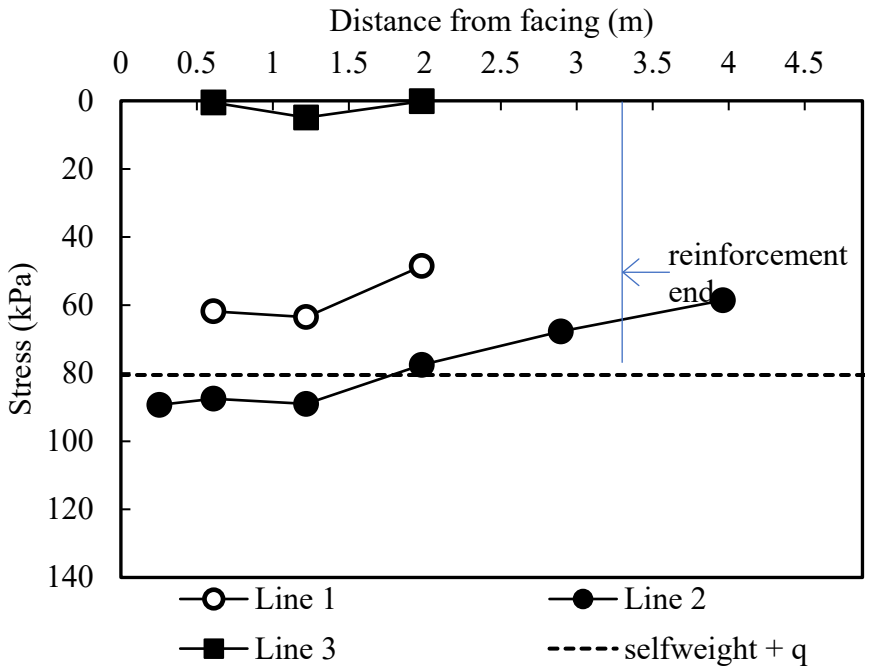

Figure 77. Measured vertical stress after inducing settlement.

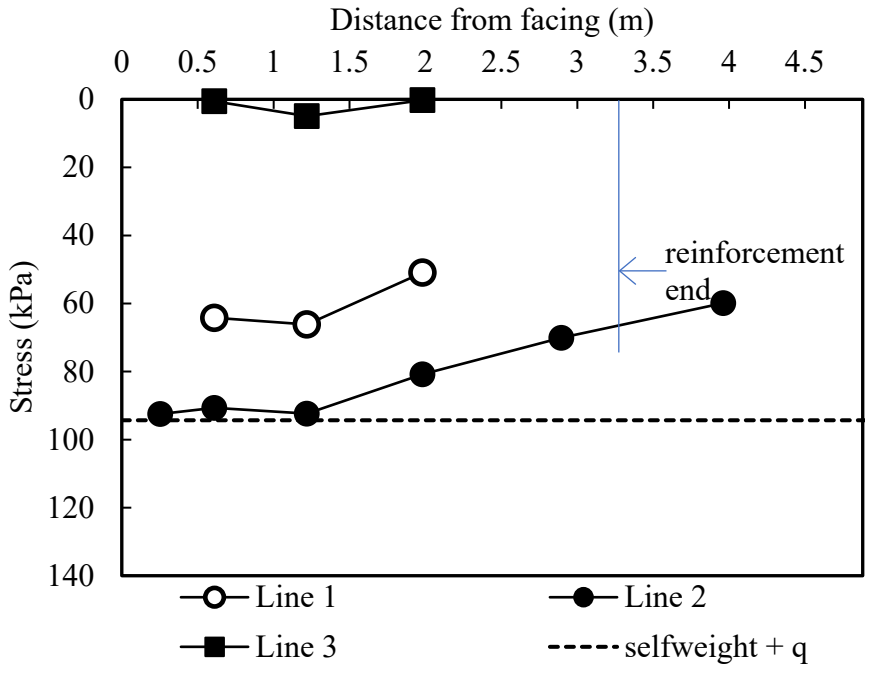

Figure 78. Measured vertical stress with 14 kPa surcharge loading.

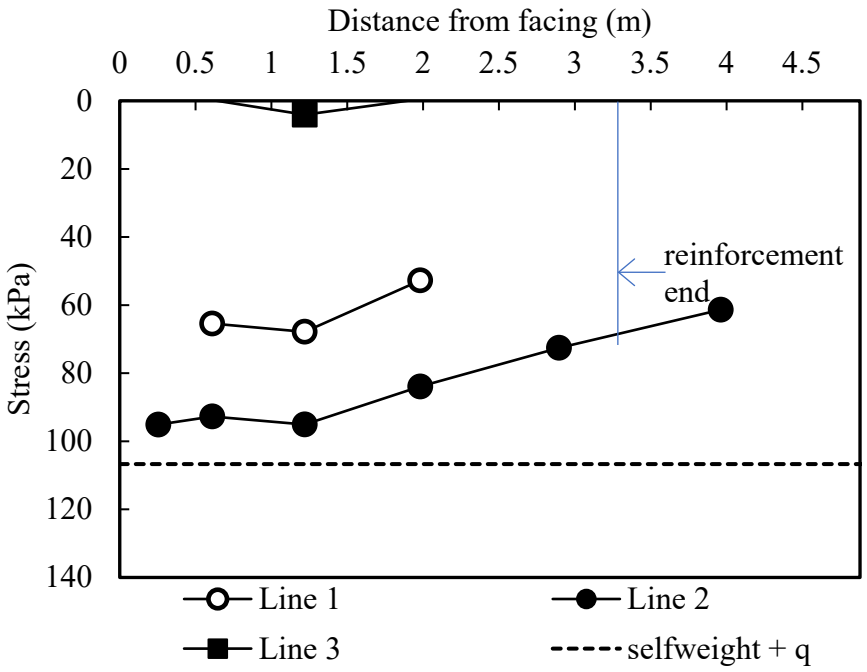

Figure 79. Measured vertical stress with 26 kPa surcharge loading.

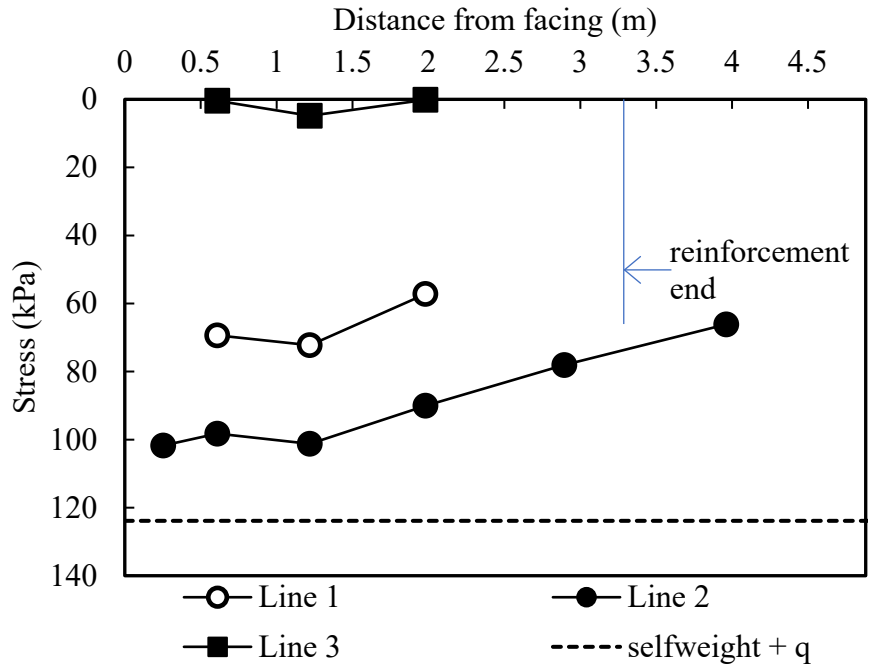

Figure 80. Measured vertical stress with 43 kPa surcharge loading.

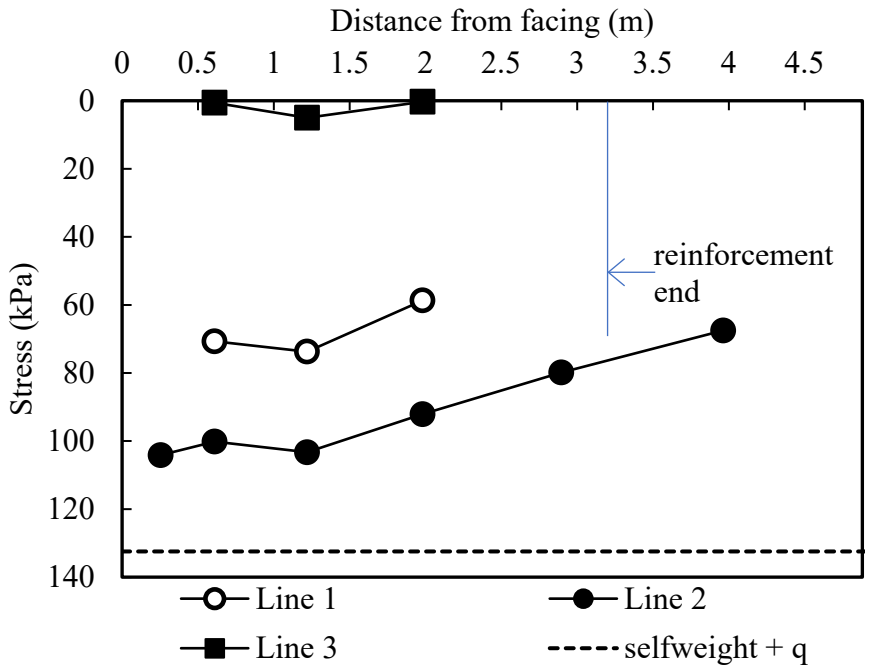

Figure 81. Measured vertical stress with 52 kPa surcharge loading.

The observed difference between the stresses on line 1 and line 2 were due to confinement and boundary effects because line 1 is close to the wall of the Geochamber. The values of the measured stresses for lines 1 and 3 should be identical based on symmetry but the stresses along line 3, over the soft zone, gradually reached 19 kPa at the end of construction but did not increase further indicating a significant compromise of the foundation bearing strength within the soft zone. After the settlement was induced by deflating the air bladders, the stresses at line 3 decreased to zero (Table 6), while the stresses on line 2 increased by about 50% of the initial stress magnitudes from line 3, indicating a redistribution of stress from the compromised zone to other intact areas of the foundation.

Table 6. Summary of measured vertical stresses at the end of construction and after inducing differential settlement.

	EPC tag	x-coord. (m)	y-coord. (m)	Vertical stress (kPa)		Change in stress (kPa)
				End of constr.	After inducing settlement	
Line 1	EPC_11	0.61	0.76	58	62	4
	EPC_07	1.22	0.76	60	64	4
	EPC_08	1.98	0.76	47	49	2
Line 2	EPC_01	0.25	1.52	79	89	10
	EPC_02	0.61	1.52	79	88	9
	EPC_03	1.22	1.52	82	89	7
	EPC_04	1.98	1.52	70	78	8
	EPC_05	2.90	1.52	66	68	2
	EPC_06	3.96	1.52	60	59	-1
Line 3	EPC_12	0.61	2.29	20	1	-19
	EPC_09	1.22	2.29	19	5	-14
	EPC_10	1.98	2.29	12	0	-12

(1 kPa = 0.145 psi, 1 m = 3.3 ft)

The changes in the stresses recorded by the earth pressure cells during surcharge loading are summarized for each load step in Table 7. The changes were estimated by calculating the measured stress difference between any load step and the values measured without surcharge after the settlement had been induced. This testing sequence was planned to observe if having induced differential settlement impairs the performance of the MSE wall with respect to supporting external loads. The results show that the applied surcharge is not entirely transferred to the foundation, indicating significant stress redistribution within the reinforced mass with only about 30% of the applied surcharge reaching the foundation. The earth pressure cell placed under the leveling pad showed no stress increase and remained relatively flat throughout construction and testing.

Table 7. Summary of changes in measured vertical stresses during surcharge loading.

	Cell tag	Vertical stress changes due to surcharge loading (kPa)			
		14 kPa load	26 kPa load	43 kPa load	52 kPa load
Line 1	EPC_11	2	4	8	9
	EPC_07	3	4	9	10
	EPC_08	2	4	9	10
Line 2	EPC_01	3	6	12	15
	EPC_02	3	5	11	13
	EPC_03	3	6	12	15
	EPC_04	3	6	12	15
	EPC_05	2	5	10	12
	EPC_06	1	3	8	10
Line 3	EPC_12	0	-1	0	0
	EPC_09	0	-1	0	0
	EPC_10	0	-1	0	0
Max $\Delta\sigma_v$		3	6	12	15
% of applied load (%)		24	24	29	29
			(1 kPa = 0.145 psi, 1 m = 3.3 ft)		

4.3 Discussion

4.3.1 Deformations

4.3.1.2 Settlement

After inducing the settlement at the soft spot zone, no further settlement was observed on all other settlement plates. The FHWA design guideline by Berg et al. (2009) states that MSE structures have significant deformation tolerance both longitudinally along a wall and perpendicular to the front face, but the settlement tolerances are focused on the facing element to preclude panel cracking. Generally, sufficient joint width and slip joints are required when differential settlement exceeds 1% of the wall height for panels with a surface area of 2.8 m^2 or less and 0.5% for panels with surface area greater than 2.8 m^2 and less than 7 m^2. A differential settlement over 2% of the wall height in this study was successfully induced without any perceived

compromise in wall performance nor facing panel distress. The leveling pad in this study was systematically placed with joints to accommodate differential settlement and facilitate stress release but no settlement occurred along the facing panel. Settlement plates placed at the top of the wall over the induced settlement zone showed no settlement as well, indicating that the settlement induced in the foundation did not continue through to the reinforced mass to the top of the wall.

4.3.1.2 Horizontal Displacement

According to the FHWA design guideline by Berg et al. (2009), no method is currently available to precisely predict lateral displacements. This is because various many factors affect lateral wall displacement including compaction, reinforced fill and reinforcement type, reinforcement length, reinforcement-to-facing connections, facing flexibility, foundation soil and the retained backfill properties. Notably, most of the lateral displacements occur during construction primarily due to compaction. Based on empirical estimates from 6 m high walls, the FHWA guideline suggests an increase of 25% of the wall height for every 19 kPa surcharge.

Lateral displacements during construction were not monitored in this study but post construction deformations were extensively monitored with various methods and no significant facing displacement was observed. It should be noted that it takes about 0.1% relative movement to reach an active state for retaining walls built with dense sand (Table 1) and may even take less for dense gravel. This is typically reached during construction, thereafter, the reinforced system acts as a composite structure with increased stiffness. The presence of the inextensible inclusions acts to restrain lateral deformation and exhibits a form of apparent confinement, leading to a higher stiffness in the reinforced zone. This behavior is judged to be enhanced by sufficient compaction

and was further corroborated during dismantling of the wall where the reinforced zone maintained a near vertical facing after the back confining wall had been removed (see Appendix A).

4.3.2 Reinforcement Tension

This section discusses the analyses of tension in the steel strips, deduced from the strain measurement and stiffness properties determined from the laboratory steel tensile tests. Interestingly, the strain observed in the steel reinforcement did not increase as the surcharge load was increasingly applied. Similar findings were reported by Christopher (1993) who attributed this behavior to soil aging, soil cementation and residual lateral stress induced by compaction. However, the findings in this study do not have soil aging and cementation as contributing factors. There was a six-week interval between end of construction and testing, during which reinforcement strain relaxation was apparent as can be seen by comparing Figure 72 to Figure 73. The strains stabilized over time indicating the mobilization of the soil-reinforcement composite strength such that magnitude of induced settlement and applied surcharge did not result in significant observable distress.

Figure 82 shows the maximum reinforcement tension at the end of construction and before inducing the settlement while Figure 83 shows the maximum reinforcement tension after inducing settlement and at the end of surcharge loading with 52 kPa surcharge. The circular markers indicate maximum measured tension in each reinforcement tie level for line 1 (further from the soft zone), the black squares show maximum measured tension in each reinforcement tie level for line 2 (close to the soft zone), the broken black line shows the tension estimated by the design guideline for reinforcement lateral pressure coefficient normalized by the active lateral pressure coefficient (K_a) calculated using a friction angle of 40^o, the solid black line shows the tension estimated by the design guideline for reinforcement lateral pressure coefficient normalized by the at rest lateral

pressure coefficient (K_0), and the solid red line shows the allowable tension which is only 55% of the yield strength. The design values presented have been evaluated without factors of safety. The measured tension is higher than the design values in the top two-thirds of the wall even after the relaxation observed between the end of wall construction and testing.

The stiffness of the soil influences the maximum tension and the stiffer the soil, the higher the maximum tension (Christopher 1993). Compaction increases the horizontal stresses which are locked due to the confining effect of the inextensible reinforcement. Both of these factors result in a higher tension than predicted by the design. The effect of the compaction stresses is apparent in the top layer of reinforcement showing a higher tension than would be expected from the amount of overburden. It is important to note that the coefficients of lateral earth pressures used in the design guideline (K_r) rely on the friction angle, the specifications given in AASHTO (2010) limits the friction angle to 40º resulting in 0.217 and 0.357 for K_a and K_o respectively (used in Figure 82 and Figure 83). Regardless, these values result in lower lateral stresses compared to locked in stresses from compaction, and consequently lower reinforcement tension in the upper half of the wall. Much like the measured strain, the deduced tension did not significantly increase as the surcharge was increased and the measured values are lower than the design prediction at a surcharge load of 52 kPa. In all cases, the maximum measured tension which occurred just after construction is only 44% of the allowable tensile strength and 24% of the yield strength.

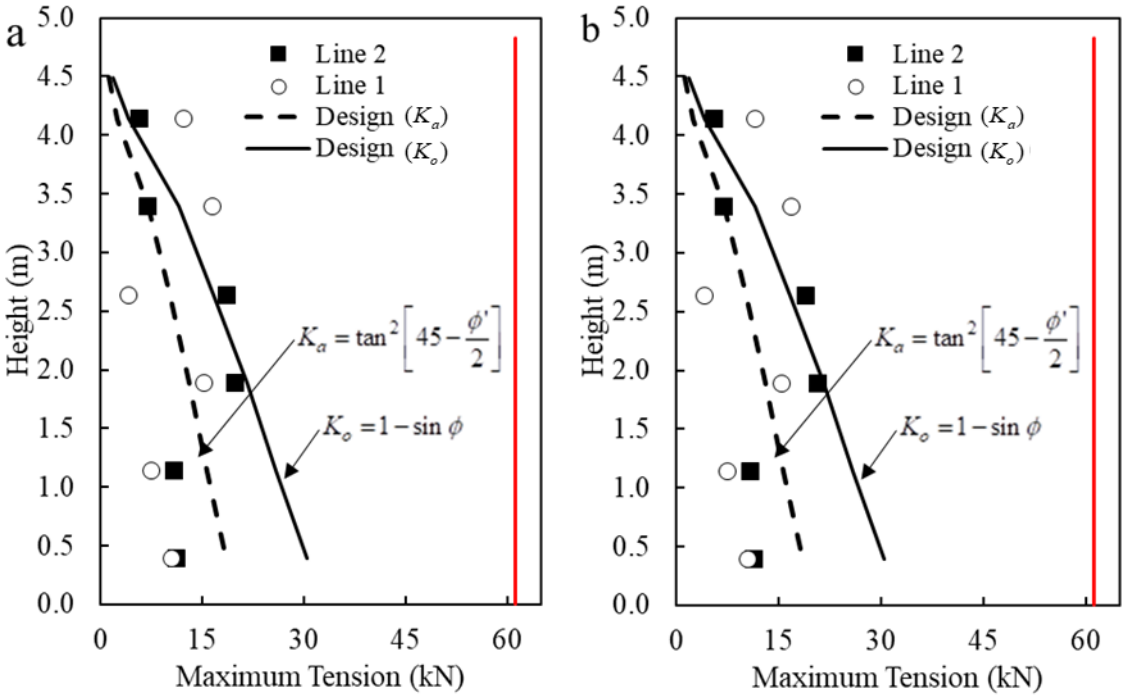

Figure 82. Maximum tension in reinforcement (a) at the end of construction and (b) before inducing settlement, red line shows the allowable tension.

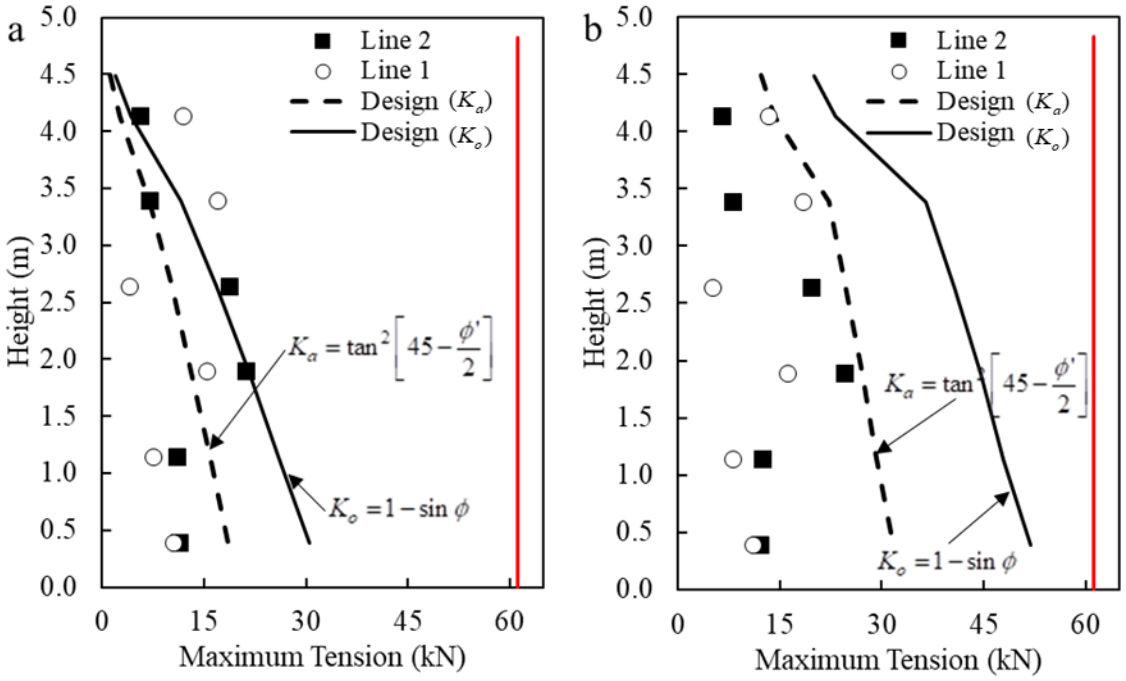

Figure 83. Maximum tension in reinforcement (a) after inducing settlement and (b) at 52 kPa surcharge load, red line shows the allowable tension.

Figure 84 shows the location of the maximum reinforcement tension at the end of construction and before inducing the settlement while Figure 85 shows the location of the maximum reinforcement tension after inducing settlement and at the end of surcharge loading with 52 kPa surcharge. The circular markers indicate the locations of maximum measured tension in each reinforcement tie level for line 1 (further from the soft zone), the black squares show the same information for line 2 (close to the soft zone), the broken black line shows location of maximum tension assumed by the coherent gravity method adopted for design using inextensible reinforcement and the solid black line shows the location of the maximum tension assumed for the tie-back wedge adopted for design using extensible reinforcement (as shown in Figure 21). The location of the maximum tension from the experiment follows the bi-linear active wedge adopted by the coherent gravity method in the design guidelines. The lower one-third of the wall follows the tie-back wedge, while the upper two-thirds follows the bilinear coherent gravity wedge. Generally, the coherent gravity wedge is still sufficient in predicting the location of the critical surface for internal stability evaluation. The lower half of the wall (reinforcement levels 1 to 3) shows high tension at the facing-to-reinforcement connection compared to the upper half. This is likely due to down drag forces which mean that some of the loads are transferred to the facing or the reinforcement connections supporting a significant amount of the facing weight. If some of the load was supported by the facing, it would have shown a stress concentration under the leveling

pad, but the earth pressure cell placed under the pad did not show this, hence, the reinforcement likely supported a significant amount of the facing weight.

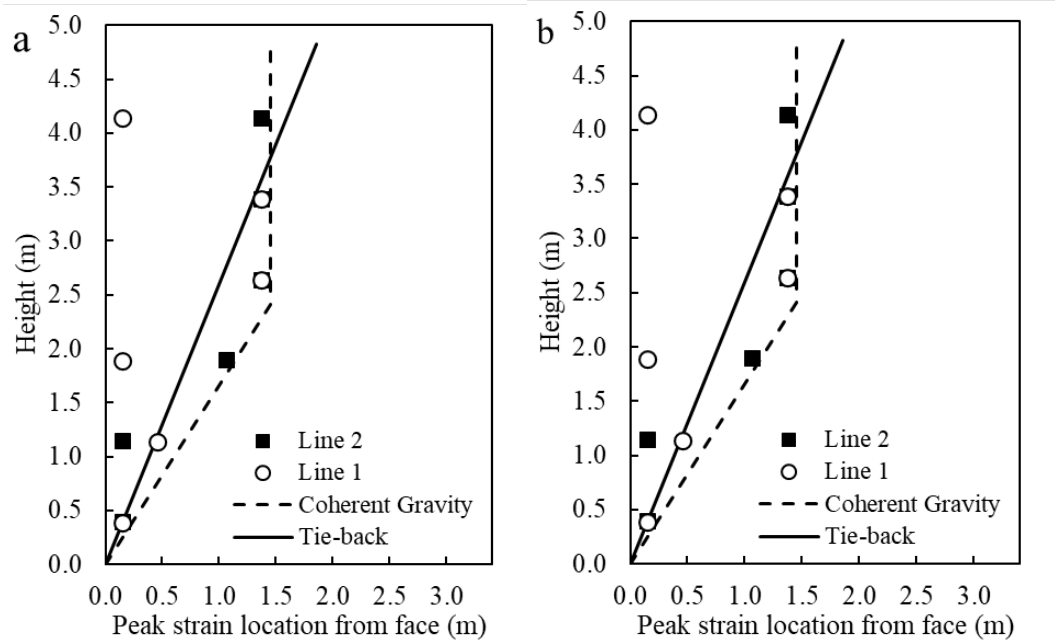

Figure 84. Location of maximum reinforcement tension within the reinforced mass (a) at the end of construction and (b) before inducing settlement.

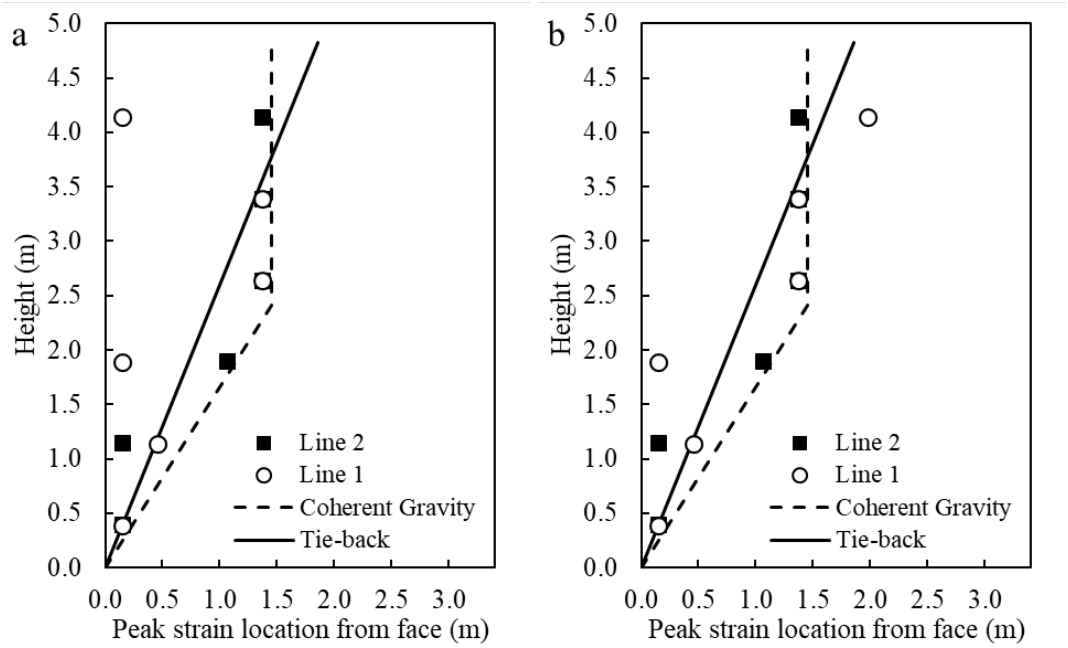

Figure 85. Location of maximum reinforcement tension within the reinforced mass (a) after inducing settlement and (b) at 52 kPa surcharge load.

4.3.3 Bearing Pressure

Recall that the leveling pad was deliberately constructed as three distinct segments and placed to establish a level surface for the facing panels. This was done to provide stress release beneath the facing panels as prior studies in the literature (Bastick et al. 1993, Runser et al. 2001) highlighted a stress concentration about two to three times the weight of the panels. The earth pressure cell placed directly underneath the leveling pad exhibited no discernible increase in stress levels. This observation indicates that a substantial portion of the weight of the panels is effectively supported by the steel reinforcement elements. This could be explained by the observation of higher tension at the connections between the panels and the reinforcement, particularly in the lower half of the wall (Figure 84 and Figure 85).

The array of cells placed at the foundation level were used to monitor the foundation stresses. At the end of construction, the measured stresses are very close to the overburden from the soil weight and showed no apparent stress increase due to eccentric loading even with the introduced poor bearing zone. After deflating the installed air bladder to trigger foundation failure and induce settlement, the stresses over the soft spot were redistributed to the rest of the foundation with about 50% of the dissipated stress reaching the cell array in line 2 (center of the wall width). Figure 86 shows the maximum measured stress (from all cells) and the design stresses for each testing stage. The assumption of a rigid reinforced mass in evaluating the bearing stresses adopted in design overestimates the actual foundation stress especially with walls supporting surcharge loads. The MSE wall is indeed flexible and significant load shedding and redistribution is apparent. Also, of all the load cases, only about 30% of the applied surcharge reached the foundation for the maximum applied load case. Other factors like wall height, reinforced soil stiffness, retained fill stiffness and applied load will affect the stress redistribution and load shedding behavior.

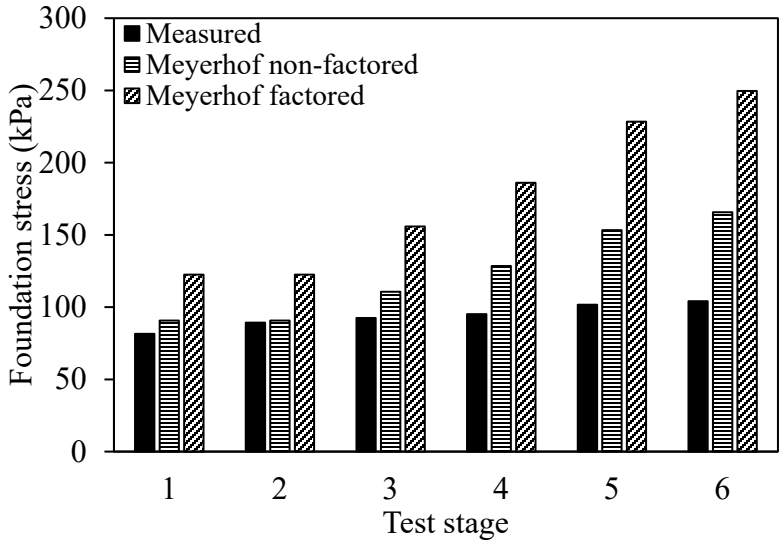

Figure 86. Measured and design foundation stress for the test stages.

Figure 87 shows the stresses at the end of construction without surcharge including the measured stress distribution, the overburden stress from the self-weight, the design stresses using Meyerhof's equation without load factors. The location of the resultant force from the measured stresses is also indicated in the figure. The resultant was calculated by solving equation 41 using the measured stresses, and the eccentricity was calculated by solving equation 42 using the resultant from each measurement and the corresponding moment arm. The same was done for other test stages to evaluate the effect of foundation failure and surcharge loading on the eccentricity. For comparison, the resulting trapezoidal distribution is also shown on Figure 87. Both the Meyerhof distribution and the trapezoidal distribution overpredicted the foundation stresses. The trapezoidal distribution closely followed the measured values in the back half of the wall but also predicted the maximum stresses of all the presented methods, showing the maximum discrepancy between predicted and measured stresses.

$$R = R_1 + R_2 + \ldots + R_n = \int \sigma_v dL \tag{41}$$

$$e = \frac{L}{2} - \frac{\sum_{i=1}^{n} R_i L_i}{R} \tag{42}$$

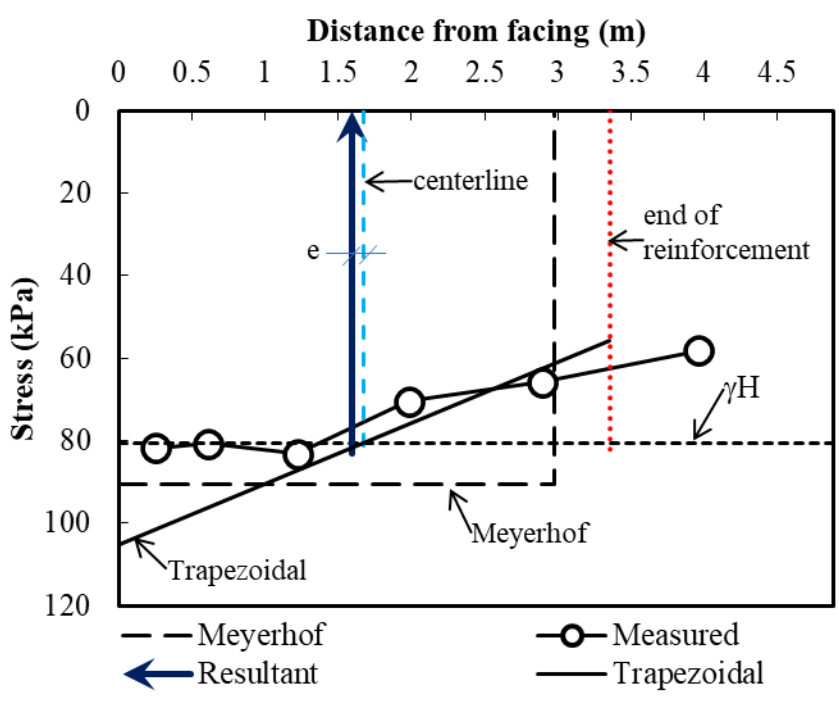

Figure 87. Measured and design stresses with location of resultant and eccentricity evaluated from measured stresses at the end of construction (Line 2)

Figure 88 shows the eccentricity determined from measured stresses from each test stage and the eccentricity predicted by the Meyerhof equations used in design with and without load factors. It follows calculated eccentricity using the design approach increases as the surcharge load increases, however, this is contrary to what was observed as the eccentricity decreased as the surcharge was increased. The maximum eccentricity observed, as expected, occurred after triggering foundation failure. The design limits eccentricity to one-sixth of the width of the wall as the worst-case condition which results in a multiplier of 1.5 for walls not supporting surcharge

(i.e., $\sigma_{V-F} = \gamma_r H\left(\frac{L}{L-2e}\right) = \gamma_r H\left(\frac{L}{L-2L/6}\right) = 1.5\gamma_r H$). However, the eccentricity observed after foundation failure is less conservative and is closer to $\frac{L}{34}$ which results in a multiplier of 1.06.

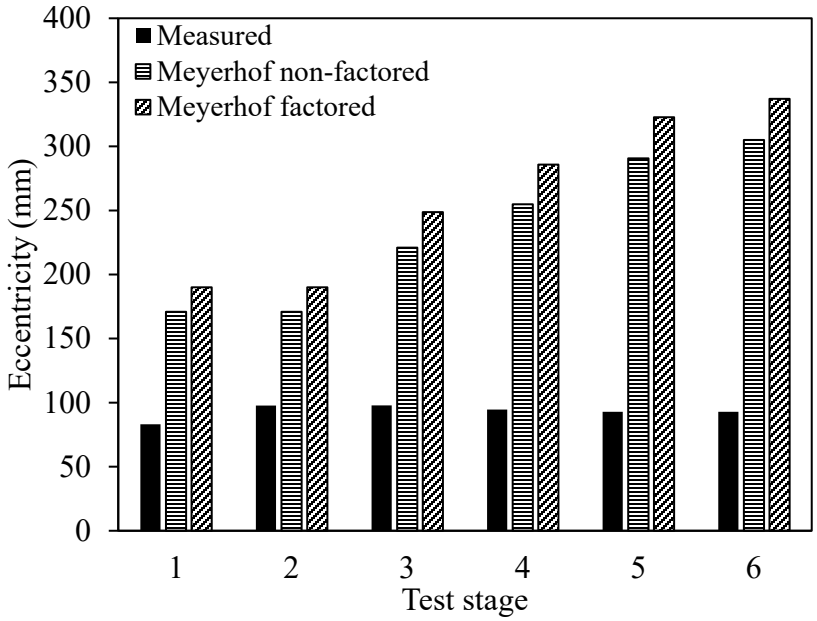

Figure 88. Measured and calculated eccentricity for the test stages.

It is important to note that the measured stresses from all cells (apart from line 3 which was placed over the soft zone) should record the weight of the overlying soil. However, there are notable differences in magnitude between the cells at line 1 and line 2. This was due to the influence of the Geochamber walls. As line 1 was close to the Geochamber walls, the cells recorded lower stresses than line 2 which was at the center of the wall width. Plastic sheets were placed between the Geochamber walls and the MSE fill to reduce the frictional resistance of the surface, however, the difference between line 1 and line 2 points to the effect of this frictional interface. This is further explored in Chapter 5 using numerical analyses.

4.4 Summary of MSE Testing and Experimental Results

The fullscale MSE wall was continuously monitored during testing, the testing stages included observations of end of construction behaviour, inducing settlement and simulating foundation failure, and various magnitudes of surcharge loading in incremental steps. The observations are summarized as follows:

- There was strain relaxation which normalized with time after the end of construction.
- A differential settlement over 2% of the wall height was induced to simulate foundation failure, with no perceptible distress in the facing panels and steel reinforcement strips.
- The lateral deformation within the reinforced mass and at the facing panels were very small, about 0.02% of the wall height at the end of surcharge loading.
- The tension in the reinforcement at the end of construction is higher than the design values but did not significantly increase as the test progressed. At the end of surcharge loading, the difference between the design prediction using K_a and the measured values greatly reduced especially for the top 2/3rd of the wall height. However, this is only because of the perceived increase in tension due to the surcharge which was not typically observed.
- In any case, the maximum measured tension which occurred just after construction is only 44% of the allowable tensile strength and 24% of the yield strength. The location of the maximum tension, which typically indicates the critical surface for internal stability, closely followed the bi-linear coherent gravity wedge used in design.
- Even with a soft zone introduced in the foundation, the measured stresses are very close to the overburden from the soil weight.

- After inducing the differential settlement and simulating foundation failure, the stresses from the zone that lost foundation support were redistributed and was observed as a marginal increase in stress seen in the array of sensors close to the subsided zone.
- The simulation of the differential settlement resulted in an eccentricity closer to L/34 compared to the L/6 given by the design, thus, a less conservative bearing stress modification factor of 1.06 for worst case foundation support instead of 1.5. Also, the observed eccentricity reduced with increasing surcharge load intensity contrary to the design assumptions.
- The MSE is not a rigid structure where all applied loads are completely transferred to the foundation.
- It is not evident that stresses from the retained zone are completely transmitted to the foundation, hence, the idea of overturning and eccentricity do not seem valid for a flexible mass.

The supposed random backfill in this study was constructed using well compacted #57 crushed aggregate which is a stronger fill material compared to in-situ backfill in field applications. While there have been field cases where the excavated material has been reinforced with geosynthetics and reused as the random backfill, it is important to note that the retained soil type and strength can potentially change the results. Many other factors like retained-to-reinforced zone interface, facing-to-reinforced zone interface, reinforced fill type, reinforcement stiffness, wall height, and compaction effect can affect the behavior of the MSE wall. The effect of these factors will be studied using numerical methods in Chapter 5. The results from the experimental study will provide a basis for the numerical analyses.

CHAPTER 5: 3D NUMERICAL MODELING OF A STEEL-REINFORCED MSE

5.1 Background

All the work presented to this point has been to observe the behavior of the MSE system when built atop a foundation with pockets of poor bearing soil, when subjected to foundation differential settlement and the additional effect of surcharge loading. Assessment of performance focused on the wall deformation, reinforcement distress and notably, the foundation bearing stress distribution, magnitude, and eccentricity of the resultant. It is apparent that the performance assessed so far is affected by some of the project specificities including wall height, reinforcement stiffness, reinforced fill type, random backfill type, etc. It will be difficult to conduct experimental studies to investigate these factors. However, this can be done with less difficulty using numerical analyses. This involves proper calibration of the various material properties, validating a baseline model to the experimental results, and finally, a parametric study to address the effects of some of these factors.

There have been numerical studies to investigate the behavior of mechanically stabilized earth retention systems (Damians et al. 2014, Damians et al. 2015, Budge et al. 2016 and Sakleshpur et al. 2017). These studies all used 2D numerical models, while this is ideal for walls with continuous reinforcement elements (Geogrids and Geosynthetics), numerical challenges arise when using 2D models for most steel reinforced MSE walls because the steel straps are discrete and discontinuous along the wall length. Wall unit width to element width ratios can be used to modify the material properties of the reinforcement and other discrete elements to approximate a three-dimensional problem using a two-dimensional plane strain model (illustrated in Figure 89, the yellow box is only an illustration of the influence zone of the reinforcement), and this has yielded reasonable results from previous numerical studies. However, the actual wall is three

dimensional and 3D numerical models best represent the case for MSE walls with discrete reinforcement. There is an added layer of difficulty introduced with the present study due to the differential settlement induced in the foundation in the experiment. This makes it pertinent to use a 3D model as the effect is not only in a plane but also across the wall width.

There have not been as many three-dimensional numerical analyses of the MSE type structures. Damians et al. (2021) conducted a 3D numerical analysis of a 6-m high steel-reinforced mechanically stabilized earth wall using the CODE_BRIGHT program. The model was limited to a slice of the wall and provides a basis for further numerical analyses conducted using a three-dimensional approach. The numerical analyses in this study will further add to the limited application of three-dimensional modeling capabilities to reinforced soil systems involving discrete reinforcement, while also exploring the factors affecting the stress distribution at the foundation of these systems.

Plaxis3D, a widely used finite element program for specifically modelling geotechnical systems was used for the numerical analyses in this study. The Plaxis finite element platform has been extensively utilized in solving geotechnical and soil-structure interaction problems, with an automated mesh refinement to increase computing efficiency and a robust library of constitutive models developed for geotechnical applications.

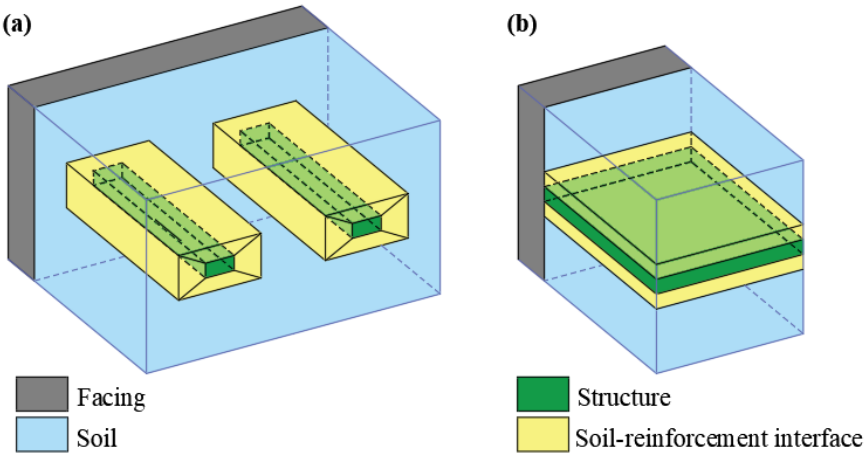

Figure 89. (a) Actual 3D soil-reinforcement interaction and (b) plane strain approximation

5.2 Element Types

5.2.1 Soil Clusters

The model was developed using Plaxis-3D. The soil volumes are modelled by means of 10-node tetrahedral elements with three degrees of freedom per node (u_x, u_y, and u_z) (Bentley 2021a) with a second-order interpolation of displacements. Figure 90 shows the 10-node tetrahedral element in three local coordinates (ξ, η, and ζ) with four integration points (Bentley 2021c)

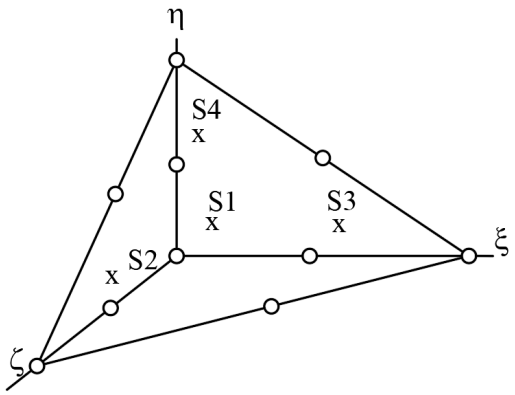

Figure 90. Local numbering and positioning of nodes (o) and integration points (x) of a 10-node tetrahedral element (after Bentley 2021c).

5.2.2 Plate Elements

Plate elements in Plaxis-3D are modelled using 6-node triangular elements, because the plate elements cannot sustain torsional moments, the plate elements only have 5 degrees of freedom per node namely one axial displacement (u_x), two transverse displacements (u_y and u_z) and two rotations (φ_y and φ_z) (Bentley 2021c).

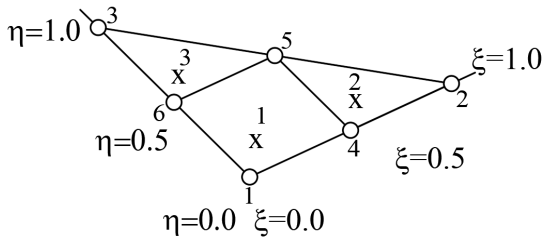

Figure 91. Local numbering and positioning of nodes (o) and integration points (x) of a 6-node plate triangle (after Bentley 2021c).

5.2.3 Soil-Structure Interaction

The interaction between two dissimilar materials is modelled using zero-thickness, 6-node triangular interface elements (Bentley 2021a). Six pairs of nodes are created (i.e 12 interface nodes) consisting of two elastic-perfectly plastic springs, where one set of six is for the soil element and the other for the structural element (Figure 92). The distance between the two nodes of a node pair is zero. Each node has three translational degrees of freedom (u_x, u_y, and u_z) which allows for differential displacements between the node pairs (slipping and gapping) (Bentley 2021c). The interface is governed by the linear elastic-perfectly plastic behavior. The Mohr-Coulomb failure criterion controls slipping at the interface, and activating tension cut-off allows for gapping (i.e., displacement normal to the interface plane).

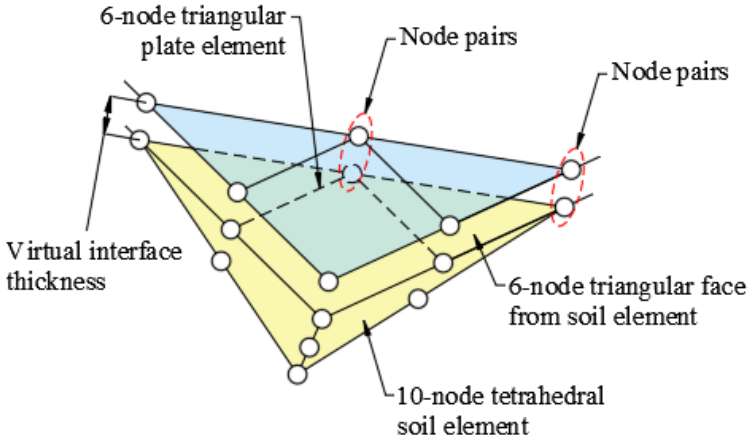

Figure 92. Illustration of 12 node (6 pairs) for interface element between soil and plate elements.

The strength property of the interface is assigned in two ways based on available material information and the level of desired control over the properties of a particular interface. For one option, a simple strength reduction factor (R_{inter}) can be entered for the adjacent soil as an input property, in this case, by default, the interface strength property is automatically taken from the adjacent soil cluster. An R_{inter} value of 1 indicates that the interface and the surrounding cluster are fully bound, a value less than 1 reduces both the shear strength parameters as well as the stiffness of the interface, however, the stiffness has a quadratic relationship with the reduction factor as shown in equations 43 through 46.

$$c_i = R_{inter} c_{soil} \tag{43}$$

$$tan(\delta_i) = R_{inter} \tan\left(\phi_{soil}\right) \tag{44}$$

$$G_i = R_{inter}^2 G_{soil} \tag{45}$$

$$v_i = 0.45 \tag{46}$$

where c_{soil} , ϕ_{soil} , and G_{soil} are the cohesion, frictional angle and shear modulus of the surrounding clusters respectively, while c_i , ϕ_i , G_i , and v_i are cohesion, frictional angle, shear modulus, and

Poisson ratio of the interface respectively (Bentley 2021a). The behavior of the interface is governed by the linear-elastic perfectly plastic model. If a more advanced material model is applied to the interface (e.g. Hardening Soil model and Hardening Soil Small Strain), the interface element will only pick up the relevant data (c, ϕ, E, ψ, and ν) for linear-elastic perfectly plastic material model.

For an alternative option, a custom material property (typically the linear-elastic perfectly plastic material model) can be specifically created and assigned to the interface elements. This offers a better control of the interface strength, and preferentially, the stiffness of the interface can be altered without having to alter that of the adjacent soil as illustrated in the R_{inter} method. This method was used for all the interface elements for the MSE finite element model.

5.3 Material Models and Calibration

Appropriate material characterization is paramount in the solution of any geotechnical engineering problem as it informs the general behavior of a system (the total load input, load resistance/transfer, yielding, volume change, etc.) (Okafor et al. 2023). Constitutive models are critical to numerical analyses as they describe the material behavior in the form of mathematical expressions that define the material's stress-strain relationships. When selecting a model, it is important to ensure the model can capture the key aspects of material behavior which control the scenario being modeled (Wood 2014). A calibration exercise typically involves determination of the material behavior from carefully conducted laboratory experiments and a reproduction of the determined behavior via a similarly configured numerical setup with justifiable material input properties.

5.3.1 Material Models Description

The material models used in the numerical analysis are briefly described below in the order of increasing complexity.

5.3.1.1 Linear Elastic Model

The linear elastic model is a fundamental constitutive model, based on Hooke's law for isotropic linear elastic behavior. The linear elastic model is typically inadequate for capturing the highly non-linear behavior of soil. However, it is well-suited for simulating the structural behavior of materials like thick concrete walls or plates, where the strength properties are significantly higher than those of soil.

The linear elastic model is expressed in terms of effective stresses as shown in equation 47:

$$\sigma' = E\varepsilon \tag{47}$$

where σ' is the effective stress, E is the effective Young's modulus, and ε is the corresponding strain.

5.3.1.2 Linear Elastic Perfectly Plastic Model

The linear elastic model with Mohr-Coulomb failure criterion (or simply the Mohr-Coulomb model), is a simple and well-known linear elastic perfectly plastic model. The linear elastic part is based on Hooke's law of isotropic elasticity (just like in the linear-elastic model) associated with elastic strains (ε^e) and perfectly plastic part, associated with plastic strains (ε^p) is based on the Mohr-Coulomb failure criterion which defines the material shear strength.

The model's input parameters include Young's modulus (E), Poisson's ratio (v), cohesion (c), friction angle (ϕ), dilatancy angle (ψ) and tensile cut off/tensile strength (σ_t).

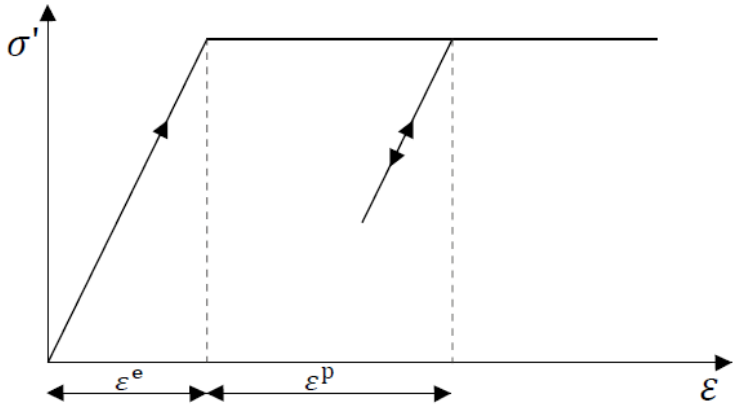

Figure 93. Basic idea of an elastic perfectly plastic model (Bentley 2021a)

5.3.1.3 The Hardening Soil Model

This previously introduced linear elastic model with Mohr-Coulomb failure criterion falls short in some key aspects of soil behavior (e.g. non-linearity, stress dependency, etc.) and serves as an approximation and is ideal for systems that stay primarily elastic.

On the other hand, the Hardening Soil model (hereafter referred to as the HS model), can simulate non-linear stress-strain behavior with a Mohr-Coulomb failure criterion, stress-dependency, and unload-reloading. The stress-strain response is defined by a hyperbolic relationship between the vertical strain (ε_1) and the deviatoric stress ($\sigma_1 - \sigma_3$) in primary loading (Figure 94).

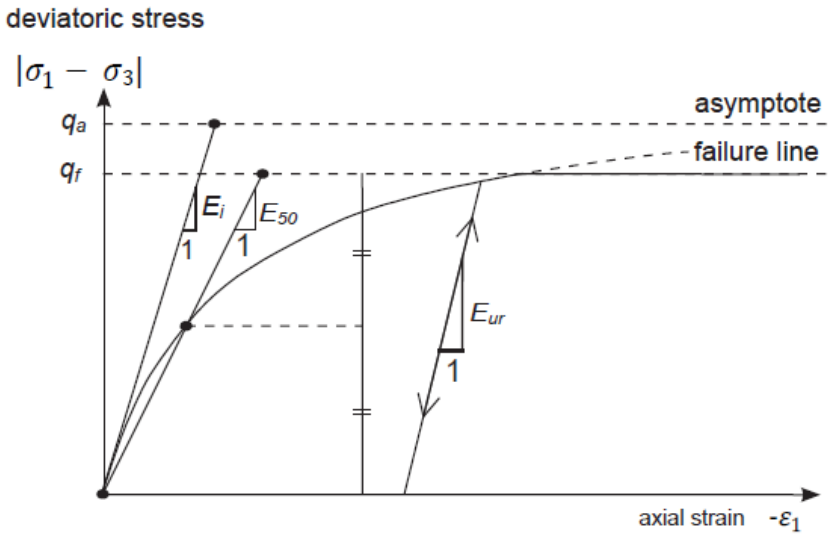

Figure 94. Hyperbolic stress-strain relation in primary loading for a standard drained triaxial test (Bentley 2021a)

The HS model simulates both shear hardening and compression hardening (Bentley 2021a). The 1D compression modulus (E_{oed}^{ref}) is expressed in equation 48 where p^{ref} is the reference stress, e_0 is the initial void ratio and λ is the standard Cam-Clay compression index. If λ is replaced by the standard Cam-Clay swelling index k, E_{oed}^{ref} is then the unloading-reloading modulus (Bentley 2021a).

$$E_{oed}^{ref} = \frac{p^{ref}\left(1+e_0\right)}{\lambda} \tag{48}$$

The stress-dependent 1D soil stiffness is expressed in equation 49 where m is the power:

$$E_{oed} = E_{oed}^{ref}\left(\frac{\sigma}{p^{ref}}\right)^m \tag{49}$$

The stress-dependent stiffness modulus E_{50} is shown in equation 50 where E_{50}^{ref} is the reference stiffness modulus corresponding to the reference pressure, σ'_3 is the minor principal stress, c is the cohesion intercept and ϕ is the friction angle (Bentley 2021a).

$$E_{50} = E_{50}^{ref}\left(\frac{c.\cos(\phi) - \sigma_3'\sin(\phi)}{c.\cos(\phi) - p^{ref}\sin(\phi)}\right)^m \tag{50}$$

Similarly, the stress-dependent unload-reload stiffness modulus E_{ur} is shown in equation 51 where E_{ur}^{ref} is the reference unloading/reloading Young's modulus corresponding to the reference pressure (Bentley 2021a).

$$E_{ur} = E_{ur}^{ref}\left(\frac{c.\cos(\phi) - \sigma_3'\sin(\phi)}{c.\cos(\phi) - p^{ref}\sin(\phi)}\right)^m \tag{51}$$

The failure ratio R_f is expressed in equation 52 where q_f is the maximum deviatoric stress on the stress-strain diagram, q_a is the asymptote maximum deviatoric stress defined by the initial stiffness E_i (Bentley 2021b).

$$R_f = \frac{q_f}{q_a} = 2\left(1 - \frac{E_{50}}{E_i}\right) \tag{52}$$

The Hardening Soil model produces more deformations than the linear elastic perfectly plastic model for systems that remain elastic, due to the initial stiffer stress-strain response of the latter (Okafor et al. 2023), however, it was used for the foundation and the wall fill layers in order to properly simulate the unloading that would inadvertently occur after triggering the differential settlement by deflating the air bladders.

5.3.2 Material Models Calibration

5.3.2.1 Soil Models

Calibration for the soil models was performed using a single point algorithm within the built-in soil test application in Plaxis. This tool was used to calibrate the soil behavior for the foundation sand and the #57 crushed stone used for the MSE fill material. R_f (ranging from 0 to

1) defines inflection between the non-linear elastic phase and the linear plastic failure and is best used to match the strain at ultimate deviatoric stress during soil model calibration to laboratory measurements (the point at which failure occurs in the stress-strain space). The soil models were successfully calibrated to the laboratory data with reasonable agreement observed between the simulated and laboratory data points. Table 8 shows the input properties and values for the calibration of the foundation sand and the #57 stone at 103 kPa and 69 kPa confining stresses respectively, while Figure 95 depicts the measured and simulated stress-strain response for the various confining stresses for (a) foundation soil and (b) #57 crushed stone.

Table 8. Calibration input data for HS model at 83 kPa confining stress

Symbol	Units	Value		Note
		Foundation sand	#57 stone	
E_{50}^{ref}	kPa	31000	31000	Estimated from triaxial tests
E_{oed}^{ref}	kPa	31000	31000	$E_{oed}^{ref} \approx E_{50}^{ref}$
E_{ur}^{ref}	kPa	110300	110300	Default value ($E_{ur}^{ref} \approx 3E_{50}^{ref}$)
m	-	0.5	0.5	Default value
v_{ur}	-	0.25	0.25	
K_o^{nc}	-	0.34	0.45	Default value ($K_0^{nc} = 1 - \sin\phi$)
p^{ref}	kPa	103	69	Taken as each confining stress
c	kPa	0	0	Cohesionless material
ϕ	º	41.5	48	Estimated from triaxial tests
ψ	º	11.5	18	Default value ($\psi^o = \phi^o - 30^o$)
R_f	-	0.76	0.93	Iterated to fit laboratory data plots (default value = 0.9)

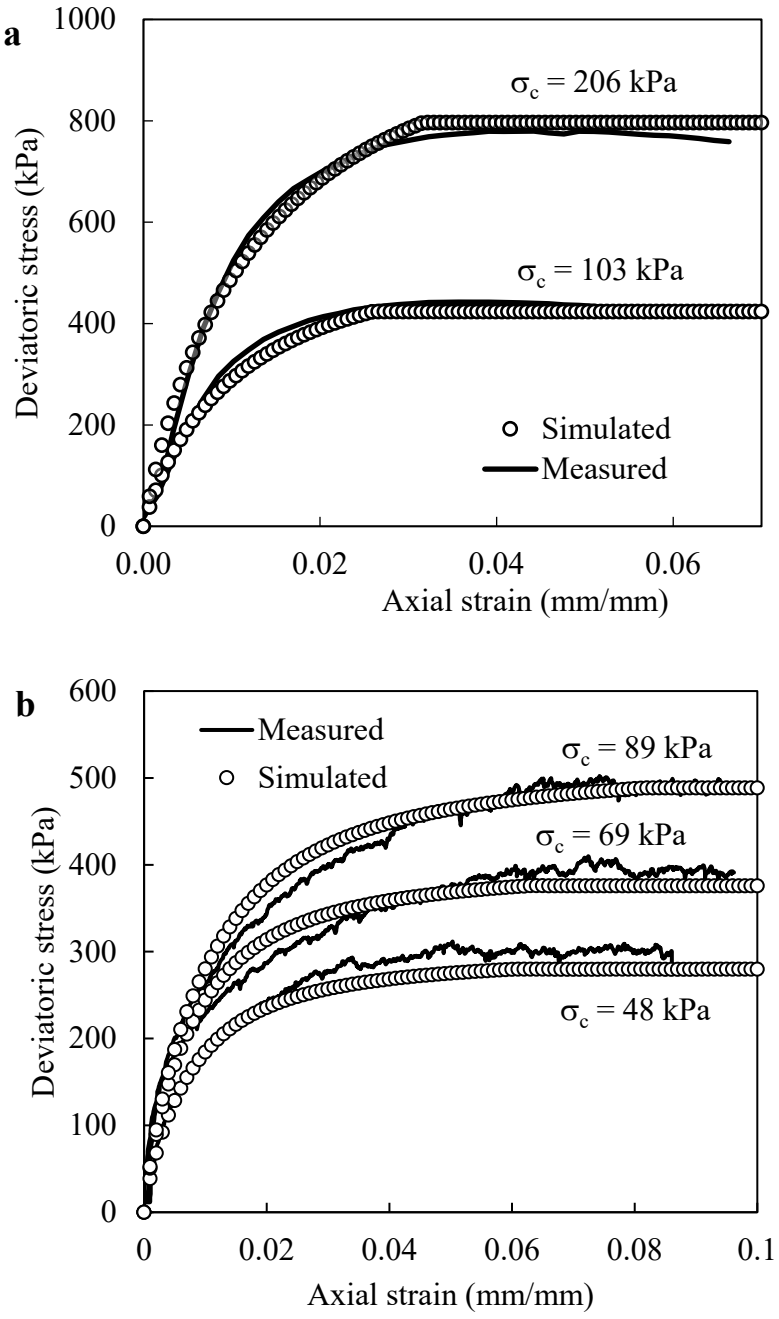

Figure 95. Measured vs simulated stress strain plots (a) foundation soil and (b) #57 crushed stone.

5.3.2.2 Steel Reinforcement

The steel reinforcement was modelled using the elasto-plastic plate model with isotropic properties. An FE tensile test was modeled similar to the laboratory steel tensile test setup. Figure

96 shows the FE model setup for simulating the steel tensile tests while Figure 97 shows the load-strain response for both the laboratory test and the numerical model. Ultimately, a simple elastic model was used instead of the elasto-plastic model because the soil clusters would fail before the failure strength of the plate element is reached.

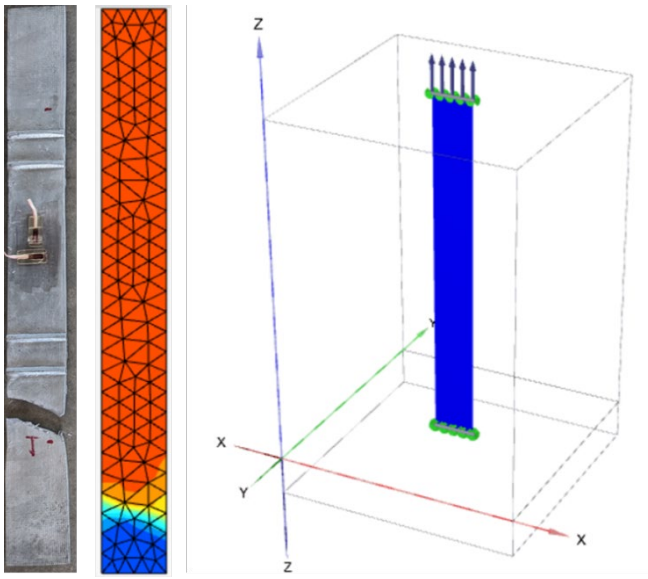

Figure 96. FE model setup of the steel tensile test

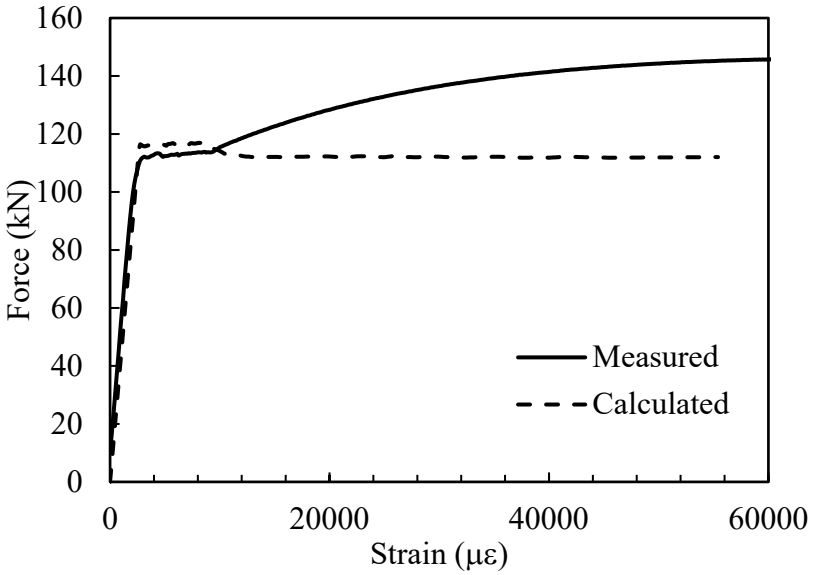

Figure 97. Simulated vs measured force vs strain behavior of the steel strips.

5.4 Modelling Procedure and Staged Construction

5.4.1 Model Description, Boundary Conditions and Meshing

Finite element models were developed following the experimental setup dimensions. The experimental results indicated that the test wall performed satisfactorily, with minimal deformations observed even under significant load conditions. Discussions during presentation of the experimental results at conferences have attracted questions regarding the influence of the confining walls on the overall performance of the MSE wall. It is apparent (as noted in Chapter 4) that the use of plastic sheets to break the frictional interaction between the fill material and the concrete walls does not eliminate this boundary influence entirely. Previous studies have shown that the sidewall friction can affect the experimental results, Wang et al (2023) conducted a parametric study that showed that an interface friction angle of 17.6° reduced horizontal wall displacements, compared to simulations neglecting wall friction and recommended use of containers with large width-to-height ratio for centrifuge experiments. It is to this effect that two numerical models were developed, one without the chamber walls (Model A) and one with the chamber walls (Model B).

The generated mesh for Model A (Figure 139 a) had 125162 soil elements and 204531 nodes, with an average element size of 20 cm, while the generated mesh for Model B (Figure 139 b) had 128928 soil elements and 218047 nodes, with an average element size of 24 cm. All four sides of the model were fixed in the normal direction, the top was free, and the base was fully fixed.

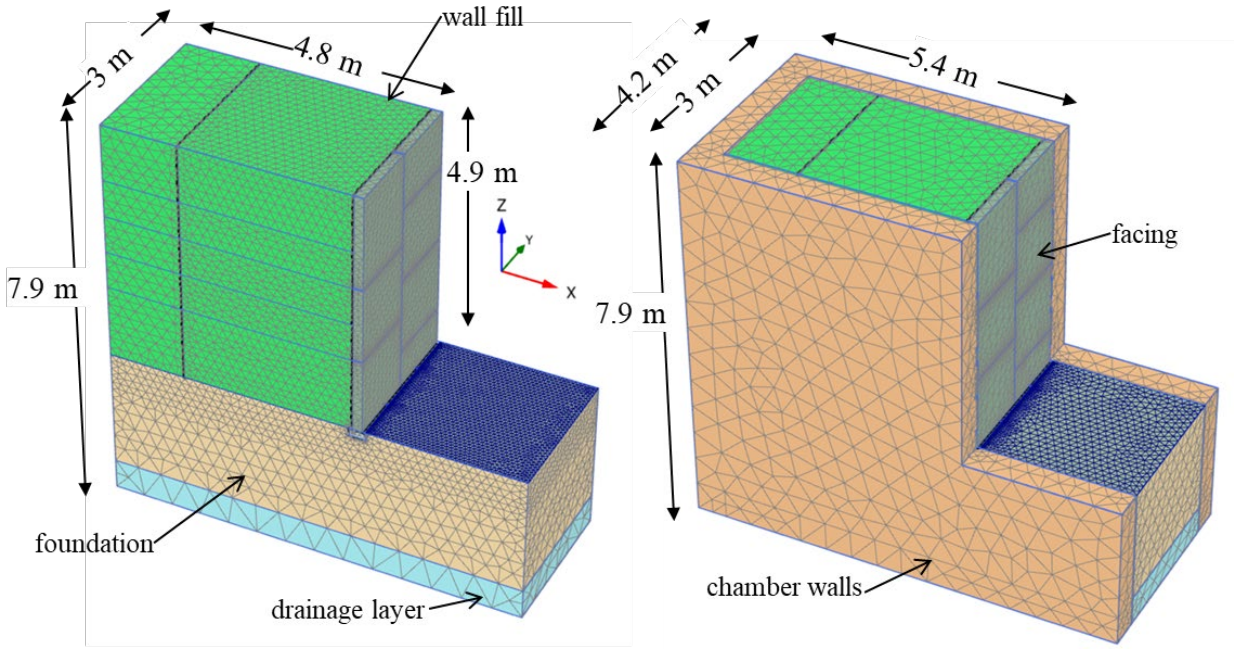

Figure 98. Generated FE mesh for (a) Model A, and (b) Model B.

Figure 99 shows the mesh quality analyses based on the Signed Inverse Condition Number (SICN), which is a measure of how regular a mesh element is. A value of 1 indicates an ideal element aspect ratio, in this case, for a tetrahedral element, indicates an equilateral tetrahedron. A value less than 1 signifies a non-equilateral tetrahedron, denoting a decrease in element quality. A minimum value of 0.1 is recommended to maintain numerical stability. A negative value means a self-intersecting tetrahedron with no meaningful interpolation function over the volume of the element and should be avoided (Bentley 2021 b). Minimum values of 0.29 and 0.28 for Model A and Model B respectively (Figure 99) in the generated mesh quality check, denotes sufficiently discretized meshes.

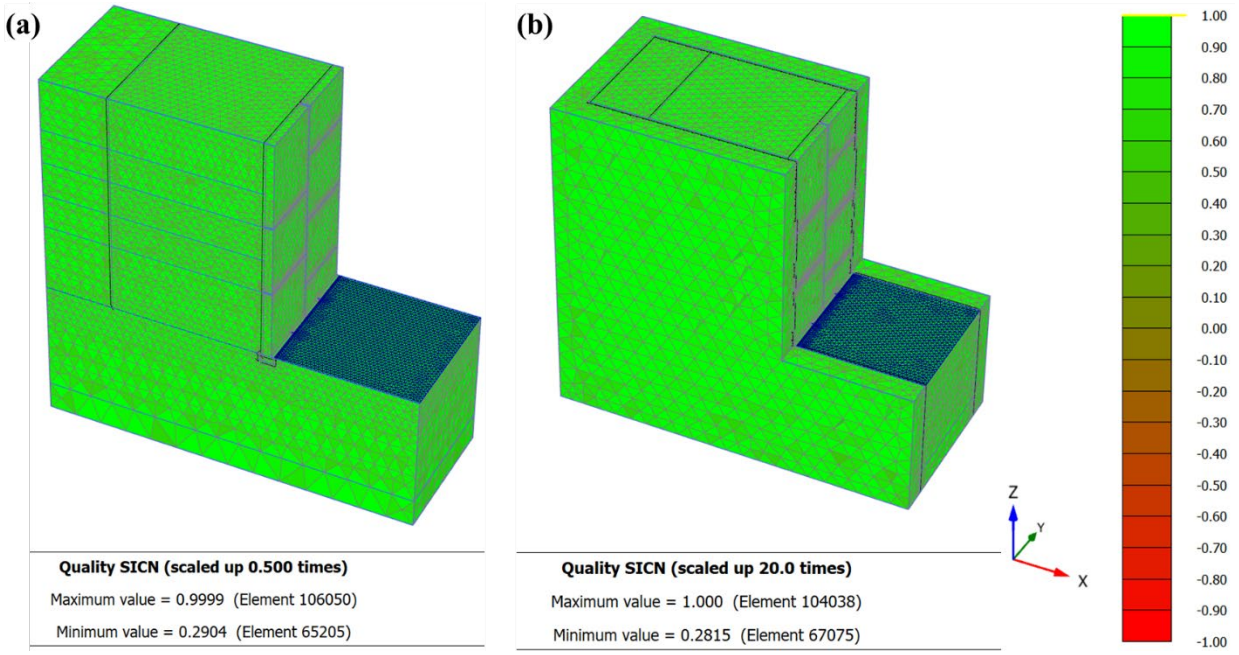

Figure 99. Mesh quality check (SICN) for (a) Model A and (b) Model B

5.4.2 Material input properties

The material properties used in the numerical models (Model A and Model B) are presented in Table 9 with the appropriate justifications and references. With an interface friction angle of 29° between the plastic sheet and the #57 stone, equations 44 through 46 were combined with equation 53 to solve for the stiffness as presented in equation 54. It is difficult to pick an stiffness value for the fill-chamber sidewalls interface, the expressions in equations 53 and 54 were used as a starting point which was further modified in a limited sensitivity study as discussed in the section 5.5.

$$G_i = \frac{E_i}{2(1+v_i)} \tag{53}$$

$$E_i = \left(\frac{\tan\delta_i}{\tan\phi_{soil}}\right)^2 \frac{E_{soil}}{(1+v_{soil})}(1+v_i) \tag{54}$$

RECo (2019) conducted an extensive test on the pullout resistance and apparent coefficient of friction (F^*) of high adherence reinforcing strips with various backfill materials. The study reported that angularity and durability of crushed stone gives high pullout resistance and recommended a default value ($F^* = 4$) for walls constructed with angular and sub angular gravels meeting AASHTO No. 3, 4, 5, **57**, 6 or 7 stone or similar. The apparent coefficient of friction was used to evaluate the soil-reinforcement interface as illustrated in equations 55 and 56.

$$F^* = R_i \tan \phi_{soil} = \tan \delta_i \tag{55}$$

$$R_i = \frac{F^*}{\tan \phi_{soil}} \leq 1 \tag{56}$$

The stress-strain response of the compression test on the soil-air bladder system indicated a modulus of 1384 kPa, a ratio of the material volume (i.e. $H_{bladder} / H_{system}$) indicates an approximate modulus of 207 kPa for the soft zone.

Table 9. Material properties input for the numerical model.

Name	Input Properties
Soil clusters:	
Foundation Sand	HS; γ =17.64 kN/m^3; c =1.4 kPa; ϕ =41.5^o; ψ =11.5$^{o\,a}$; p^{ref} =103kPa E_{50}^{ref} =37x10^3 kPa; E_{oed}^{ref} =37x10^3 kPa [b]; E_{ur}^{ref} =110x10^3 kPa [c]; m = 0.5 [d]
#57 Backfill	HS; γ =16.29 kN/m^3; c =1.4 kPa; ϕ =48^o; ψ =18$^{o\,a}$; p^{ref} =69kPa E_{50}^{ref} =31x10^3 kPa; E_{oed}^{ref} =31x10^3 kPa [b]; E_{ur}^{ref} =93x10^3 kPa [c]; m = 0.5 [d]
Facing Panel	LE; γ =24 kN/m$^{3\,e}$; E =32x10^6 kPa [e]; ν =0.20 [e]
Concrete Pad	LE; γ =25 kN/m$^{3;}$ E =25x10^6 kPa [e]; ν =0.20 [e]
Drainage Layer	LE; γ =16 kN/m^3; E =31x10^3 kPa; ν =0.25
Soft Zone	LE; γ =5.4 kN/m^3; E =207 kPa [f]; ν =0.35
HDPE Bearing Pad	LE; γ =10 kN/m$^{3\,e}$; E =12x10^3 kPa [g]; ν =0.01 [e]
Reinforcement:	
Steel Straps	Elastic; Isotropic; E =211x10^6 kPa; ν =0.27
Interfaces:	
Backfill-Retained [h]	MC; c =1.4 kPa; δ_i =48^o; E =24x10^3 kPa; ψ =0^o; ν =0.45.
Concrete-Soil	MC; c =1.4 kPa; δ_i =30$^{o\,i}$; E =9.7x10^3 kPa [n]; ψ =0^o; ν =0.45.
Soil-Reinforcement	MC; c =1.4 kPa; δ_i =48$^{o\,j}$; E =24x10^3 kPa [k]; ψ =18$^{o\,l}$; ν =0.45.
Soil-chamber-wall	MC; c =0 kPa; δ_i =29$^{o\,m}$; E =138 kPa; ψ =0^o; ν =0.45.

MC = Mohr-Coulomb, HS = Hardening Soil, LE = Linear Elastic,

[a] default value $\psi^o = \phi^o - 30^o$

[b] default value $E_{oed}^{ref} \approx E_{50}^{ref}$

[c] default value - estimated using $E_{ur}^{ref} \approx 3E_{50}^{ref}$

[d] default value

[e] Damians et al. 2021

[f] approximated from compression test

[g] Damians et al. 2016

[h] same #57 stone for both reinforced and retained zones

[i] adopted from interface properties for mass concrete to gravel-sand mixture as reported by NAVFAC (1982)

[j] fully bound to soil *F** from pullout tests by RECo (2019)

[k] E_{soil} at lower confining stress

[l] same as soil dilation due to the ribbed steel

[m] from laboratory direct shear test.

5.4.3 Staged construction.

The construction process outlined in Chapter 3 was simulated in phases in the numerical analyses. Firstly, the stress initialization included the first fill which was the drainage layer (Figure

100a). The first foundation fill layer was placed with a surface load to simulate compaction (Figure 100b), which was then removed (Figure 100c) before placing the next fill and compaction load (Figure 100d). The compaction load was estimated as 45 kPa using the centrifugal force and compactor footprint (Bomag 2023) (i.e., $q_{compaction} = \frac{Force_{centrifugal}}{Area_{footprint}}$). This step was repeated till the foundation was completed (Figure 100e). The soft zone, level pad, first row of facing panel first reinforced wall fill and the compaction load were activated in the next phase (Figure 100f). the compaction load was removed in the next phase (Figure 100g). The first reinforcement layer, next reinforced wall fill, and the compaction load were activated in the next phase (Figure 100h), and in the phase after that, the compaction load was removed. A lateral restraint was used to limit horizontal movement only to simulate the propping detailed in the construction process. The lateral restraint on each panel was removed when the panel above it was activated (Figure 100i and j). This sets of processes were repeated till the wall was completed (Figure 100k). the last facing lateral restraint was then removed and the soft zone was deactivated to simulate the deflation of the air bladders as was done in the MSE experiment (subsequently referred to as inducing differential settlement). The applied surcharge loads were then applied in the next phase. The same simulation procedure was used for Model B, the only addition was the chamber sidewalls that were activated in the stress initialization stage (i.e. initial phase).

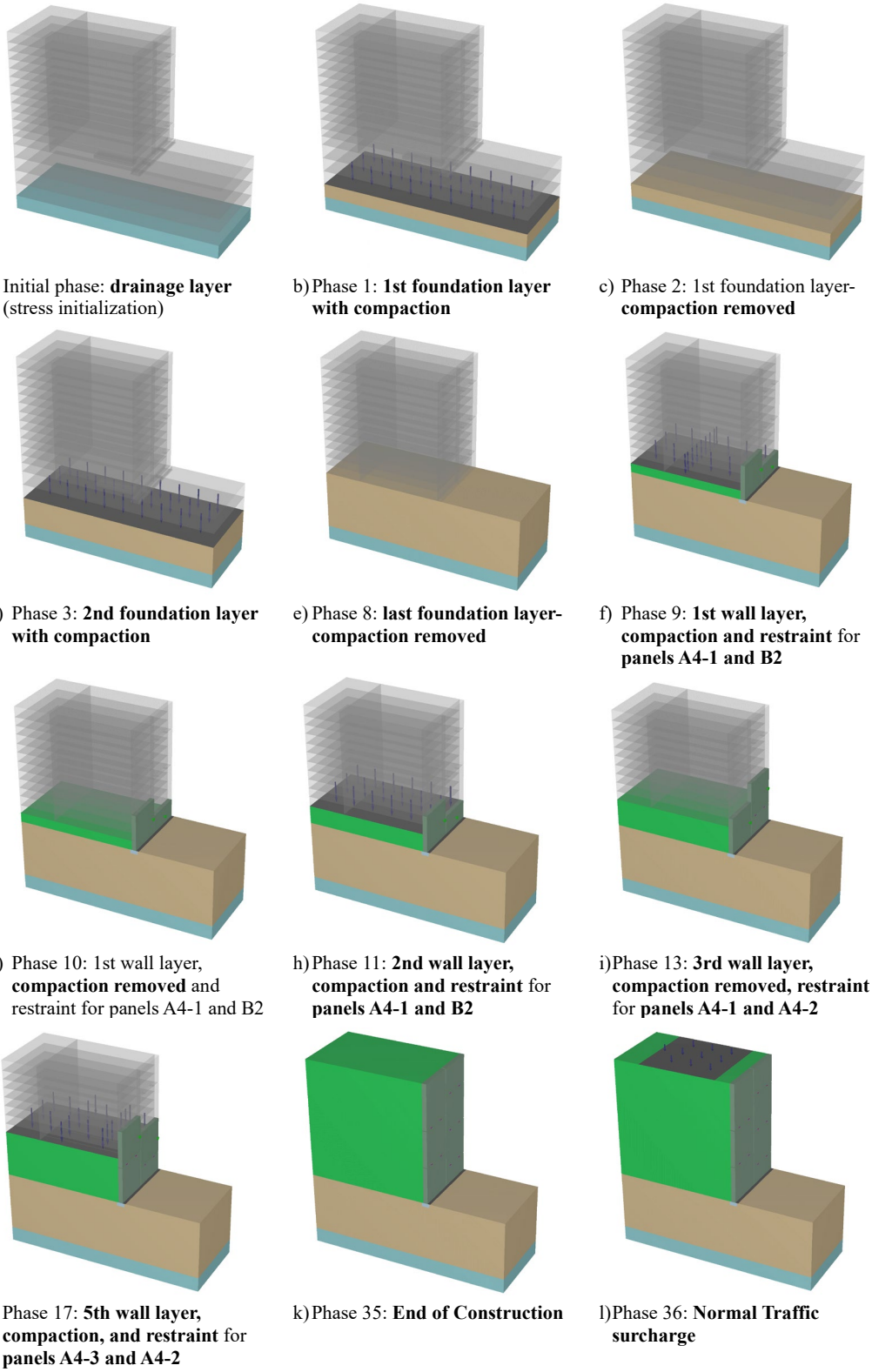

a) Initial phase: **drainage layer** (stress initialization)

b) Phase 1: **1st foundation layer with compaction**

c) Phase 2: 1st foundation layer-**compaction removed**

d) Phase 3: **2nd foundation layer with compaction**

e) Phase 8: **last foundation layer-compaction removed**

f) Phase 9: **1st wall layer, compaction and restraint** for **panels A4-1 and B2**

g) Phase 10: 1st wall layer, **compaction removed** and restraint for panels A4-1 and B2

h) Phase 11: **2nd wall layer, compaction and restraint** for **panels A4-1 and B2**

i) Phase 13: **3rd wall layer, compaction removed, restraint** for **panels A4-1 and A4-2**

j) Phase 17: **5th wall layer, compaction, and restraint** for **panels A4-3 and A4-2**

k) Phase 35: **End of Construction**

l) Phase 36: **Normal Traffic surcharge**

Figure 100. Staged construction phases for the numerical simulations

5.5 Experimental versus Numerical Results

This section presents the numerical results from simulations using both Model A and Model B, in comparison to the observed response from the laboratory experiment. As mentioned earlier, it is not feasible to eliminate the boundary effects. The purpose of using both models is to evaluate to what extent the experimental constraints influenced the results.

As discussed in section 5.4.2, it is challenging to pick a value for the stiffness of the interface between the fill and the chamber sidewalls in Model B. The default value according to the formulations of an interface element (Bentley 2021a) was used as an initial value, which was then reduced to reach a similar settlement magnitude observed in the experiment (Figure 101). The changes in the stiffness of the interface between the fill and the chamber sidewalls did not result in significant changes in other responses.

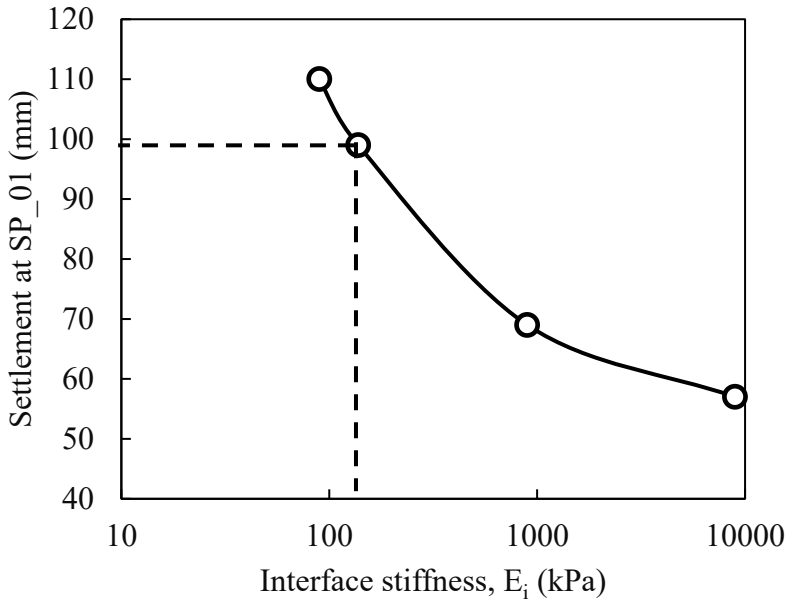

Figure 101. Limited sensitivity study on influence of fill-chamber sidewalls interface stiffness on observed settlement

5.5.1 Deformations

5.5.1.1 Settlement.

Settlement monitoring began after the construction of the wall was complete and no significant additional settlement was observed at any of the settlement plate locations before and after the induced settlement stage. Significant settlement was observed only at the soft zone after deflating the air bladders resulting in a differential settlement of 100 mm. Observations showed no settlement at all other settlement plates. Analysis of routine monitoring results from the 3D lidar scanner confirmed this observation as described in Chapter 4. Figure 102 shows the results from the numerical simulations as well as the experimental observation for a line drawn over the center of the soft zone. Model A predicted a settlement of 98 mm while Model B (with chamber walls modelled) predicted a settlement of 99 mm.

Figure 103 shows a horizontal section at the foundation level to show distribution of settlement for (a) Model A and (b) Model B after the differential settlement was induced. The contour patterns show that, as observed in the experiment, the settlement is concentrated in the soft zone, and this is the case for both models. Figure 103 3D shows cumulative settlement patterns for (c) Model A and (b) Model B for the same phase but including results from previous construction up to inducing the differential settlement. The contour scale was modified to reveal the settlement patterns even though the magnitudes are very small. The patterns show lower magnitudes in Model B compared to Model A and that the magnitudes decrease from the center towards the sides across the wall width (along y-coordinate) especially in the first row of panels. Figure 103 also shows cumulative settlement contours of a section through the center of the soft zone for the 3D contours previously described for (e) Model A and (f) Model B. The section shows

that the settlement was not transmitted fully through the reinforced mass to the top of the wall, which was also observed in the experiment.

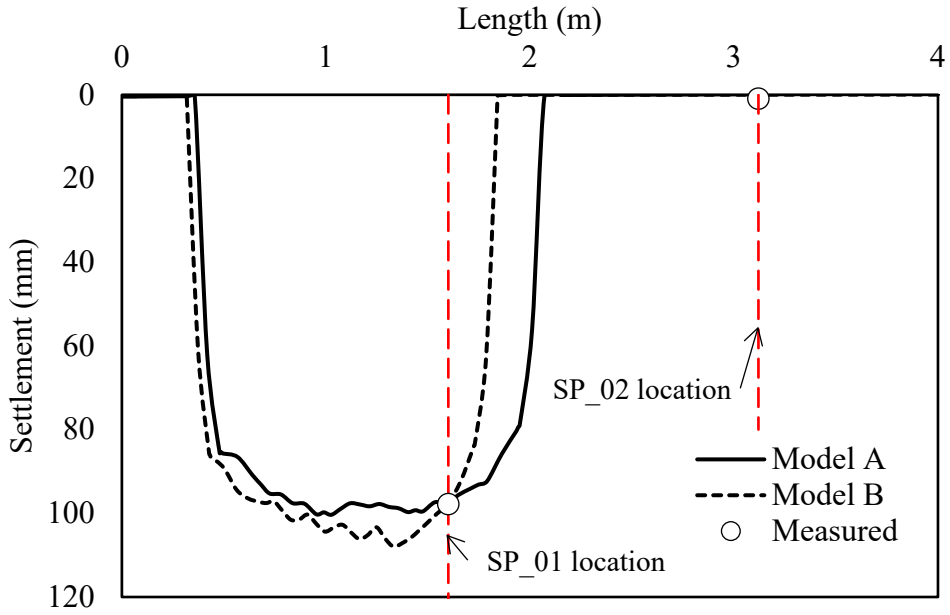

Figure 102. Numerical and measured foundation settlement results through the soft zone

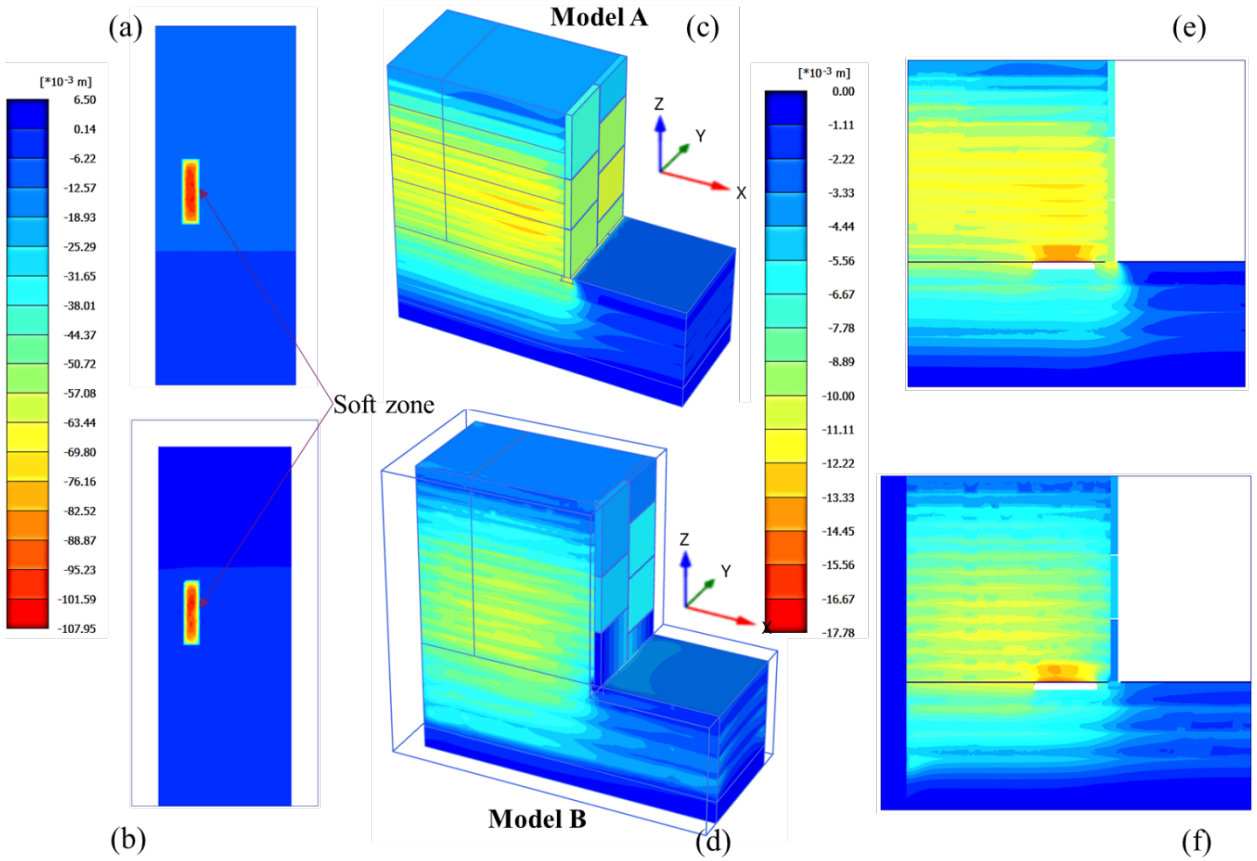

Figure 103. Horizontal section at the foundation level to show distribution of settlement for (a) Model A and (b) Model B; 3D cumulative settlement patterns for (c) Model A and (b) Model B; and section through center of soft zone showing cumulative settlement patterns (e) Model A and (f) Model B.

5.5.1.2 Lateral Displacement.

Horizontal displacement within the reinforced mass also began after the construction of the wall was complete using an inclinometer and a vertical shape array. Figure 104 shows the horizontal displacement at the location of the inclinometer and shape array casings for (a) induced differential settlement and (b) application of traffic surcharge. As depicted in the plots, Model A overpredicted the displacements (about 3 times) while Model B was closer to the measured values albeit less. This is expectedly due to the sidewall friction interaction, and it is important to note that the measurement location is close to the chamber side walls and is easily affected by the

sidewall friction. This is also the case for the facing panel displacement which was measured even closer to the sidewalls (< 0.6 m).

Figure 105 shows the lateral facing displacement at the locations of the string potentiometers for (a) induced differential settlement and (b) application of traffic surcharge. As depicted in the plot, Model A overpredicted the displacements (about 3 times) while Model B was closer to the measured values albeit less in magnitude.

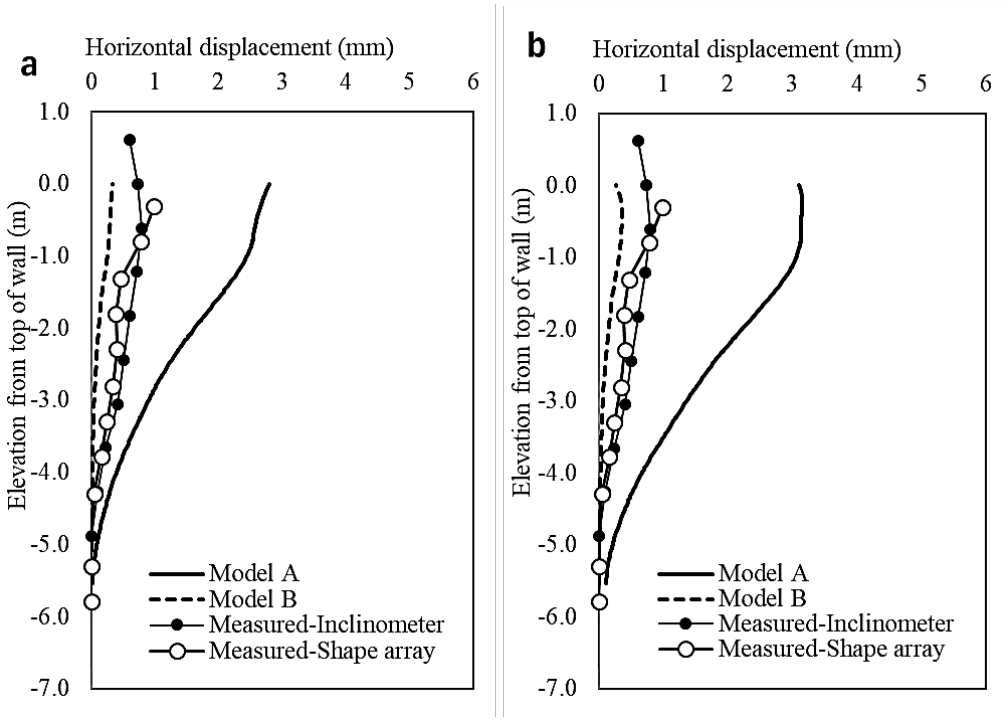

Figure 104. Horizontal displacement within the reinforced mass (a) induced settlement and (b) application of traffic surcharge.

Figure 106 shows the 3D contour plots of the lateral displacement after applying traffic surcharge for (a) Model A and (b) Model B. This shows uniform maximum displacement within the lower one-third height for Model A, a more realistic displacement profile for retaining walls.

This is also true for Model B, but additionally, the sidewalls limit the outward displacement causing the most displacement to occur towards the center of the wall width (along y-coordinate).

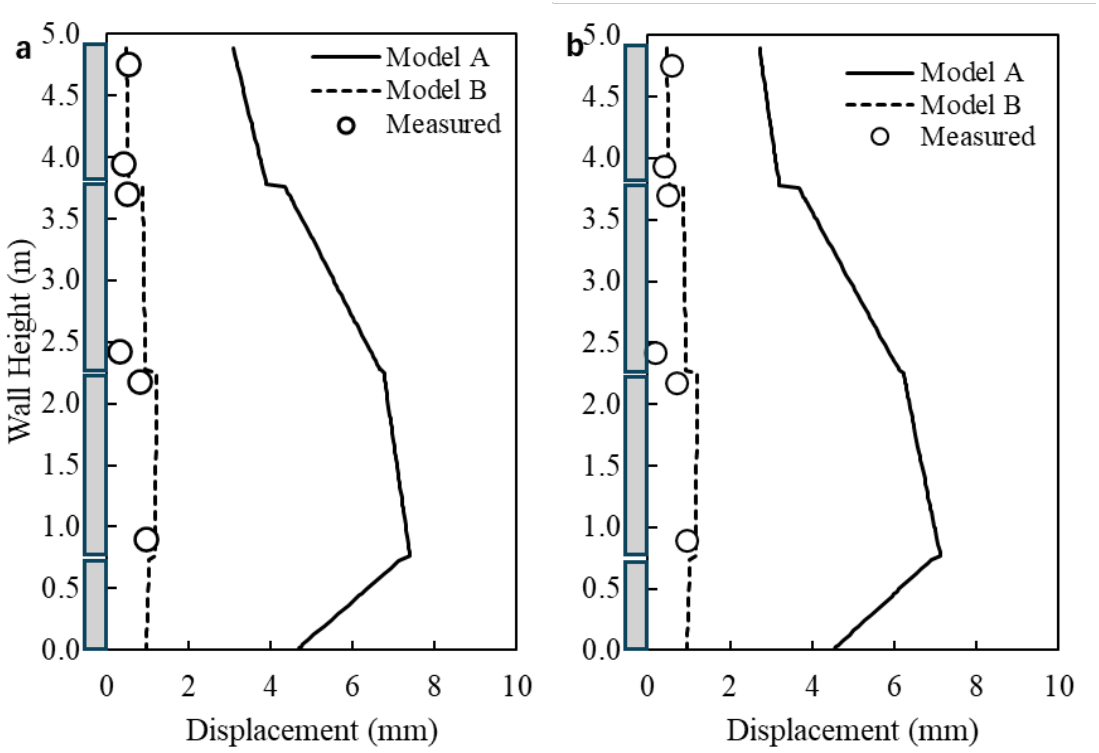

Figure 105. Facing displacement within the reinforced mass (a) induced settlement and (b) application of traffic surcharge.

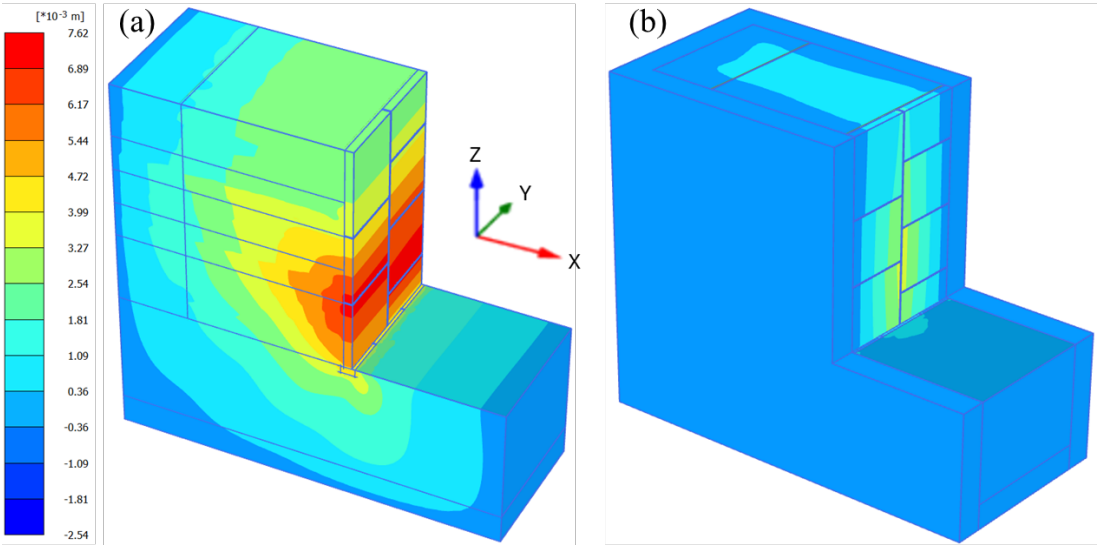

Figure 106. 3D contour plots of the lateral displacement after applying traffic surcharge (a) Model A and (b) Model B.

5.5.2 Stresses

5.5.2.1 Foundation Bearing Stress.

Results of vertical foundation stresses from both model A and Model B were compared to the experimental measurements. Foundation stresses are extracted from same locations (Line 1, Line 2, and Line 3) as described in Chapter 4 (Table 6 and Table 7). Figure 107 shows measured and calculated vertical foundation stresses for Line 1, Line 2, and Line 3 at (a) end of construction (EOC), (b) after inducing differential settlement, and (c) after imposing traffic surcharge. The circular markers show the measured stresses at these testing stages, the closely spaced dashes are the self-weight plus surcharge values, the solid black lines are the numerical results from Model A while the widely spaced dashes are the numerical results from Model B.

The numerical results show similar trends with the measured stresses. It was noted in Chapter 4 that at the end of construction, it was expected that all pressure cells would correspond to the self-weight ($\gamma H_{backfill}$) and that the discrepancy between line 1 and line 2 was likely due to the effect of sidewalls friction. This is confirmed by the numerical results as Model B showed stress magnitudes that are closer to the measured values compared to Model A which showed higher stresses for line 1. The results for line 2 show that Model B predicted stress magnitudes that were closer to the measured values compared to Model A for cells closer to the back of the reinforced mass while Model A sufficiently predicted the stresses from pressure cells closer to the front half of the reinforced mass, accurately predicting the maximum vertical stresses. It was also noted that the difference in measured stresses between line 1 and line 2 is solely due to the installation of the soft zone to simulate loss of foundation support. This is also confirmed by the numerical results as both models showed an increase in stress up to about 20 kPa with no further

increase, followed by a decrease to 0 kPa after the soft zone was deactivated (See Appendix C for stress history plot at for each pressure cell).

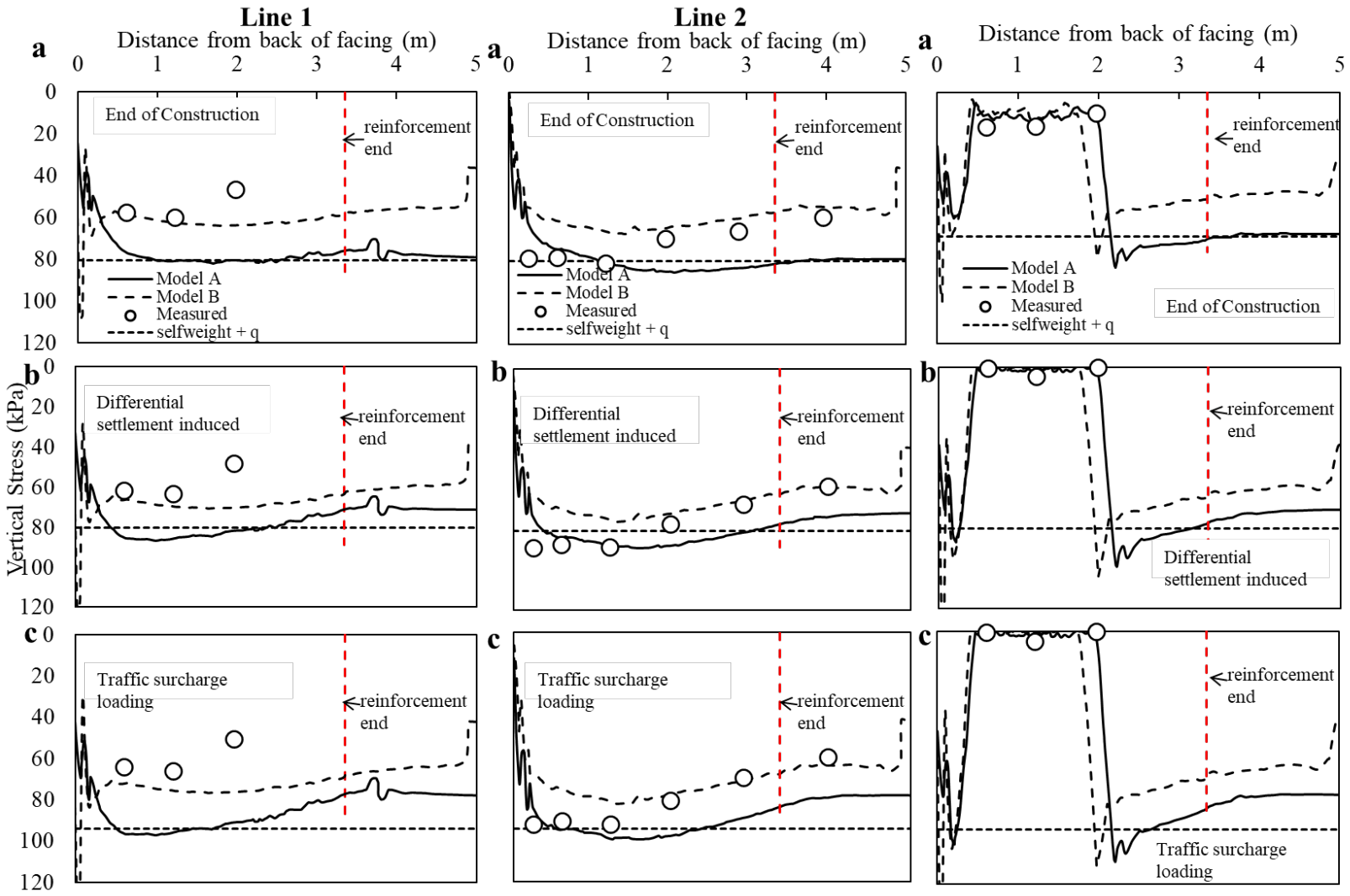

Figure 107. Vertical foundation stresses for Line 1, Line 2 and Line 3 at (a) End of construction, (b) after inducing differential settlement, and (c) after imposing traffic surcharge.

Figure 108 shows the vertical stress contours beneath the reinforced mass after inducing the differential settlement. This shows the soft zone with no bearing stress (i.e. 0 kPa vertical stress), and the resulting loss of capacity redistributed to the surrounding soil clusters over a short distance. This plot also shows the interaction of the reinforcement elements, especially towards the reinforced-retained zone. The patterns show that higher stresses directly beneath each reinforcement column and lower stresses in the adjacent soil clusters. The soil clusters just behind the facing panels show lower stress magnitudes as expected due to the influence of the interface strength between the facing panels and the reinforced zone. But for the inclusion of the soft zone, the stress distribution seems uniform across the wall width.

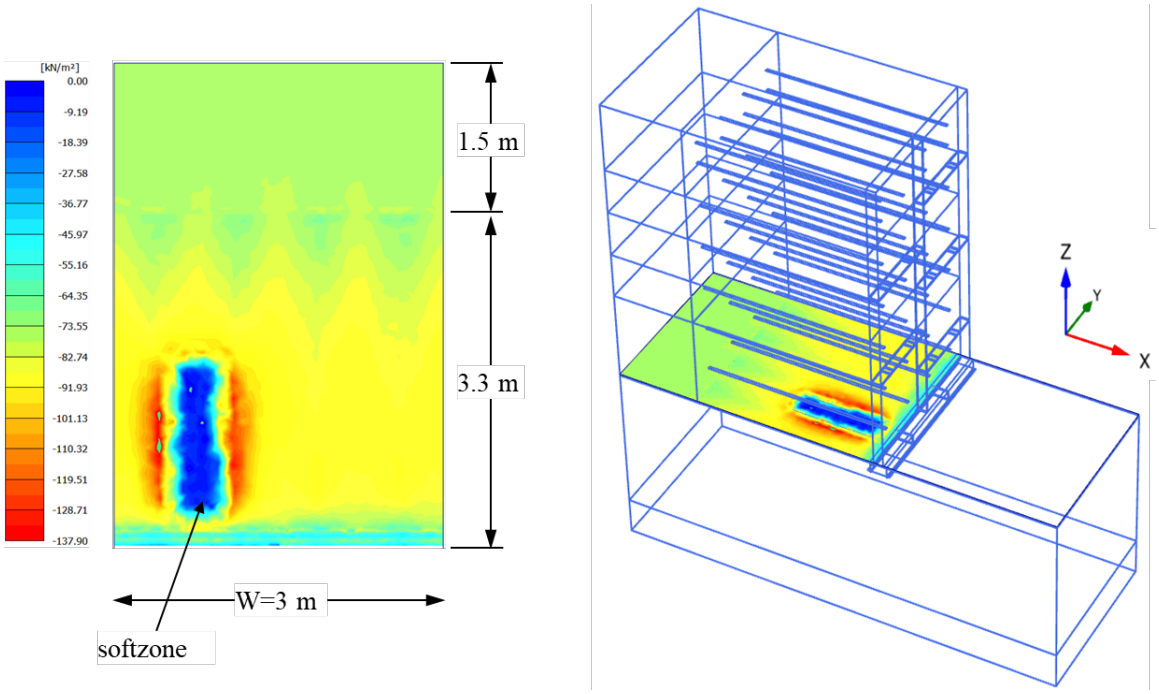

Figure 108. Vertical stress contours beneath the reinforced mass after inducing the differential settlement (Model A).

Figure 109 shows vertical stress contours after inducing the differential settlement for Model A and Model B at sections through (a) Line 1 and (b) Line 3. These sections show a fairly uniform distribution that decreases across intersecting interfaces. This is also well observed in

Figure 110 which shows vertical stress patterns for a section through a typical reinforcement column (reinforcement Line 1 as described in Chapter 4) for (a) iso-stress lines and (b) contour shading. The iso-stress lines show a better delineation between the various stress magnitudes which better presents the distribution patterns around each reinforcement strip. The contour shading in Figure 110 b shows higher stress magnitude just above the reinforcement-to-panel connection and a significantly lower stress magnitude just below which is an indication that the reinforcement to panel connection affects the stress distribution likely through stress transfer to panel-backfill interface or directly to the facing panels.

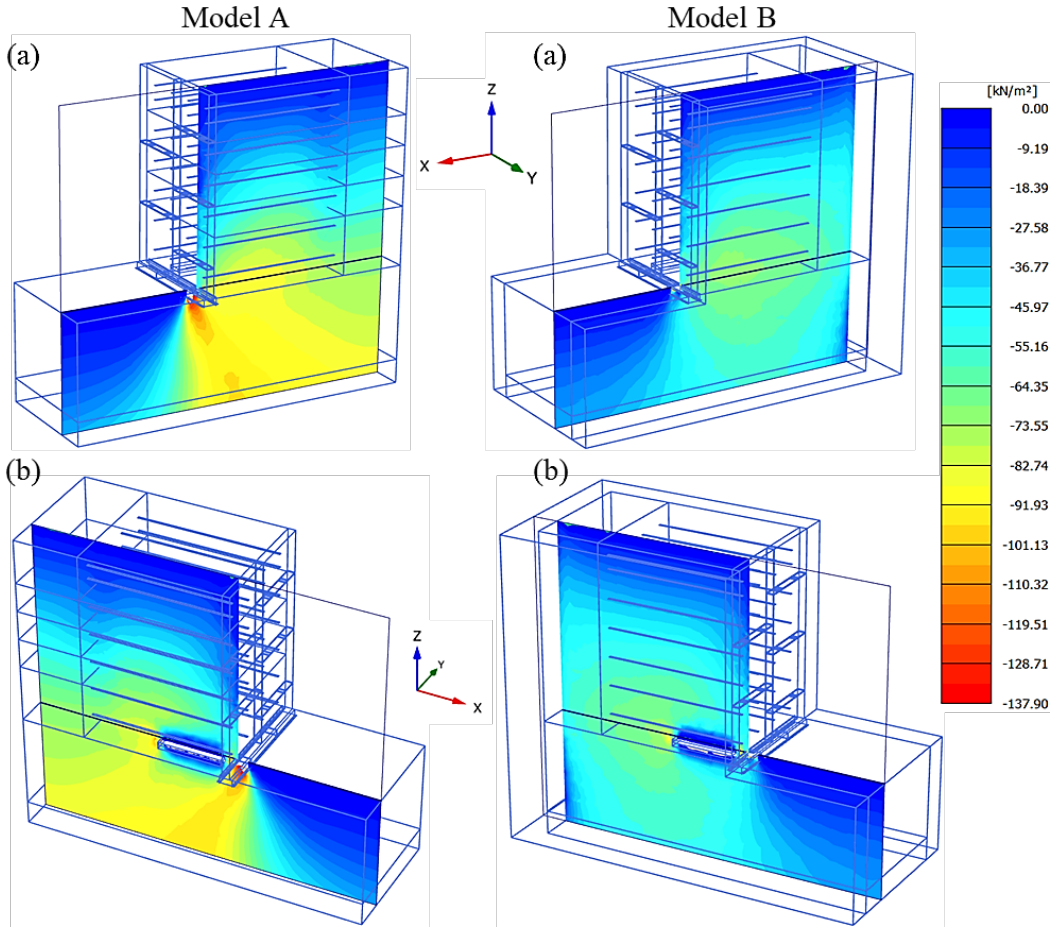

Figure 109. Vertical stress contours after inducing the differential settlement for Model A and Model B at sections through (a) Line 1 and (b) Line 3

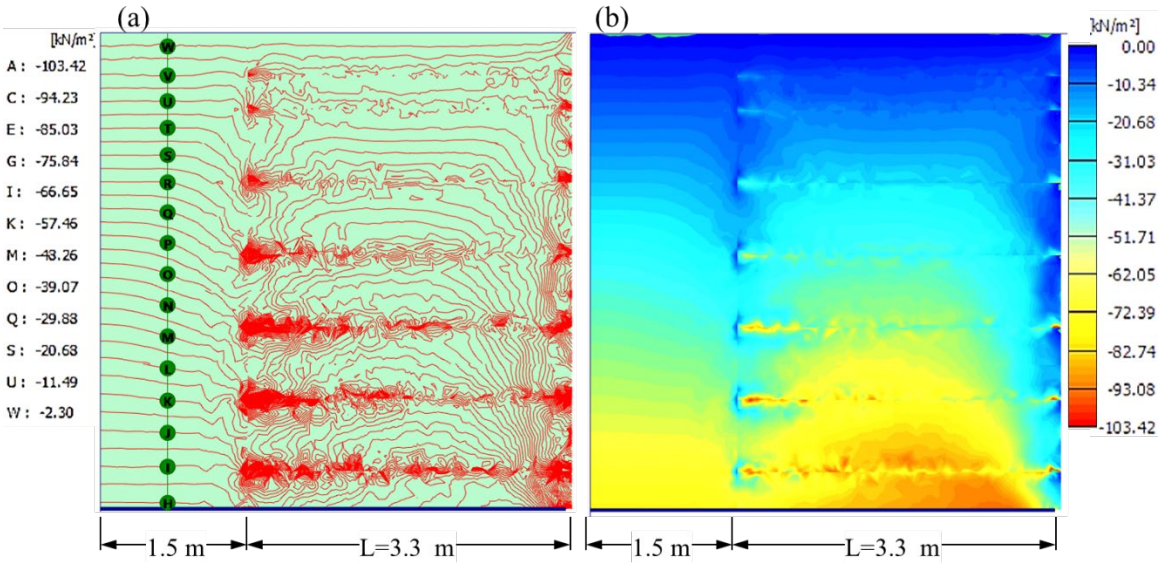

Figure 110. Vertical stress patterns for a section through a typical reinforcement column (a) contour iso-stress lines and (b) contour shading.

5.5.2.2 Lateral Stress.

The lateral stresses were not directly measured during the laboratory experiment; however, results are presented for the numerical solutions and evaluations from classical lateral earth pressure theory used in the design of reinforced earth walls. Figure 111 shows the lateral effective stresses through Line 2, behind facing panels after (a) induced differential settlement and (b) application of traffic surcharge. Figure 111 shows the lateral stresses for the same cases on Line 2 but at a distance 0.3H from the facing panels. The results are quite similar for both Model A and Model B. Also shown on the plots are lateral geostatic stresses estimated using active lateral earth pressure coefficient (K_a) indicated by the black dashed lines, and reinforcement lateral earth pressure coefficient (K_r) indicated by the solid black line. In the design of MSE walls, evaluation of K_r is typically expressed as a ratio to K_a, the solid black lines in the plot correspond to $K_r / K_a = 2.5$. For Figure 112 (i.e. at a distance 0.3H from the panels), the stresses are greater than the active case and are close to the lateral stresses with $K_r / K_a = 2.5$.

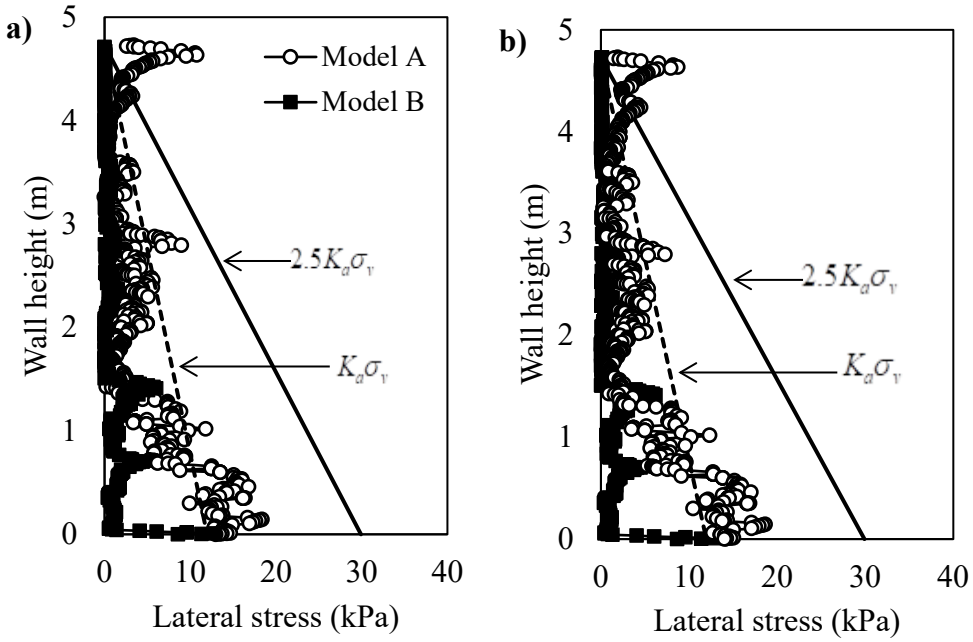

Figure 111. Lateral effective stress plots through Line 2, behind facing panels (a) after inducing differential settlement and (b) after application of traffic surcharge.

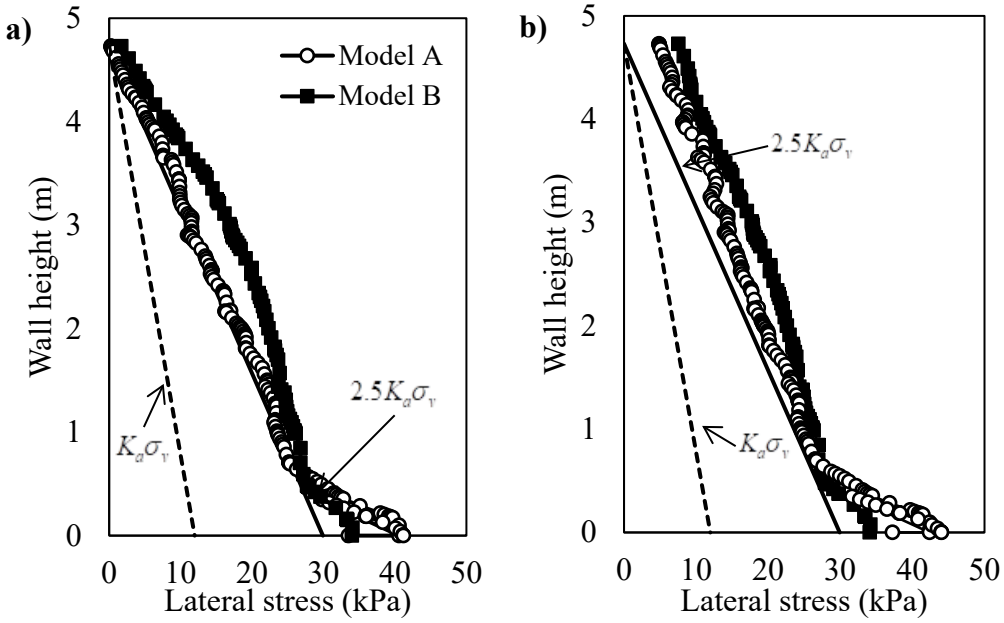

Figure 112. Lateral effective stress plots through Line 2, 0.3H from the facing panels (a) after inducing differential settlement and (b) after application of traffic surcharge.

5.5.3 Reinforcement Load

Figure 113 shows the tensile loads in the reinforcements after inducing the differential settlement for reinforcement Line 1 and Line 2, and for levels 1 through 6. The solid black lines correspond to numerical results from Model A, the dashed black lines correspond to numerical results from Model B while the solid black squares correspond to the measured values.

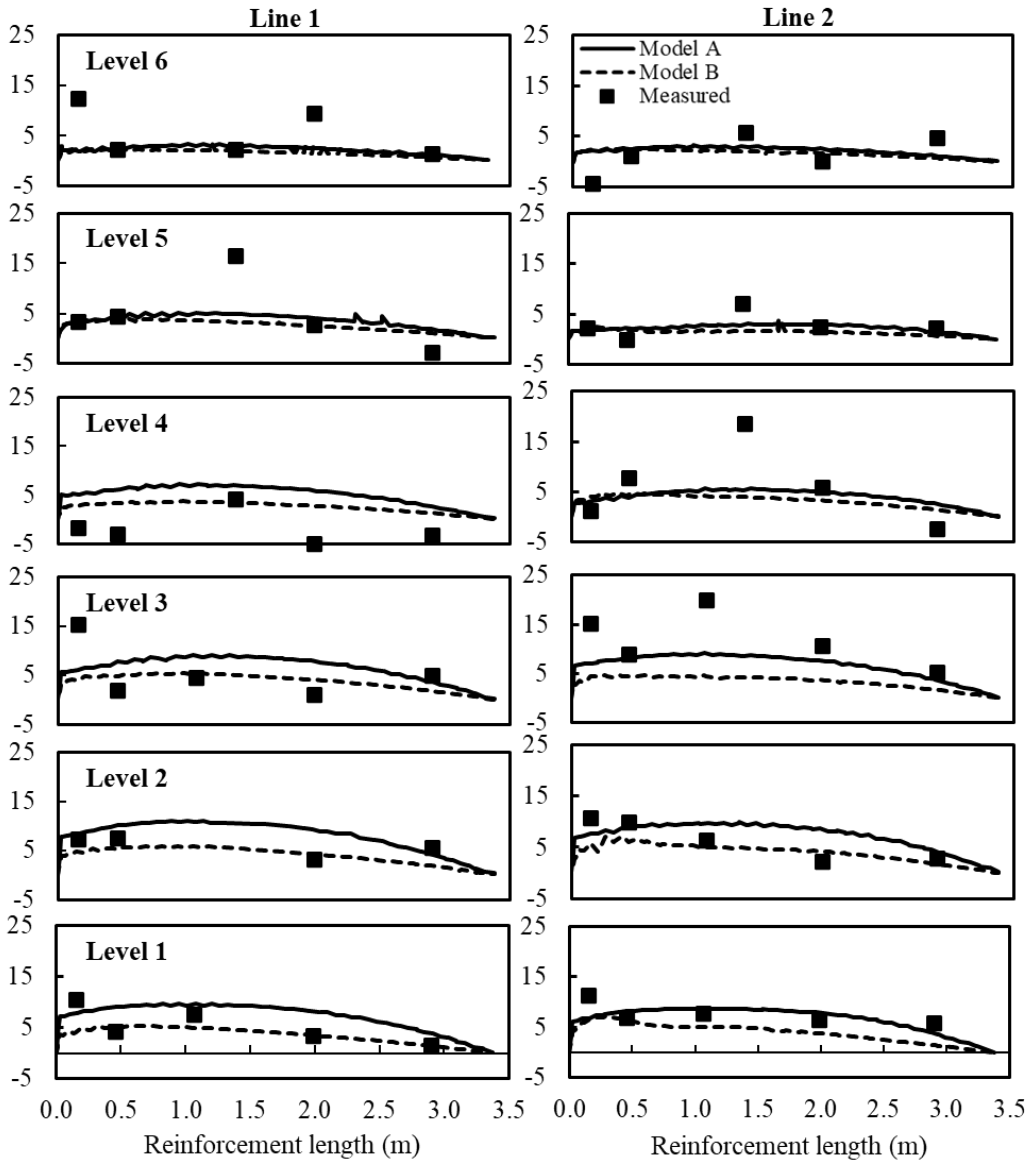

Figure 113. Reinforcement loads for reinforcement Line 1 and Line 2 for levels 1 through 6 after inducing differential settlement.

The measured values were evaluated using the recorded strain and the force-strain response obtained from the laboratory tensile test. Figure 114 shows the maximum tensile loads at each level from measured values, numerical results, design values using coherent gravity methods and allowable strength for (a) Line 1 and (b) Line 2. Model A showed higher reinforcement loads than Model B especially for reinforcement line 1.

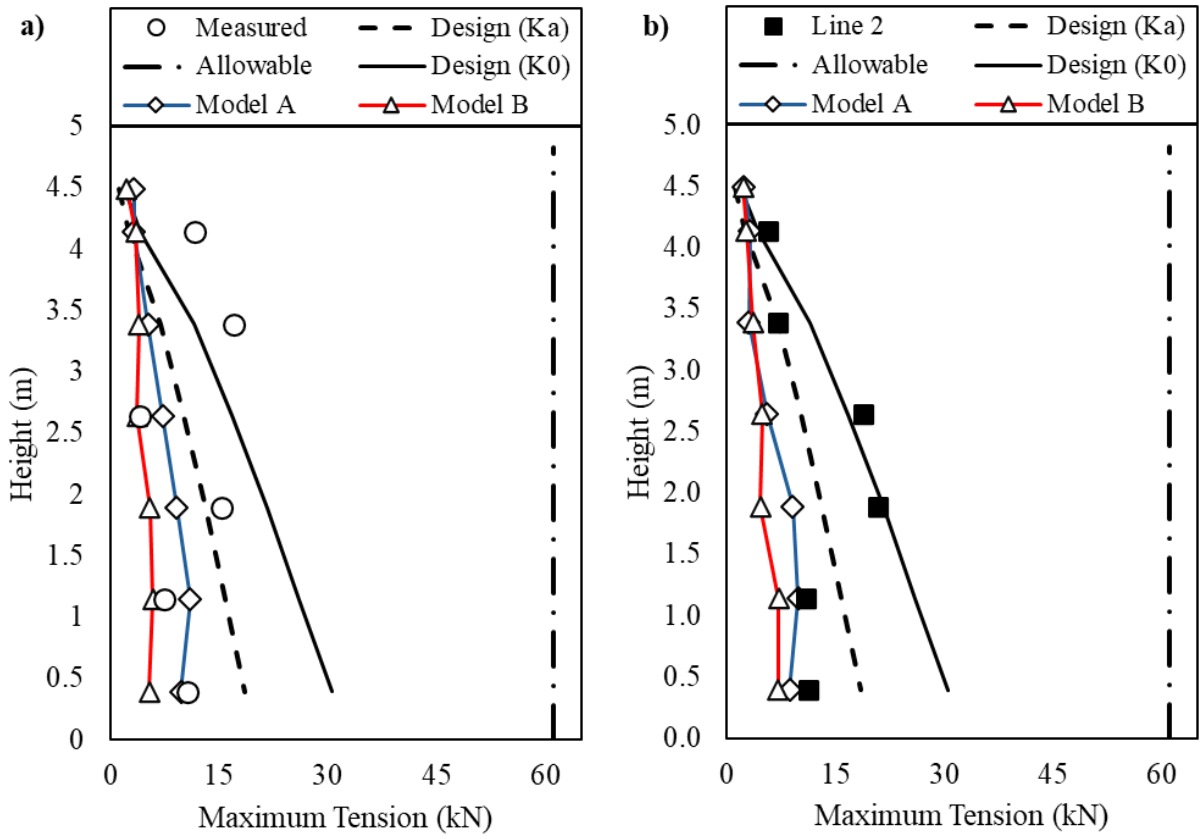

Figure 114. Maximum tensile loads showing measured values, numerical results, design values using coherent gravity methods and allowable strength for (a) Line 1 and (b) Line 2.

5.5.4 Shear Strain

Figure 115 shows the 3D total shear strain contour shadings for (a) Model A, and (b) Model B, and for sections drawn through the soft zone for (c) Model A and (d) Model B. The figures show that the model remained elastic throughout all the construction stages although with

localizations of higher strains ($\geq 2\%$) occurring at the interfaces between the facing panel and the backfill, and in Model B, between the chamber walls and the backfill. It is important to note that

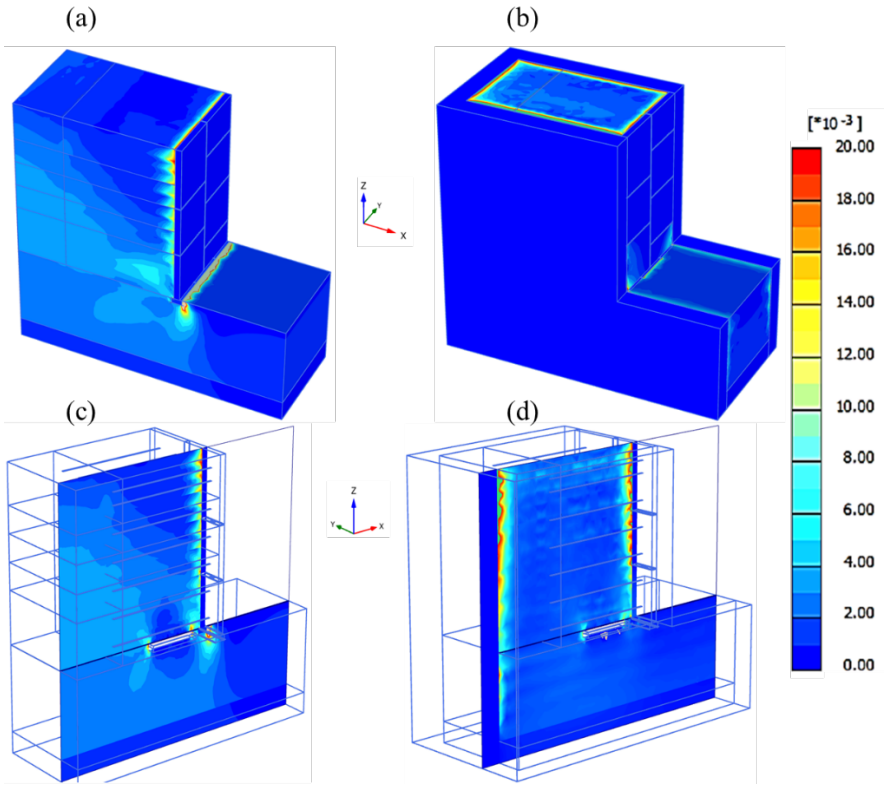

Figure 115. Total deviatoric strain contour shadings for (a) Model A, and (b) Model B; sections over the soft zone for (c) Model A and (d) Model B.

Figure 115 shows accumulated strains from all prior construction stages which. This is ultimately not a representation of the actual strains due to the several unloading apparent in these construction stages. However, it is useful in estimating maximum possible strains and locations of plastic zones. The plots show that the highest strains occur at interfaces between the facing panels and the soil, at the interfaces between the chamber walls and the soil, and at the edges of the poor bearing zone. These are all zones of higher relative movement between dissimilar materials.

On the other hand, Figure 116 shows incremental deviatoric strain contour shadings for (a) Model A, and (b) Model B; sections over the soft zone for (c) Model A and (d) Model B. The

contours of shear strain increment are typically useful for observing localization of shear strain within the soil when failure occurs. As shown in Figure 116, the system remained elastic. The maximum calculated shear strain was 0.6% around the deactivated soft zone, which is well within the elastic region of Figure 95b.

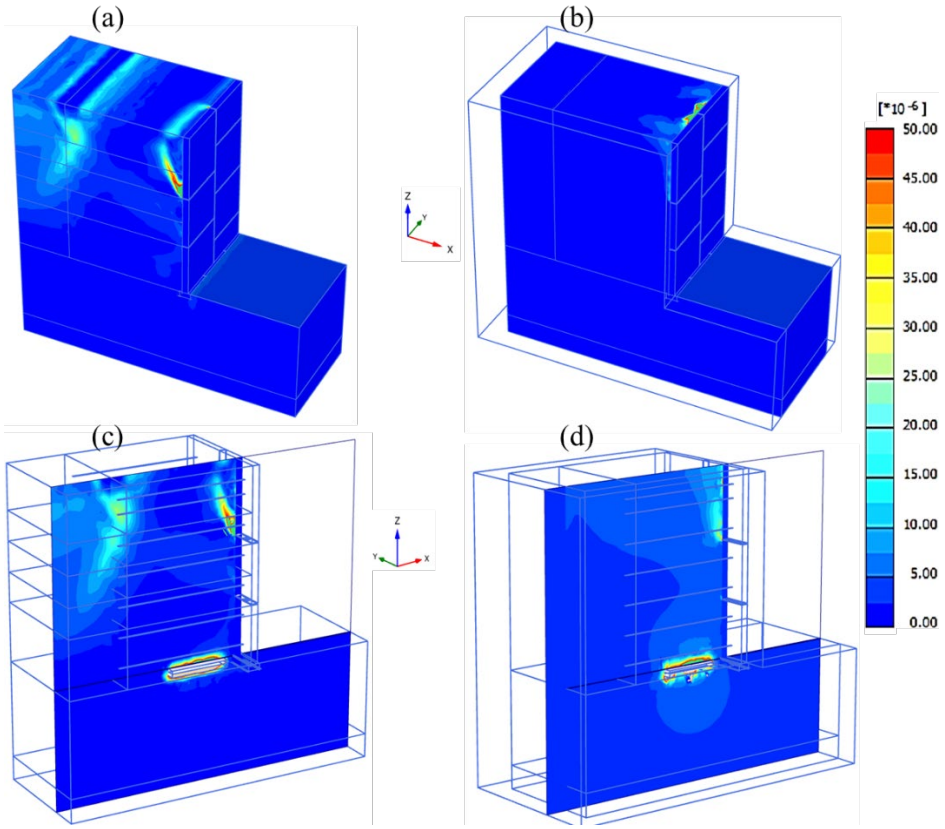

Figure 116. Incremental deviatoric strain contour shadings for (a) Model A, and (b) Model B; sections over the soft zone for (c) Model A and (d) Model B.

5.6 Discussion

The modelling approach outlined in this chapter was successfully used to develop two numerical models carefully simulating the construction procedures carried out during the experiment. Two models were created to fully analyze the MSE wall experiment, namely Model A (without including the chamber side walls and side wall friction) and Model B (with the chamber walls and side wall friction fully modelled). The same modelling procedure was adopted in both

cases and the only difference is the addition of the side walls and interface in Model B. This was done to study the influence of side wall friction on the experimental outcomes.

For the measurement points (SP_01 and SP_02), both models showed similar settlement magnitudes compared to the measured values. At SP_01, Model A showed about 98 mm of foundation settlement, while Model B showed about 99 mm. At SP_02, both Model A and Model B showed no settlement which is in line with the experimental observations. The induced differential settlements did not fully transmit through to the top of the wall in both models and much less so in Model B, reaffirming the stability of the reinforced soil system after being subjected to foundation differential settlement.

Model A predicted more lateral deformations than Model B, both for lateral displacements within the reinforced mass and at the facing panels. Model A visibly overpredicts the lateral deformation. The results showed that the limiting effect of the side wall friction reduced from both side walls towards the center of the model, and is least at the center of the model, indicating that this effect can be further reduced by using higher width to height ratio (i.e. increasing W / H ratio). In any case, the maximum lateral deformation is about 0.15% of the MSE wall height.

For the vertical stresses, Model B showed similar trends and magnitudes for locations close to the chamber walls compared to Model A for line 1. However, Model A better predicted the maximum measured stresses which were recorded at the cells at middle of the wall width closer to the first half of the reinforced zone length (with magnitudes closer to the geostatic stresses). This means that the influence of the chamber walls side friction on the bearing stresses is limited as the measurement location is positioned away from the wall. This also indicates that the deduced eccentricity from the experimental results may be exaggerated by the stress reduction caused by the confinement behind the retained zone and that the stress distribution might be more uniform

than measured. Both models produced similar responses to the experimental observation regarding the stress magnitudes at the cells placed over the poor bearing zone. However, Model A showed about the same magnitude of the redistributed stress to the array of pressure cells in line 2 (observed in the experiment) as a result of the loss of support induced at line 3.

The lateral earth pressure from the numerical simulations using both models were similar in trends and in magnitude. The lateral stresses just behind the facing panels were similar to the active lateral earth pressure. While the lateral stresses from a vertical line, about 1.5 m (0.3 H) behind the facing panels are closer to about 2.5 times the active lateral stresses (i.e. $K_r / K_a = 2.5$. In the design of MSE walls, this factor varies linearly between 2.5 to 1.2 for depths of 0 to 6 m respectively, beyond which it remains at a constant value of 1.2, which has been shown in previous studies (Christopher 1993) to be influenced by compaction effects, and K_a is calculated using friction angle limited to a maximum of 40°. For the wall configuration in this study, the design values vary from 1.67 to 1.34, and perceived higher K_r is likely due to over compaction resulting to locked in stresses.

The reinforcement tensile force from the numerical simulations compared to the deduced values from the reinforcement strain measurements generally showed similar trends, with some measured points significantly higher than the corresponding calculated values from both numerical models (about 40% higher). However, Model A predicted higher tensile loads than Model B especially for reinforcement line 1.

5.7 Summary

This chapter extends the experimental observations by employing 3D numerical modeling to investigate the performance of the MSE system under conditions of poor foundation support,

differential settlement, and surcharge loading. The numerical approach allows exploration of the influence of the experimental constraint on the measured responses.

The model was developed using Plaxis-3D, employing 10-node tetrahedral elements for soil volumes and 6-node triangular elements for plate elements. Soil-structure interactions were modeled with zero-thickness interface elements to simulate slipping at various interfaces.

Calibration of material properties was successfully completed, matching the stress-strain behavior from laboratory tests with the numerical model's output. The foundation sand and #57 crushed stone were modeled using the Hardening Soil model, while steel reinforcement was modeled with an elastic plate model.

Two models were developed: Model A (without chamber sidewalls) and Model B (with chamber sidewalls). This was done to evaluate the influence of the confining walls on the observed responses from the experimental study. To follow the steps executed in the experiment, the construction sequence was replicated numerically, including fill placement, compaction, and subsequent load applications. The results from the numerical study are summarized as follows:

- Settlement: Both models showed similar settlement profiles, for the measurement position directly above the soft zone, Model A showed a settlement magnitude of 98 mm while Model B showed 99 mm compared to the measured value of 97 mm.
- Lateral Displacement: Similar to observations in the experiment, Model B did not show significant lateral displacement at the measurement locations (which were close to the chamber sidewalls), highlighting the influence of sidewall friction on lateral displacement measurements near the confining sidewalls. Model A, however, showed higher lateral displacements.

- Foundation Bearing Stress: The calculated stresses from Model B were closer to the measured values near the chamber sidewalls while Model A sufficiently predicted the maximum measured stresses.
- Reinforcement Load: Both models showed similar trends to experimental data, however regarding the tensile loads in the steel strips, some measured values were higher than the calculated values from both models. For reinforcement line 1, Model A generally predicted higher reinforcement loads.
- Numerical results for lateral stresses at the back of the facing panels were consistent with classical lateral earth pressure theory.
- Shear strain results from both models showed that the system stayed primarily elastic through all simulated stages, confirming the experimental observations that the wall remained stable, even with an inclusion of a soft bearing zone, partial loss of foundation bearing support and the consequent differential settlement.
- The inclusion of chamber walls (as illustrated in Model B) affected the experimental response due to increased frictional resistance, highlighting the significance of boundary effects. Both models confirmed the stability of the MSE wall under differential settlement.

Physical and experimental testing of geotechnical systems are crucial in understanding the mechanical behavior of these systems and are critical in validating numerical approaches. However, there are unavoidable constraints that impact the measured responses. The chamber side wall friction has been shown to affect the wall response in this study. Using a higher width to height ratio will logically minimize this influence but can be rather expensive or just fixed, as was the case in this study. A plastic sheet was used to cover the chamber side walls in order to reduce

this effect. It is possible to further reduce these effects by using a more compliant media between the angular backfill and the chamber walls. It is also important to monitor wall response in areas where the effects may be pronounced (close to the sidewalls) as well as further away from the sidewalls in order to evaluate the extent of interference.

Regardless, the experimental results and the numerical approach have provided insights into the behavior of the reinforced soil system, and the validated numerical approach will be used to study other factors that affect the bearing stress distribution at the base of the MSE wall.

CHAPTER 6: BEARING STRESS FUNCTIONS

6.1 Background

Mechanically Stabilized Earth (MSE) walls have been extensively used in various geotechnical applications due to their economic efficiency and versatility in various construction environments. Traditional design methodologies often simplify the complex behaviors of MSE walls by assuming rigid wall behavior and neglecting the interactions between facing panels and backfill materials. However, field observations and experimental studies have increasingly demonstrated that these assumptions can lead to inaccuracies, particularly in predicting bearing stress distributions which are crucial for ensuring the stability and performance of MSE structures.

Stress distributions within MSE structures have been a significant measure of interest. Bastick et al. (1993) and Runser et al. (2001) found that measured foundation bearing stresses were generally equivalent to the geostatic stresses but noted significant effects from wall facing connections and reinforcement arrangements. Liang and Almoh (2004), and Budge (2004) argued for reconsideration of traditional vertical earth pressure distribution functions, such as Meyerhof and Trapezoidal distributions, suggesting that these models do not adequately account for the flexible nature of MSE walls and the complex interactions at the panel-to-backfill interfaces.

Hence, there is a clear need for developing a bearing stress function that better reflects the actual behavior of MSE walls, considering their flexibility and the interactions at the panel-to-backfill interface. This chapter addresses this need by:

- Alternative Functions: Presenting alternative bearing stress functions considering flexibility and panel-to-backfill interface effects.

- Sensitivity Study: Conducting a comprehensive parametric study to investigate the influence of key factors such as wall height, reinforcement type and stiffness, backfill properties, and surcharge loads on the stress distribution.
- Function Refinement: Refine the alternative bearing stress functions if needed, based on insights gained from the numerical simulations, incorporating wall flexibility and panel-to-backfill interface effects.
- Comparison and Validation: Comparing the newly developed function with existing bearing stress functions (i.e. Meyerhof) and validating its efficiency and accuracy against numerical simulation results.
- Recommend an appropriate function for bearing stress at the base of typical MSE walls.

6.2 Alternative Bearing Stress Functions

Liang and Almoh (2004) expressly called for reconsideration of traditional vertical earth pressure distribution functions to account for the flexible nature of MSE walls and the complex interactions at the panel-to-backfill interfaces amongst other factors. The current design guidelines by the FHWA use the Meyerhof approach which exaggerates the design stresses due to the limited length used in the distribution, i.e., accounting for eccentricity due to overturning from the retained backfill. The problem with this approach is the assumption that the reinforced mass is a rigid block which is fundamental as it was originally developed using a metal plate footing model on sand (Meyerhof 1953), with the plate stiffness orders of magnitudes greater than the stiffness of the foundation sand.

Obviously, this assumption does not apply to MSE systems. It is unlikely external overturning force from the retained backfill is transmitted through the reinforced mass, and as

such, the bearing stress function should be reconsidered without the overturning effect (limiting eccentricity) that would otherwise apply to rigid structures.

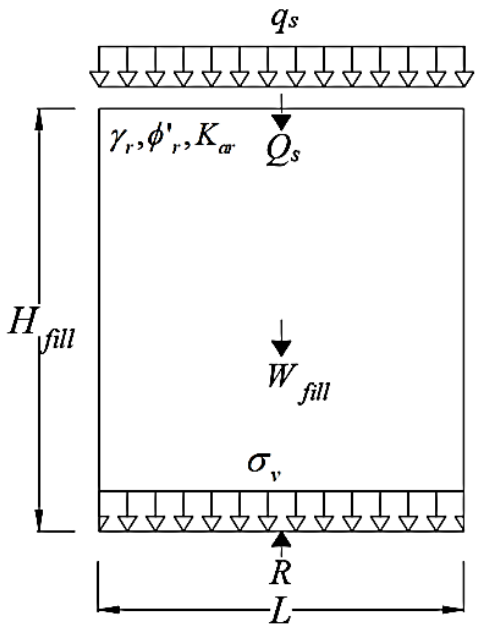

Figure 117. Nominal earth pressures; horizontal backslope with traffic surcharge, ignoring overturning forces.

Figure 117 shows stresses for a typical MSE structure with horizontal backslope, and traffic surcharge, when overturning from the retained fill is ignored. For this case, the bearing stress is simply the summation of the geostatic stresses and the traffic surcharge as formulated in equation 57 through 60:

$$\sum Fy = 0 \tag{57}$$

$$R - Q_s - W_{fill} = 0 \tag{58}$$

$$R = Q_s + W_{fill} \tag{59}$$

$$\sigma_v = \frac{R}{L} = \frac{W_{fill} + qL}{L} \tag{60}$$

where R is the resultant force, W_{fill} is the weight of the reinforced fill, Q_s is the force from the surcharge stress, q, and L is the length of the reinforced zone.

If the traffic surcharge is not considered, then equation 60 reduces to $\sigma_v = \frac{W_{fill}}{L}$ which is just the self-weight of the reinforced mass (i.e. $\sigma_v = \gamma H_{fill}$) which is consistent with the findings in the experiment in this study. Some studies in such cases, have reported higher stresses than the geostatic stresses at some distance behind the facing panel (Liang and Almoh 2004, Budge 2004, and Runser et al. 2001, Christopher 1993), however, the overturning effect still does not account for the stress increase as stated by Liang and Almoh (2004), and Budge (2004). Moreso, it does not account for the lower stresses observed at other points along the base of the wall. Equation 60 is also justified by the fact that in some cases, such as in this study and the study conducted by Murray and Furrar (1990), the foundation stress never exceeded the geostatic stresses.

A significant reduction in the stresses just behind the facing panels has also been reported in many of these cases (Liang and Almoh 2004, Budge 2004, Runser et al. 2001, Christopher 1993, and Murray and Furrar 1990). Christopher 1993 attributed this to the stress transfer from the reinforced soil to the facing panels resulting in downdrag forces. This adds to Liang and Almoh (2004) call to account for the influence of dissimilar zones (reinforced zone-facing panel interface, and reinforced zone to retained zone interface) on the bearing stress function. To account for this, a vertical component of the lateral stress (P_v in Figure 118) is considered a as presented in equation 61 through 63. It is worth noting that the reduced stress is limited to a certain distance from the back of the facing panel, hence, equation 63 may not apply uniformly all through the base of the reinforced wall. It is also possible that the interaction between the steel strips, backfill and facing

panels contribute to stress reduction as there exists a concentration of higher stress above, and lower stress below each reinforcement-facing panel connection.

$$P_a = K_a\left(\frac{\gamma_r H_{fill}}{2} + q_s H_{fill}\right) \tag{61}$$

for walls without surcharge, $q_s = 0$

$$P_v = P_a \tan\delta_i \tag{62}$$

$$\sigma_v = \frac{R - P_v}{L} = \frac{W_{fill} + qL - P_v}{L} \tag{63}$$

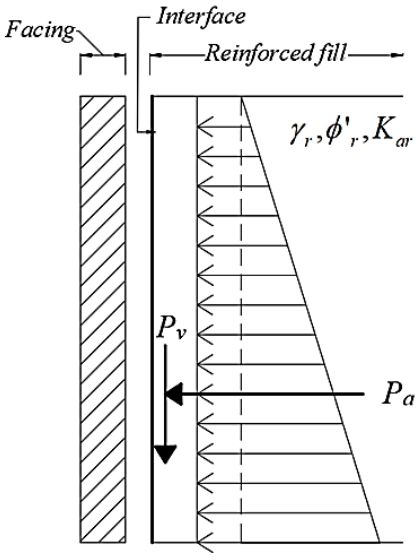

Figure 118. Reinforced fill-facing panel stress transfer mechanism.

6.3 Sensitivity Study

It is obvious that there is a lot of variability in the measured foundation stresses. This could be as a result of various factors as already discussed. It is also important to note that installation method and earth pressure cell type can affect the measured stresses due to the obvious stiffness incompatibility, non-compliance of the pressure cells and thickness of the cells. Hence, a

parametric study was conducted to investigate the influence of various factors on the bearing stress at the base of an MSE wall using the validated numerical modelling approach discussed in Chapter 5.

6.3.1 Finite Element Model Size Optimization

The least calculation runtime for the finite element models developed and analyzed in Chapter 5 was about 28 hours using a windows 10 64-bit computer with 20 cores @ 2.2 GHz each and 16 GB of RAM. This was due to the mesh fineness, chosen constitutive model, and the model dimensions. Both of the first two factors (mesh quality and constitutive model) are of key importance to ensure a properly discretized model and to simulate soil behavior as realistic as possible, respectively, especially with the series of loading and unloading involved in simulating the experimental setup. However, the model dimensions can be further optimized to reduce computing time given the observations from the modelling results, a narrower model would still yield reasonable results and the critical foundation stress distribution is aligned with the reinforcement position along the wall width.

A size optimization sensitivity analysis was performed to ensure that numerical response is similar for similarly configured models with varying model width (W_{model}). Three models were analyzed for this purpose namely Model C ($W_{model} = 3m$), Model D ($W_{model} = 1.5m$) and Model E ($W_{model} = 1.5m$) as shown in Figure 119 a, b and c respectively. Model C consisted of two panels width with four columns of reinforcement, Model D had one panel width with two columns of reinforcement while Model E had one panel width with one column of reinforcement.

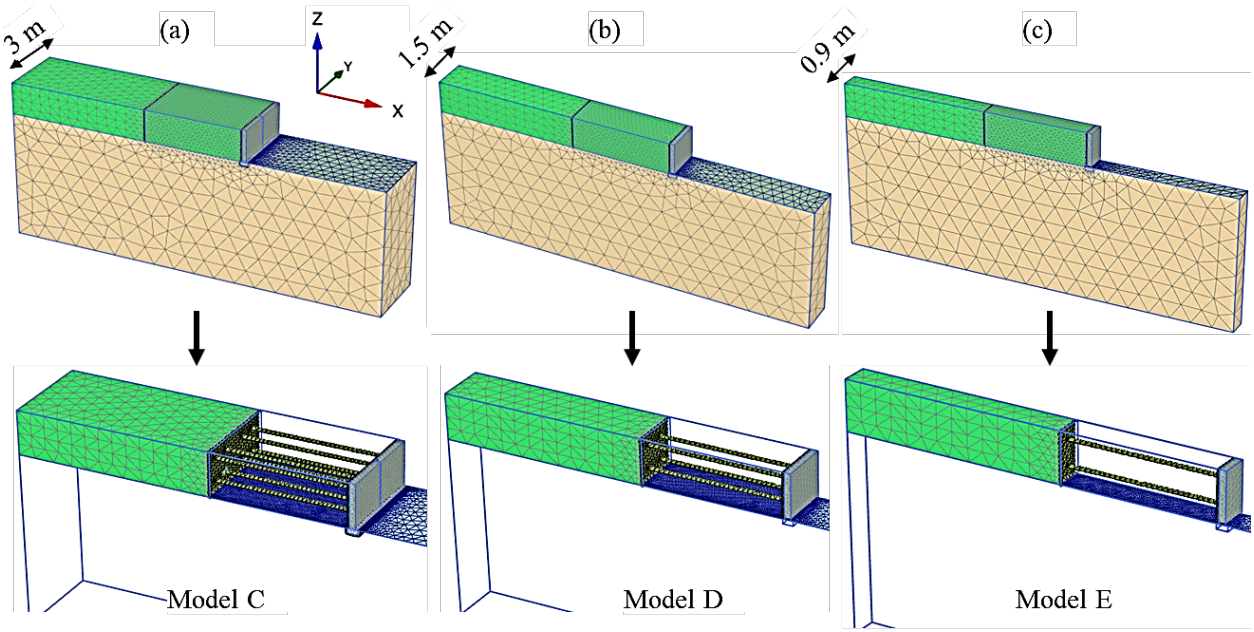

Figure 119. FE model size optimization with model width of 3 m, 1.5 m and 0.9 m for (a) Model C, (b) Model D, and (c) Model E.

The same model input properties from Chapter 5 were used in this exercise as well as the same staged construction. To be more general, a temporary compaction load of 16 kPa was used to simulate compaction to follow similar values used in previous studies (Hatami and Bathurst 2005, Yan et al. 2016) and general field compaction requirements.

The results do not show any notable differences between the models regardless of the model width, this is as expected following the numerical results obtained from Model A as discussed in Chapter 5. Figure 120 shows vertical stress from numerical simulations for Models C, D and E, normalized by the geostatic stress for (a) and (b) without final traffic surcharge, and (c) and (d) with traffic surcharge, and normalized by the summation of the geostatic stress and the traffic surcharge. Figure 120 (a) and (c) were extracted from a line at the foundation located along the reinforcement centerline while (b) and (d) were extracted from a line at the foundation located 380 mm away from the reinforcement centerline. All the results are similar both in magnitudes

and trend indicating that the smaller width (Model E) can be used to obtain reasonably similar results compared to double panel width (Model C), and single panel width (Model D).

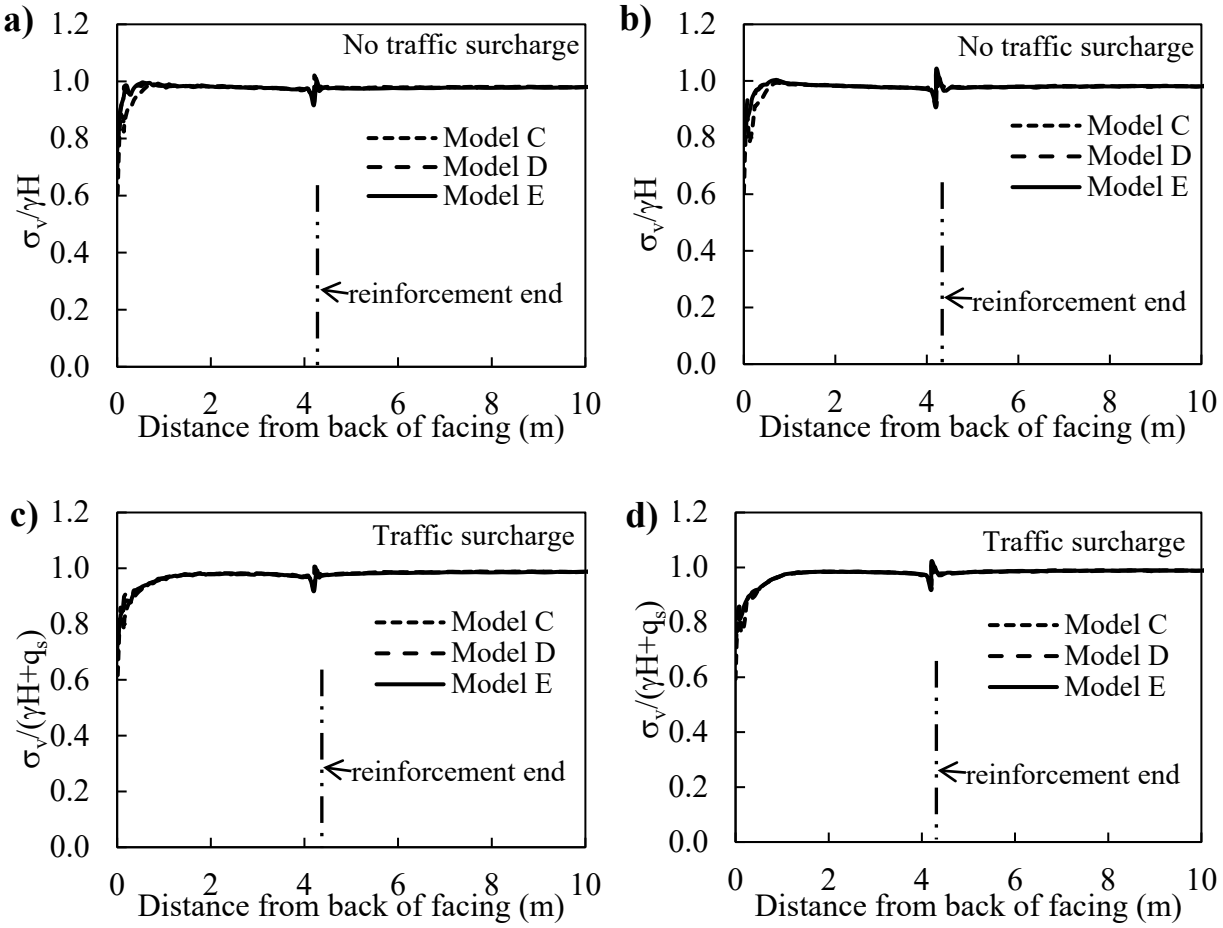

Figure 120. Vertical stress from numerical simulations for Models C, D and E, normalized to the geostatic stress for (a) No traffic surcharge, aligned with reinforcement centerline, (b) No traffic surcharge, 380 mm from reinforcement centerline, (c) Traffic surcharge, aligned with reinforcement centerline, and (d) Traffic surcharge, 380 mm from reinforcement centerline.

Figure 121 shows examples of the lateral deformation 3D plots for (a) Model C, (b) Model D, and (c) Model E. Again, as expected, apart from the width of the models, there is no notable difference in the 3D contour shadings between Model C, Model D, and Model E. This justifies the use of the narrow width model (Model E) in the subsequent sensitivity analyses as the solution of the model takes less time to compute.

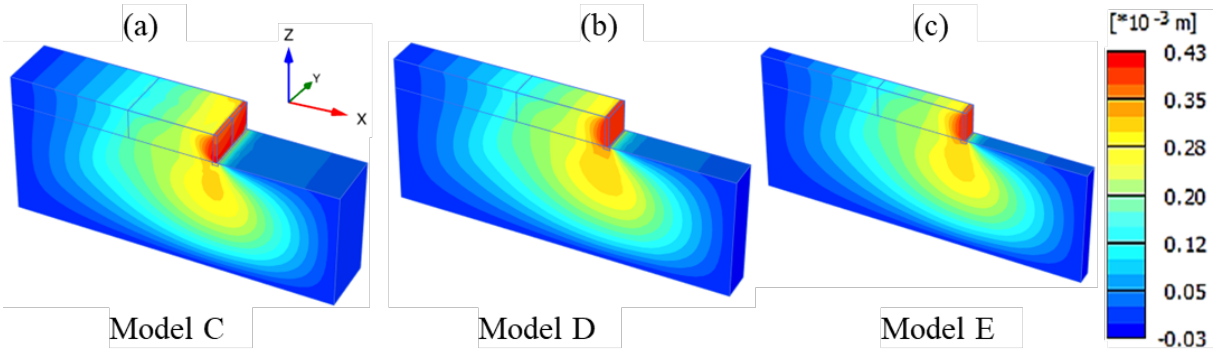

Figure 121. Lateral deformation 3D plots for (a) Model C, (b) Model D, and (c) Model E.

6.3.2 Parametric Study

A parametric study was conducted to investigate the influence of various factors on the bearing stress distribution at the base of the wall, including model height, reinforcement length, reinforcement stiffness, and various input properties. The results from models with various configurations are compared to a 4.5-m high model used as the base case. Table 10 shows a matrix of the various influencing factors that were analyzed. The same numerical modelling approach was adopted for all the models. The parametric study was designed to investigate the influence of wall height, facing-retained zone interface, reinforcement-soil interface, compaction load, surcharge load, reinforcement stiffness, and reinforcement length on the resulting bearing stress. The model geometry and mesh quality check are shown in Figure 122.

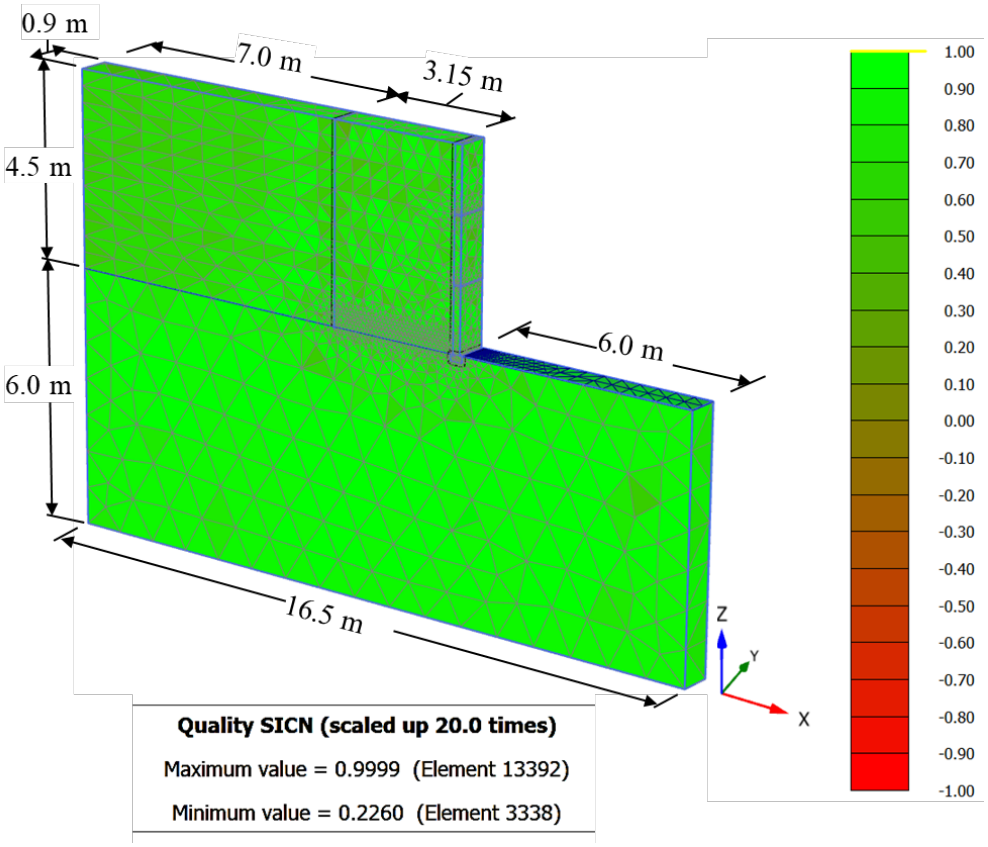

Figure 122. Mesh quality check (SICN) and model dimensions for the base case.

Table 10. Various model features used in the parametric study

Model No.	Height	Soil-facing interface			Soil-reinforcement interface			Compaction load	Reinforced fill		Retained fill		Foundation stiffness	Strip stiffness	Length/Height
		δ_i	R_{inter}	E_i	δ_i	R_{inter}	E_i	q_c	ϕ	E_{50}	ϕ	E_{50}	E_{50}	E	L/H
#	m	°	-	kPa	°	-	kPa	kPa	°	kPa	°	kPa	kPa	x10^6 kPa	-
Base	4.5	30	0.52	9700	48	1	24000	17	48	31000	48	31000	37000	211	0.7
1	**3**	30	0.52	9700	48	1	24000	17	48	31000	48	31000	37000	211	0.7
2	**6**	30	0.52	9700	48	1	24000	17	48	31000	48	31000	37000	211	0.7
3	4.5	**25**	**0.42**	**6300**	48	1	24000	17	48	31000	48	31000	37000	211	0.7
4	4.5	**20**	**0.33**	**3800**	48	1	24000	17	48	31000	48	31000	37000	211	0.7
5	4.5	30	0.52	9700	**40**	**0.75**	**20500**	17	48	31000	48	31000	37000	211	0.7
6	4.5	30	0.52	9700	**35**	**0.63**	**14300**	17	48	31000	48	31000	37000	211	0.7
7	4.5	30	0.52	9700	**30**	**0.52**	**9700**	17	48	31000	48	31000	37000	211	0.7
8	4.5	30	0.52	9700	**25**	**0.42**	**4900**	17	48	31000	48	31000	37000	211	0.7
9	4.5	30	0.52	9700	48	1	24000	**43**	48	31000	48	31000	37000	211	0.7
10	4.5	30	0.52	9700	48	1	24000	**35**	48	31000	48	31000	37000	211	0.7
11	4.5	30	0.52	9700	48	1	24000	**8.5**	48	31000	48	31000	37000	211	0.7
12	4.5	30	0.52	9700	48	1	24000	**0**	48	31000	48	31000	37000	211	0.7
13	4.5	30	0.52	9700	**40**	1	24000	17	**40**	31000	**40**	31000	37000	211	0.7
14	4.5	30	0.52	9700	**30**	1	24000	17	**30**	31000	**30**	31000	37000	211	0.7
15	4.5	30	0.52	9700	48	1	**15500**	17	48	**15500**	48	**15500**	37000	211	0.7
16	4.5	30	0.52	9700	48	1	**46500**	17	48	**46500**	48	**46500**	37000	211	0.7
17	4.5	30	0.52	9700	48	1	24000	17	48	31000	**40**	31000	37000	211	0.7
18	4.5	30	0.52	9700	48	1	24000	17	48	31000	**30**	31000	37000	211	0.7
19	4.5	30	0.52	9718	48	1	24000	17	48	31000	48	**15500**	37000	211	0.7
20	4.5	30	0.52	9700	48	1	24000	17	48	31000	48	**46500**	37000	211	0.7
21	4.5	30	0.52	9700	48	1	24000	17	48	31000	48	31000	**18500**	211	0.7
22	4.5	30	0.52	9700	48	1	24000	17	48	31000	48	31000	**9250**	211	0.7
23	4.5	30	0.52	9700	48	1	24000	17	48	31000	48	31000	**4600**	211	0.7
24	4.5	30	0.52	9700	**29**	**0.50**	**9100**	17	48	31000	48	31000	37000	**5**	0.7
25	4.5	30	0.52	9700	**29**	**0.50**	**9100**	17	48	31000	48	31000	37000	**0.5**	0.7
26	4.5	30	0.52	9700	48	1	24000	17	48	31000	48	31000	37000	211	**1**
27	4.5	30	0.52	9700	48	1	24000	17	48	31000	48	31000	37000	211	**0.5**

The fonts in bold indicate properties for FE models other than the base case.
Base case is the first entry in the table.
The yellow-filled cells are cases where the retained-reinforced zone interface properties were adjusted according to the properties of the retained zones.
The green-filled cells are cases the soil-reinforcement interface properties were consequently adjusted according to the reinforcement type.

6.4 Results from Sensitivity Study

6.4.1 Wall Height

Figure 123 presents the foundation vertical stress distribution for models with various MSE wall heights. The base case was 4.5 m high, case 1, and 2, had heights of 3 m, and 6 m, respectively. A length-to-height ratio of 0.7 was maintained for these cases The vertical axis in Figure 123 is normalized by the wall self-weight while the horizontal axis is normalized to the length of the reinforced zone. This was done to have a normalized comparison of the results from each model due to the varying height and the consequent varying length of the reinforced zone. The results reveal stress reduction very close to the back of the facing panels over a very short length (about 0.2L for case 1, 0.1L for the base case, and 0.09L for case 2,). The stress reduction is likely due to the stress transfer from the reinforced fill to the facing panel (which is further discussed later). The implication is that the higher the wall, the shorter the zone of the reduced stresses. It is also possible that at a certain height, the retained backfill active pressure from the retained backfill becomes transmitted through the reinforced fill. A similar behavior is observed close to the interface between the reinforced fill and the retained fill. The stress transfer causes a stress reduction within the reinforced zone and a stress increase within the retained zone. The properties of the retained soil in these cases were the same as that of the reinforced fill. It is unclear at this time, how changes in the retained fill properties affects the resulting stresses, however, so far, the maximum stresses observed in the given distributions are closer to the geostatic stress which would be equivalent to equation 60 disregarding overturning effects.

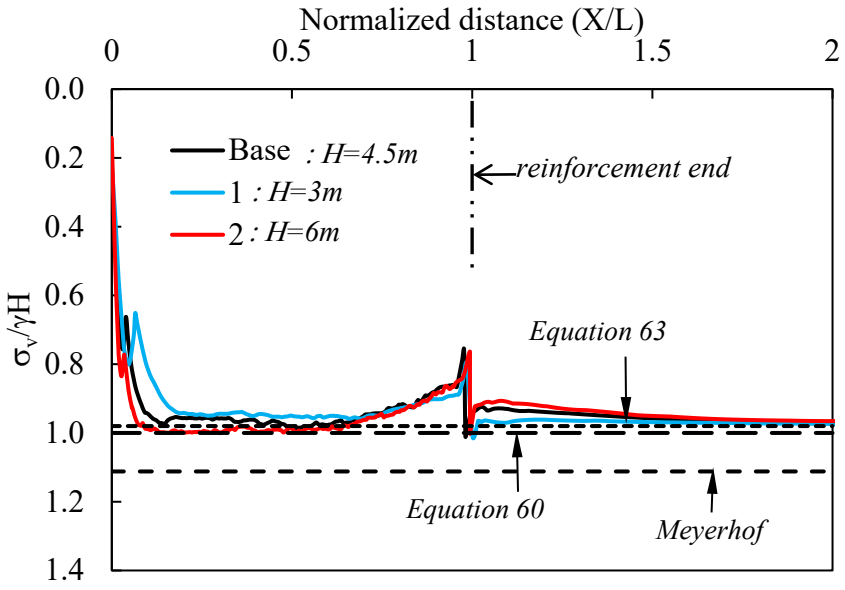

Figure 123. Foundation stress distribution for FE models with various wall heights

6.4.2 Facing-Retained Zone Interface

Figure 124 presents the foundation stress distribution for FE models with various facing-to-reinforced zone interface friction. The base case interface friction was 30°, case 3, and 4, had interface friction of 25° and 20°, respectively. A length-to-height ratio of 0.7 was also maintained for these cases. Similarly, the vertical axis in Figure 124 is normalized by the wall self-weight while the horizontal axis is normalized to the length of the reinforced zone. Also shown in Figure 124 are the resulting stresses from a typical Meyerhof distribution. The facing-retained fill interface friction affects the stress distribution specifically for the zone right behind the facing panels. The results show a stress reduction zone very close to the back of the facing panels over a very short length (about 0.1L for the base case and case 3, and 0.08 for case 4). Clearly, the stress reduction reduces as the interface friction reduces. Alongside this reduction, is a notable increase in the stress magnitude which increases as the interface friction reduces. On a first glance, it seems reasonable to attribute this to overturning moments and eccentricity, however, as shown in Figure

124, the Meyerhof approach did not predict any of the cases considered with any reasonable accuracy. If this was truly as a result of overturning, then it follows that the Meyerhof approach should account for the increase, which it clearly does not.

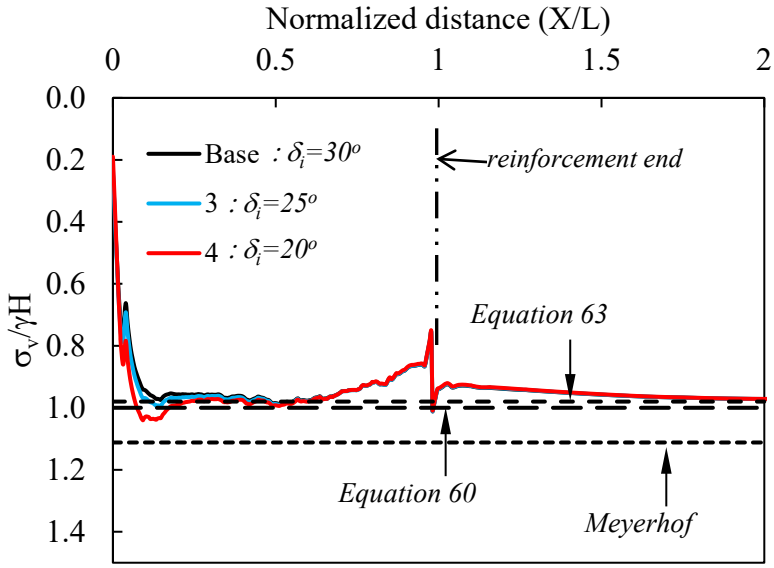

Figure 124. Foundation stresses distribution for FE models with various facing-to-reinforced zone interface friction.

6.8.3 Reinforcement-Soil Interface

Figure 125 shows the foundation vertical stress distribution for models with various soil-reinforcement interface friction. A fully bound soil-reinforcement interface was used for the base case with a friction angle of 48°, which was then reduced to 40°, 35°, 30°, and 25° (i.e. cases 5, 6, 7, and 8) to investigate the influence of the soil-reinforcement interface strength on the foundation stress distribution. The results do not show any delineable difference in the maximum calculated stresses, however, as the interface friction was reduced, the stress magnitude just behind the facing panels (about 0.1L from the back of the facing) significantly reduced. This is due to the additional deformation associated with each reduction of soil-reinforcement interface strength, resulting in

stress release within the zone 0.1L from the facing panels. Ultimately, the stress distributions are closer to equations 60 and 63 and notably lower than the Meyerhof distribution.

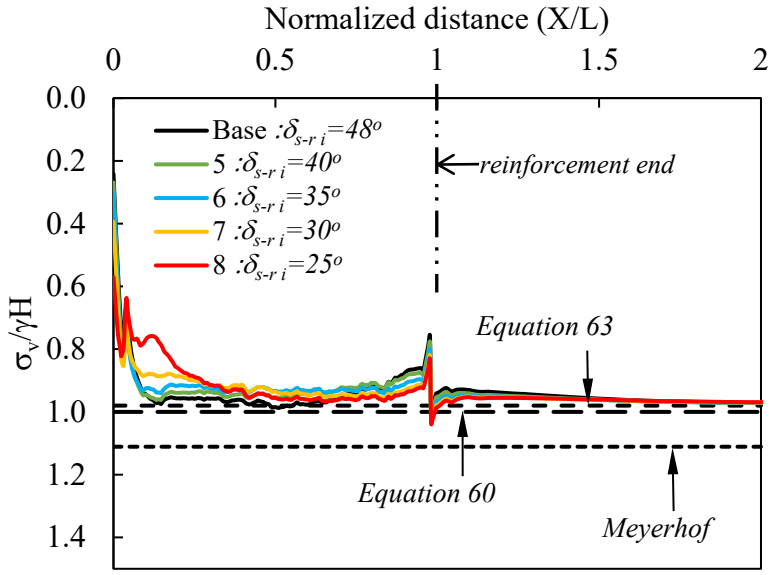

Figure 125. Foundation stress distribution with various soil-reinforcement interface friction.

6.8.4 Compaction Load

Figure 126 shows the foundation vertical stress distribution for models with various compaction loads. A temporary compaction load is placed after each fill which is then removed before the next fill is placed. The base case was simulated with a compaction load of 17 kPa, which was then changed to 43 kPa, 35 kPa, 8.5 kPa, and 0 kPa (i.e. cases 9, 10, 11, and 12 respectively) to represent various compaction efforts. The general trend, as presented in Figure 126, shows a subtle increase in the foundation stress as the compaction load increased. There was very little difference in the results between a compaction load of 43 kPa and 35 kPa. The same is observed for models with compaction load of 8.5 kPa and the base case with a compaction load of 17 kPa. This general trend of increasing stress magnitude with increasing compaction loads shows that higher compaction efforts increase the stiffness of the reinforced soil composite. However, the

perceived stiffness increase does not amount to a rigid composite and the obtained stress distributions are closer to equations 60 and 63 and significantly less than the Meyerhof approach.

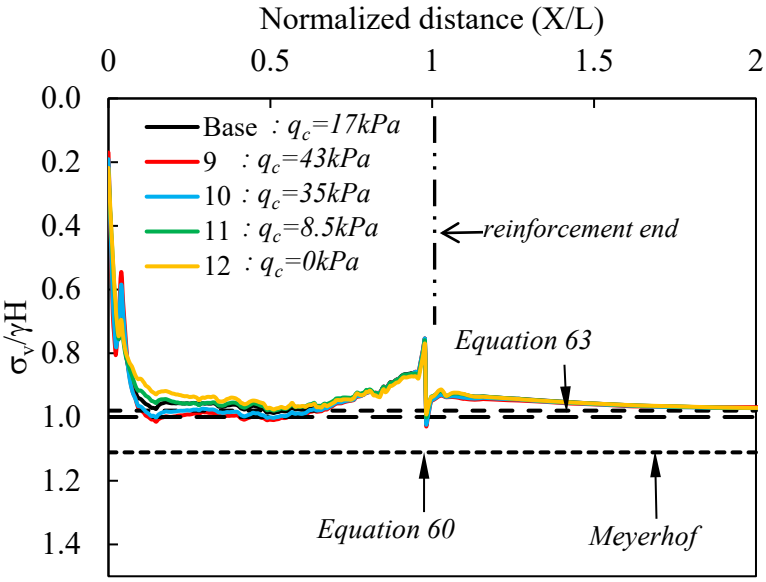

Figure 126. Foundation stress distribution with various compaction load magnitudes.

6.8.5 Reinforced Fill Properties

Figure 127 shows the foundation vertical stress distribution for models with various friction angles for the fill material. Figure 127a shows results for the base case (with friction angle of 48°) versus a case with a 40° friction angle (case 13), while Figure 127b shows results for the base case versus a case with a 30° friction angle (case 14), which is the minimum friction angle for select backfill materials. The respective maximum foundation stresses from the presented equations and the Meyerhof approach are also shown for a friction angle of 40° and 30° on Figure 127a and Figure 127b respectively. The results do not show any difference when the friction angle was reduced from 48° to 40°, while there was a slight increase (about 5%) when the friction angle was reduced to 30°, with the maximum calculated stresses in all three cases similar to equations 60 and 63, and well below the respective maximum stresses predicted by the Meyerhof expressions.

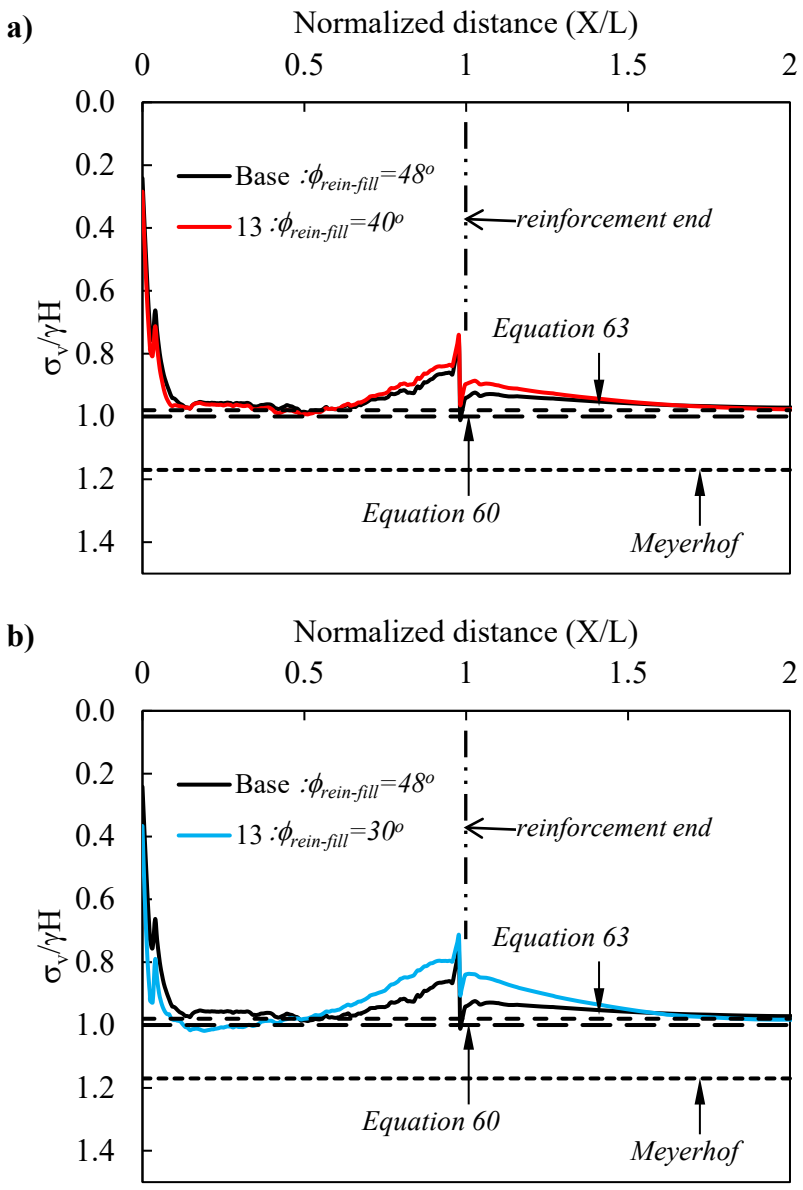

Figure 127. Foundation stress distribution with reinforced fill friction angle (a) $\phi_{rein-fill}$ = 48° vs 40° and (b) $\phi_{rein-fill}$ = 48° vs 30°

Figure 128 shows the foundation vertical stress distribution for models with various fill material elastic modulus. The base case was simulated with a value of 31000 kPa as obtained from laboratory tests and was then increased to 466500 kPa to simulate a stiffer fill material in case 15, and 15500 kPa to simulate a softer fill material (case 16). The results show a gradual increase in

the foundation stress as the fill stiffness was increased but the obtained stresses are closer to equations 60 and 63 and also significantly lower than the prediction from the Meyerhof approach.

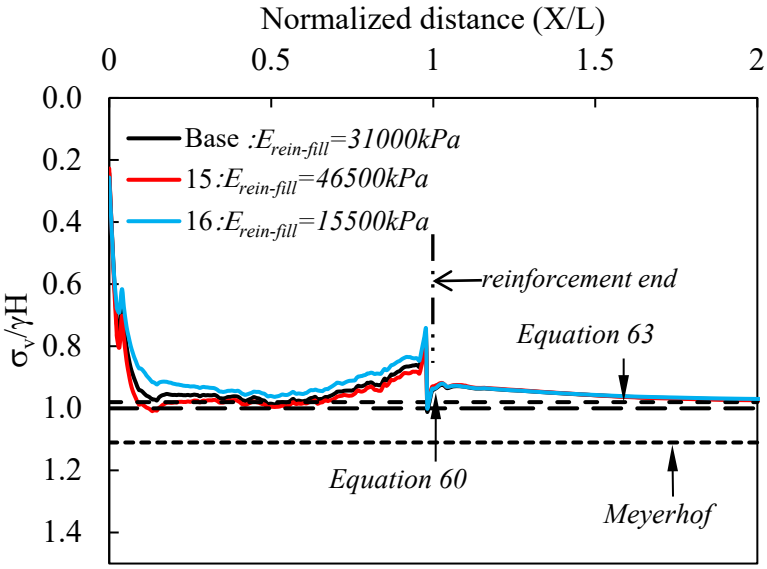

Figure 128. Foundation stress distribution with various reinforced fill stiffness.

6.8.6 Retained Fill Properties

Figure 129 examines the impact of varying friction angles in the retained fill on the distribution of the foundation vertical stress. This was done to understand how different properties of the retained zone affect the reinforced mass and the resulting stresses. Figure 129a shows results for the base case (with friction angle of 48°) versus a case with a 40° friction angle (case 17), while Figure 129b shows results for the base case versus a case with a 30° friction angle (case 18). The respective maximum foundation stresses from the presented equations and the Meyerhof approach are also shown for a friction angle of 40° and 30° on Figure 129a and Figure 129b respectively. The stress magnitude as given by the Meyerhof expressions increases as the friction angle of the retained fill decreases. This is because the coefficient of active lateral pressure in the retained fill increases, thereby increasing the lateral stress magnitude, which increases the eccentricity and

thus, the magnitude of the bearing stress is increased. However, this was not observed, and the results do not show any difference when the friction angle was reduced from 48° to 40°, while there was a slight increase (only about 1.2%) when the friction angle was reduced to 30°. The maximum calculated stresses in all three cases are similar to equations 60 and 63 and remain well below the respective maximum stresses predicted by the Meyerhof expressions.

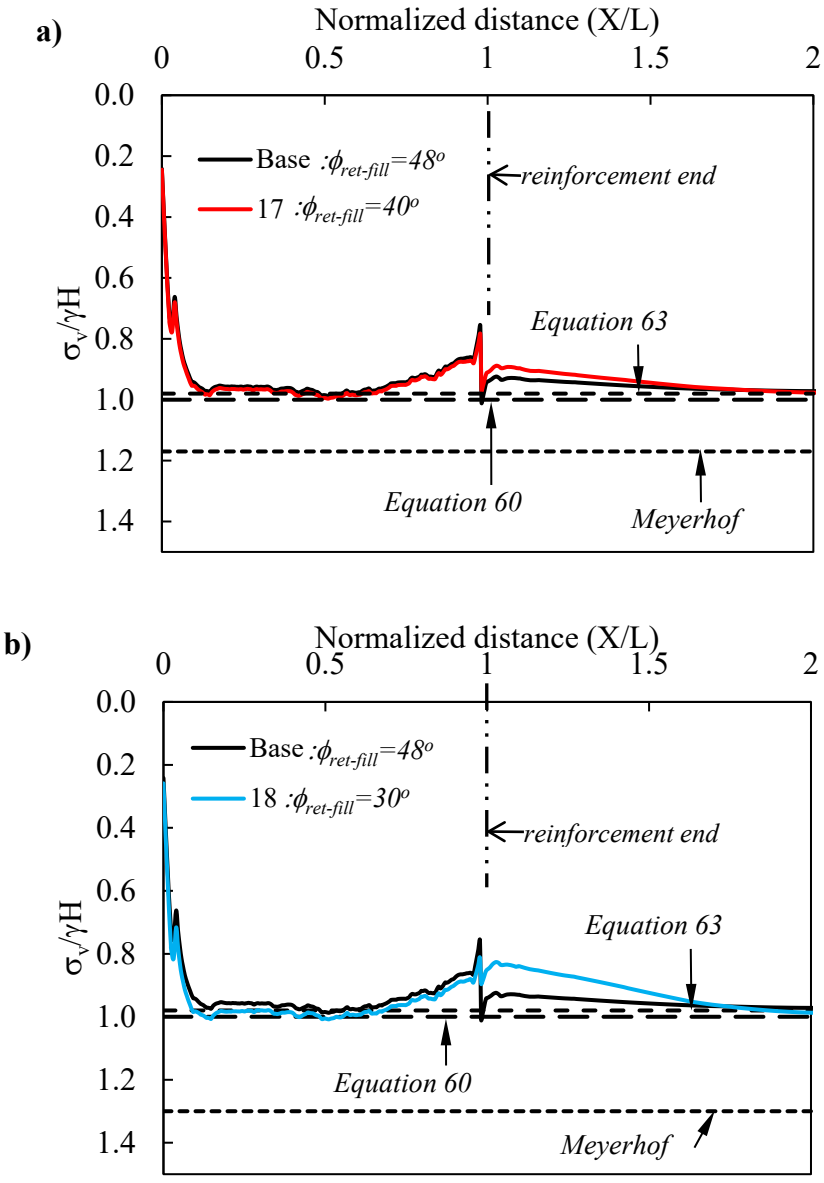

Figure 129. Foundation stress distribution with retained-fill friction angle (a) $\phi_{ret\text{-}fill}$ = 48° vs 40° and (b) $\phi_{ret\text{-}fill}$ = 48° vs 30°

Figure 130 shows the foundation vertical stress distribution for models with various elastic moduli for the retained material. The base case was simulated with a value of 31000 kPa, which was then decreased to 15500 kPa and 7550 kPa for cases 19 and 20 respectively to simulate progressively softer and more compressive retained material. The results do not show any clear difference in the maximum foundation stresses as the retained fill stiffness was varied and the obtained stresses are closer to equations 60 and 63 and also significantly lower than the prediction from the Meyerhof approach.

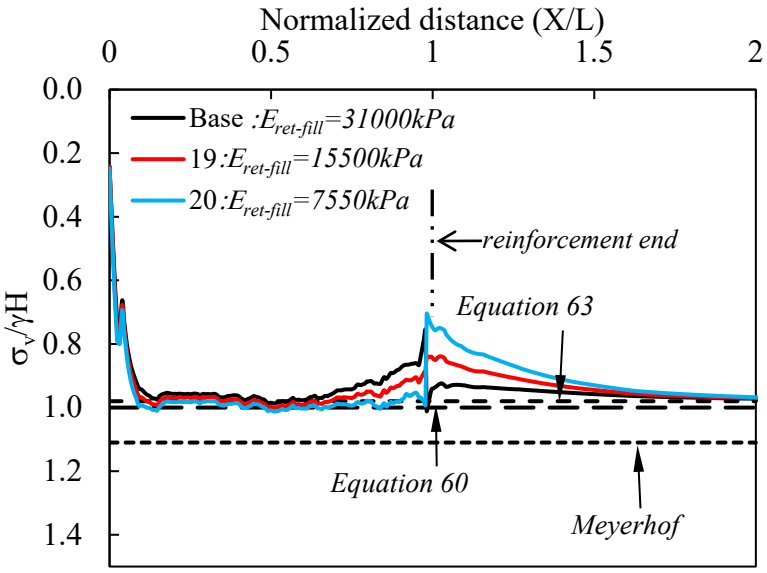

Figure 130. Foundation stress distribution with various retained-fill stiffness

6.8.7 Foundation Fill Properties

Figure 131 shows the foundation vertical stress distribution for models with various elastic moduli for the foundation fill material. The base case was simulated with a value of 37000 kPa and was then decreased to 18500 kPa, 9250 kPa, and 4625 kPa for cases 21, 22 and 23 respectively to simulate progressively more compressive foundation. The friction angle of the foundation was left unchanged and only the various elastic moduli were varied. The results also do not show any

clear difference in the maximum foundation stresses as foundation was made more compressible and the obtained stresses are closer to equations 60 and 63 and significantly lower than the prediction from the Meyerhof approach.

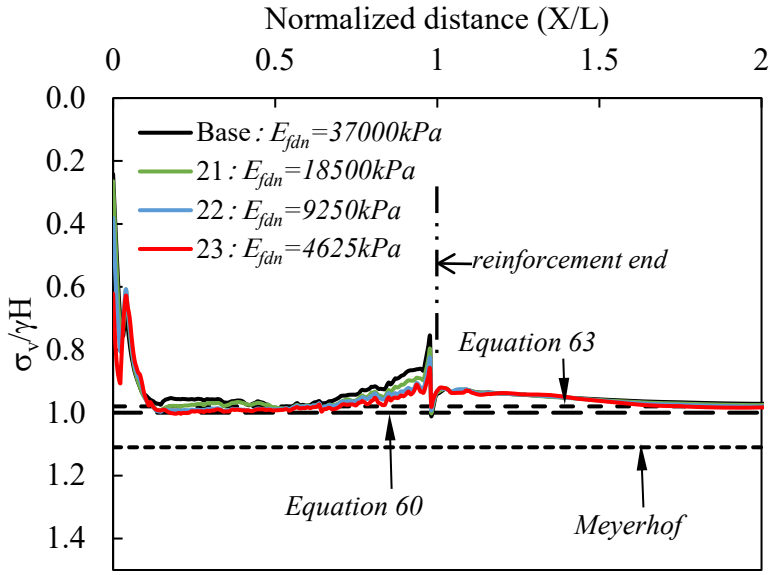

Figure 131. Foundation stress distribution with various foundation-fill stiffness.

6.8.8 Reinforcement Stiffness

Figure 132 shows the foundation vertical stress distribution for models with strip reinforcement stiffness to represent various reinforcement flexibility. The base case was simulated with a value of 211×10^6 kPa following laboratory tensile tests and was then decreased to 5×10^6 kPa (case 24) and 0.5×10^6 kPa (case 25) following Damians et al. (2021) for polymeric straps. The results do not show any delineable difference in the maximum calculated stresses, however, as the reinforcement stiffness was reduced, the stress magnitude just behind the facing panels (about 0.1L from the back of the facing) significantly reduced. This is due to the additional deformation associated with the increasing reinforcement flexibility and the consequent reduction of soil-reinforcement interface strength, resulting in stress release within the zone 0.1L from the facing

panels. Ultimately, the stress distributions are closer to equations 60 and 63 and still lower than the Meyerhof prediction.

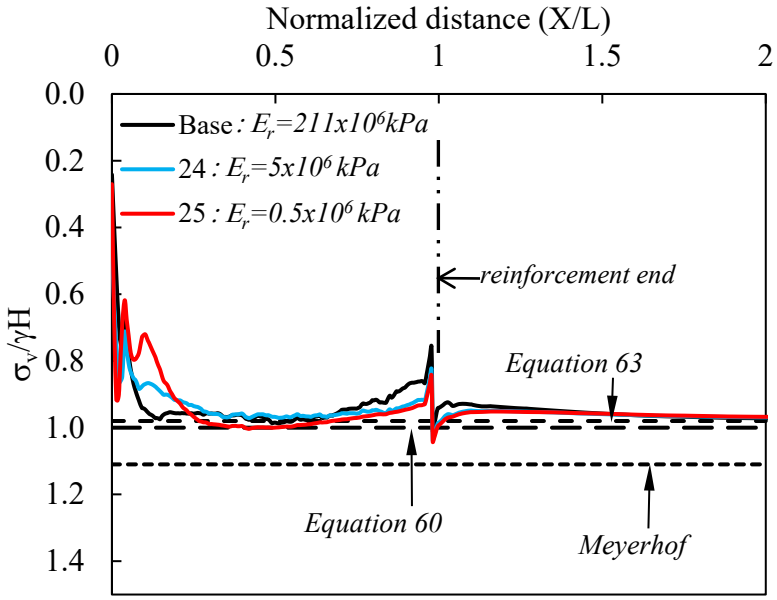

Figure 132. Foundation stress distribution with various strip reinforcement stiffness.

6.8.9 Reinforcement Length

This section presents the results for various reinforced length-to-wall height ratios. The base case (Figure 134) was simulated using a length-height ratio of 0.7, Figure 133 shows the stress distributions for a reinforced length to wall height ratio of 0.5, while Figure 135 shows that of a length to height ratio of 1.0. The Meyerhof approach indicates that increasing the reinforcement length reduces foundation vertical stress magnitude due to the increased distribution length and the reduced eccentricity. Different reinforced zone lengths used in the simulations did not lead to any major differences in the resulting stresses, in all three cases, the Meyerhof approach overpredicted the stresses by as much as 24% for the case where L/H = 0.5, and by 5% for the case where L/H = 1.0.

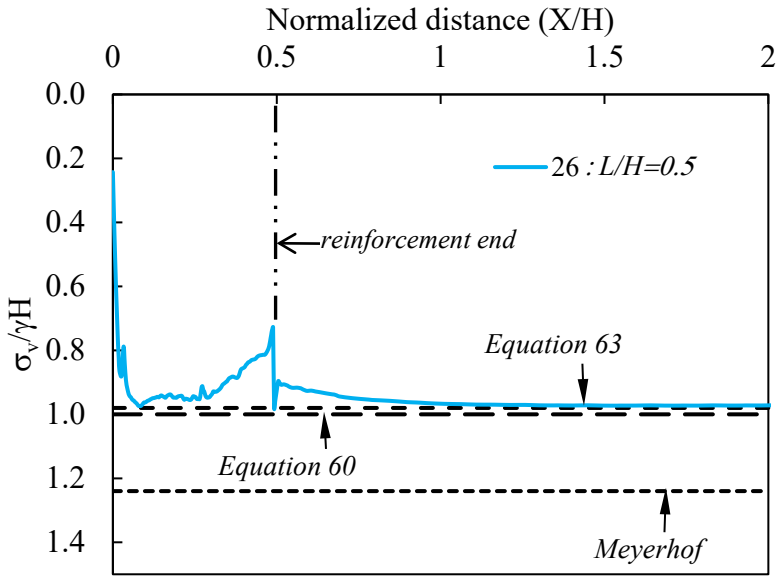

Figure 133. Foundation stress distribution with length to height ratio of 0.5.

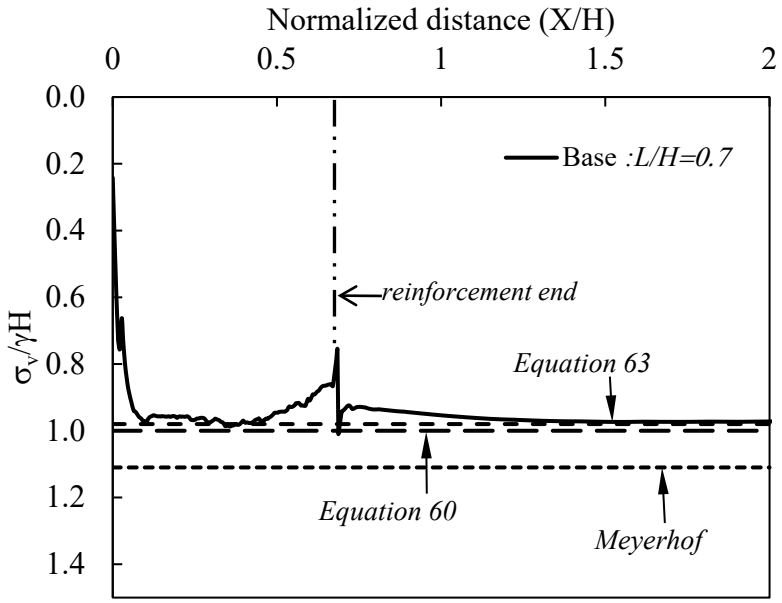

Figure 134. Foundation stress distribution with length to height ratio of 0.7.

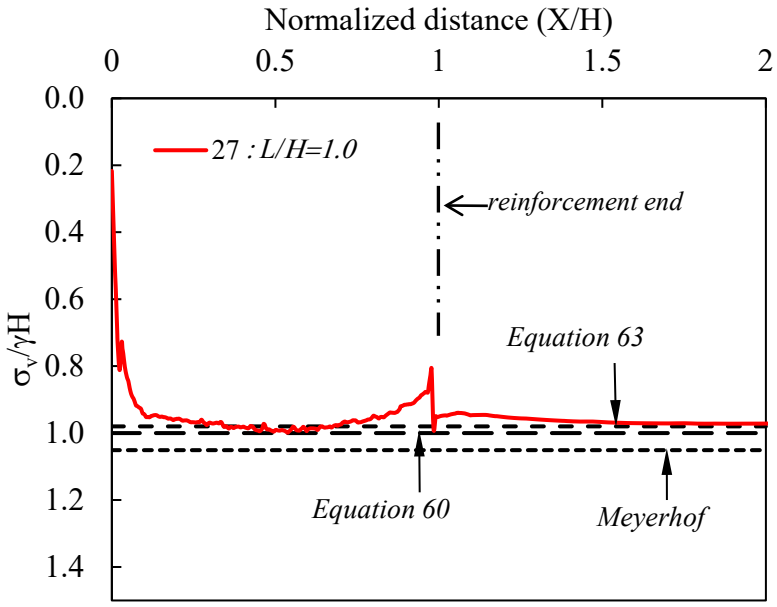

Figure 135. Foundation stress distribution with length to height ratio of 1.0.

6.5 Discussion

Various studies have pointed out that the Meyerhof approach to foundation design stresses for the MSE structure tends to overestimate the stresses. Studies that have compared measured and/or numerically simulated results to values that are used in design have concluded that the methods adopted in the current design procedure just do not sufficiently predict the actual stresses. To address the shortfalls of the equivalent rigid footing methods, two functions were presented that would account for the flexibility of the MSE (equation 60), and the additional facing-to-reinforced fill interface friction (equation 63). The numerical modelling approach developed in Chapter 5 was used to conduct a limited sensitivity analyses to give insight into the various features of an MSE system given in Table 10.

A study using various heights for the MSE structure revealed that the foundation stresses are closer to the geostatic stresses which would agree with equation 63. There seems to be a minor

increase in the stresses as the height increases but not so much as to be accounted for by a rigid approximation.

A study on the effect of the facing-retained zone interface revealed a decrease in the amount of stress transferred to the facing, especially for an interface friction angle of 20^{o}. This resulted in an increase in the maximum bearing stress which could not be accounted for by any of the methods. However, the change was only about 4% of the maximum bearing stress value.

Simulations conducted with various soil-reinforcement interface strength showed similar behavior with those conducted with various reinforcement stiffness where a decrease in the soil-reinforcement interface strength as well as a decrease in the reinforcement strength resulted in a decreased stress magnitude only within 0.1L behind the facing panels due to the stress relief accompanying the consequent additional deformation. The temporary compaction load magnitude did not have any profound influence on the resulting bearing stress, however, a general trend of minor increase in vertical stress with increasing compaction load was noticed. This was also the case when the stiffness of the reinforced fill was varied. Varying the stiffness of the retained fill and the foundation fill did not seem to influence the obtained stress distributions. Similarly, reducing the friction angle of the retained fill did not increase the stress in any major way, in contrast with the prediction from the Meyerhof approach where a lower retained fill friction angle leads to higher lateral stresses to be supported thereby increasing eccentricity and vertical stress magnitude. This indicates that for the cases studied so far, the stresses from the retained fill actually are not transferred through the reinforced mass to the foundation, further weakening the case for an eccentrically loaded rigid footing assumption.

Figure 136 shows maximum vertical stress comparison using the two presented functions (1-equation 60, 2-equation 63), the Meyerhof function (equation 28), the numerical results, and

the experimentally measured values. This shows that the Meyerhof approach clearly overestimates the bearing stresses while all other methods produce similar stress magnitude. It is also important to note that using equation 63 did not show any substantial benefit compared to equation 60 for the cases presented here. The differences in the values calculated using both equations is only about 4%.

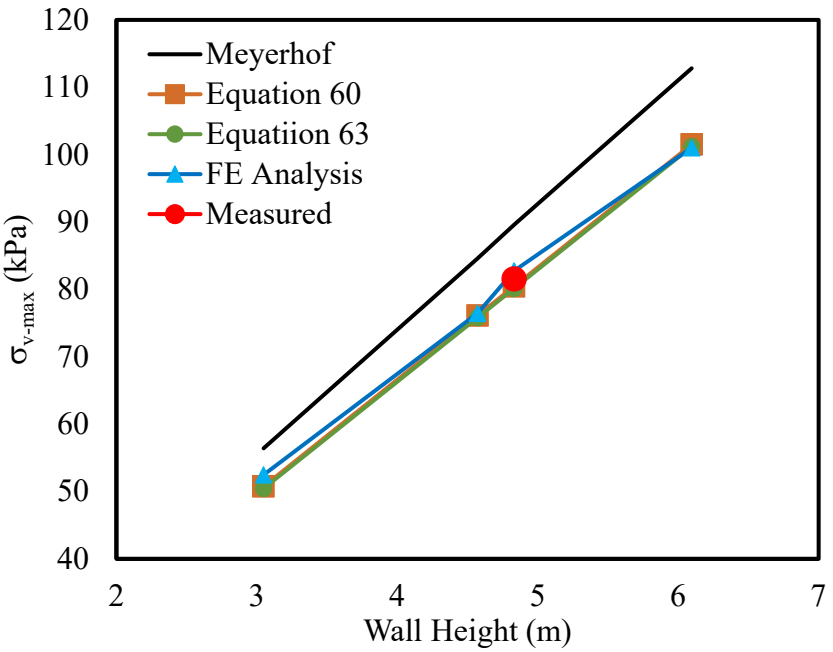

Figure 136. Maximum foundation vertical stress versus wall height showing various methods including measured values and numerical results.

6.6 Summary

Various researchers have noted the significant discrepancy between design stresses estimated using equivalent rigid footing approaches and the actual measured stresses beneath reinforced soil walls with Liang and Almoh (2004) expressly calling for reconsideration of traditional vertical earth pressure distribution functions. Also, experiments and measurement presented so far have shown that the design stresses are too conservative.

The current design guidelines by the FHWA use the Meyerhof approach, which often exaggerates design stresses due to assumptions of rigid behavior. New bearing stress functions that better represent the flexible nature of MSE systems have been presented. The presented functions do not incorporate the overturning forces, focusing instead on the geostatic stresses and traffic surcharge.

A parametric study was then conducted to investigate the influence of various factors on the bearing stress at the base of an MSE wall using a validated numerical modeling approach with the following observations:

- Stress reduction near the back of the facing panels over short distances (0.2L for 3 m height, 0.1L for 4.5 m, and 0.09L for 6 m), which were likely due to stress transfer from the reinforced fill to the facing panel.
- A similar stress transfer mechanism near the interface between the reinforced and retained fill, causing stress reduction within the reinforced zone and stress increase in the retained zone.
- Decrease in interface friction angles from 30°, to 20°, and to 10°, shortens the length of the reduced stress zones near the facing panels from 0.1L to 0.08L, and to 0.01L, respectively
- Lower interface friction also results in higher stress magnitudes. The Meyerhof approach failed to accurately predict these stress distributions, indicating that the observed stress increases are not solely due to overturning moments and eccentricity.
- Reducing the retained fill friction angle did not significantly increase the foundation stress, this is in contrast with the Meyerhof approach's where a lower friction angle would lead to higher lateral stresses, increasing eccentricity and consequently increasing foundation stress magnitude.

- In general, foundation stresses were closer to the geostatic stress, supporting the presented function assuming a flexible reinforced mass.

Higher than geostatic stresses were only observed in extreme cases of weak material, which is not typically encountered. It follows that the Meyerhof approach does not reasonably predict the stresses. Notably, the application of various load factors or resistance factors typically used during design will further exaggerate the design stresses, leading to cases where expensive foundation improvement is then required.

It is therefore recommended that the design stresses be estimated with an upper bound using equation 60, and a lower bound using equation 63 for walls with $H \leq 6m$. Additionally, it is worth noting that using equation 63 did not offer a significant advantage over equation 60 in the cases examined here, with the differences in calculated values between the two equations being approximately 4%.

CHAPTER 7: CONCLUSIONS AND RECOMMENDATIONS

7.1 Summary

The construction of new or expansion of existing roadways often requires establishing grade separation. While sloping is an option, very often, difficult access, limited real estate and limited right-of-way inhibits the use of stable slopes. Earth retention systems (retaining walls) provide the required grade changes within the limited amount of right-of-way. There are several types of retaining walls used in highway infrastructure: concrete cantilever, sheet piling, soil nails, and mechanically stabilized earth (MSE) walls, etc.

MSE type walls are reinforced soil systems that employ a combination of soil and tensile inclusions to improve shear strength, with a host of advantages over traditional reinforced concrete retaining wall systems including significant cost savings, flexibility and high deformation tolerance.

Recently, there have been many recent cases where MSE walls involved significant, costly foundation strengthening to meet bearing capacity requirements. However, the method for estimating design stresses used in the bearing capacity check was never specifically developed for the flexible reinforced soil structures. Full scale testing and numerical simulations were used to study the mechanical behavior of an MSE system. The reinforced soil is a complex system due to the combination of many components with varying degrees of non-linearity, hence, it is difficult to fully address all the contributing factors in one simple expression for the bearing stress.

The objective of this study was to determine the stress distribution at the base of the reinforced mass, and to present a simple alternative function(s) to estimate the foundation bearing stresses in order to minimize the over-conservatism associated with current design methods.

7.2 Conclusions

Two functions are suggested as alternatives to the current design approach. Comparing results from experimental testing, numerical simulations, to the two alternative functions and the current design approach have yielded the following major observations and conclusions:

- The maximum bearing stress for reinforced soil structures could be estimated using:

  1: $\sigma_v = \dfrac{W_{fill} + qL}{L}$

  or

  2: $\sigma_v = \dfrac{W_{fill} + qL - P_v}{L}$ when $H \le 6m$

where:

	W_{fill}	is weight of the MSE reinforced fill
	q	is the traffic surcharge stress
	L	is the width of the MSE reinforced fill
	H	is the height of the MSE reinforced fill
	P_v	is the vertical loading on the facing panels due to friction

- To use the second function, the facing panel-to-backfill interface friction angle (δ_i) must be carefully determined, to avoid over-estimating the shear strength of the interface.
- The Meyerhof approach adopted in the design guidelines for estimating the vertical foundation stress significantly overestimates the bearing stress due to the assumption of a rigid block system.
- The stress distribution beneath the reinforced zone was determined through experimental testing and numerical analyses to be significantly lower than the design estimates and the developed alternative functions (1 and 2) are more reflective of the behavior of the MSE system.

If implemented, this will lead to a more optimal design outcome, and consequent cost savings as expensive foundation strengthening should not be justified based on a bearing capacity check that does not reflect the behavior of the reinforced system. Of course, foundation improvement is always an option if properly justified (based on excessive deformations and/or poor bearing). Note that this study deals with the issue regardless of the design platform used (ASD or LRFD). If the current methods overestimate the stresses, clearly, applying safety factors, or load and resistance factors surely leads to heavily overdesigned systems.

Additionally, the physical testing and numerical analyses conducted in this study informed several observations providing more details on the behavior of the MSE structure including the following:

- The MSE is a flexible structure capable of tolerating higher than usual differential settlement. In this study, a differential settlement over 2% of the wall height was induced to simulate foundation failure, with no perceptible distress in the facing panels and steel reinforcement strips.
- The parametric numerical studies have indicated more stress release/redistribution for more flexible reinforced soil composit subsequently leasing to lower fouundation stresses.
- When isolated pockets of poor bearing soils are encountered, there is stress redistribution to areas with sufficient bearing capacity.
- The limiting failure criteria for the eccentricity check is too punitive. The simulation of the differential settlement resulted in an eccentricity closer to L/34 compared to the L/6 given by the design, thus, a less conservative bearing stress modification factor of about 1.1 for worst case foundation support instead of 1.5.

- The observed eccentricity reduced with increasing surcharge load intensity contrary to the design assumptions.
- Even with the inclusion of a compromising feature to sabotage the foundation, the measured stresses were still closer to the geostatic stresses compared to the Meyerhof's equivalent rigid footing approach adopted in current design.
- If sufficiently compacted, the MSE attains a heightened stiffness due to the provision of confinement by the tensile inclusions and can withstand load with little to no distress whatsoever to the reinforcement.
- It has been shown through measurements and numerical analyses that the confining walls in the MSE experiment affected some of the results, a more compliant media should be used on the sidewalls of chambers and containers for future experiments especially when angular backfill materials are used and/or when deformation measurements are paramount.
- Instrumentation should be deployed in zones of any expected external influence to enable subsequent evaluation of the influence.
- More field cases should be sufficiently instrumented to give a better understanding of the behavior of reinforced fill walls in various conditions.

7.2 Limitations

The experimental results presented herein are subject to the limitations of the size of the geochamber. Every effort was made to create a plane strain condition in the central part of the MSE structure, but edge boundary affects were unavoidable. The experiment was limited to a single construction, so the material types and properties were unique to the test. The numerical results were based on thousands of hours of computer computations to simulate the construction of the MSE system and provide insight into the sensitivity of these results to a range of soil

parameters and geometric configurations. These models were limited by the capabilities of Plaxis3D version 8 and computational time.

7.3 Recommendations for Future Work

- The work covered herein addresses the bearing stress function, however, on the other hand, evaluation of the bearing capacity also assumes a rigid footing. So, these design assumptions are doubly punitive to the design outcomes of reinforced soil walls. It will be useful to conduct a physical experiment starting with reduced scale testing using Digital Image Correlation as well as numerical analyses to investigate the bearing capacity factors for reinforced soil walls.
- A study that applies further differential settlement to push the system to the limit would give beneficial information on the behavior of MSE walls at ultimate states.
- Conduct experiments to subject the reinforced soil system to a much larger external loading.
- Conduct a test using weak backfill materials to see if the retained fill lateral stress eventually gets transmitted to the foundation of the reinforced soil.
- The department of transportation should consider the development of a database of reinforced soil systems with documented properties, instrumentation, and load response data for sites in Alabama.

REFERENCES

AASHTO 2007. “LRFD Bridge Design Specifications: 4th Edition, with 2008 and 2009 Interims.” American Association of State Highway and Transportation Officials, Washington, D.C.

AASHTO 2010. “LRFD Bridge Design Specifications” 5th Edition, American Association of State Highway and Transportation Officials, Washington, D.C.

AASHTO. 2014. “LRFD Bridge Design Specifications, 7th Edition.” American Association of State Highway and Transportation Officials *Washington, D.C.*

ASTM. 2004. “D3080-04 Standard Test Method for Direct Shear Test of Soils Under Consolidated Drained Conditions.” ASTM International, West Conshohocken, Pennsylvania.

ASTM. 2019. “D6598-19 Standard Guide for Installing and Operating Settlement Points for Monitoring Vertical Deformations.” ASTM International, West Conshohocken, Pennsylvania.

ASTM. 2020. “A449-14 Standard Specification for Hex Cap Screws, Bolts and Studs, Steel, Heat Treated, 120/105/90 ksi Minimum Tensile Strength, General Use.” ASTM International, West Conshohocken, Pennsylvania.

ASTM. 2020. “C136/C136M-19 Standard Test Method for Sieve Analysis of Fine and Coarse Aggregates.” ASTM International, West Conshohocken, Pennsylvania.

ASTM. 2020. “D7181-20 Standard Test Method for Consolidated Drained Triaxial Compression Test for Soils.” ASTM International, West Conshohocken, Pennsylvania.

ASTM. 2021. “A370-21 Standard Test Methods and Definitions for Mechanical Testing of Steel Products.” ASTM International, West Conshohocken, Pennsylvania.

Bastick, M., Schlosser, F., Segrestin, P., Amar, S., and Canepa, Y. 1993. “Experimental Reinforced Earth Structure of Bourron Marlotte: Slender Wall and Abutment Test” *Renforcement Des Sols: Experimentations en Vraie Grandeur des Annees 80*, Paris, pp. 201-228

Bentley 2012. "Modelling soil-structure interaction: interfaces." Bentley communities: Plaxis-3D. https://communities.bentley.com/products/geotech-analysis/w/plaxis-soilvision-wiki/45944/modelling-soil-structure-interaction-interfaces.

Bentley 2021a. "Plaxis 3D: Material Models Manual." Plaxis connect edition v21.01. Last updated: March 04, 2021. https://communities.bentley.com/cfs-file/__key/communityserver-wikis-components-files/00-00-00-05-58/PLAXIS3DCE_2D00_V21.01_2D00_03_2D00_Material_2D00_Models.pdf

Bentley 2021b. "Plaxis 3D: Reference Manual." Plaxis connect edition v21.01. Last updated: March 04, 2021. https://communities.bentley.com/cfs-file/__key/communityserver-wikis-components-files/00-00-00-05-58/PLAXIS3DCE_2D00_V21.01_2D00_02_2D00_Reference.pdf

Bentley 2021c. "Plaxis 3D: Scientific Manual." Plaxis connect edition v21.01. Last updated: March 04, 2021. https://communities.bentley.com/cfs-file/__key/communityserver-wikis-components-files/00-00-00-05-58/PLAXIS3DCE_2D00_V21.01_2D00_04_2D00_Scientific.pdf

Berg, R. R., Christopher, B. R., and Samtani, N. C. 2009. “Design of Mechanically Stabilized Earth Walls and Reinforced Soil Slopes – Volume I” Publication No. FHWA-NHI-10-024,

Federal Highway Administration, Washington, DC. https://www.fhwa.dot.gov/engineering/geotech/pubs/nhi10024/nhi10024.pdf

Bomag. 2023. “Technical Data Multipurpose Compactor BMP 8500.” September 10, 2023, from https://www.bomag.com/us-en/machinery/categ;ories/light-equipment/bmp-8500-72013/

Budge, A. S. 2004 "Analytical and Numerical Investigation of a Mechanically Stabilized Earth Wall on I-15". All Graduate Theses and Dissertations. 8059. *Utah State University*. DOI:10.26076/d10f-f49e. https://digitalcommons.usu.edu/etd/8059.

Budge, A., S., Bay, J., A., and Anderson, L., R. 2006. “Calibrating Vertical Deformations in a Finite Element Model of an MSE Wall”. *GeoCongress 2006*. https://doi.org/10.1061/40803(187)243

Campbell Scientific. 2023. “4WFBS120, 120-Ohm, Four-Wire Full-Bridge Terminal Input Module.” Retrieved August 29, 2023, from https://www.campbellsci.com/4wfbs120

Cedergren, H.R. 1989. “Seepage, Drainage, and Flow Nets, Third Ed.”, John Wiley and Sons, New York.

Christopher B. R. 1993. “Deformation Response and Wall Stiffness in Relation to Reinforced Soil Wall Design.” Purdue University e-Pubs: AAI9420806. https://docs.lib.purdue.edu/dissertations/AAI9420806/

Christopher, B.R., Gill, S.A., Giroud, J.P., Juran, I. Schlosser, F., Mitchell, J.K. and Dunnicliff, J. 1990. “Reinforced Soil Structures. Volume I. Design and Construction Guidelines.” U.S. Department of Transportation, Federal Highway Administration, Washington D.C., Report No. FHWA-RD-89-043, 287 p.

Clayton, C.R.I., Woods, R.I., Woods, R.I., and Milititsky, J. 2014. "Earth Pressure and Earth-Retaining Structures (3rd ed.)". *CRC Press*. https://doi.org/10.1201/b16967

Clough, G.W., Duncan, J.M. 1991. "Earth Pressures." In: Fang, HY. (eds) Foundation Engineering Handbook. *Springer, Boston, MA*. https://doi.org/10.1007/978-1-4615-3928-5_6

Coulomb, C. A. 1776. "Essai sur une application des règles de maximis & minimis à quelques problèmes de statique, relatifs à l'architecture." *De l'Imprimerie Royale, Paris.*

Damians, I.P., Bathurst, R.J., Josa, A., and Lloret, A., 2014. "Numerical study of the influence of foundation compressibility and reinforcement stiffness on the behavior of reinforced soil walls". *International Journal of Geotechnical Engineering*, 8(3): 247-259. http://dx.doi.org/10.1179/1939787913Y.0000000039

Damians, I.P., Bathurst, R.J., Josa, A., and Lloret, A., 2015. "Numerical Analysis of an Instrumented Steel-Reinforced Soil Wall". *International Journal of Geomechanics*, Vol. 15, No. 1. https://doi.org/10.1061/(ASCE)GM.1943-5622.0000394

Damians, I.P., Bathurst, R.J., Lloret, A., and Josa, A. 2016. "Vertical Facing Panel-Joint Gap Analysis for Steel-Reinforced Soil Walls". *International Journal of Geomechanics*, 16(4): 04015103. https://doi.org/10.1061/(ASCE)GM.1943-5622.0000632

Damians, I.P., Bathurst, R.J., Olivella, S., Lloret, A., and Josa, A. 2021 "3D modelling of strip reinforced MSE walls". *Acta Geotech*. 16, 711–730 (2021). https://doi.org/10.1007/s11440-020-01057-w

Elias, V., Christopher, B. R., and Berg, R. R. 2001. "Mechanically Stabilized Earth Walls and Reinforced Soil Slopes: Design and Construction Guidelines (Updated Version)." *National*

Highway Institute & Federal Highway Administration. FHWA-NHI-00-043. https://rosap.ntl.bts.gov/view/dot/48689

Farrag, K. and Morvant, M. 2004. "Evaluation of Interaction Properties of Geosynthetics in Cohesive Soils: LTRC Reinforced Soil Test Wall." 379 (2004): n. pag. Web. 16 May 2017.

Hatami, K., and Bathurst, R.J. 2005. "Development and Verification of a Numerical Model for the Analysis of Geosynthetic-Reinforced Soil Segmental Walls under Working Stress Conditions." *Canadian Geotechnical Journal*, 42(4), doi:10.1139/T05-040

Holtz, R. D. and Kovacs, W. D. 1981. "An Introduction to Geotechnical Engineering." Prentice Hall. New Jersey.

Ingold, T. S. 1982. "Reinforced earth." Thomas Telford, London

Jaky, J. 1948. "Pressure in silos". Vol. 1, 103–107.

Jewell, R. A. and Wroth, C. P. 1987. "Direct shear tests on reinforced sand." *Géotechnique* 37 (1), 53-68. https://doi.org/10.1680/geot.1987.37.1.53

Jones, C.J.F.P. 1996. "Earth Reinforcement and Soil Structures." Thomas Telford. ASCE Press

Kezdi, A. 1972. "Stability of Rigid Structures." *Proceedings, 5th European Conference on Soil Mechanics and Foundation Engineering*, Vol 2, 105-130.

Leshchinksy, D., Berkheimer, S., A., and Meehan, C., L. 2007 "Instrumented Geogrid Reinforced Mechanically Stabilized Earth Wall Undergoing Large Settlement." Order No. 1444648 University of Delaware, 2007. Ann Arbor: *ProQuest.*

Liang, R. Y., and Almoh'd, I. M. 2004. "Instrumentation Monitoring Results of an Instrumented Reinforced Earth Wall: Comparison with Current Practice". Transportation Research Record 2004 1868:1, 53-67. https://doi.org/10.3141/1868-06

Mayne, P. W., and Kulhawy, F. H. 1982. "K0-OCR relationships in soil". Vol. 108 *(GT6)*, 851–872.

Meyerhof, G. G., 1953, "The Bearing Capacity of Foundations Under Eccentric and Inclined Loads," Proceedings of the Third International Conference of Soil Mechanics and Foundation Engineering, Vol. 1, pp. 225-244.

Mohr, O. 1900. "Welche Umstande Bedingen die Elastizitatsgrenze und den Bruch eines Materiales?" Zeitschrift des Vereines Deustcher Ingenieure, Vol. 44, pp. 1524-1530; 1572-1577

Murray, R. T., and Farrar, D. M., 1990, "Reinforced Earth Wall on the M25 Motorway at Waltham Cross," Proceedings Institution of Civil Engineers, Part 1, No. 88, pp. 261282.

NAVFAC, 1982. "Foundations and Earth Structures." *Design Manual* 7.02 86. Department of the Navy Facilities Engineering Command, Alexandria, Virginia 22332-2300. https://web.mst.edu/~rogersda/umrcourses/ge441/DM7_02.pdf

Nicks, J. E. 2013. "Friction Angles of Open Graded Aggregates from Large-Scale Direct Shear Testing." Report No. *FHWA-HRT-13-068*, Federal Highway Administration, Mclean, VA.https://www.fhwa.dot.gov/publications/research/infrastructure/structures/bridge/13068/13068.pdf

Okafor, C. C., Dunlop S., Anderson, J. B., and Montgomery, J. 2023. "Laboratory Testing and Model Calibration of a Crushed Stone Backfill in a Geosynthetic Reinforced Soil Wall."

IS-Porto 2023 8th International Symposium Proceedings. https://www.issmge.org/uploads/publications/121/122/isdcg2023-76-1-c.pdf

Potts, D. M., and Zdravkovic, L. 2001. "Finite Element Analysis in Geotechnical Engineering Application." Thomas Telford.

Rankine, W. 1857. "On the Stability of Loose Earth." *Royal Society of London.*

RECo. 2018. "Mechanically Stabilized Earth Walls." Reinforced Earth Brochure. The Reinforced Earth Company – USA https://reinforcedearth.com/content/uploads/2018/07/Brochure_Reinforced_Earth_2.pdf

RECo. 2019. "Pullout Resistance and Apparent Coefficient of Friction (f*) of High Adherence (HA) Reinforcing Strips in AASHTO MSE Backfill." The Reinforced Earth Company – USA Tech Bulletin 2019.

RECo. 2020. "Construction and Quality Control Manual.", Reinforced Earth Construction Manual: Square Panels v2020.1. The Reinforced Earth Company – USA

RECo. 2023. "The 2002's ammunition storage igloo for the Battle Creek Air National Guard in Michigan." *LinkedIn*. https://www.linkedin.com/posts/the-reinforced-earth-company_throwback-to-2002s-ammunition-storage-igloo-activity-7072604498183028736-ztPU?utm_source=share&utm_medium=member_desktop (last accessed 6/18/2024)

Runser, D. J., Fox, P. J., and Bourdeau, P. L. 2001. "Field performance of a 17 m-high reinforced soil retaining wall". *Geosynth Int* 8(5):367–391. DOI: 10.1680/gein.8.0200

Sakleshpur, V. A., Prezzi, M., and Salgado, R. 2017. "Performance assessment of MSE abutment walls in Indiana." Joint Transportation Research Program Publication No.

FHWA/IN/JTRP-2017/06. West Lafayette, IN: Purdue University. https://doi.org/10.5703/1288284316390

Schlosser, F., and Long, N. T. 1974. “Recent results in French research on reinforced earth.” J. Constr. Div., 100(3), 223–237.

Schlosser, F., Bastick, M. 1991. “Reinforced Earth. In: Fang, HY. (eds) Foundation Engineering Handbook.” Springer, Boston, MA. https://doi.org/10.1007/978-1-4757-5271-7_21

Stuedlein, A., W., Allen, T. M, Holtz, R., D., Christopher, B., R., 2011. “Assessment of Reinforcement Strains in Very Tall Mechanically Stabilized Earth Walls.” *Journal of Geotechnical and Geoenvironmental Engineering* 138.3 (2011): 345–356.

Stuedlein, A., W., Michael Bailey, Doug Lindquist, John Sankey, and William J. Neely. 2010. "Design and Performance of a 46-m-High MSE Wall." *Journal of Geotechnical and Geoenvironmental Engineering* 136.6 (2010): 786-96.

Terzaghi, K., Peck, R.B., and Mesri, G. 1996. “Soil Mechanics in Engineering Practice, Third Ed.”, John Wiley & Sons, New York, pp 330-332.

Tschebotarioff, G. P. 1973. “Foundations, Retaining and Earth Structures: The Art of Design and Construction and its Scientific Basis in Soil Mechanics.” *Mcgraw-Hill, New York.*

Wang, R., Liu, H., Kutter, B. L., and Zhang, J. 2023. “Influence of Centrifuge Test Soil-Container Friction on Seismic Sheet-Pile Wall Response in Liquefiable Deposit: Insights from Numerical Simulations.” *J. Geotech. Geoenviron. Eng.* Vol 149(9) pp 04023068 1-14. https://ascelibrary.org/doi/abs/10.1061/JGGEFK.GTENG-11064

Wood, D. M. 2014. Geotechnical Modelling. CRC Press, Florence.

Woods, R. I., and Jewell, R. A. 1990. “A computer design method for reinforced soil structures.” *Geotextiles and Geomembranes*, Volume 9, Issue 3, pp 233-259, ISSN 0266-1144, https://doi.org/10.1016/0266-1144(90)90055-H

Yan Yu, Richard J. Bathurst, Tony M. Allen, and Renald Nelson. 2016. “Physical and numerical modelling of a geogrid-reinforced incremental concrete panel retaining wall.” *Canadian Geotechnical Journal*. 53(12): 1883-1901. https://doi.org/10.1139/cgj-2016-0207

Yang, Z. 1972. “Strength and deformation characteristics of reinforced sand.” Ph.D. dissertation, University of California, Los Angeles.

APPENDIX A: MSE WALL CONSTRUCTION AND TESTING

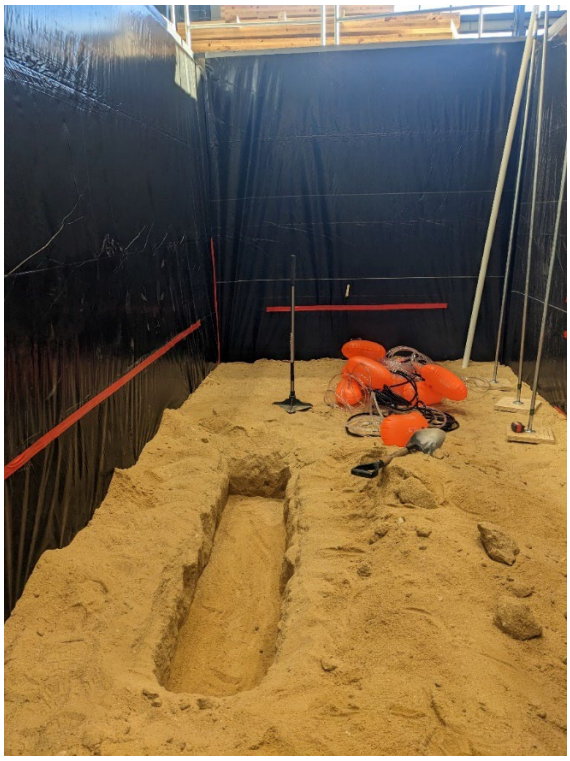

Figure 137. Installing air bladders to induce settlement.

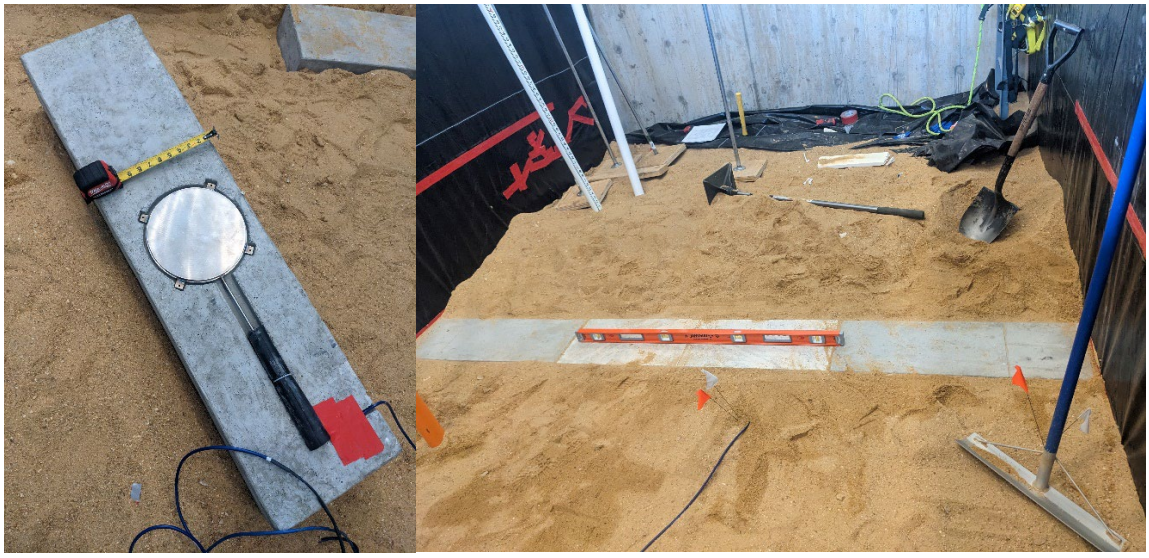

Figure 138. Installation of leveling pad.

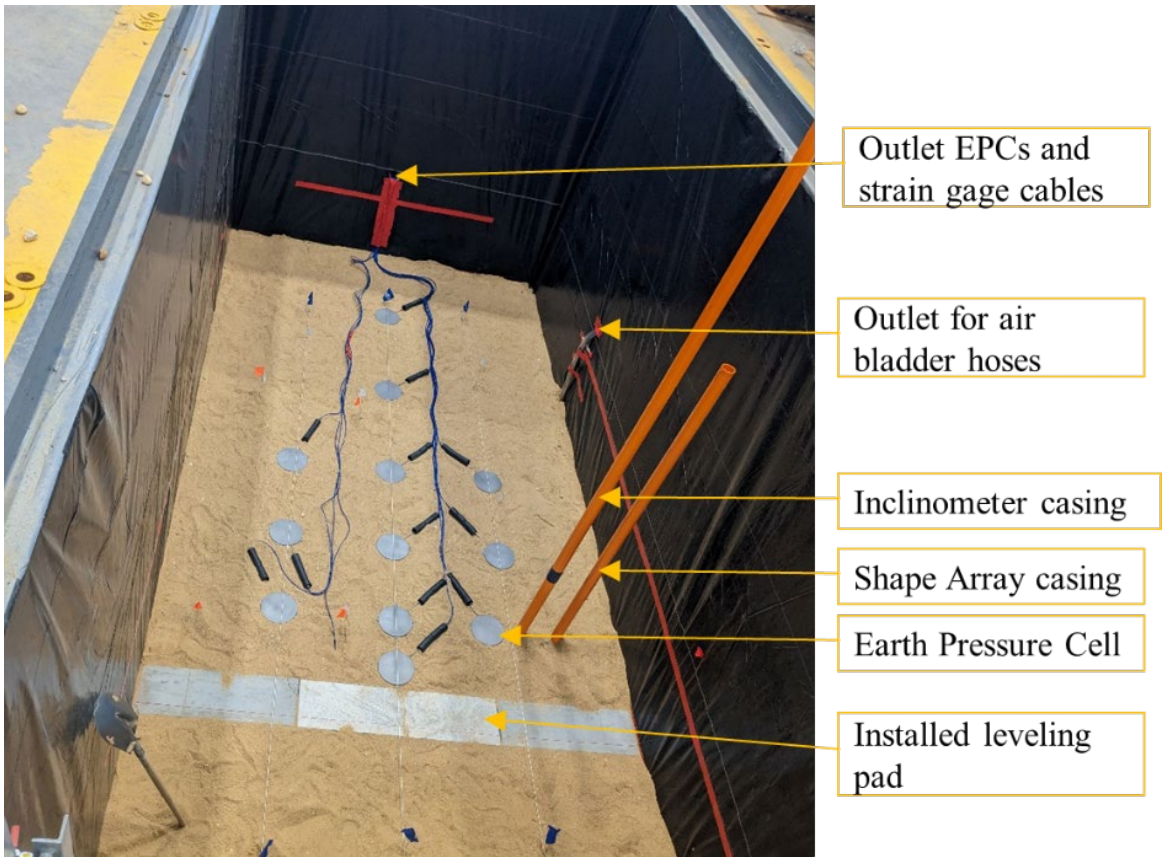

Figure 139. Image showing installed leveling pad and placed earth pressure cells.

Figure 140. (left) first panel placed with external bracing and wedge. (right) Image showing Styrofoam filling.

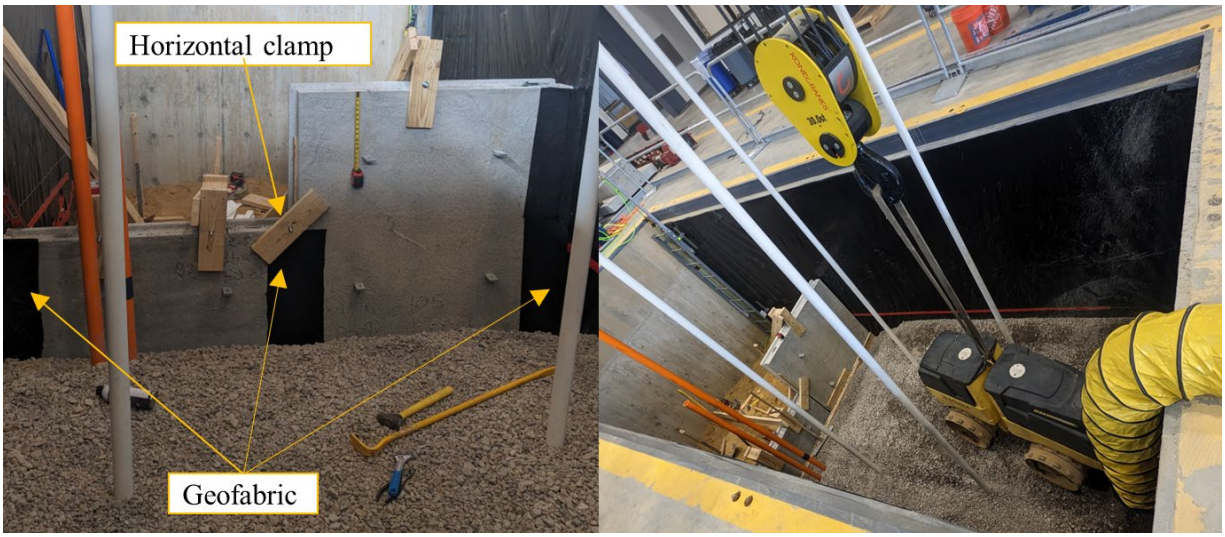

Figure 141. (left) first row of panels placed showing placed geofabric. (right) compaction of first lift of backfill.

Figure 142. (left) first row of panels with reinforcement. (right) strain gage cable protection and cutting of PVC pipe.

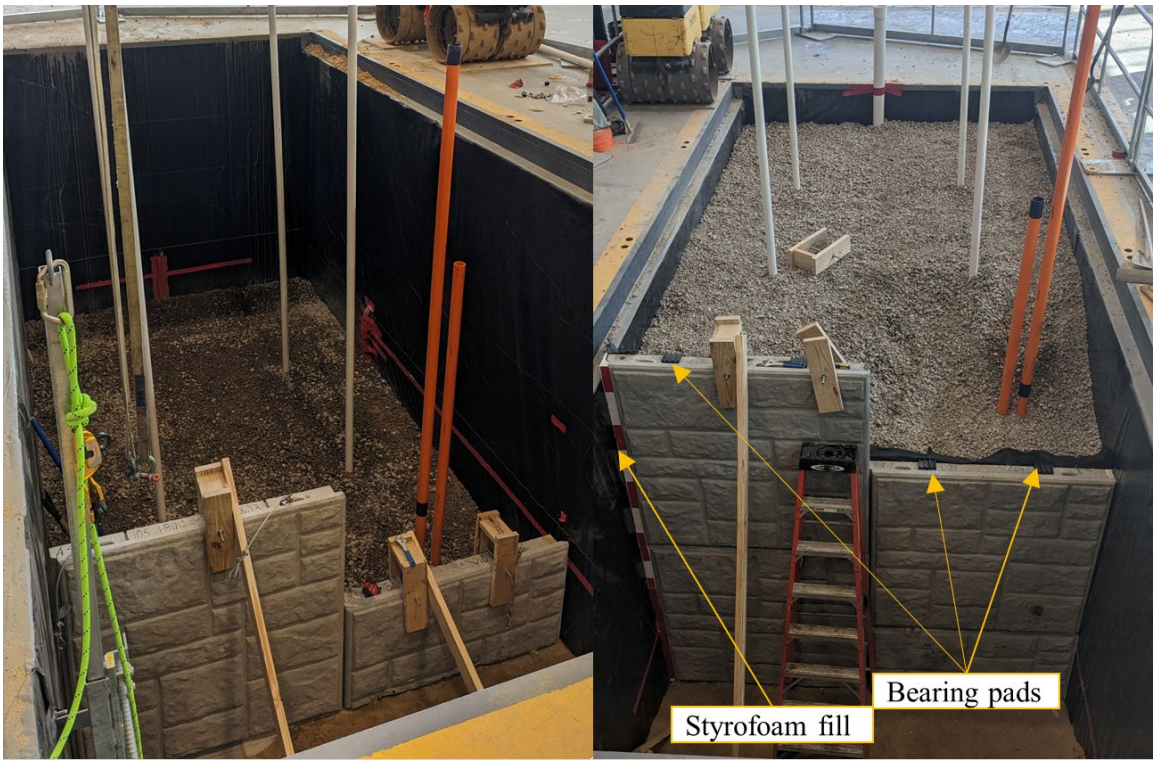

Figure 143. (left) first row of panels placed with external bracing and wedge. (right) second row of panels placed with external bracing and wedge.

Figure 144. Placing confining walls and tractor tubes.

Figure 145. Wall construction completed.

Figure 146. Final Wall Surcharge Loading

Figure 147. Apparent confinement effect resulting in near vertical face of the granular backfill during dismantling.

APPENDIX B: MSE WALL TESTING RESULTS

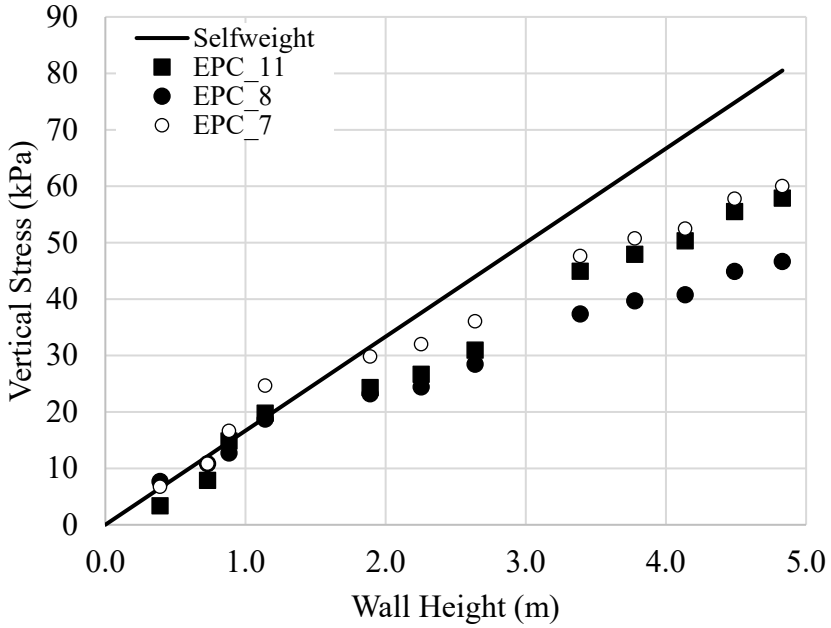

Figure 148. Stress history with wall height for earth pressure cells in Line 1.

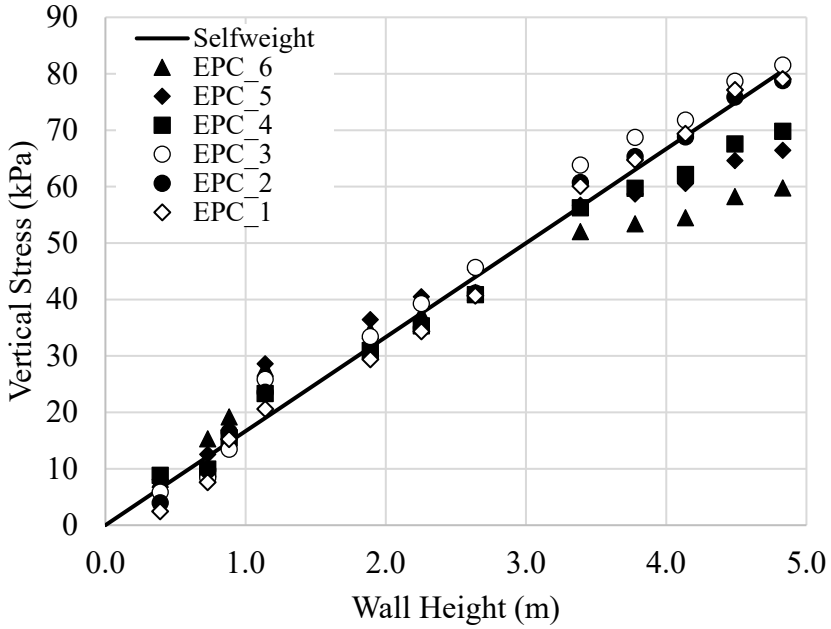

Figure 149. Stress history with wall height for earth pressure cells in Line 2

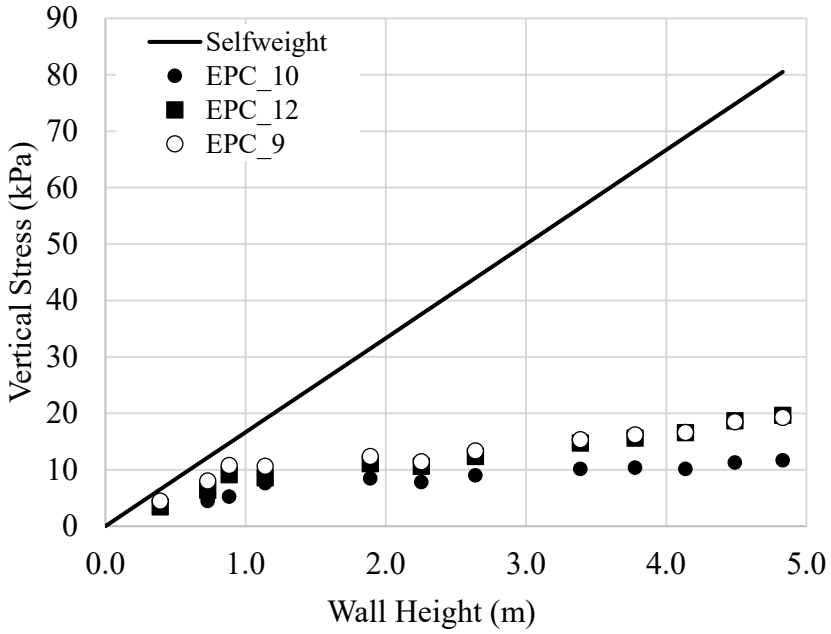

Figure 150. Stress history with wall height for earth pressure cells in Line 3

APPENDIX C: 3D FINITE ELEMENT MODELLING OF MSE WALLS

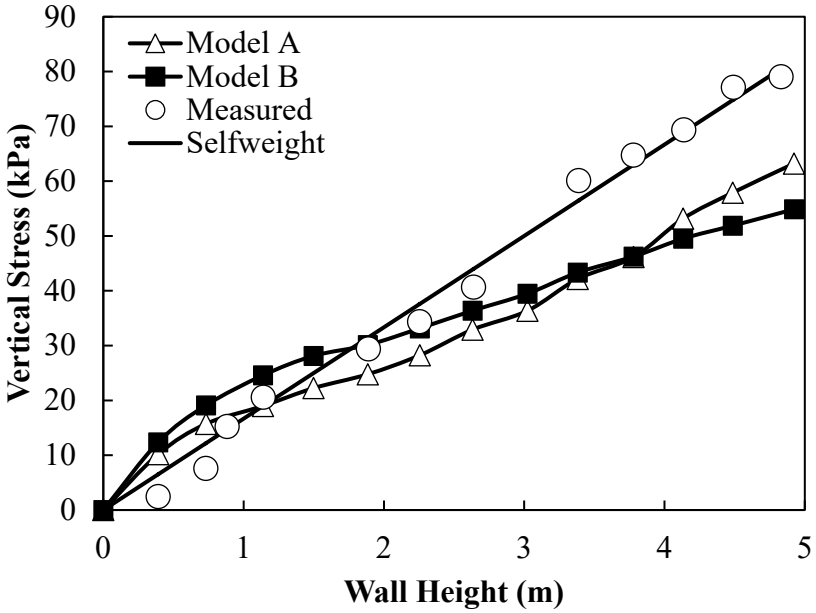

Figure 151. Stress history with height including geostatic stresses, measured values, and numerical simulation results for EPC_01

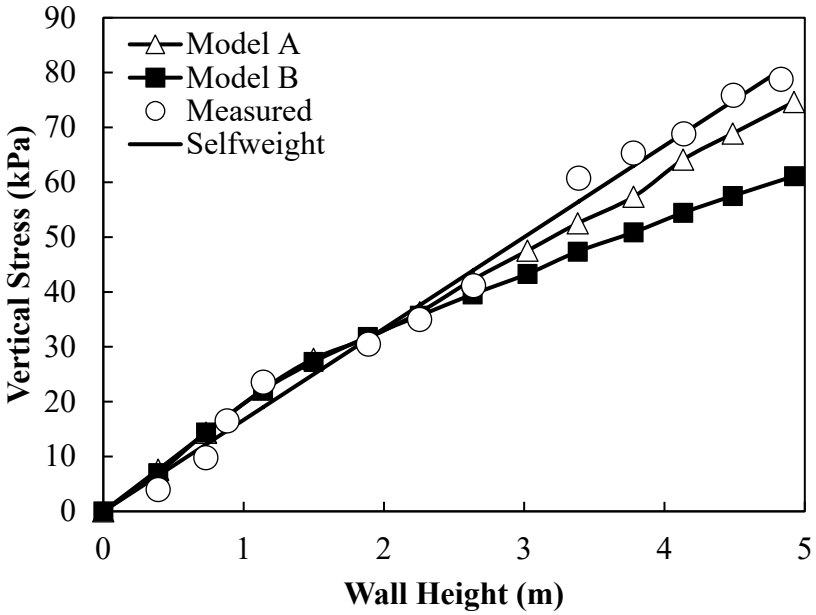

Figure 152. Stress history with height including geostatic stresses, measured values, and numerical simulation results for EPC_02

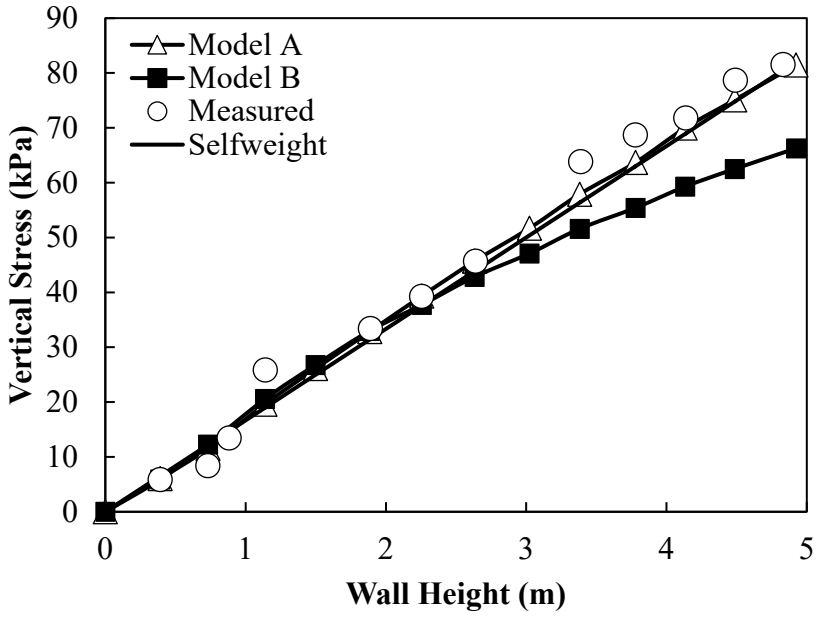

Figure 153. Stress history with height including geostatic stresses, measured values, and numerical simulation results for EPC_03

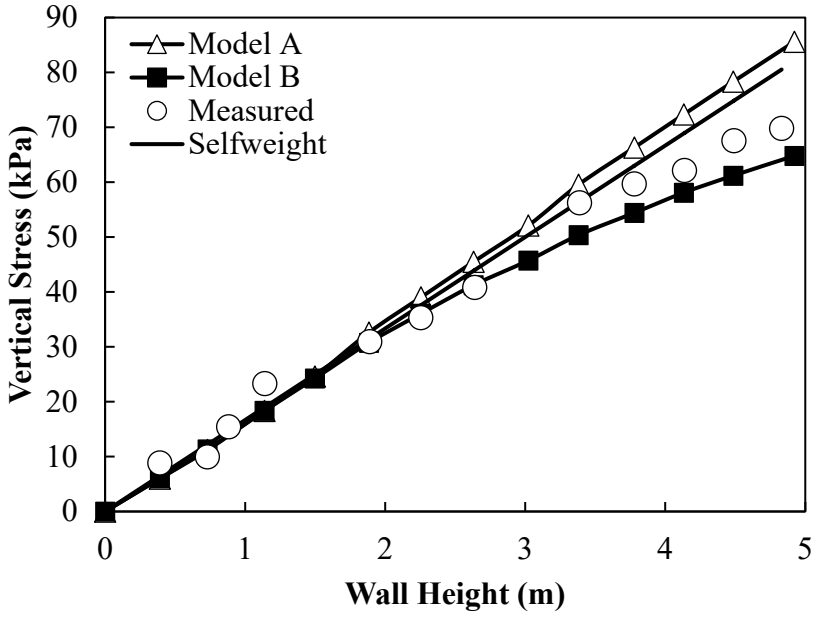

Figure 154. Stress history with height including geostatic stresses, measured values, and numerical simulation results for EPC_04

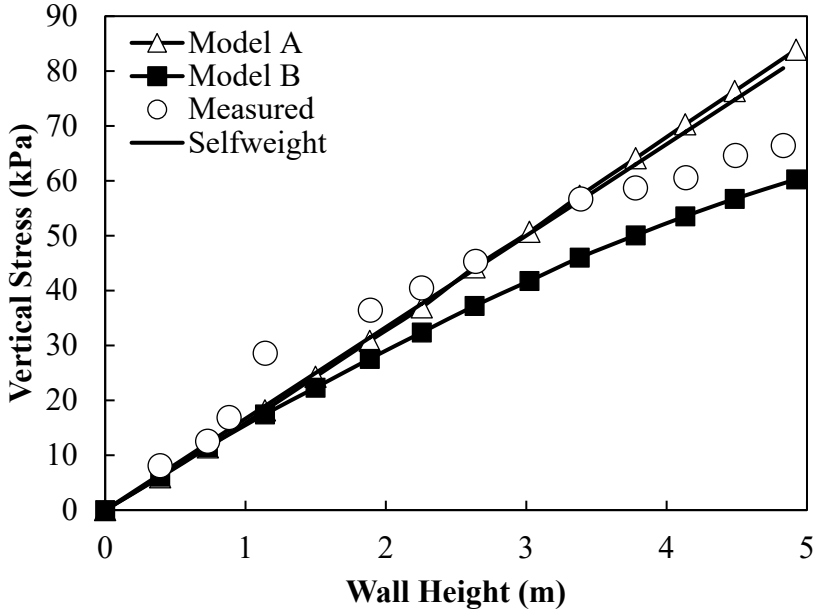

Figure 155. Stress history with height including geostatic stresses, measured values, and numerical simulation results for EPC_05

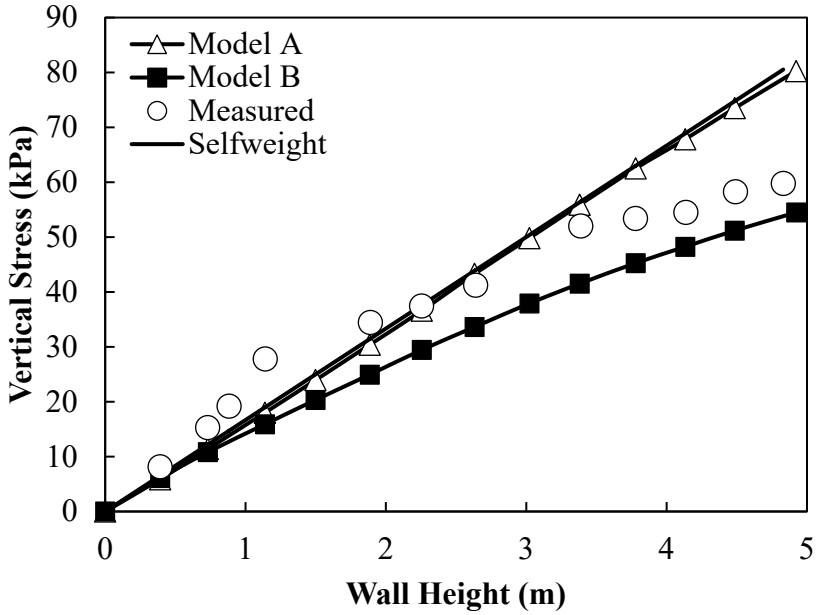

Figure 156. Stress history with height including geostatic stresses, measured values, and numerical simulation results for EPC_06

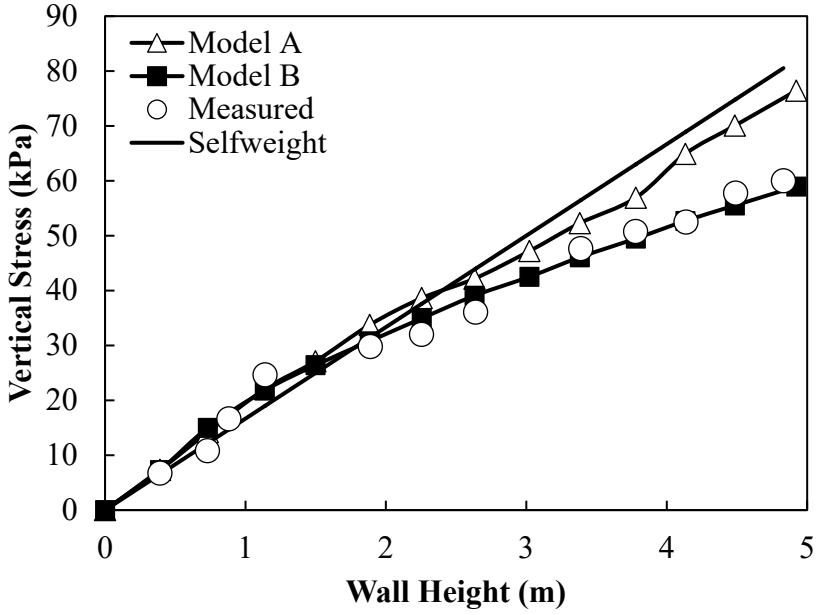

Figure 157. Stress history with height including geostatic stresses, measured values, and numerical simulation results for EPC_07

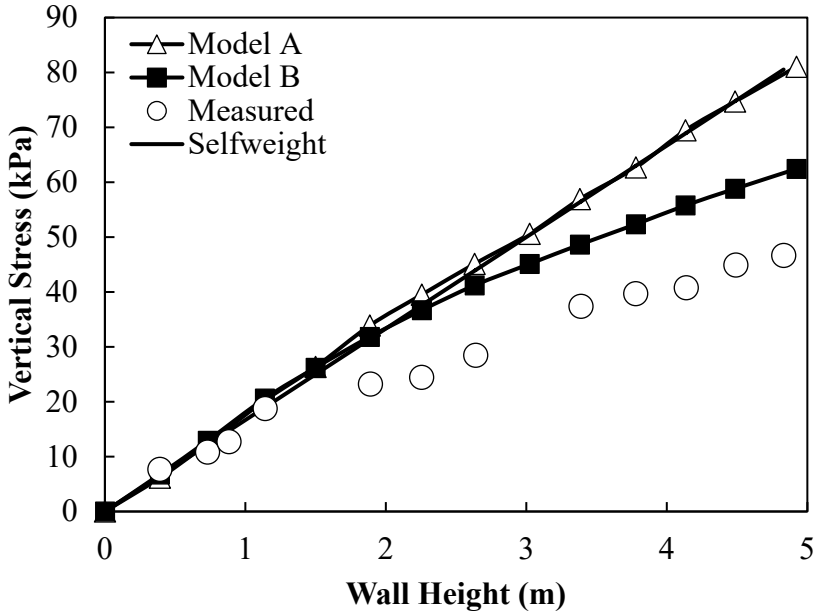

Figure 158. Stress history with height including geostatic stresses, measured values, and numerical simulation results for EPC_08

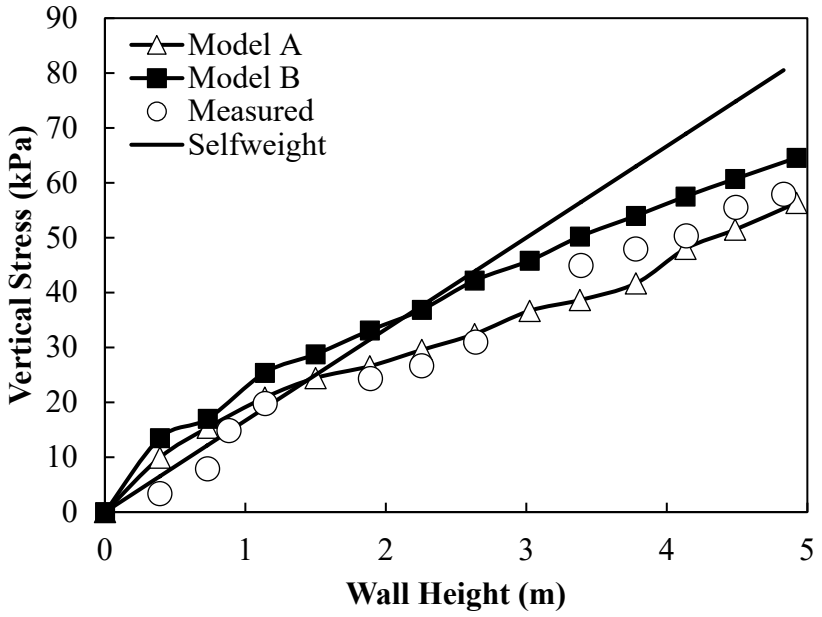

Figure 159. Stress history with height including geostatic stresses, measured values, and numerical simulation results for EPC_11

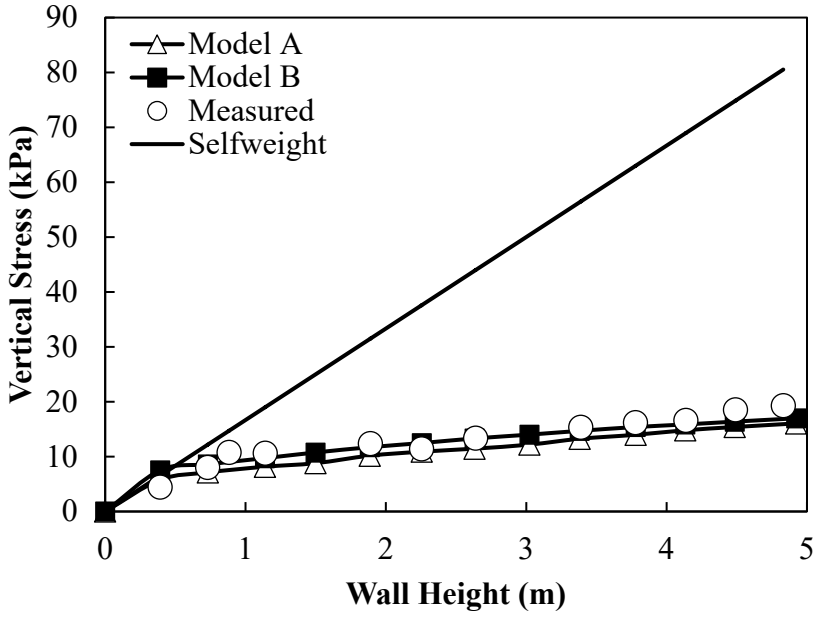

Figure 160. Stress history with height including geostatic stresses, measured values, and numerical simulation results for EPC_09

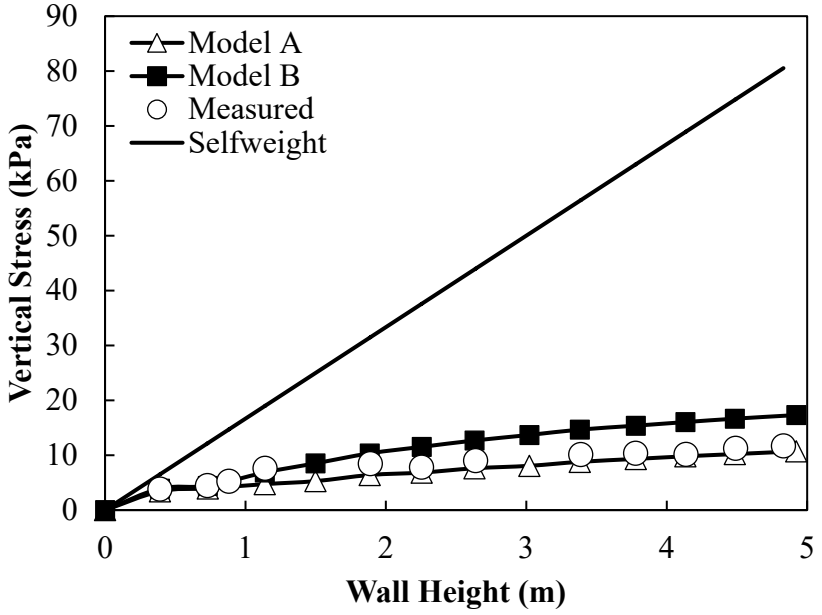

Figure 161. Stress history with height including geostatic stresses, measured values, and numerical simulation results for EPC_10

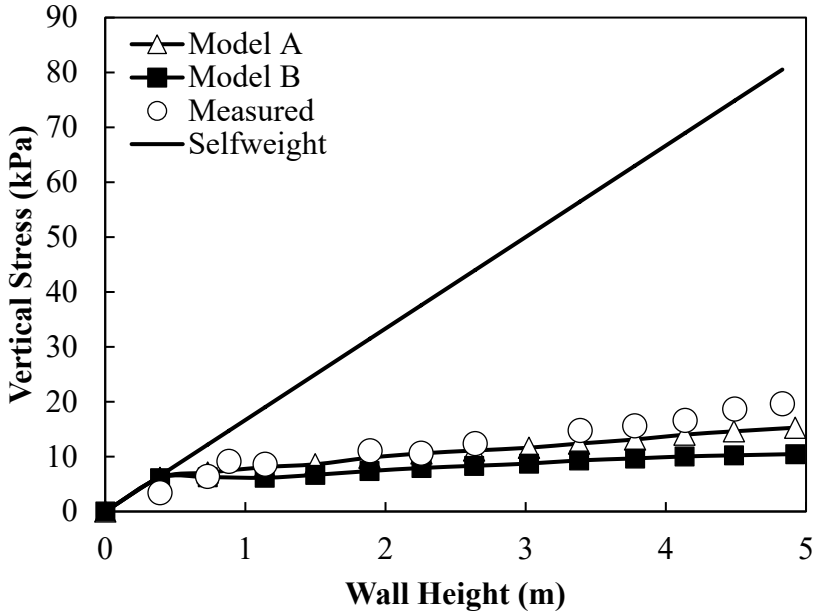

Figure 162. Stress history with height including geostatic stresses, measured values, and numerical simulation results for EPC_12